High-Resolution Experimental Measurements and Mechanistic Modelling of Saturated Cryogenic Pool Boiling Heat Transfer

by

Florian Chavagnat

M.S.E. Energy and Propulsion, National Institute of Applied Sciences of Rouen, 2016

Submitted to the Department of Nuclear Science and Engineering in partial fulfillment of the requirements for the degree of

Doctor of Philosophy in Nuclear Science and Engineering

at the

MASSACHUSETTS INSTITUTE OF TECHNOLOGY

MAY 2024

Authored by: Florian Chavagnat
Department of Nuclear Science and Engineering
April 9, 2024

Certified by: Matteo Bucci
Esther and Harold E. Edgerton Associate Professor of Nuclear Science and Engineering
Thesis Supervisor

Certified by: Emilio Baglietto
Professor of Nuclear Science and Engineering, Associate Department Head
Thesis Supervisor

Accepted by: Ju Li
Battelle Energy Alliance Professor of Nuclear Science and Engineering and Professor of Materials Science and Engineering
Department Committee on Graduate Students

High-Resolution Experimental Measurements and Mechanistic Modelling of Saturated Cryogenic Pool Boiling Heat Transfer

by

Florian Chavagnat

Submitted to the Department of Nuclear Science and Engineering on April 9th, 2024
In partial fulfillment of the requirements for the degree of
Doctor of Philosophy in Nuclear Science and Engineering

ABSTRACT

Refueling cryogenic rockets in low Earth orbits has the potential to significantly enhance the duration and the reach of future space missions. However, the development of such capabilities is not without challenges, which exacerbated by the complexity and the cost of testing such equipment in microgravity, e.g., a fuel depot placed in orbit. The low boiling point of cryogenic fuels (hydrogen, methane, oxygen) makes them prone to boil when transferred through superheated pipes, or simply stored in fuel tanks, resulting in the presence of two-phase mixture. Boil-off gas can lead to pressurization of components like fuel line and tanks, cause two-phase flow instabilities during fuel transfer, or significantly reduce the usable amount of cryogenic fuel. Progresses in multiphase computational fluid dynamics (mCFD) can be leveraged to predict the two-phase flow behavior in such cases. However current boiling models offer poor prediction accuracy of the boiling heat flux in most applications, but also miss critical boiling characteristics, e.g., the amount of vapor produced.

This thesis proposes a fully closed formulation of a mechanistic boiling model adapted to saturated cryogenic pool boiling. The model leverages exhaustive measurements of boiling parameters. A new pool boiling setup was designed for that purpose, using pressurized nitrogen as a proxy for cryogenic fuel. The apparatus allows to measure the typical boiling curves, i.e., boiling heat flux and wall temperature, measurement of dry area fraction, triple contact line density as well as more fundamental parameters such as bubble lift diameter, nucleation frequency and nucleation site density among others. The heating surface inclination was varied between 0° (upward facing horizontal) and 179° (downward facing horizontal) to probe for the effect of buoyancy on the boiling parameters and overall heat transfer.

The analysis of individuals bubble using both phase-detection and shadowgraphy showed the lack of microlayer. Instead, the large size of the bubble footprint observed experimentally strongly suggested an intense evaporation process at the triple contact line of the bubbles and occurring right after nucleation. Based on this observation, the evaporation rate at the triple contact line has been indirectly estimated on numerous bubbles and appeared consistent with analytical models describing such evaporation mechanism in other fluids. In the tested operating conditions, the linear evaporation rate was measured at around 5 W/m, accounting for 20% of the boiling heat flux. The amount of heat removed by quenching of the heating surface through transient conduction has also been evaluated using phase-detection recordings and was

shown account for an additional 20% of the boiling heat flux. The remaining portion of the boiling heat flux could be explained by neither triple contact evaporation nor transient conduction during quenching.

The heat flux partitioning model proposed in this work allows to predict the quenching heat flux, the triple contact line evaporation as well as the observed dry area fraction, contact line density and bubble density during nitrogen boiling. Minimal effect of surface inclination has been observed on the nucleate boiling heat transfer, except at the departure from nucleate boiling.

Thesis Co-supervisor: Matteo Bucci

Title: Esther and Harold E. Edgerton Associate Professor of Nuclear Science and Engineering

Thesis Co-supervisor: Emilio Baglietto

Title: Professor of Nuclear Science and Engineering, Associate Department Head

ACKNOWLEDGEMENTS

First, I would like to thank both of my thesis supervisors, Prof. Matteo Bucci and Prof. Emilio Baglietto. This work would not have been possible with your help and guidance over the years. This work, the first work on cryogenic boiling of our laboratory, has been filled with challenges that I could face with the comfort of your support.

Next, I would like to thank Dr. Bren Phillips. You have a bottomless well of advice throughout this Ph.D. thesis. I cannot be grateful enough for the hours of your time you dedicated helping me design experiments. I would like to acknowledge the members of the Redlab and Greenlab for the enjoyable environment they brought. These years of work have been delightful thanks to you.

I would also like to acknowledge Dr. Jason Hartwig at NASA to be part of my thesis committee and for supporting this research financially and intellectually. I would like to thank Dr. Ashvin Hosangadi at Craft-Tech for supporting this project as well. I would also like to thank Prof. Jacopo Buongiorno for chairing my thesis defense.

Finally, I would like to thank my parents Carole and Richard, and my brother Tony for their support all these years. To my dad, you have been my role-model and I owe you my education and the opportunity of pursuing this doctorate.

TABLE OF CONTENTS

LIST OF FIGURES

LIST OF TABLES

1. INTRODUCTION

1.1. Motivations

Cryogenic liquids are fluids with a boiling point below -150ºC at atmospheric pressure [1]. This class includes the liquid states of several diatomic gases (Nitrogen, Oxygen, Hydrogen), some of the noble gases (Helium, Argon, Neon, Krypton), a hydrocarbon gas (Methane) and a halogen (Fluorine). From the first liquefaction of oxygen in 1887, cryogenic liquids have been used in countless applications, and obtained a special interest in modern applications, after 1950s. In the gas industry, cryogenic liquids are used as intermediate media for the transportation and storage of gases. In the medical field, the use of cryogenic liquids allowed major breakthroughs like the development of Magnetic Resonance Imaging and the conservation of living tissues, like blood, over a long period of time. Cryogenically-cooled electronics have led to the development of efficient infrared cameras and superconducting electronics, used in military industry or in physics and earth science research. Finally, the space industry has been a major consumer of cryogenic liquids. Apart from their uses in numerous pieces of satellite equipment (e.g., spectrometer, sensors [2]), liquid hydrogen and liquid oxygen have been used in rocket engines as propellant and cooling fluids [3]. The very high energy density of liquid hydrogen allows the design of very efficient rocket engines, i.e., producing high thrust per mass of burned LH_2/LOx mixture. Despite several advantages, the use of LH_2 as propellant for space mission is severely hindered by the difficulty of its storage, which requires, as for all cryogens, the use of efficient insulation to overcome the large gradient of temperature between the environment and its low boiling temperature (20 K at atmospheric pressure), and large container due to its low density (0.07 g/cm^3, compared to the 1 g/cm^3 of LOx). This issue is currently driving research to store cryogenic liquids, like LH_2/LOx in low earth orbit in fuel depots, to allow an intermediate refueling in space between the rocket launch and the completion of the space missions [4, 5].

Boil-off naturally occurs when storing cryogens due to the difficulty of perfectly insulating cryogenic tanks from ambient heat. The same situation will occur for cryogenic fuel depots in space, with the heat from the environment almost exclusively consisting of background radiation (mostly from telluric or solar origin). The amount of fuel boiling-off will depend how much heat is transferred from the environment to the cryogen, including boiling of the propellant itself inside the vessel. Accurate prediction of the heat transfer become are necessary to prevent by design large losses of fuel through boil-off and to design safety features (e.g., relief valve). During operations, predicting boil-off is crucial for the management of the stored cryogens (i.e., maximizing its use, plan for refueling, etc.)

Chilling down rocket engine components and transfer lines between future spacecrafts and fuel depot has an additional set of challenges. Chilling down engine components and fuel transfer lines is a necessary step to prevent boiling of the propellant within the different pieces of cryogenic equipment and parts. Two-phase flow limits the flow of propellant due to the very low density of vapor, may create flow instabilities, and also destructive vibrations and cavitation [6]. Quenching, which consists of bringing down the temperature of the components to the saturation temperature of the cryogens (20 K for LH_2 at atmospheric pressure), is conveniently performed by using the propellant itself. Thus, more fuel than the one strictly needed for propulsion needs to be transported.

For these reasons, intensive research has been initiated to optimize the chill-down process of rocket engine components and transfer lines as well as the boil-off of cryogenic tanks, with the end goal of minimizing the loss of cryogens [7-10] during operations, allowing cost-effective space-missions.

1.2. Cryogenic boiling

1.2.1. General aspect and current modelling issues

Cryogenic chill-down consists of a complex multi-stage heat transfer process lowering the temperature of a component or a transfer line from its initial temperature down to the inlet temperature of the flowing cryogenic liquid, usually equal to its saturation temperature. At any point of the transfer line, four distinct, consecutive heat transfer regimes are commonly observed as the wall temperature drops to the liquid inlet temperature. Figure 1.1 shows a qualitative plot of the boiling curve during chill-down. When the cryogenic liquid starts flowing through a relatively hot line (e.g., a tube at room temperature), it almost instantaneously forms a vapor film on the tube surface. This heat transfer regime is called film boiling (1. in Figure 1.1). Once the wall temperature drops below the Leidenfrost temperature (LFP), quenching starts with a partial and intermittent contact between the liquid phase and the tube surface. This is the so-called transition boiling regime (2.). When the wall temperature goes below the temperature of departure from nucleate boiling, the whole heating surface is quenched intermittently at the rhythm of bubbles nucleation cycles (3.). Finally, below the wall temperature required for bubbles to nucleate (ONB point in Figure 1.1), the whole heating surface is only in contact with the liquid phase and heat excess remaining in the transfer line is carried out by liquid single-phase heat transfer (4.).

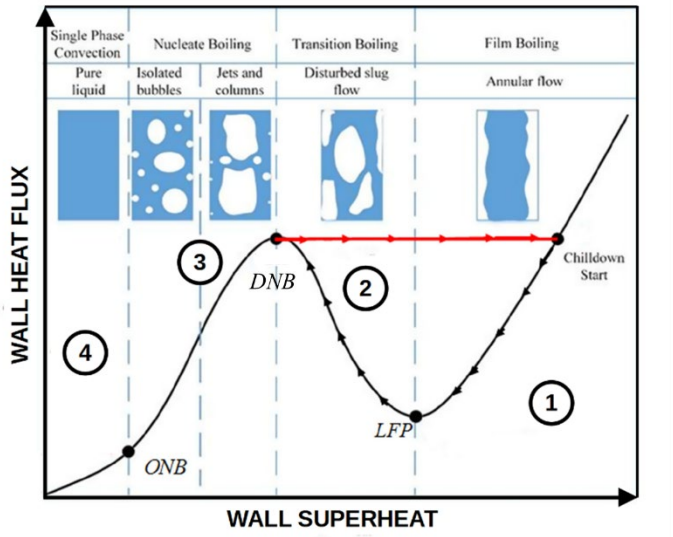

Figure 1.1. Typical chill-down curve drawn in black, taken from Hartwig et al. [9]. The arrows indicate the direction of time.

These heat transfer regimes are very diverse in term of involved mechanisms. For instance, nucleate boiling heat transfer is largely dominated by vapor bubbles nucleating and growing on the heated surface, while film boiling heat transfer is dominated by heat conduction and radiation through a continuous vapor film in contact with the surface and by droplets impinging the surface intermittently. For this reason, prediction of boiling heat transfer during quenching has been usually done by modeling each regime separately. In the case of cryogenic boil-off in the fuel depot, the situation is simpler as the boiling surface (corresponding to the inner surface of the tank in contact with the cryogenic fuel) is kept at wall superheat below the point of DNB, i.e., within heat transfer regimes of liquid single-phase convection (4) and nucleate boiling (3).

Hartwig et al. [9] recently published an exhaustive review on how state-of-the-art boiling correlations perform in predicting the heat transfer coefficients measured in selected cryogenic quenching experiments. This review covers 14 correlations in both nucleate boiling and film boiling heat transfer, developed between 1966 and 2014. As reference, Hartwig used boiling data obtained in quenching experiments from 7 published sources totalizing roughly 30,000 data points. Overall, the study highlights the lack of accuracy of available correlations to predict cryogenic boiling heat transfer, irrespective of the boiling regime. However, errors are particularly significant in the nucleate boiling regime. None of the 10 correlations tested in this boiling regime can predict the boiling heat transfer coefficient with a reasonable accuracy over the entire range of experimental data. The best and most recent correlation, developed by Mustafi [11] using data obtained with Helium IV, overpredicts all sets of experimental data by 500%, while other correlations show overpredictions as much as 20,000%, with a very broad range of predictive error from data set to data

set. Multiple factors can explain the poor accuracy observed in most correlations as detailed in Ref. [9]. However, it is worth mentioning that overpredictions of heat transfer coefficient are particularly significant over liquid hydrogen data, even against correlation specifically targeting cryogens (e.g., Shah's correlation [12]). This suggests importance differences in boiling behavior between hydrogen and higher temperature cryogens (e.g., nitrogen or argon), likely related to the peculiar physical and thermal properties of hydrogen as we will illustrate in the next section.

We can note that this mismatch between cryogenic boiling data and correlation prediction is not recent and not limited to data performed in quenching tests. In 1984, Shah [12] compared several available boiling heat transfer correlations with heat transfer coefficient measurements in cryogenic flow boiling. Only correlations accounting for the surface physical properties were considered, as they are known to influence significantly boiling heat transfer [13]. Shah showed that none of the reviewed correlations (i.e., Shah [12], Klimenko [14] and a superposition model using Rohsenow's correlation [15]) could predict within 30% the heat transfer coefficient over the 240 data points used as reference.

As discussed previously, the use of cryogens for space applications brings the question of the effect of microgravity on cryogenic boiling heat transfer, or in other words, the effect of suppressing buoyancy. Unfortunately, only few studies of cryogenic boiling in microgravity are available. Most of the work concerns tube quenching with liquid nitrogen (Antar and Collins [16], Darr et al. [17,18], Kawanami et al. [19], Chung et al. [20], Hartwig et al. [21]) with no detailed analysis of the nucleate boiling regime.

1.2.2. Cryogens physical properties and peculiarities

Countless correlations have been published in literature to estimate nucleate boiling heat transfer coefficients for both non-cryogenic and cryogenic fluids (see Ref. [9]). These correlations are always semi-empirical and their range of validity is typically as narrow as the range of experimental data points used to derive them, resulting in a wide range of predictive errors between correlations and different sets of experimental data [9]. Boiling is a very complex phenomenon to model, even with common fluids (e.g., water), and the use of the much less experimented cryogenic fluids adds up to this complexity. The physical and thermal properties of cryogenic fluid differ significantly from more commonly experimented fluids such as water, as shown by Table 1.1. With exception of hydrogen and helium, cryogens share similar properties in addition to their low boiling point (see fluids framed in red in Table 1.1): a density ratio ρ_V/ρ_L slightly higher than water at atmospheric pressure, a lower specific latent heat, a lower liquid thermal conductivity and a lower surface tension. A certain proximity exists in terms of physical properties between some refrigerants (R114 or R134-a), dielectric (FC-72) and the cryogens framed in red in Table 1.1, e.g.,

similar specific latent heat, surface tension, and liquid/vapor density ratio. The same applies to pressurized water and the cryogens (in red) when we look at the liquid dynamic viscosity for instance. Since the similarity in thermal and physical properties between cryogens and any other fluid is not obvious, it is incautious to predict the boiling behavior of cryogens using experimental data of fluid that are easier to work with (e.g., FC-72) without a thorough understanding of all the heat transfer mechanism involved. Table 1 also highlights the difference of properties between hydrogen and higher temperature cryogens. Specific experimental studies with hydrogen are seemingly required to assess how the differences in properties translates into differences in boiling behavior.

Table 1.1. Physical properties of water and common cryogenic fluids and refrigerants (NIST [22])

Properties at saturation and atmospheric pressure unless otherwise mentioned		T_{SAT} [K]	ρ_V/ρ_L (*10^3)	h_{lv} [MJ/kg]	ε_L [kWs$^{1/2}$/m^2/K]	k_L [W/m/K]	μ_L [µPa.s]	σ [N.m]
Reference	Water	372.8	0.62	2.26	1.656	0.679	283.3	0.059
	Water (1 MPa)	453	5.80	2.17	1.620	0.673	150.0	0.042
	Water (10 MPa)	584	80.67	1.32	1.490	0.527	81.8	0.012
Dielectric	FC-72	327	8.20	0.10	0.324	0.057	436	0.008
Refrigerants	R114	276.4	5.09	0.14	0.316	0.068	441.9	0.014
	R134-a	246.8	3.77	0.22	0.428	0.104	380.3	0.015
Cryogens	Nitrogen	77.4	5.73	0.20	0.490	0.146	160.6	0.009
	Oxygen	90.2	3.92	0.21	0.542	0.152	195.8	0.013
	Argon	87.3	4.14	0.16	0.443	0.126	270.7	0.013
	Neon	27.1	7.95	0.08	0.590	0.155	116.1	0.005
	Methane	111.7	4.31	0.51	0.520	0.184	116.7	0.013
	Hydrogen	20.4	18.8	0.45	0.268	0.104	13.3	0.002
	Helium-4	4.2	134.7	0.02	0.111	0.019	3.2	≈8*10^{-5}

Researcher have found a certain number of peculiarities about cryogenic boiling associated with the physical differences between cryogens and more commonly used fluids. Stephan and Abdelsalam [13] showed that the heat transfer coefficients measured in pool-boiling experiments are particularly sensitive to the thermal properties of the heating surface at low temperature. They suggested that this behavior is due to the larger variability in the solid thermal properties of the surface or, potentially, in the wettability of the surface (i.e., the liquid-solid contact angle) at low temperatures. Recently, Bombardieri and Manfletti [23] measured boiling heat fluxes in a LN_2 pool-boiling setup with 3 different heating surfaces (copper, aluminum and stainless steel) and observed different boiling heat transfer behaviors, corroborating the

findings of Stephan and Abdelsalam [13]. However, their study does not allow to elucidate the reasons of the observed behavior. The experimental results of several investigators also suggest that cryogenic boiling is very sensitive to frozen impurities. Müller-Steinhagen [24] published a review on the effect of fouling in cryogenic boiling from liquid impurities. The experimental results of Müller-Steinhagen [25] showed that the addition of only 5 ppm of dissolved CO_2 in liquid nitrogen is sufficient to cause a normally stable boiling state to slowly and spontaneously transition to a boiling crisis within an hour. Bewilogua et al. [26] reported a similar behavior in liquid hydrogen at high heat flux, where the temperature of the heated surface was spontaneously drifting at a rate of 0.5 K/min. Even though the effect of fouling on cryogenic boiling have been identified experimentally, it is yet not clear mechanistically how frozen impurities alter the boiling heat transfer process. Cryogens are known to wet most surfaces with static contact angles commonly reported below 15°, and often down to few degrees[27, 28]. Brennan and Skrabek [29] published detailed measurements of contact angle for oxygen and nitrogen using a tilted plate method at atmospheric pressure and for different surfaces. On clean metallic plates (aluminum and platinum), they measured static contact angles below 10°. While no uncertainty measurement was associated with the measurement, in practice, an uncertainty about +/- 10° is usually the norm for this kind of measurement (with low contact angle values). The contact angle, and in general the wetting properties of the liquid, plays a critical role on the bubble dynamics in nucleate boiling (from bubble nucleation to bubble departure and lift-off, also including possible bubbles coalescence). Some consequences of highly wetted liquids on boiling heat transfer will be discussed in Section 1.4 The need for models which can predict with accuracy the nucleate boiling heat transfer regime with cryogenic fluid is evident. Several methods are available to develop such models and one could generate a correlation based on dimensional analysis and optimize a set of coefficients with experimental data. However, like the correlation presented by Stephan and Abdelsalam [13], the model will likely suffer from the lack of predictability outside the fitting conditions.

1.3. Mechanistic modeling of cryogenic boiling heat transfer

1.3.1. Model description

Mechanistic boiling models, e.g., Heat Flux Partitioning models, offer the possibility to predict boiling heat transfer over wide range of operating conditions. They consist in de-constructing the boiling process into elementary mechanisms (e.g., microlayer evaporation, natural circulation, etc.) and predicting mechanistically their contribution to the overall heat transfer process. Thus, these models start from a high-fidelity description of the involved physical mechanisms.

A first heat flux partitioning model was introduced by Browning [30] to evaluate the void fraction in a heated channel with subcooled flow boiling water (with application for nuclear reactors). Due to the subcooling conditions, only a portion of boiling heat flux is transferred to the flow by producing vapor. The partitioning model proposed by Browning [30] allowed a decomposition of boiling heat flux such that the amount of vapor generated can be calculated. Later, Mikic and Rohsenow [31] proposed an alternative formulation by with two components: transient conduction heat flux occurring after bubble departure from active nucleation sites and natural circulation on the area of the heating surface which does not boil. Judd and Hwang [32] proposed the addition of a component to account for the evaporation of a liquid microlayer forming underneath growing bubbles, which they observed in dichloromethane pool-boiling. Thus, according to Judd and Hwang [32], the boiling heat flux can be partitioned as:

$$q''_{\mathrm{tot}} = q''_{\mathrm{c}}(N'', D_{\mathrm{d}}, h_{\mathrm{c}}) + q''_{\mathrm{q}}(N'', D_{\mathrm{d}}, f) + q''_{\mu\mathrm{L}}\left(N'', f, V_{\mu\mathrm{L}}\right) \tag{1.1}$$

where q''_{c}, q''_{q}, and $q''_{\mu\mathrm{L}}$ represent the liquid convective heat flux, the quenching heat flux and the evaporation heat flux, accounting for the evaporation of the microlayer, respectively. These heat flux terms depend on several boiling parameters, the active bubble nucleation site density N'', the bubble departure diameter D_{d}, the frequency of nucleation at a particular nucleation site f, the volume of evaporating microlayer underneath bubbles $V_{\mu\mathrm{L}}$, and the single-phase convective heat transfer h_c accounting for the heat removed by conduction and natural circulation where no boiling occurs. Judd and Hwang [32] showed that model predictions were consistent with heat flux measurements, when the required boiling parameters were experimentally obtained. Unfortunately, these boiling parameters, such as the volume of evaporated microlayer, are very difficult to predict with dedicated closure models limiting the use of Judd and Hwang's partitioning approach.

To circumvent this issue, Kurul and Podowsky [33] proposed an alternative partitioning formulation. In their model, they approximated the mass of liquid microlayer as equal to the total mass of vapor in the bubble at departure. This assumption is not rigorous, as part of the heat required to grow the vapor bubble is already included in the quenching term q''_{q}. However, this formulation avoids the issue of predicting the volume of liquid microlayer. Therefore, Kurul and Podowsky [33] provided a closed formulation of heat flux partitioning with a specific model for each unknown boiling parameter (i.e., D_{d}, f and N''). By construction, the accuracy of any heat flux partitioning model over broad range of conditions is limited by how well all the boiling mechanisms are understood and modeled. Despite the simplification introduced by Kurul and Podowsky, developing accurate closure models is particularly challenging as explained by Dhir [34], and requires thorough experimental works. Figure 1.2 shows the mind map of the mechanistic boiling model developed at MIT for flow boiling of water [35]. On this mind-map, each circle represents a

particular mechanism (e.g., bubble lift-off) which often depends on more elementary mechanisms and physical properties (i.e., in the lift-off case, we have buoyancy, surface tension, etc…).

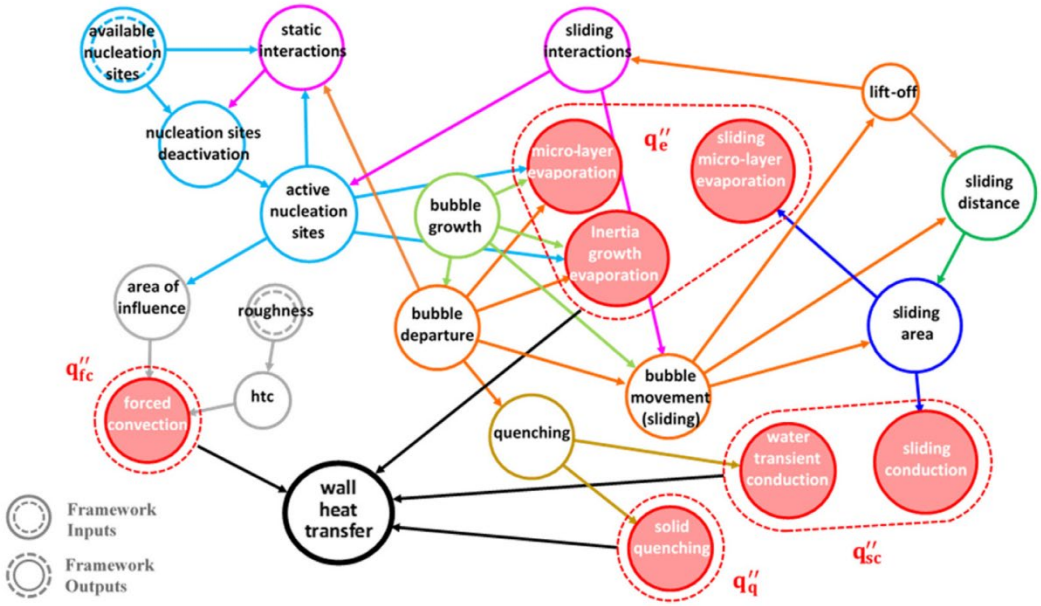

Figure 1.2. Mind map of the boiling heat transfer mechanisms [35].

It should also be noted that heat flux partitioning models are typically build using only average quantities (c.f. Kurul Podowsky [33]). E.g., the bubble departure diameter used in Eq. 1.1 is in fact the average diameter that one would observe for an infinite set of departing bubbles. By doing so, it is assumed that these quantities are statistically independent. In general, this is not correct as stressed by numerous models relating D_d and f (c.f. Zuber [36], Cole [37] and others). However, it is not clear yet how large is the error introduced by this assumption.

Recent experimental works (e.g., see Ref [38]) have shown using infrared thermometry and high-speed video measurement on flow boiling water that heat flux partitioning models can predict with some success the correct boiling heat flux decomposition and overall heat transfer. However, accurate predictions come with the cost of collecting exhaustive measurement of boiling parameters which are required to draw the model's closure formulations (as discussed above). For cryogens, such experimental data are not available or only partially available as discussed hereafter which limits significantly the development of a heat flux partitioning model. One of the main reasons is simply the lack of experimental technique to measure the different boiling parameters, since infrared thermometry (used in boiling water) ceases to be a solution at low temperature.

1.3.2. Current limitations in experimental data

Numerous boiling experiments with cryogenic liquids have been performed over the last 70 years. Extensive reviews of cryogenic steady-state boiling experiments have been published by Brentari [39] and Stephan and Abdelsalam [13], while a list of the published quenching experiments can be found in Hartwig et al. [9]. However, only a few of the proposed experiments have measurements of the boiling parameters required for the development of heat flux partitioning closure models. Table 1.2 list these published experiments. Among these experiments, Kirichenko et al. [43] reported bubble departure diameters and bubbles time scales (wait time and growth time) at low heat flux in pool boiling of LN_2 and LO_2 at different pressures. At each tested pressure, the heat flux was kept around 3 kW/m^2 in LO_2 and 2 kW/m^2 in LN_2, limiting the measurements to near-ONB conditions. As a reference, CHF is commonly measured between 100 and 300 kW/m^2 with these fluids in their operating conditions [39]. Chen et al. [42] reported similar measurements in CH_4. Bland et al. [39] measured bubbles growth from nucleation to departure in LN_2 on sub-millimetric artificial conical cavities with a mouth cavity radius between 73 to 190 µm. All bubbles were also obtained by heating the metallic stage with a low heat flux, around 1 kW/m^2, with a corresponding wall superheat around 1 K. It is worth noting that the measurements performed by Bland et al. show slower bubble growth (typ. in $R \propto t^{\frac{1}{3}}$) than observed experimentally by Kirichenko et al. [43] and predicted by Mikic'sgrowth model [45], both showing a growth in $R \propto t^{\frac{1}{2}}$ indicative of heat-diffusion controlled growth. This translates to significantly larger growth times in the experiment of Bland et al. (i.e., between 65 and 475 ms) compared to growth times between 2 and 31 ms in LN_2 and LO_2 measured by Kirichenko et al. [43] and between 10 and 30 ms in CH_4 measured by Chen et al. [42]. No measurement of individual bubble length scale and time scale has been published with flat heaters at high heat flux as well as no measurement of bubble nucleation sites densities irrespective of the heat flux. No evidence about the presence of liquid microlayer during bubble growth has reported either.

Table 1.2. Published experimental works with measurements of boiling parameters

Author	Type of experiment	Heating geometry[1] and surface condition	Fluid	Conditions	Output of the experiments[2]
Kida et al. [40]	Pool boiling	Platinum wire	N_2	Saturated at atm. pressure	Bubble departure diameter, nucleation frequency and nucleation site density
Jin et al. [41]	Pool boiling	Metallic plate (copper, brass and aluminum alloy), sandpapered to 5000# grit	N_2	Saturated at atm. pressure	Coalesced bubble departure diameter
Chen et al. [42]	Pool boiling	Nano-smooth copper plate	CH_4	Saturated at P = 0.15-0.4 MPa	Bubble departure diameter and frequency
Kirichenko et al. [43]	Pool boiling	Outer surface of polished 321 stainless steel tube	N_2	Saturated at P = 0.02-0.2 MPa	Bubble departure diameter, bubble nucleation frequency, bubble wait time and growth time
			O_2	Saturated at P = 0.01-0.08 MPa	
Kirichenko et al. [28]	Pool boiling	Downward-facing aluminum alloy and copper plate	N_2	Saturated at P = 0.02-0.9 MPa	Bubbles height and diameter during growth
		Downward-facing copper plate	O_2	Saturated at P = 0.01 MPa	
Bland et al. [44]	Pool boiling	Nano-smooth copper and brass plate with engineered cavities	N_2	Saturated at P = 0.10-0.31 MPa	Bubbles diameters from nucleation to departure
Bewilogua et al. [26]	Pool boiling	Stainless steel cylinder	H_2	Saturated at P=0.10-1.12 MPa	Bubble departure diameters and frequency

[1] All experiments have been performed with upward facing plate, except in Kida et al. [40] and Kirichenko [28].

[2] Space-averaged boiling heat flux and wall temperature have been measured in all experiments, except in Kirichenko [28] in which only the wall temperature is reported.

The observations and measurements of the published experiments listed in Table 1.2 are insufficient to develop a self-consistent heat flux partitioning model for cryogenic nucleate boiling. To do so, all boiling parameters must be measured in the same boiling conditions, which not only includes operating fluid, pressure, and temperature, but also heating surface conditions and material. Additionally, the knowledge of the boiling parameters is insufficient for the construction of a heat flux partitioning model as described in Section 1.3.1. The individual mechanisms themselves have to be known and described accurately, e.g., whether microlayer formation and evaporation can occur.

1.4. Objectives of the thesis and scientific questions

The work aims at developing a fully-closed formulation of heat flux partitioning for cryogenic fluids, by leveraging high-resolution diagnostics and measurements of boiling heat transfer of saturated nitrogen in pool boiling. This involves the measurement of all the necessary boiling parameters, the understanding of the different dominant boiling heat transfer mechanisms and the formulation of the partitioning model itself with the necessary set of closure models. Crucially, several scientific questions about cryogenic nucleate boiling mechanisms need to be answered. They are discussed hereafter.

Does heterogeneous spontaneous nucleation play a role in nucleate boiling of cryogenic fluids? Current theory of bubbles nucleation suggests that in room-temperature liquids, the low bubble nucleation temperature is driven by the presence of gases or contaminants in the cavities of the heated surface. In cryogenic liquid the situation may be different due to the potential lack of gas trapped inside surface cavities and the exceptionally low superheat required to nucleate without seeding (i.e., without vapor and non-condensable gases). The low contact angle of cryogenic fluids on most surfaces, typ. <15°, reduces the capability of cavities to retain vapor as understood from Bankoff's model [46]. The lack of non-condensable gases is due to the low boiling temperature of cryogens. In the case of liquid nitrogen, only helium, hydrogen and neon gas have a lower liquefaction temperature and are therefore susceptible to be dissolve in the liquid. Finally, calculations of the kinetic superheat limit and thermodynamic spinodal limit with liquid nitrogen suggest that the wall temperature required to nucleate in flooded cavity is drastically smaller than in water (see Ref. [47] for the expression of the limits). Both limits indicate a homogeneous nucleation occurring only few tens of degree above saturation in liquid nitrogen, and likely smaller in surface cavities, compared to the few hundreds of degrees in water at atmospheric pressure. It is therefore possible that heterogenous spontaneous nucleation, i.e., nucleation in cavities with no initial seeding (e.g., contaminants, trapped gas, etc.) contributes significantly to the overall boiling heat flux. This type of nucleation, occurring at a wall superheat about 20 K, was reported by Sakurai [48] and Shiotsu [49] in cryogenic pool boiling to explain direct transition between natural circulation and film boiling observed on heated surfaces with no prior boiling history and at pressure below 0.3 MPa. The heat flux observed at this point of direct transition to film boiling appeared to be significantly lower than the critical heat flux measured in case of departure from nucleate boiling, typically around 20 kW/m2 instead of 200-300 kW/m2 observed at DNB at higher pressure by the same authors. No observation of heterogenous spontaneous nucleation has been reported outside the research group of Sakurai. Instead, the measurements of boiling curves by other authors (Bewilogua et al. [26], Kida et al. [40] and more recently Jin et al. [41]) shows high heat flux in similar conditions, i.e., between 200 and 300 kW/m2 in saturated pool boiling of liquid nitrogen at atmospheric

pressure. This large difference may be explained by different operating procedures to collect the boiling data as well as the amount of non-condensable gases or impurities at the heated surface, which may vary from one study to the another.

There is an uncertainty on whether heterogenous spontaneous nucleation plays a role in cryogenic boiling. For modeling perspectives, it is critical to know if it does and in which conditions heterogenous spontaneous nucleation (HSN) should be considered. More generally, the bubble nucleation mechanism will determine the wall superheat required for the nucleation events to occur, and subsequently the bubble growth rate, nucleation site density and more generally the boiling heat transfer coefficients. A detailed visualization of the boiling surface with phase-detection and accurate measurement wall temperature is enough to clear this uncertainty. The occurrence of heterogeneous spontaneous nucleation, as described in Ref. [49], is only possible at wall superheat above ~20 K and should rapidly trigger a transition to film boiling.

Is cryogenic boiling heat transfer sensitive to dissolved contaminant?

Cryogens are notoriously pure compared to common fluids used in boiling heat transfer processes (e.g., water), with only small amounts of contaminants typically present in solution (e.g., the solubility of CO_2 in LN_2 is only ~ 10^{-5} g per kg [50]). Therefore, fouling phenomena in cryogens can easily be overlooked. Preliminary nucleate boiling experiments we conducted in a pool of saturated nitrogen with an initial purity of ~99.998%(vol) revealed solid particles on the boiling surface, as illustrated in Figure 1.3 using a phase-detection technique, which will be explained later on.

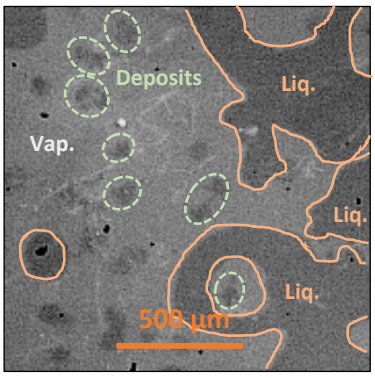

Figure 1.3: Phase-detection image of surface contamination after boiling nitrogen. The vapor in contact with the substrate appears light gray while the liquid and the deposits appear darker, and are highlighted in orange and green, respectively.

The deposits appeared at high heat flux, precipitating out of the boiling nitrogen and changing the aspect of the boiling surface and the boiling dynamics. The source or the nature of this contamination could not be assessed at the time. Many authors have experienced similar issues with various cryogens. Fouling phenomena have been reported in boiling nitrogen [51-54], hydrogen [26], oxygen [55], argon [24,55] and methane [55]. The effect of fouling is generally unwanted and detrimental for the reproducibility of experimental data, inducing uncertainties for boiling model development. The work Ortega et al. [56] highlighted significant repeatability issues of wall superheat measurements in nitrogen flow boiling and indicated fouling as potential cause.

Most of the literature studies reported a degradation of the cryogenic boiling heat transfer with fouling. Degradation of boiling heat transfer was observed either on boiling curves by cycling the heat input [26] or by maintaining a constant heat input overtime and monitoring the increase of the heated surface temperature [24, 51, 57, 58]. Except Scurlock [58], all cited works used heating elements consisting of metallic surfaces with mirror polish finish, either bare or coated with platinum [55] or gold [54]. A continuous degradation of boiling heat transfer on polished copper (e.g., as observed by Bland et al. [53] and Thome [51]) was attributed to the formation of a thermally resistive layer on the heating surface, as typical cryogenic contaminants such as ice water and carbon dioxide, exhibits rather low thermal conductivity, 1-10 W/m/K [59, 60]. Scurlock [58] explored the effect of fouling on different heating surfaces, polished and rough, by boiling contaminated nitrogen at a very low heat flux (1 to 2 W/cm^2) for long periods of time (up to 60 hr). While a degradation of the boiling heat transfer was observed on polished stainless steel and porous aluminum, a noticeable improvement was observed on polished aluminum. The heat transfer enhancement or degradation was monotonous in time. After a certain time, dependent on the surface, the boiling heat transfer coefficient would reach a constant asymptotic value, also surface dependent. The heat transfer improvement on certain surfaces appears inconsistent with the build-up of a thermally resistive layer. These observations suggest that the effect of fouling may depend on the surface finish, as surface finish may affect the boiling dynamics and the foulant deposition rate on the surface.

Interestingly, Müller et al. [57] observed clear heat transfer degradation flow boiling with argon after dissolution of carbon dioxide, but did not observe any degradation with liquid nitrogen, although the solubility of carbon dioxide in nitrogen and argon are similar. While Müller's observations are not consistent with liquid nitrogen results discussed above, they would explain that the inverted boiling curve hysteresis found with some cryogens are caused by fouling, as suggested by Müller-Steinhagen [24], and also observed by Kosky and Lyon in liquid argon and oxygen, but not in nitrogen [55].

Direct observations of cryogenic fouling have been extremely limited. Only Bewilogua et al. [26] noted the presence of a coating on their mirror-polished heated surface after boiling contaminated liquid hydrogen.

The coating vanished when the surface temperature reached about 60 K, suggesting that it consisted of solid nitrogen or oxygen. No details on the aspect of the coating were reported. To our knowledge, no author visualized the fouling formation and their effect on the boiling dynamics or boiling characteristics (e.g., on the nucleation site density) in cryogenic fluids.

The understanding on how cryogenic boiling heat transfer is modified by fouling of dissolved contaminants is relatively shallow. A deeper analysis of the topic will help to understand the source of the discrepancy observed in the literature data, to design better operating procedure to avoid repeatability issues in experimental investigations, and to support the development of ad-hoc models to predict the boiling heat transfer coefficient.

Do microlayers appear in saturated cryogenic boiling under terrestrial gravity?

Bubble growth occurs thanks to the evaporation of liquid, which can occur at the liquid-vapor interface. Figure 1.4 summarizes three possible types of evaporation we can have during bubble growth. The left case represents evaporation at the interface with the bulk liquid. Typical bubble growth model adopts this evaporation mechanism as the main source of the growth (e.g., Plesset and Zwick's model [47]), and treat bubble growth as a 1-D problem. Practically, this is not the only evaporation mechanism when boiling on a heated surface. Also, one should note that the surrounding liquid is only superheated when the bubble nucleates. As the bubble grows and the thermal boundary layer gets depleted, most of the bubble becomes surrounded by cooler liquid (at saturation or below saturation). Strong evaporation may occur at the base of the bubble, near the hot surface. Microlayer evaporation (shown in the middle of Figure 1.4) is very complicated phenomenon, which have been observed experimentally in various fluids (e.g., pool boiling water [61, 62], toluene [63], dichloromethane [32], ethanol [64]). Recent experimental work of Richenderfer et al. [38] with low pressure flow boiling water have shown that microlayer evaporation

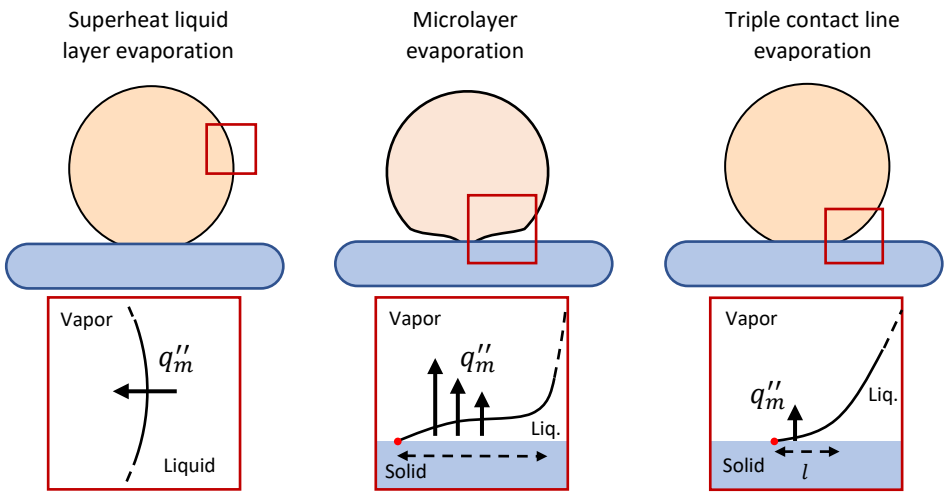

Figure 1.4. Schematics of evaporation mechanism at bubble's interface. q''_m represented the evaporated liquid mass flux during bubble growth.

can account for a significant part of the total boiling heat transfer, making it a critical component of any mechanistic boiling model. The liquid microlayer forms during bubbles growth when this growth is sufficiently fast such that a thin layer of liquid is trapped between the solid surface and the vapor of the growing bubble. Its formation depends on a Capillary number, i.e., it depends on fluid viscosity, surface tension, and the rate of growth of the bubble base. Specifically, in a purely hydrodynamic problem (i..e, without evaporation), its appearance is determined by the relative motion of the near-wall liquid/vapor interface compared to the triple contact line (i.e., the line where the vapor and the liquid are in contact on the solid surface). However, in boiling, the presence of an extended microlayer is determined by both hydrodynamics and heat transfer mechanisms. As a result, the presence of a microlayer depends on a large amount of physical and thermal properties of the fluids (i.e., liquid and vapor) and the heated solid surface. Some of the challenges associated with the prediction of microlayer formation have been reviewed by Guion et al. [65]. Phase-detection measurements performed by Kossolapov et al. [66] have shown that microlayers get smaller in boiling water when the pressure increased, and seemingly disappear completely at sufficiently high pressure. The similarities between the physical properties of pressurized water and cryogenic fluids (see surface tension, density ratio and dynamic viscosity in Table 1.1) lead us to think that microlayer evaporation may not be a significant heat transfer removal process in cryogenic boiling, if it forms at all. However, this is only speculative due to the lack of published experimental evidence on whether microlayer appears in cryogenic boiling. It is also worth noting that low temperatures are known to scatter differences in the thermal properties of metals, glass and common plastics. For instance, sapphire used in boiling experiment to make transparent heating element, has a thermal conductivity about 200 times

higher than 304L stainless steel at 78 K. Therefore, the thermal properties of the heating surface may impact significantly the evaporation of the microlayer in cryogenic temperature and the motion of the triple contact line during bubble growth. If microlayer does not form, vigorous evaporation can still occur very locally near the bubble triple contact line (shown on the right in Figure 1.4). The scale of the heated surface area affected by the triple contact line evaporation is significantly smaller compared to microlayer evaporation. While this area depends on multiple factors such as the wettability of the surface and bubble growth rate, it essentially scales with the length of triple contact line on the heated surface and the distance in the liquid (normal to the contact line) affected by the evaporation. This distance (noted l in Figure 1.4) is expected to be inthe order of microns according to numerical calculation (67, 68). The length scale of the mechanism makes direct observations of the evaporation on bubbles, e.g., using infrared thermometry, particularly challenging in non-cryogens, and impossible in cryogens due to the lack on infrared photons. Instead, triple contact line evaporation can be inferred from measurable characteristics of growing bubbles, e.g., an apparent contact angle much larger than the equilibrium contact angle (e.g., see Ref. [68].

Knowing the type of evaporation is useful from a modeling point of view, as each of these mechanisms described above are expected to behave, *a priori*, differently with respect to other parameters (e.g., the surface roughness, the wettability of the heated surface, gravity level or heated surface orientation with respect to the gravity field, etc.).

How bubble growth, departure and lift-off is affected by buoyancy in cryogenic pool boiling?

In nucleate boiling regime, bubble dynamics is affected by all the forces acting on the vapor molecules of the bubbles. Hence, major boiling mechanisms such as bubble departure and lift-off depend on the balance between these forces. Typical modelling of bubble growth available in literature assumes that the bubble growth finishes at the moment of the bubble departure from the nucleation site. This assumption may be appropriate in pool boiling on a horizontal surface or even in flow boiling at low mass flux. In highly wetting liquid like cryogens, surface tension forces are highly reduced due to their exceedingly low surface tension (c.f. Table 1.1) and the low contact angle of bubbles on most solid surfaces [39]. On the other hand, Bland et al. [44] showed experimentally in liquid nitrogen that buoyancy is still the dominant force acting on isolated bubble and in absence of forced flow. The off-balance resulting from low surface tension forces suggests that bubbles should be highly mobile, i.e., having early departure from their nucleation site or lift-off from the surface. At high-heat flux the contribution of other forces (e.g., bubble-induced turbulence or vapor recoil forces during bubbles coalescence) may be large enough to trigger premature bubble departure or lift-off as well. Results of a preliminary experiment conducted in liquid nitrogen pool boiling with a

tilted heating surface revealed a high mobility of vapor bubbles and show that they tend to slide on the surface after a partial growth at the nucleation site. The large uncertainty on contact angle of cryogenic fluid and the potential high mobility of bubbles makes unclear how we can predict bubble time scales (growth time and wait time) and length scale (bubble footprint), and how bubbles sliding affects their growth when the boiling surface is tilted.

In microgravity, buoyancy is almost inexistent and the mechanisms dominating bubble departure or lift-off are unknown. The boiling heat transfer efficiency is expected to reduce as the gravity field intensity weakens as inferred by typical correlations for nucleate boiling heat transfers [69] and shown by measurements with non-cryogenic fluids [70] and with cryogens [71]. This consensus on the general influence of the gravity intensity on boiling contrasts with the uncertainty on the magnitude of this influence. Typical pool boiling correlations often assumed that bubble lift-off is driven solely by buoyancy, which almost disappears in microgravity (e.g., correlations based on Rohsenow's correlation like Clark's [69]). Therefore, these models only predict a negligible boiling heat flux in boiling in microgravity. On the other hand, Zell (see the review from Straub [70] for reference) demonstrated that the gravity field intensity influence on boiling heat transfers is not as significant as correlations based on buoyancy as bubble departure mechanism would predict. His measurements have been performed in a R-113 and R12 pool boiling setup. This strongly suggests that bubbles lift-off in microgravity is dominated by forces other than buoyancy. It is worth mentioning that Nishikawa et al. [72] proposed a pool boiling experiment with different orientations of the heating surface in terrestrial gravity. Using a tilted heating surface is an interesting experimental method to understand the effect of buoyancy on bubble dynamics and therefore estimate what would cause the lack of buoyancy in microgravity. In particular, buoyancy should not contribute significantly to bubble lift-off when the heating surface angle is close to 90°. Nishikawa's results indicate that the boiling heat transfer coefficient increases with the inclination angle from 0° to 175°, 0° being the heating surface facing upward and 175° being the surface facing almost downward. Their results seem to contrast with the results obtained in microgravity, as the heat transfer coefficient is increased when the effect of buoyancy on bubble departure is reduced. Carey [47] suggested two explanations for this behavior: a thicker conduction layer allowing bubbles to nucleate at a lower nucleation temperature at the heated surface and additional turbulence near the wall as bubbles slide to the edges of the heating surface. It appears from the results of Nishikawa et al. [72] that no heating surface orientation can simulate fully microgravity conditions.

This scientific question can be answered experimentally by a systematic analysis of bubbles dynamics for different orientations of heating surface at 1g with a cryogenic pool boiling setup. In particular, we can track bubbles from nucleation to lift-off from the surface based on their footprints using phase-detection

measurements on the boiling surface. In complement, synchronized backlit shadowgraphy recordings can be used to track the evolution of the bubble diameter, including at departure from the nucleation site and at lift-off from the boiling surface. Collecting measurements in reduced gravity (and microgravity) are out of the scope of this work, but would constitute a necessary step to validate cryogenic boiling heat transfer for space applications.

The analysis of individual bubbles trajectory and the evolution of their diameter from the nucleation to the lift-off for different orientation of heating surface in terrestrial gravity give us a good understanding on how buoyancy affects the bubble departure and lift-off, how bubbles sliding affect their growth and the heat removed by quenching, and how strong are the forces trying to keep the bubbles on the heating surface.

1.5. Structure of the thesis and contributions

This thesis is organized in seven chapters, including this introductory chapter, as discussed hereafter.

- A novel experimental apparatus, who made in-depth investigation of cryogenic boiling and the development of partitioning model for cryogens possible, is presented along with the various measurement technique is presented in Chapter 2.

- In Chapter 3, we explore the characteristics of uncoalesced bubbles. We present experimental data on inclined boiling surfaces to investigate the effect of buoyancy on the growth rate of these bubbles as well their departure and lift-off diameter. Despite bubble sliding being highly dependent on the surface inclination, most of the metrics used to characterize uncoalesced bubbles (i.e., growth modulus, departure and lift-off diameter) are independent of the surface inclination. Finally, we infer the existence of a strong evaporation mechanism at the triple contact line of bubbles, necessary to explain the bubbles footprint radius which are found larger than expected. The triple contact line evaporation rate has been indirectly measured for numerous bubbles and appeared consistent with analytical model describing this evaporation mechanism.

- Interactions between cryogenic bubbles is studied in Chapter 4. Integral characteristics of the boiling process are measured (e.g., dry area fraction and contact line density). We show that buoyancy effects arise when sufficient bubble coalescence take place producing large vapor patches. The effect of buoyancy become important at high heat-flux and in particular at the departure from nucleate boiling. We show the variation of critical heat flux with different heating surface inclinations. Finally, we also provide estimate of the different boiling heat flux components that we can inferred from our experimental data.

- In Chapter 5, we revisit the long-standing issue of fouling in cryogenic boiling. We show that no fouling occurs on the boiling surface when our standard experimental procedure for nitrogen boiling is followed. However, our investigation shows that cryogenic fouling can occur when carbon dioxide is dissolved in liquid nitrogen, despite the extremely low solubility of carbon dioxide in nitrogen. Contrary to most published work, we show that the resulting fouling during boiling can lead to an enhancement of the boiling heat transfer on a smooth boiling surface. The enhancement is evident in the decrease of the surface temperature required to nucleate bubbles and consequently in a modification of the boiling dynamics (typ., toward higher nucleation site density and smaller bubbles), which we were able to visualize
- Using the knowledge and data acquired in Chapters 3 throughout 5, we propose a heat flux partitioning formulation that we present in Chapter 6. The heat flux partitioning model is compared to our measured boiling curves at different inclination angle and an error analysis is presented.
- The conclusion of the thesis, as well as open questions, are presented in Chapter 7.

2. EXPERIMENTAL METHODS

This section describes the experimental apparatus and techniques developed to collect detailed cryogenic boiling data.

2.1. Experimental apparatuses

Two test-sections have been built during this study. A preliminary test-section was made at low cost as proof-of-concept for us to test our capabilities to carry cryogenic boiling experiments and explore the potential difficulties. A second test-section was made based on the acquired experience, with which we could carry out our experimental campaign.

2.1.1. Preliminary experimental study

A preliminary experimental apparatus was built to test our capabilities of carrying out essentially phase-detection and surface temperature measurement in a cryogenic setting. Figure 2.1 shows a schematic of the setup and a photo of it in our laboratory.

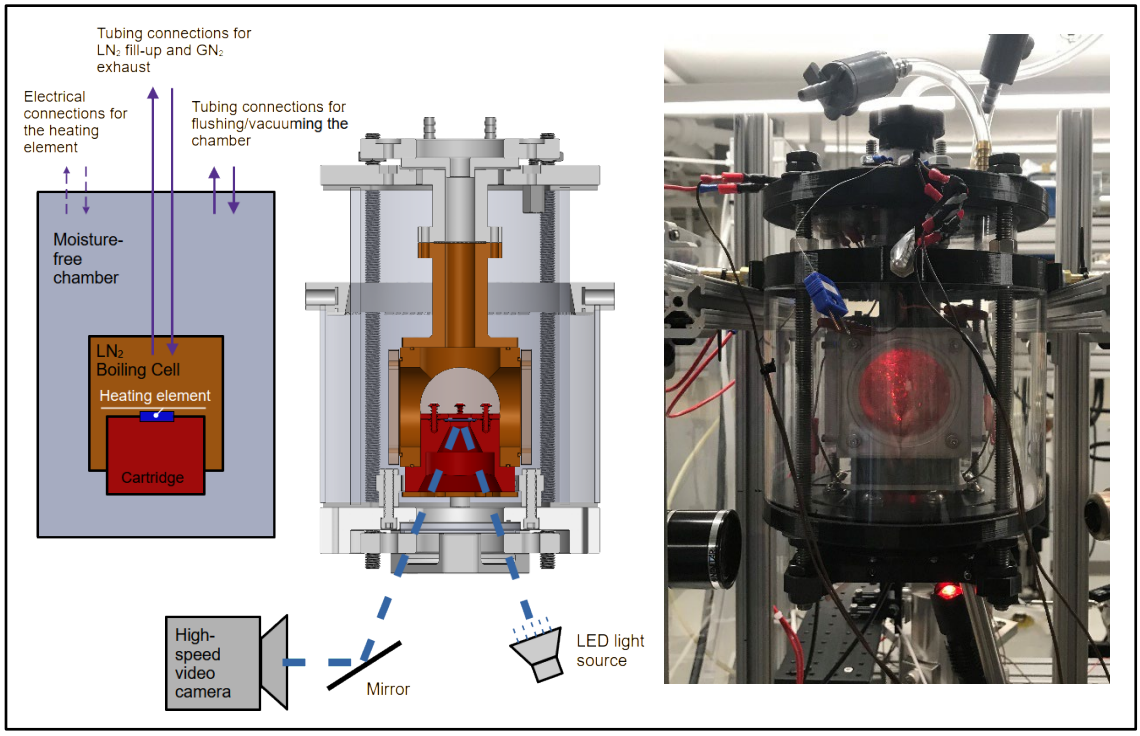

Figure 2.5. Different representations of the test-section with a schematic of the design concept (left), a cross-section of the CAD model with the optical setup for phase detection (center) and a photograph of test-section setup in the laboratory (right).

The test-section consists of two main parts: a boiling cell containing the liquid nitrogen and a moisture-free chamber surrounding it filled with nitrogen gas. The boiling cell consists of a 6061-aluminum 3-inch hollow cube with six openings to integrate five clear polycarbonate windows and a PETG cartridge holding a heating element. At each opening, PTFE O-rings are used to seal the boiling cell and minimize liquid nitrogen leakage. The heating element consists of an indium-tin oxide thin film coated on a sapphire substrate. An optical access through the bottom of the test-section allows us to perform phase-detection measurement. The simplicity of this test-section also allowed us to test different temperature sensors measurement techniques. More details on the heating element, different optical techniques, and our temperature measurement method will be given in the following sections.

The setup highlighted several difficulties that were later considered in the design of the second experiment. In particular, we noticed some cryogenic fouling during boiling with a visible effect on the boiling dynamics. No initial contamination of the surface could be seen either visually or through phase-detection, and the amount of deposit appear related to the amount of nitrogen evaporated on the surface suggesting that the contamination comes from the liquid nitrogen itself. We could also notice some interactions between the triple contact line, i.e., the line formed at the intersection of the liquid-vapor interfaces and the heating surface, and the deposits. Figure 2.2 shows two examples of such interactions from raw phase-detection images, demonstrating how the triple contact line can be pinched by these deposits at high heat fluxes. Precisely, in these images, the liquid in contact with heating surface appears dark gray, while the vapor is light gray. The solid deposits have a similar color than the liquid, but they are static on the recordings. Figure 2.2 shows two bubbles approaching and coalescing (left). After coalescence, liquid-vapor contact line remains pinned to the solid deposit. Once this connection is broken, the coalesced bubble grows with a more circular footprint.

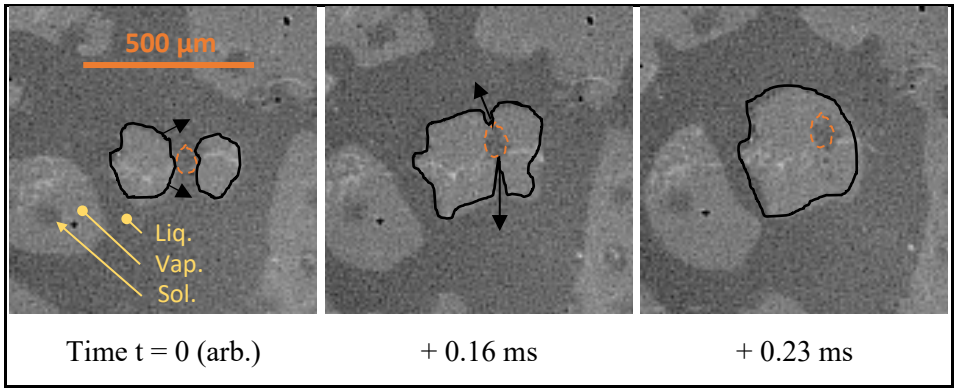

Figure 2.6. Phase-detection images showing two bubbles coalescing with their triple contact line getting pinned to a deposit in liquid nitrogen. The black line indicates the liquid-vapor-solid (not deposit) triple contact lines, while the orange line corresponds the deposit contour. The back arrows indicate the movement direction of the triple contact line.

The phase-detection images of Figure 2.3 show another potential influence of the deposits on nucleate boiling heat transfer. Precisely, it shows a bubble seemingly nucleating on a deposit, with the triple contact line moving radially from the deposit with time. It is not obvious without further analysis (which will be presented in Chapter 6) if the deposit caused the nucleation.

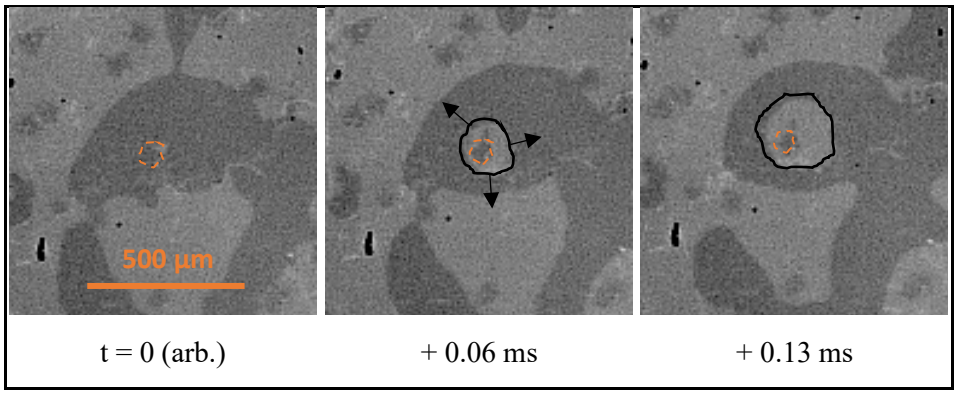

Figure 2.7. Phase-detection images of a nucleating bubbles from a nucleation site on a deposit in liquid nitrogen. The black line indicates the triple contact lines, while the orange line corresponds the deposit contour. The back arrows indicate the movement direction of the triple contact line.

The possibility of having deposits or contaminants in liquid nitrogen boiling is not new and has been postulated by several other researchers [26, 44 and 54]. The source and nature of contamination remained undetermined. Efforts for maintaining the test-section cleaned didn't results in a decrease of the contamination. In this preliminary test-section, the liquid nitrogen has a free surface in contact with the ambient atmosphere (i.e., our laboratory), which could potentially result in gases dissolving (e.g., CO_2 or water vapor) or liquefying (e.g., oxygen) in the liquid nitrogen.

Based on the lessons learned using this experimental rig, we designed a more complex apparatus that we later used to run our experimental campaign.

2.1.2. Description of the main experimental apparatus

2.1.2.1. Overview

The experimental setup consists of small boiling cell containing liquid nitrogen and auxiliary systems controlling the vacuum insulation around the boiling cell, supply and venting of liquid nitrogen as well as instrumentation system gathering data about the boiling process inside of the cell. Figure 2.4 shows a simplified schematic. Figure 2.5 shows the P&ID of the experimental setup.

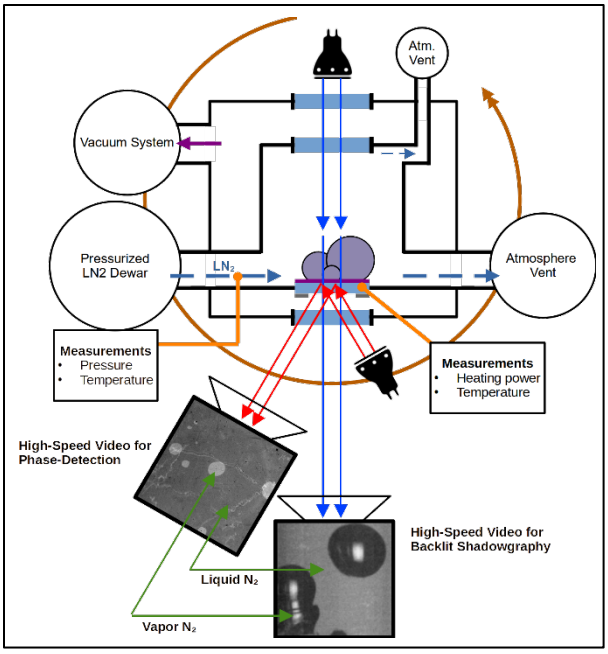

Figure 2.8. Simplified schematic (left) and P&ID (right) of the experimental setup.

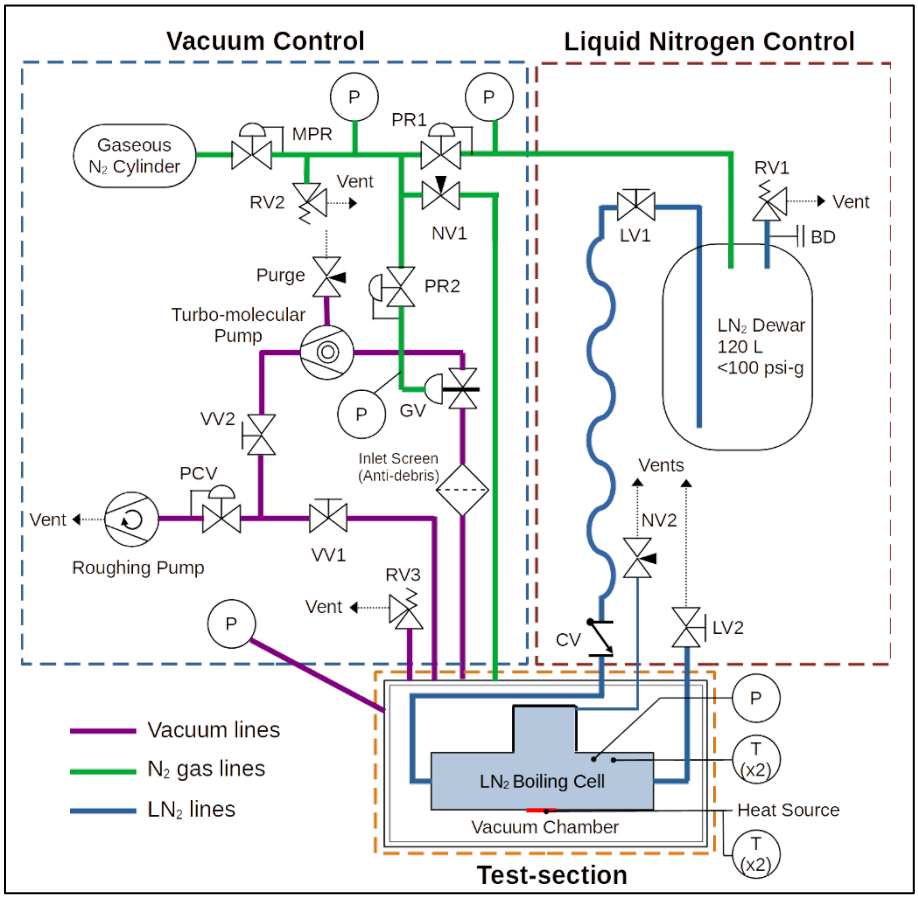

Figure 2.9. Piping and instrumentation diagram of the experimental setup.

The instrumentation is designed to enable high-speed optical recordings of the boiling process as well as the temperature of the heating surface for a prescribed heating power.

One side of the boiling cell houses a cartridge, where the heater is installed. This cartridge (see Figure 2.6) consists of two parts: an insulator part and a metallic flange. The insulator is made of a plastic resistant to cryogenic temperatures (Torlon PAI or G10-CR). This part is used as an electrical insulator separating the heating element from the metallic flange and is bolted to it. The heating element consists of a sapphire slab (20 mm x 20 mm x 1 mm) coated on one side with 700 nm of transparent indium tin oxide (ITO) film. To run the experiments, the liquid nitrogen is heated by Joule effect using the conductive ITO film. Chromium pads are wrapped around each side of the sapphire substrate to provide electrical connection between the ITO and the power supply. These 4 connections are used to energize the ITO as well as measuring the voltage with a 4-point probe technique. Thin chromium-oxide (Cr_xO_y) films coated on the sapphire substrate are used as resistance thermometers (RTDs) to measure the substrate temperature.

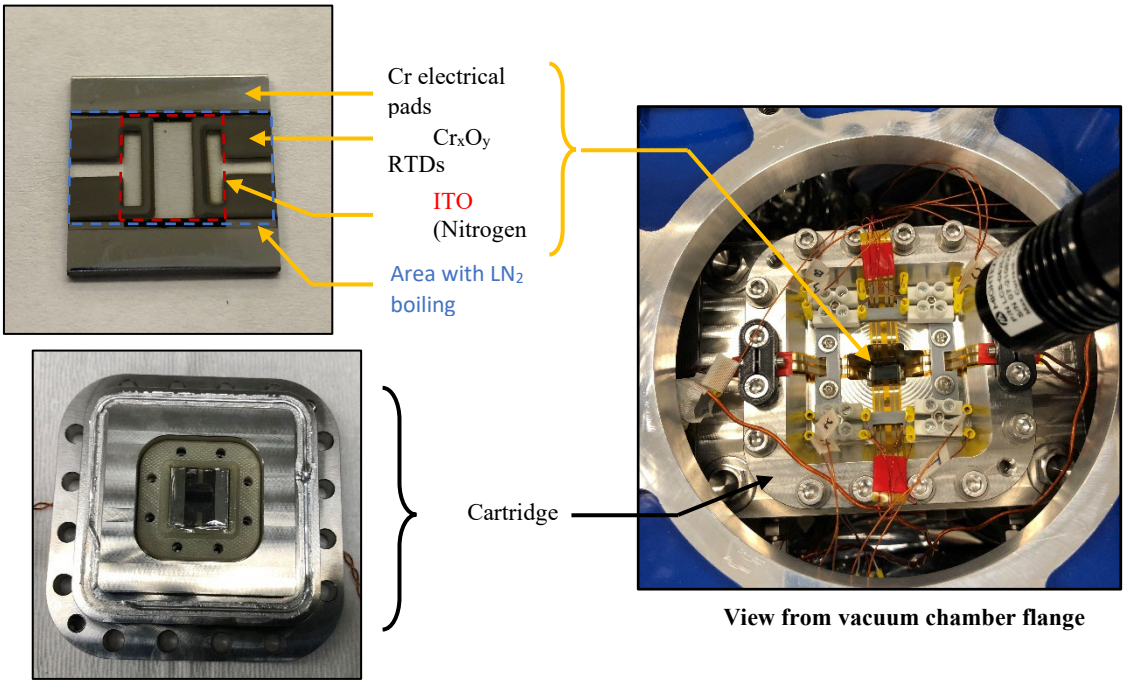

Figure 2.10. Photos of the heating surface alone (top-left), mounted on in its cartridge (bottom-left) and inside the vacuum chamber (right).

All sealings in the vacuum chamber are made using indium wire with exception of the sapphire substrate which is glued using a cryogenic epoxy (3M™ Scotch-Weld™ Epoxy Adhesive 2216 B/A). Four Swagelok fittings welded to the main body of the test section enable access to the liquid nitrogen to measure the temperature in the channel upstream and downstream the boiling surface with thermocouples and the pressure with a cryogenic pressure transducer. Figure 2.7 shows a photo of the boiling cell.

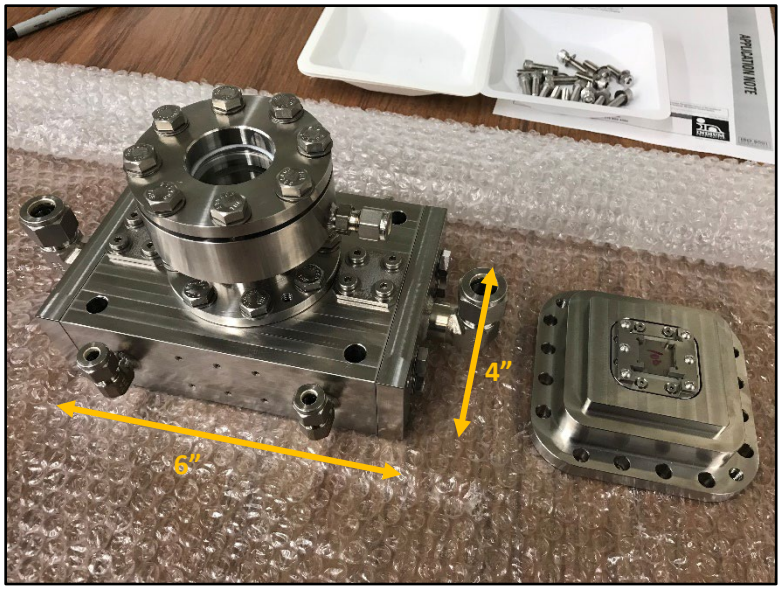

Figure 2.11. Photo of the boiling cell.

The boiling cell is mounted inside a moisture-free chamber (see Figure 2.8) filled with rarefied gaseous nitrogen (GN_2), vacuumed down to ~10^{-3} Torr using a combination of dry scroll pump and turbomolecular pump. The vacuum chamber fulfills two critical requirements for the proper operation of the experiment by:

1) thermally insulating the boiling cell from the external environment to keep the nitrogen in a saturated liquid state unless heated and

2) preventing contact between humid atmospheric air and the boiling cell to avoid the formation of water ice on the polycarbonate windows and maintain clear optical access to the heater.

The vacuum chamber is a 12-in side aluminum cube with 6 openings. Each opening is closed by a specific flange allowing us to mount optical access, feedthrough, electrical connections, and vacuum ports. The vacuum chamber is mounted on a rotary table allowing us to rotate the test-section at any inclination angle. Figure 2.8 shows pictures of the experimental setup for different inclination angles.

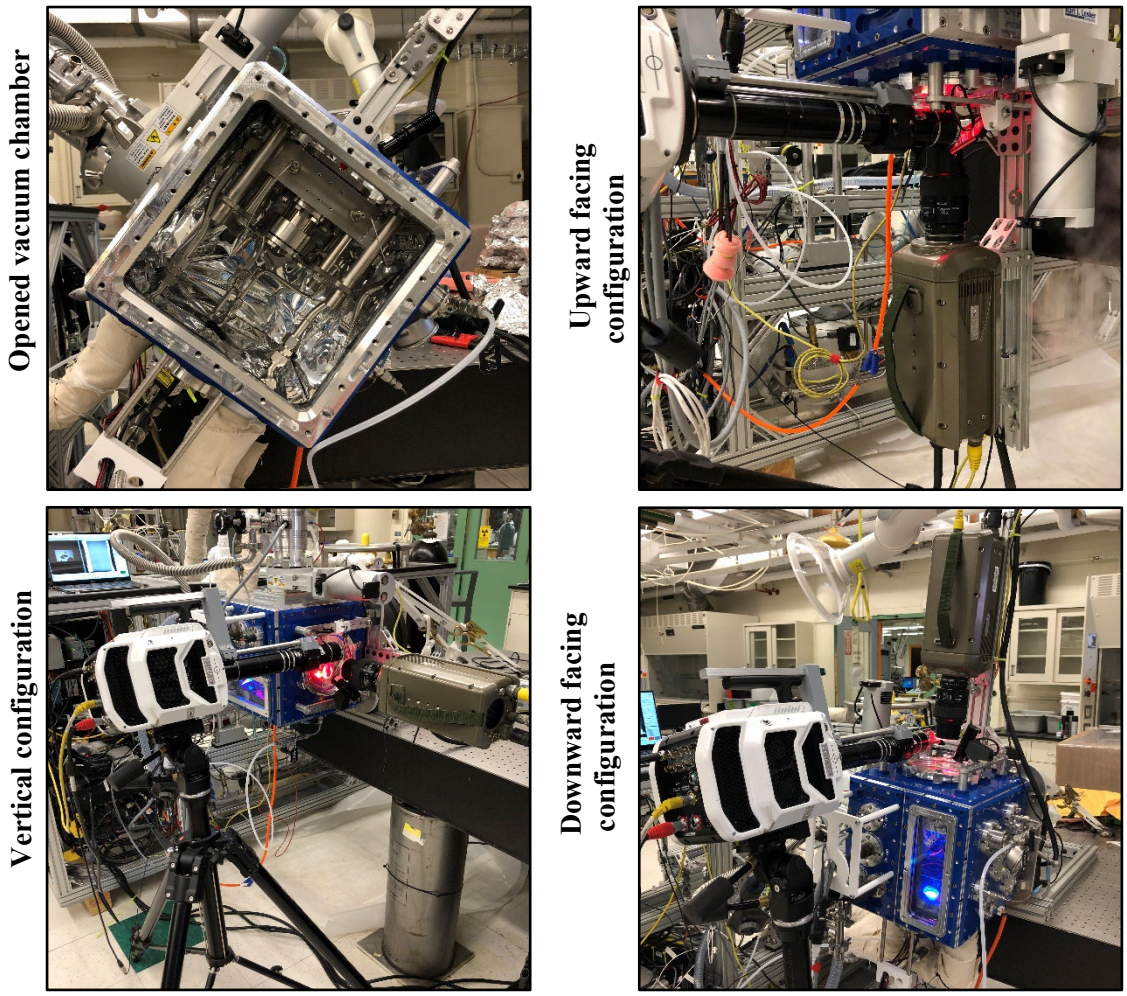

Figure 2.12. Pictures of the opened vacuum chamber with its test-section (A) and optical setup for different inclinations of the heating surface (B, C and D).

2.1.2.2. Instrumentation

The electrical power required to energize the ITO film is supplied by a *Chroma* 62006P-100-25 DC power supply and controlled by the analog output of a *Keysight* U2356A high-speed data acquisition system. The current supplied by the power supply is measured using a precision LEM LA 25-NP Hall-effect current sensor. Low steady currents (~ 3 mA) are supplied to the RTDs using 2 *Lakeshore Cryotronics* Model 121 DC current sources. The voltages across the ITO film and the RTDs are measured with the analog inputs of the *Keysight* U2356A high-speed data acquisition system. A Keysight 34980A controller is used to retrieve the measurements from the thermocouples and the cryogenic pressure transducer.

The vacuum system controls are independent from the rest of the experiment. An *Agilent* TwisTorr 74FS AG controller ensures the proper operation of the turbo-molecular pump and allows to set its operating

setpoint (i.e., the rotor speed) and to monitor the pressure in the vacuum chamber measured from the Pirani gauge. Only measurement signals acquired by the TwisTorr controller 74FS are retrieved by the Keysight 34980A (error status, frequency and pressure).

2.1.2.3. Optical arrangement

Two complementary imaging techniques are used simultaneously on the experiment setup: phase detection (based on light reflection at the solid-vapor and solid-liquid interface) and backlit shadowgraphy. The following acronyms will be used in the text when referring to these visualization techniques: PIR for Partial Internal Reflection, and BS for backlit shadowgraphy. A *Phantom* V2512 high-speed video camera is used on a tripod to image the heating element illuminated with a quasi-monochromatic 625-nm collimated LED for the phase detection measurement. A second camera rotating with the vacuum chamber, a *Phantom* V12.1 high-speed video camera, is used for backlit shadowgraphy. In this case, a quasi-monochromatic 470-nm collimated LED illuminates the heating element from the opposite side of the vacuum chamber through dedicated optical accesses. A Schott BG39 bandpass filter is used on the backlit shadowgraphy to optically isolate the camera sensor from the red LED light used for phase-detection. Figure 2.9 shows a close-up photo of the optical setup.

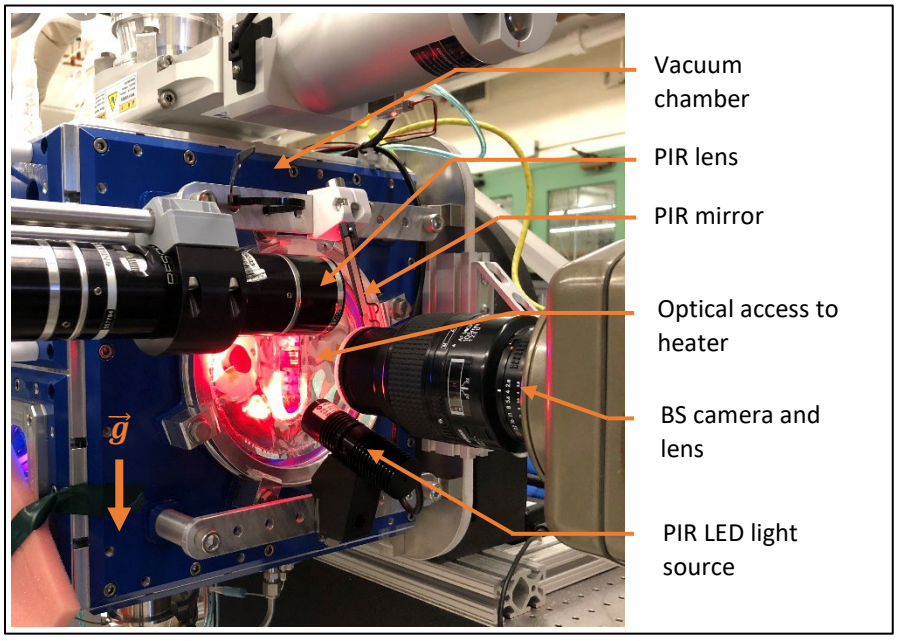

Figure 2.13. Photo of the optical setup for a boiling test with the heating surface inclined at 90º.

The phase-detection technique used in this study is described by Kossolapov et al. [66]. It consists in illuminating the boiling surface from the adiabatic side of the heating substrate and collecting the light

reflected back to the camera. The amount of light reflected at the boiling surface depends mainly on 2 factors: the angle of incidence of the light and the index of refraction of the medium on either side of the boiling surface. At a wavelength around 625 nm, sapphire has an index of refraction of 1.7, while liquid nitrogen is around 1.2 and nitrogen gas around 1.0. At the optical interface, the larger mismatch of index of refraction between nitrogen vapor and sapphire results in more light being reflected when vapor is in contact with the surface compared to liquid nitrogen. Therefore, dry areas will appear brighter than wet areas on phase-detection recordings. The ITO film has an index of refraction close to sapphire and therefore it does not impact the path of the light. Figure 2.10 shows a simplified schematic of the optical path used to image phase distribution at the boiling surface.

On the other hand, backlit shadowgraphy consists in illuminating the bubbles from the back (i.e., from the opposite side of the camera) and observing their shadows. Bubbles shadows are formed as the light diverges after passing through the bubble curved interface. Figure 2.10 shows also a schematic of the optical path used to image bubbles shadows.

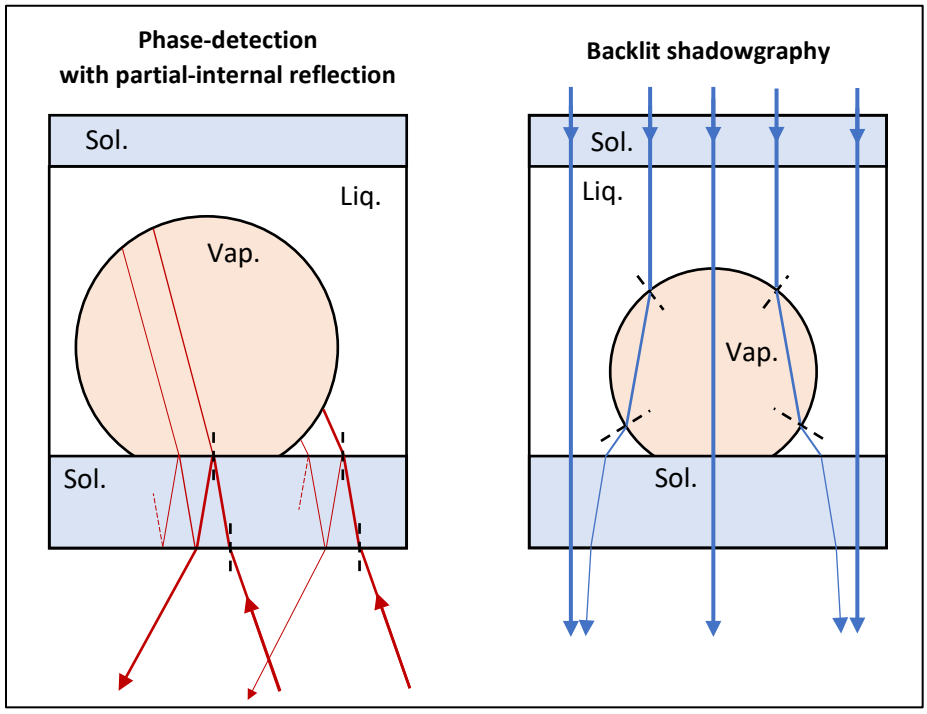

Figure 2.14. Qualitative schematics of the light paths through the boiling cell for the phase-detection and shadowgraphy setups with $n_{Vap.} < n_{Liq.} < n_{Sol.}$ The intensity of the light is schematically represented by the thickness of the lines.

2.1.3. Temperature measurement

2.1.3.1. Temperature measurement sensor

There have been considerable advances in the measurement of boiling surface temperature using high-speed infrared thermometry (e.g., see Ref. [38]). However, this technique is conditioned by the quantity of infrared photons emitted by the surface, limiting its use to temperature measurement exceeding 50 to 100ºC. Figure 2.11 shows a plot of Plank's law for black body radiation at different temperatures. Usually, high-speed infrared cameras are sensitive to photons in the 3 to 5 microns range. One can see that the quantity of photons emitted at nitrogen saturation temperature (and atmospheric pressure) is orders of magnitude smaller than the quantity of photons available at water saturation temperature (i.e., at ~373 K), even if longer wavelengths were used (e.g., up to 14 microns).

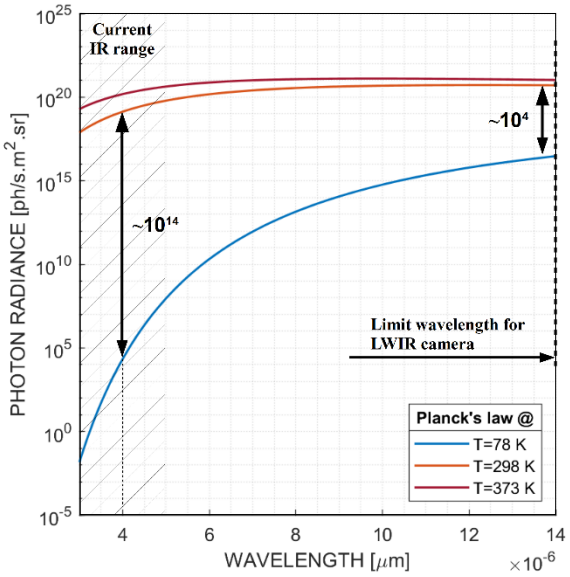

Figure 2.15. Black body radiation expressed as photon radiance vs. wavelength for different temperatures (from the nitrogen to water saturation temperature at 1 atm, i.e., from ~78 K to ~373 K).

Several solutions are available to measure low temperatures. The most popular are thermocouples (typ., type T, K or E) and resistance thermometers (e.g., using pure metals like platinum or oxides like zirconium nitroxide). Commercially available solutions to measure temperature have been excluded as they require to attach the sensor to the sapphire substrate, which results in several complications: significant obstruction of the optical access through the sapphire substrate, slower thermal response of the sensor due to the added thermal resistance of the sensor and how it is attached (e.g., with epoxy), parasitic heat input depending on how the sensor is connected thermally to the experiment structures and potential temperature differences

between the sensor and the substrate which can be difficult to estimate resulting from both parasitic heat leaks and potential thermal resistance between the substrate and the sensor.

Therefore, we investigated the manufacturing of resistance thermometers (RTDs) which can be directly coated on the sapphire substrate leveraging our capability to perform physical vapor deposition (PVD) coatings. We excluded other potential measurement methods such as thermocouples or silicon diodes due to their higher complexity to manufacture. A RTD is relatively simple and works based on the idea that most materials have their electrical resistivity changing with temperature. The resistance of a RTD element depends on its geometry (assumed here as a line) and on the resistivity of the used material ρ:

$$R(T) = \rho(T)\frac{L}{wt} = R_{\square}(T)\frac{L}{w} \tag{2.1}$$

L is the electric current path length and wt the cross-section of the conductor. $R_{\square}$ is often used to characterize thin-film resistance and is called "sheet resistance." Figure 2.12 shows the variation of bulk electrical resistivity for several metals.

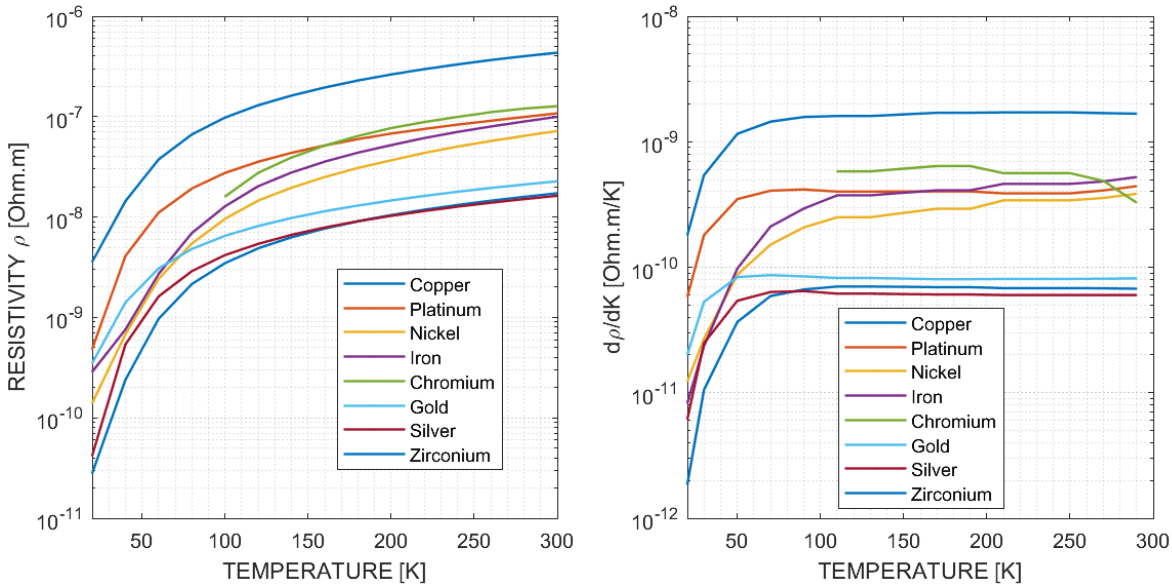

Figure 2.16. Electrical resistivity of bulk pure metals (left) and resistivity change with temperature (right), from [73]

A large resistance is desirable for the RTDs in order to minimize driving current and the heat dissipated by Joule-effect, while keeping a voltage across the resistor high enough to avoid measurement uncertainties at the data acquisition system. Metallic RTDs have the advantage of being simple to coat, but the low resistivity results in requiring a long current path for the sensors to have significant resistance. For instance, a platinum track with a cross section of 100 nm x 250 µm should be 61 mm long (i.e., about 3 times the side length of our sapphire substrate) to reach 1000 Ohm at 0ºC and only ~200 Ohm at 77 K. A solution would be to coat thinner track, however, the bulk temperature coefficient of resistivity (TCR) of metals do

not apply for very thin films, and generally the TCRs reduces with the thin-film thickness (see e.g., Refs. [74-75]). Another solution would be to reduce the width of the tracks, but then the manufacturing is increasingly complex, e.g., due to the need of mask with 10-100 μm-wide slits and a thickness even thinner to avoid shadowing effect during coating. The use of photolithography would circumvent that issue. Overall, initial trials using metallic films, in particular made of chromium and titanium, have been unsuccessful.

The use of metal oxide for RTDs have several advantages over bare metals: a higher resistivity for the same geometry, i.e., a higher TCR, a better chemical stability and an additional parameter, namely the oxygen content, which can be tuned during the manufacturing process to obtain the desired resistance.

We opted for chromium-oxide RTDs, for which the resistance was measured at low-temperature for different oxygen content by Nash et al. [76]. Chromium-oxide behaves as a semi-conductor and has a negative TCR, i.e., its resistivity decreases with increasing temperature. Nash et al. [76] showed that larger amount of oxygen increases the resistivity of the chromium-oxide thin-film as well as its TCR.

The procedure giving the best results consists of sputtering chromium with DC power at 250 W in an atmosphere of argon-oxygen at 3 mTorr with a flow rate of oxygen of 10% (total standard flow rate). The deposition is stopped when the coating reaches a thickness of 700 nm. Figure 2.6 shows the design of RTDs retained for this study. The resulting resistance of the RTDs is about 1 kOhm at 77 K for a relative short current path length of 9 mm and a width of 1 mm.

Two RTDs are coated on the sapphire substrate, on its adiabatic side. The electrical connections to these two RTDs are made using polyimide flexible printed circuit boards. Each RTD is wired using the 4-point probe technique. The heat dissipated by the RTDs is about 9 mW/sensor for a driving current of 3 mA, which is negligible compared to the heat supplied by the ITO.

2.1.3.2. Thermocouple calibration method

The thermocouples have been calibrated against the pressure sensor assuming saturation conditions. The measurement errors from T-type thermocouples were unacceptable at cryogenic temperature. Figure 2.13 shows a calibration test where the saturation temperature of nitrogen at atmospheric pressure is measured by the thermocouples installed at the inlet and outlet of the test section. The measurement apparatus is the same used during normal operation of the experiment setup, in terms of wiring and acquisition system. The thermocouples are simply dipped into a 1-L dewar of nitrogen, at least 3 inches below the free surface. The dewar is left open to the atmosphere during the tests. 273 measurement points are taken for each thermocouple in three separate 3 trials. Between each trial, the thermocouples are removed from the dewar

and warmed up to room temperature. The pressure in the room was measured with an Omega PX119 pressure transducer to 14.37 ± 0.75 psi-a. Therefore, the saturation temperature of the nitrogen can be estimated to 77.17 ± 0.44 K.

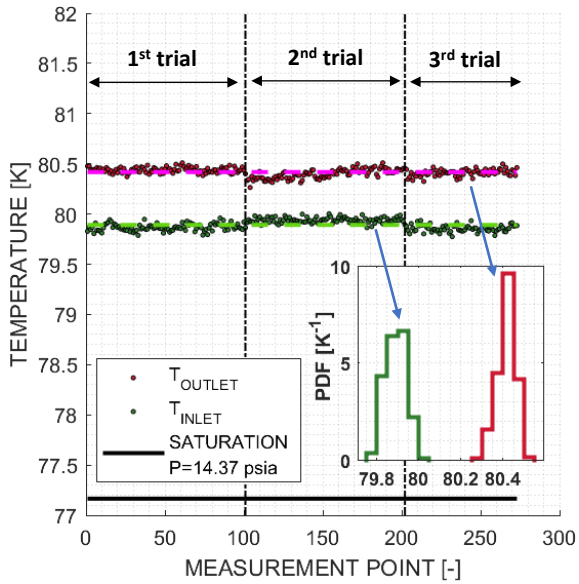

Figure 2.17. Temperature measured by the inlet and outlet thermocouples in liquid nitrogen at atmospheric pressure. The measurement apparatus used (cables and acquisition system) is identical as during normal operation of the experimental setup.

The error between the thermocouple readings and the actual temperature consists of 2 parts whether is it is random or time-independent. Figure 2.13 shows that the thermocouples give consistent readings over all 3 trials, with a standard deviation of 41 and 49 mK for the inlet and outlet thermocouple, respectively. However, they suffer from an unacceptable bias error. A bias of +2.73 K and +3.25 K was measured with the inlet and outlet thermocouple, respectively, at atmospheric pressure. The bias has been corrected by using the reference temperature evaluated from the cryogenic pressure sensor. Figure 2.14 shows the saturation temperature of nitrogen against pressure.

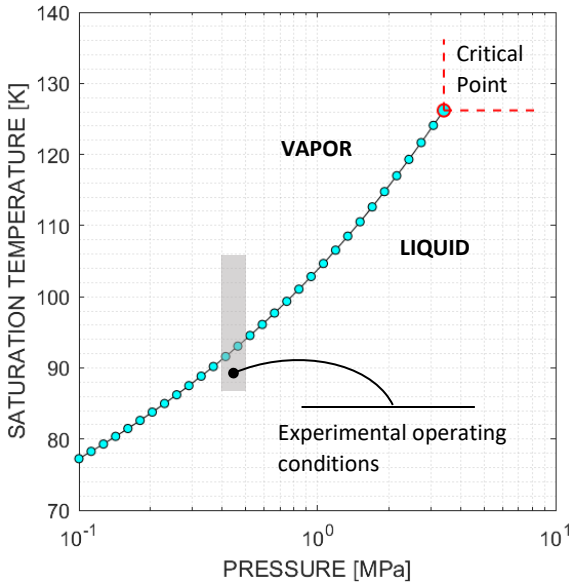

Figure 2.18. Liquid-vapor saturation curve of nitrogen.

It is unclear whether the bias is temperature-dependent on a broad temperature range. To circumvent this unknown, the thermocouple readings were corrected on the temperature range used in this study, i.e., 90 to 100 K. Another difficulty to face when calibrating the thermocouple against the saturation temperature is to know if the liquid-vapor in contact with the thermocouple is actually at saturation. The thermocouples can be potentially in contact with subcooled liquid due to the initial subcooling in the nitrogen dewar (i.e., 86.0 K at 22 psi-g) or superheated vapor obtained by conductive heating between the environment and the thermocouples tip.

Figure 2.15 shows the measurements of inlet temperature against saturation temperature during operation of the experiment. About 5 hours of data are presented in Figure 2.15 with each black dot representing a measurement point, taken every 2 second.

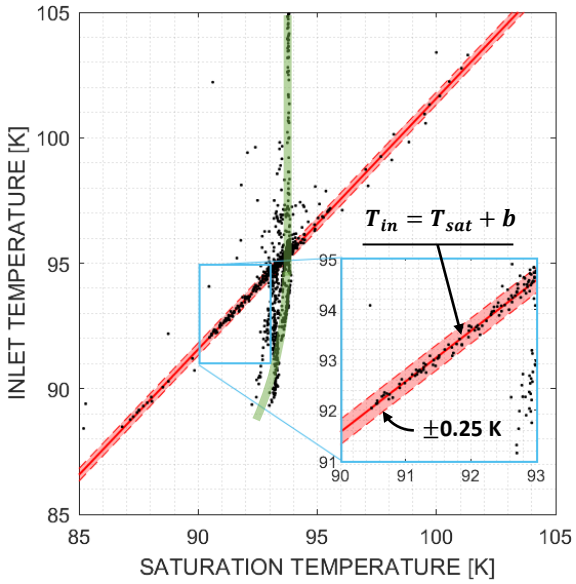

Figure 2.19. Example of inlet thermocouple readings against saturation temperature during 5 hours measuring at 0.5 Hz.

When the temperature readings from the thermocouples are plotted against the saturation temperature as shown in Figure 2.15, one can immediately see the points mostly aligning along 2 lines. Measurement points along the green line indicates only weak or no correlation between the thermocouple reading and the saturation temperature. This is the case during the initial chill down of the test-section performed mostly at constant pressure with superheated vapor in contact with the thermocouple, or during conditioning of the test-section before tests where a forced nitrogen flow is used to slightly subcooled the nitrogen and fully flood the boiling cell. The flow induced a slight drop of the pressure in the cell and the nitrogen saturation temperature, which is visible in Figure 2.15 by a slight bending a green line. On the other hand, a strong correlation between the thermocouples and saturation temperature measurements is observed when the thermocouples are contact with saturated nitrogen, as highlighted by the red line in Figure 2.15. The red area indicates a band of temperature at +/- 0.25 K around the fitting line. The slope of the line is naturally equal to unity. The value of b shown in Figure 2.15 corresponds to the measured thermocouple bias. The bias has been estimated using the data of 7 different tests over the entire experimental campaign. For the temperature of interest for the experiments, an average bias of +1.79 ± 0.09 K and +2.39 ± 0.06 K was measured for the inlet and outlet thermocouple, respectively. The standard deviation corresponds to the spreading of the bias value measured on each test. These bias values are lower than measured at 77 K (see Figure 2.13), suggesting that the error worsens at lower temperature.

2.1.3.3. RTD calibration method

The RTD sensors are calibrated once the heater is installed in the test-section. They are calibrated against the 2 type-T calibrated thermocouples inserted inside the test-section. The pool of liquid nitrogen temperature is varied by changing its pressure and the temperature of the bulk liquid is monitored by the two thermocouples until stabilization. Figure 2.16 shows an example of calibration over 11 data points for pressure ranging from 16 psi-a to 95 psi-a, and bulk temperature ranging from 80 K to 96 K. The calibration curve obtained for each RTDs is assumed linear over the temperature range. This assumption is not valid over a broad temperature range as the change of resistivity with temperature for chromium oxide thin-film is more complex. Additional calibration points are measured at each day of the experiment to track changes in resistivity.

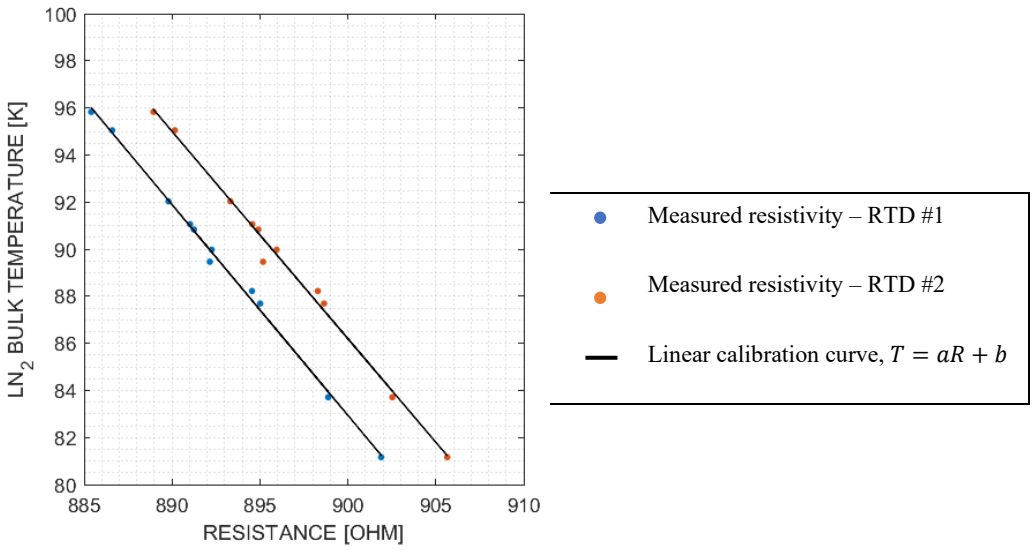

Figure 2.20. Example of calibration curve for chromium-oxide RTDs. An uncertainty on the thermocouple temperature of +/- 1 K can be assumed.

2.1.4. Power curves

Figure 2.17 shows the heat input profiles used to run the boiling experiment. We can run tests by increasing or decreasing the heat input. Running tests with increasing heat input is simpler from a practical point of view than decreasing the heat input, especially for acquiring data close to DNB. In the case of decreasing heat input, the initial step must be a bit lower than the critical heat input to prevent a risk of direct transition to film boiling. Also, the large generation of vapor caused by the initial high heat input steps limit the use of backlit shadowgraphy even when lower heat input steps are reached due to the accumulation of vapor

throughout the test, blocking the necessary illumination. On the other hand, a decreasing heat input may mimic better nucleate boiling during quenching. In most test cases, a pre-heating step is performed when the heat input is increased (see left figure). This initial step allows to saturate the cavities of the heating surface with vapor and ensuring that the measurements are not influenced by how much time has passed after the previous run. A total of 20 boiling steps is gather for each boiling curve, lasting each 3 seconds.

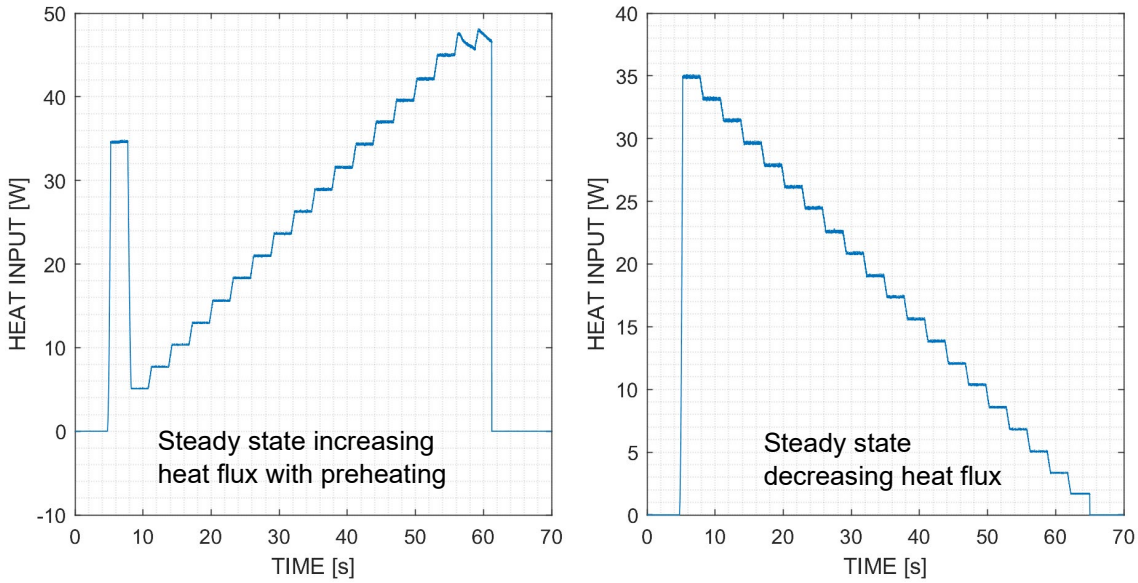

Figure 2.21. Heat input profile s prescribed in boiling tests. On the left, the profile corresponds to a steady-state increasing heat input with an initial pre-heating at 70% of the final power, while on the right, the profile corresponds to a steady-state decreasing heat input.

2.2. Post-processing procedures

2.2.1. Wall heat flux and wall temperature reconstruction

Experimentally, we measure the heat dissipated by the ITO thin film from Joule's heating and the average surface temperature on the sapphire substrate covered by the two RTD sensor (i.e., 11 mm^2 each), located on the vacuum side of the substrate (see Figure 2.6). The large thermal conductivity of sapphire in cryogenic temperature (~ about 476 W/m/K at 93.5 K) makes the heat spread in the sapphire. Thus, heat is transferred to the fluid all over the sapphire surface, not just the surface covered by the ITO film (see Figure 2.6). Therefore, it is rather clear that a gradient of temperature is present in the substrate. This gradient has 2 consequences: the temperature measured by the RTD is expected to slightly differ from the ITO temperature and the boiling heat flux cannot be obtain by a simple scaling of the heat input (e.g., with the heater area) due to the typical non-linearity of boiling curves with temperature. Instead, a 3D inverse conduction problem must be solved to get boiling heat flux and the wall temperature. Two major assumptions are made for the reconstruction process: (1) a unique boiling curve has to represent the boiling

heat transfer everywhere the nitrogen is boiling and (2) little to no liquid nitrogen is boiling on the smooth chromium pads coated on the substrate (see Figure 2.6). This last assumption is made based on our observation of the substrate surface during boiling. Figure 2.18 shows a schematic of the problem.

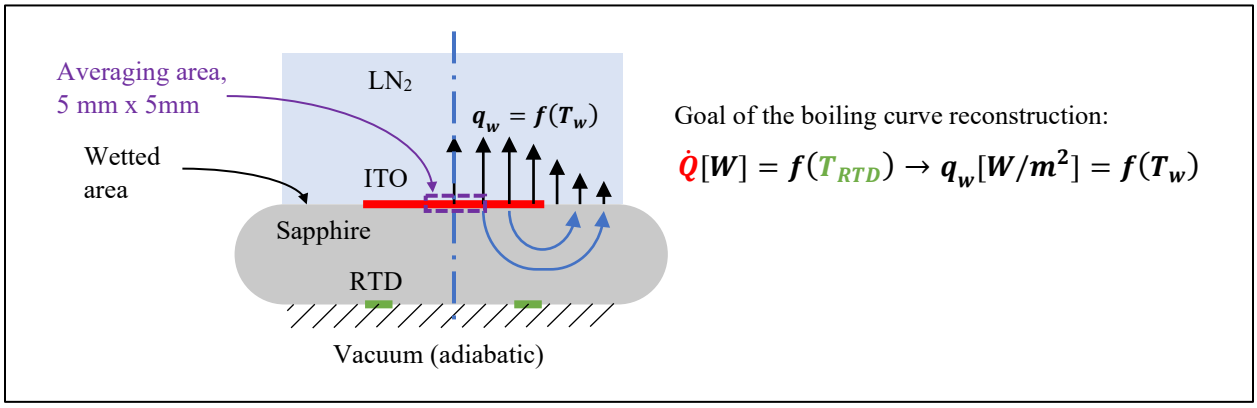

Figure 2.22. Schematic of the heat path in our heating element.

The algorithm used to solve this reconstruction problem is given in Figure 2.19 and consists of the following steps:

i. Provide an initial guess for the boiling curve.

ii. Take the first non-zero heat input $\dot{Q}_{j=1}$ (i.e., the lowest heat input of the test) and solve the heat equation in the sapphire assuming initially guessed boiling curve. Details on how the heat equation is solved are given afterwards.

iii. Evaluate the difference between the RTD temperatures measured experimentally and given by the numerical solution, noted ΔT_{err} $(T_{RTD,exp} - T_{RTD,sim})$.

iv. Shift the boiling curve by ΔT_{err} with the following operation:

$$q_w = f(T_w) \rightarrow q_w = f(T_w - \Delta T_{err}).$$

v. Repeat steps iii and iv until ΔT_{err} falls below a given threshold (typ., 10 mK).

vi. Measure the wall temperature and boiling heat flux given by the simulation. These two quantities $(q_{w,j=1}, T_{w,j=1})$ are measured only on the reduced area of the ITO, in which they are roughly constant (see purple box on Fig. 2.18). The point $(q_{w,j=1}, T_{w,j=1})$ will constitute a point of our new guess for the boiling curve.

vii. Take the next heat input point (i.e., $\dot{Q}_{j=2}$) and restart the process described between iii. and vi. Once all experimental data points $\left(\dot{Q}, T_{RTD}\right)$ have been treated, we obtained our second guess for the boiling curve given by all points $\left(q_{w,j}, T_{w,j}\right)$.

viii. Run the process described between ii. and vii. using the new boiling curve guess.

ix. The final boiling curve is obtained when the error $\left|T_{RTD,exp} - T_{RTD,sim}\right|$ is small enough, e.g., below 0.2 K.

The ITO film is assumed thin enough (~ 700 nm) to be correctly modeled as a boundary condition. The boiling heat flux is calculated using a given boiling curve and the local wall temperature. For the reconstruction, only a quarter of the sapphire is considered, assuming a one-quarter plane symmetry. Presently, only the temperature recording of one RTD sensor is used for the reconstruction. Temperature-dependent heat capacity and thermal conductivity of sapphire are implemented using the correlations of Dobrovinskaya [77]. No parasitic heat input is considered. Experimental and analytic estimates of the parasitic heat input shows that its order of magnitude is 100 mW, therefore negligible compared to the ITO heat input (i.e., at least few watts). The heat input generated by the RTD sensors (~ 16 mW total) is included in the calculation due to the simplicity of implementation but could be neglected as well.

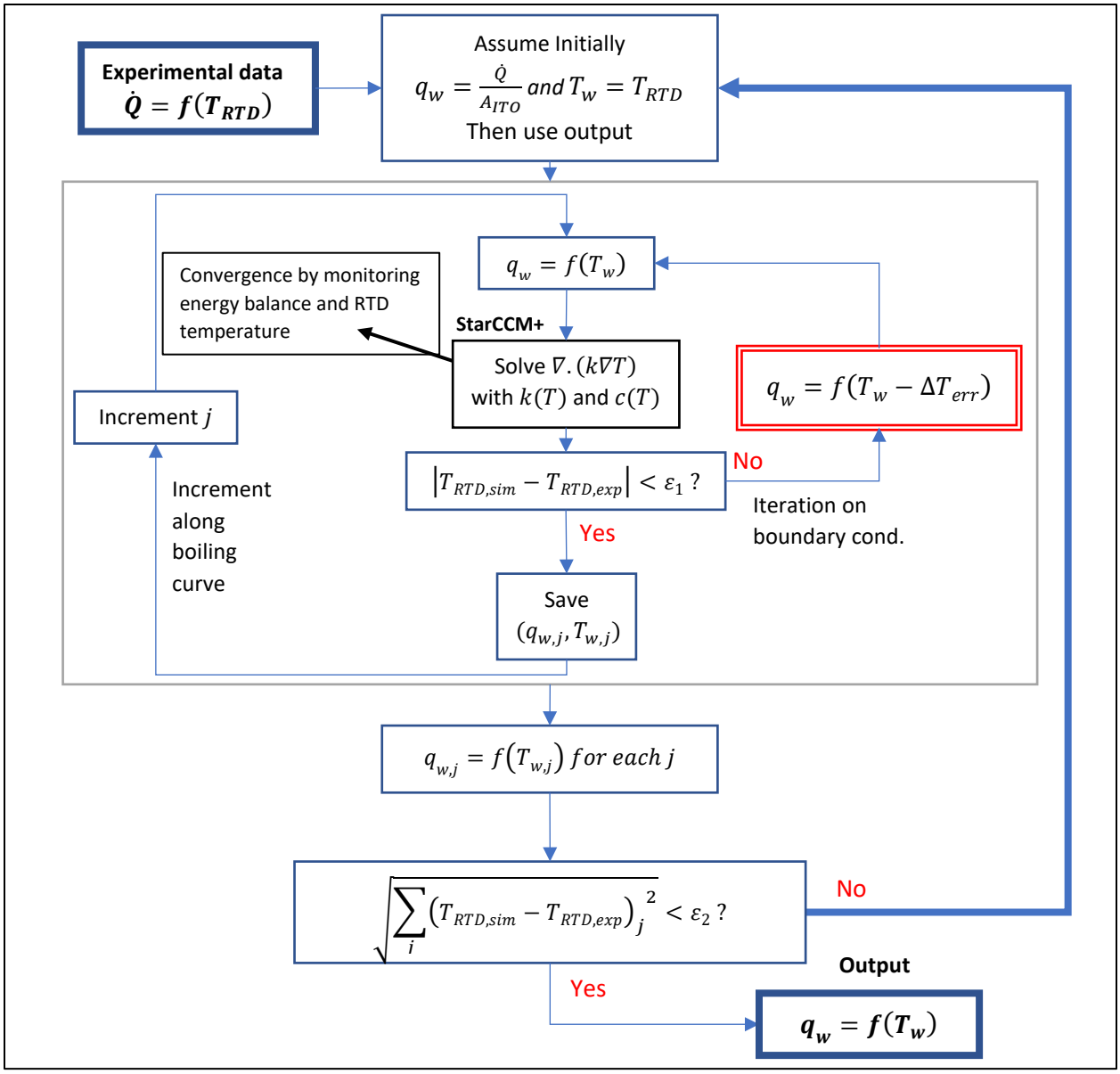

Figure 2.23. Algorithm of boiling curve reconstruction from heat input and RTD temperature.

Figure 2.20 shows the typical results obtained after reconstruction on one experimental case as example. The algorithm was run for 11 successive guesses of boiling curve until a solution with an error small enough is obtained. The different color shows the successive guesses. We can see on Figure 2.20 (left) that the guesses converge to a solution. We can also see that assuming boiling only on the ITO area, as done to generate our initial guess of boiling curve leads to an over-estimation of the boiling heat flux by roughly 33%. On the other, only a small error in the wall temperature (i.e., about 2 K close to CHF) is obtained by neglecting thermal gradient in the substrate. Figure 2.20 (right) shows how the converged solution reduces

the error between the RTD temperature measured experimentally and the RTD temperature simulated by the solver given the boiling curve.

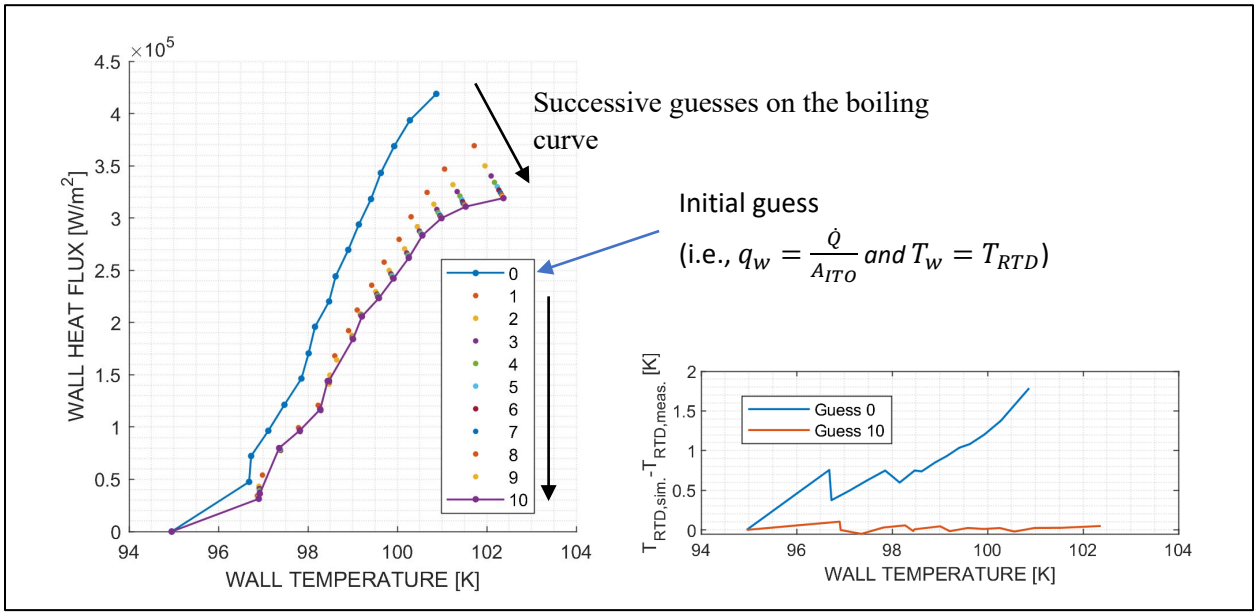

Figure 2.24. Plots of the reconstructed boiling curve after successively guesses (left), and reconstruction error estimated as discrepancy between the measured RTD temperature and simulated temperature given the reconstructed boiling curves (right). The example shown corresponds to a LN_2 pool boiling case with an inclination angle of 30°.

2.2.2. Images treatment for phase-detection recordings

Figure 2.21 shows an overview of the procedure used to post-process phase-detection recordings and extract meaningful data. The procedure relies on traditional image-processing techniques. First, the recordings are filtered, and the background is removed to enhance the contrast. The recordings are also filtered to remove high-frequency flickering of the LED light. Then, all the recording of a same boiling curves are gathered to determine thresholding values to segment the vapor and liquid phases. An adaptative thresholding is used to perform the segmentation. To find the threshold values, the stack of 42,000 frames (i.e., 21 recordings of 2000 frames each) is divided into blocks of 5 pixels by 5 pixels. The interest of treating the recordings all at once is to ensure that almost each block contains pixels associated with both fluid phases. The histogram of pixel values is calculated for each block from which we extract the position of the 2 main peaks, indicative of the pixel values associated with vapor and liquid. The local threshold value is evaluated as the mean of the two peaks value with weights 1/3 and 2/3 for the liquid and vapor peaks, respectively. The results of the thresholding are shown for couple of phase-detection images in Figure 2.22.

Once the binarized recordings are obtained, we proceed to track each bubble and build a registry where they can be referenced. Given a recording, the method consists of assigning a unique integer value at each distinct regions of the first frame of the binarized recording. Then, at the next frame, each distinct region is

checked to determine if it overlaps with a region of the previous frame. If it does, the new region inherits the integer value used as identifier. Regions with no overlapping are assigned a new integer value. Regions which overlap with more than one region of the previous frame indicates coalescence. Instead, two or more regions overlapping with a region of the previous frame is indicative of bubble breakup. In both cases, coalescence and breakup, the new regions received new integer values and the coalescence or breakup events are written in the registry. The method of detection of coalescence and breakup events using only phase-detection is not very robust for multiple reasons, e.g., a bubble coalescing may be confused with a bubble lifting off the surface if the 2 coalescing bubbles have very different sizes.

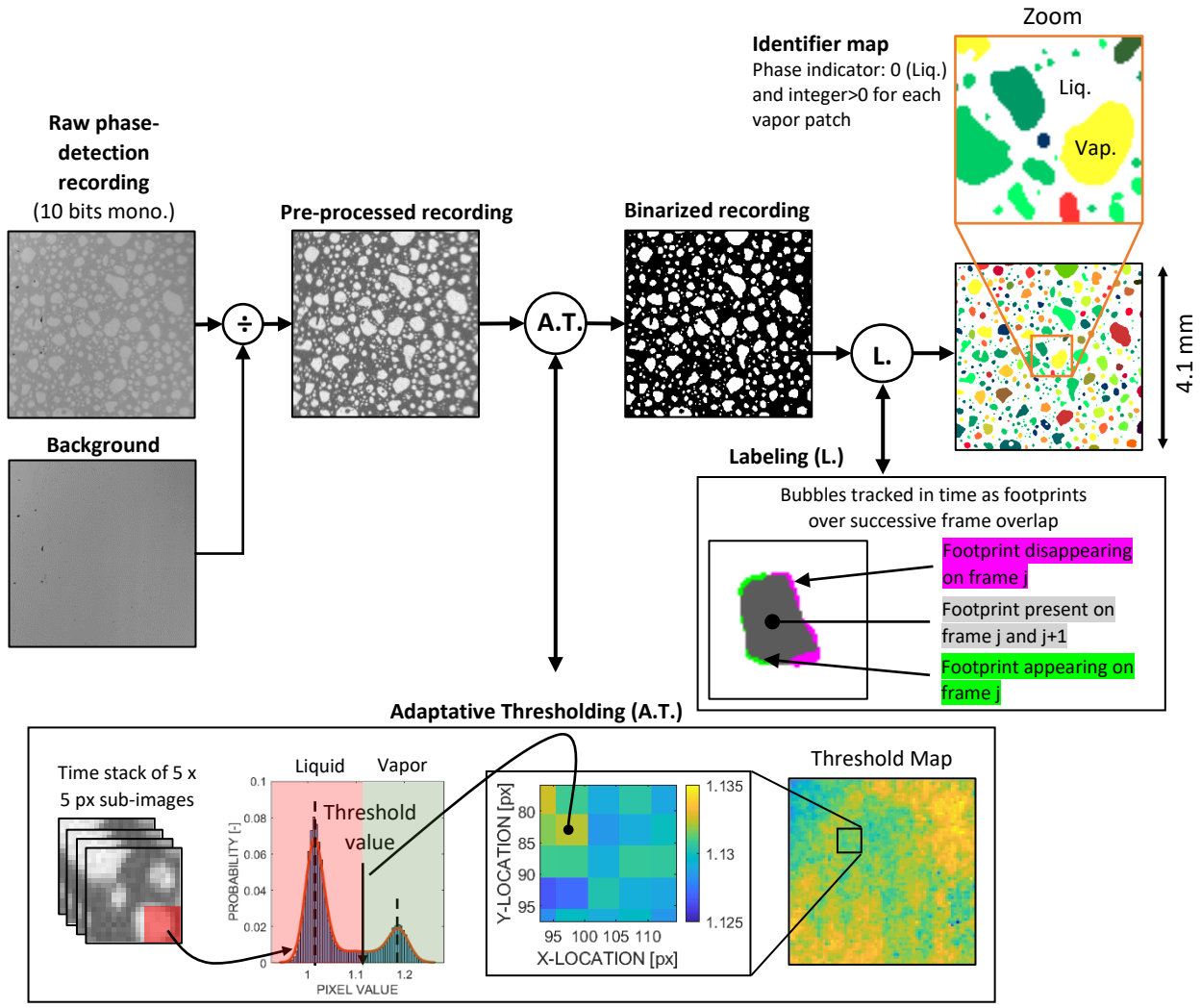

Figure 2.25. Overview of the image-processing used for segmenting the vapor phase from the liquid phase on phase-detection recordings.

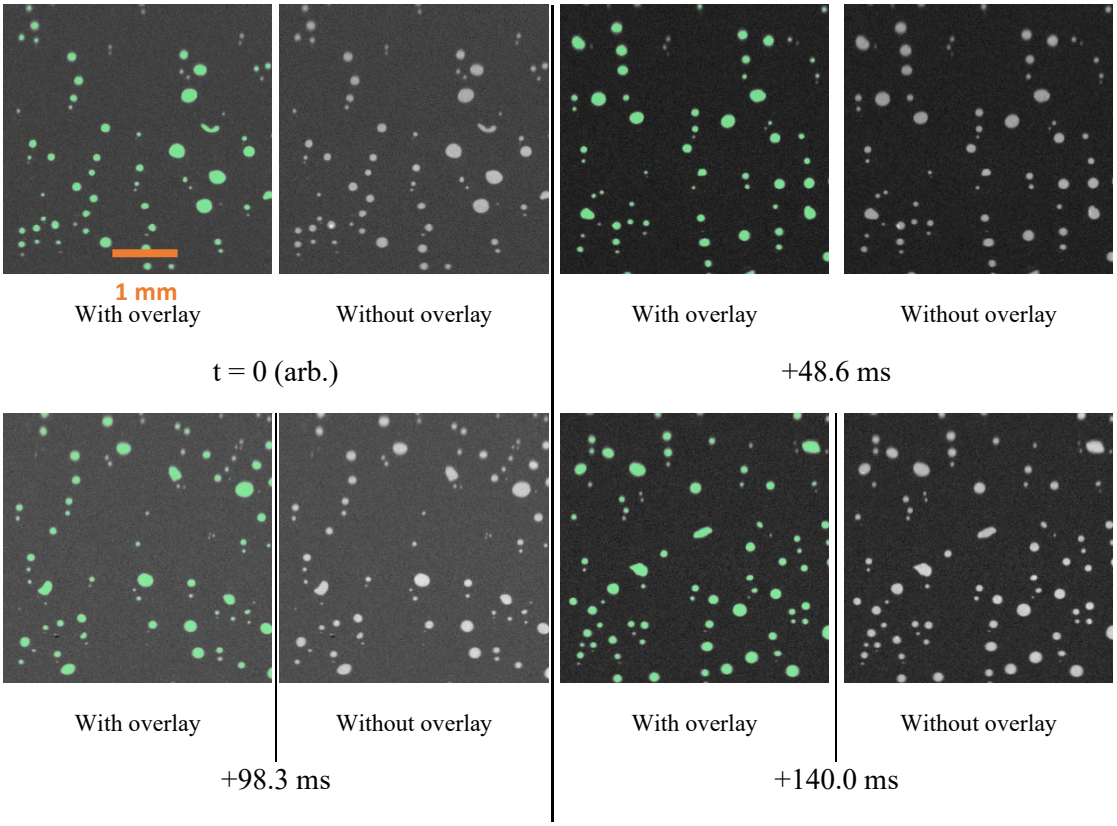

Figure 2.26. Series of phase-detection images with binary masks as overlay for a nitrogen boiling test on an inclined surface (α~60º). The average wall superheat is +1.2 K. Images without overlay are added for comparison.

An uncertainty analysis of the segmentation procedure was carried out by segmenting bubbles manually on a number of pre-processed phase-detection images and comparing them with the segmentation algorithm. Figure 2.23 shows the results of the analysis. The counting error is between 10% close to ONB to 50% near DNB. The segmentation algorithm always underpredicts the number of bubbles as it misses the very small bubbles (i.e., 2-3 px in diameter). Since the error is mainly due to such bubbles, the segmentation errors on the dry area fraction or contact line density is likely lower.

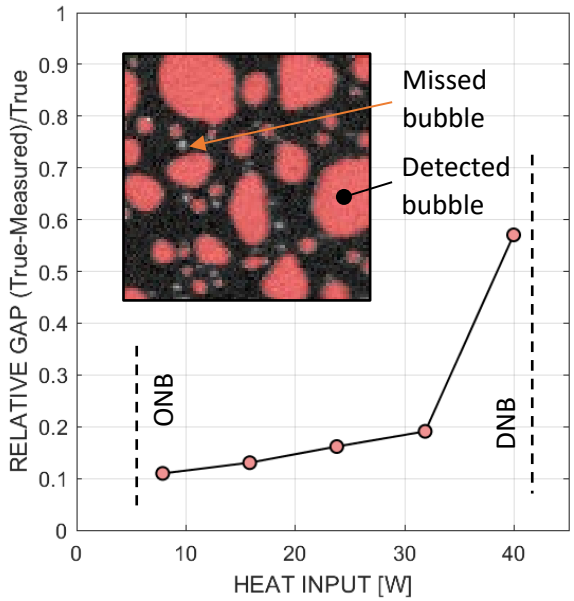

Figure 2.27. Segmentation error measured based on bubble counting.

2.2.3. Measurement of active nucleation site density

Nucleation site density is a complicated quantity to measure experimentally. Our phase-detection shows the phase distribution in contact with the heated surface at a given instant. Since the space and time resolution are limited, bubble footprints are never points, but always appear as a patch with a certain surface area much larger than the nucleating cavity size, even at the first frame they can be tracked on the recording.

We first tried to estimate the nucleation site density based on the centroid of the bubble footprint right after nucleation. Of course, multiple bubbles can come from a same active nucleation site, and therefore the challenge of this method is to determine when distinct centroids correspond to a same site. Figure 2.24 illustrates the issue. The centroids corresponding to the initial bubble footprint, i.e., the first footprint observed on the heat surface for several bubbles (marked 1 throughout 5), are marked by red crosses. Over time, multiple bubble can nucleate on the heated surface generating the map shown in Figure 2.24, with bubbles 1-5 appearing at the same or distinct time. Using this map which can be generated from phase-detection recordings, it is not clear whether bubbles 2 and 3 should be considered coming from the same nucleation sites. Our method to tackle this problem was to impose a minimum distance to consider 2 nucleation sites to come from the same site. We chose the minimum distance to be equal to a fraction of average bubble footprint diameter observed on the boiling surface (typ. around 100 μm). The nucleation site density is therefore dependent from the chosen distance. Also, the order chosen to group the centroids matters. E.g., in Figure 2.24, if we were to group the centroids of the bubbles 4 and 5 and mark the potential

nucleation site at half the distance between 4 and 5, then we could group this new potential site with the centroid of bubble 1, even if the centroids of the bubble 1 and 5 were initially sufficiently spread not to be considered coming from the same nucleation site. Note that counting nucleation sites by hand results in the same problem. A judgement call has to be made to decide whether multiple bubbles come from a same nucleation site.

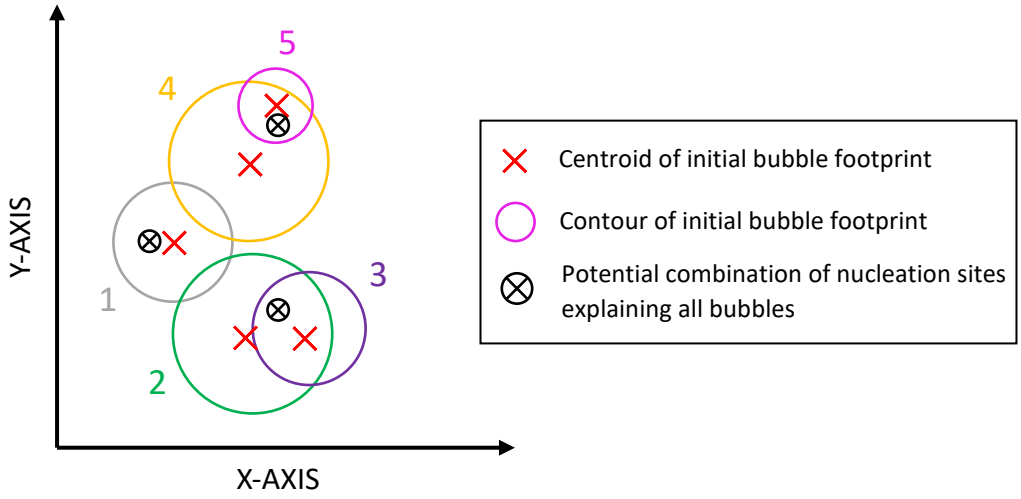

Figure 2.28. Schematics of initial bubble footprints and potential placements of nucleation sites.

We developed a more robust and rigorous approach to estimate the active nucleation site density. In particular, the proposed method aims to provide the minimum number of active nucleation site, noted N_{min} (N''_{min} for the density) required to explain all bubbles nucleating on the boiling surface recorded using phase-detection. Using the example of Figure 2.24, the goal is to evaluate the minimum number of active sites required to explain the nucleation of bubbles 1 throughout 5. To perform this evaluation, we assume that the nucleation site generating a given bubble lies necessarily below its initial footprint. For instance, the nucleation site explaining the bubble 3 shown in Figure 2.24 has to be inside the circle colored in purple. Consequently, the same nucleation site can explain the bubble 2 if the site is also inside the circle colored in green. The problem is then purely mathematical and doesn't rely on further assumption. The actual nucleation site density could potentially be higher than N''_{min}, but cannot be evaluated from phase-detection without further assumptions. It is rather clear that N_{min} depends on the number of bubbles generated on the boiling surface, the number of intersections between their initial footprints and the level of these intersections, i.e., the number of bubbles intersecting at a given point on the surface. In the example of Figure 2.24, we can see that at least 3 nucleation sites (e.g., the set identified by circled cross) are required to explain all visible bubbles. Figure 2.25 (left) shows an example of a frame where a single initial bubble

footprint has been isolated. Figure 2.25 (right) shows a map of boiling surface constructed by summing the phase maps for all frames recorded at a given boiling step, and showing only the initial footprints of bubble. The color-scale shows the level of intersection, i.e., the number of initial footprints that had overlapped on a given pixel during the recording. We can see a wide range of situations, with regions where up to 20 successive bubble footprints would intersect and other where a single bubble footprint is seen. This recording lasted about 140 ms and was obtained for a saturated nitrogen, horizontal upward facing pool boiling experiment at a pressure of 70 psi-a.

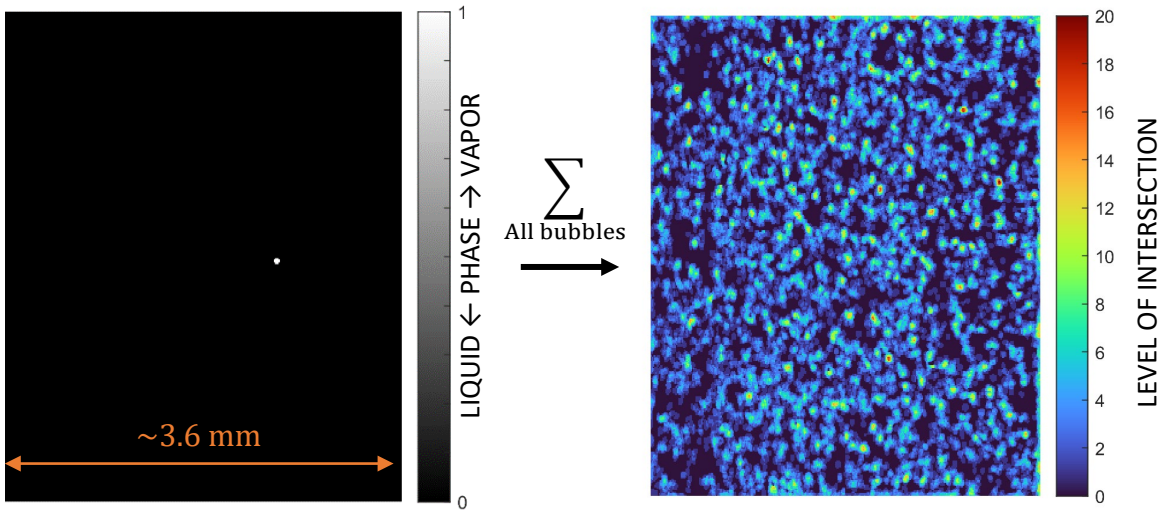

Figure 2.29. Map of initial bubble footprint used to identify active nucleation site, for a single bubble (left) and all bubbles of a recording (right).

Finding an analytical expression of $N_{\min}$ is not straightforward. Instead, $N_{\min}$ is found by numerical analysis. The algorithm used relies on finding the largest set of bubble footprints for which footprints do not intersect one another. Since there are no intersecting footprints, the minimum number of nucleation sites necessary to explain all footprints of the set is equal to the number of footprints in the set. Figure 2.26 shows the largest number of separated footprints found for the case presented in Figure 2.25, i.e., upward facing saturated nitrogen boiling. In this particular case, we find at most 2149 separated bubble footprints, and therefore at least 2149 nucleation sites, giving a minimum active nucleation site density $N''_{\min}$ around $167*10^6$ sites/m^2.

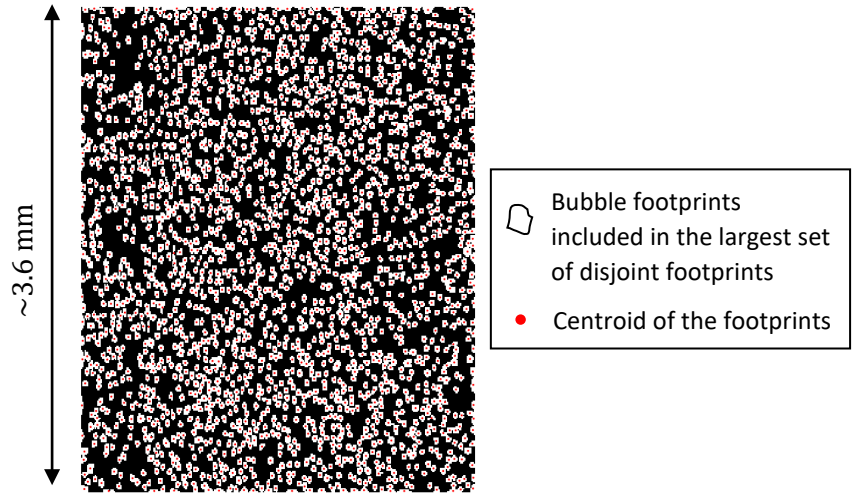

Figure 2.30. Map of the largest set of initial bubble footprints, which don't overlap with one another.

We should stress that the method described provides an estimate of the active nucleation sites density rather than the nucleation sites density. A site can be detected only if at least one bubble nucleates from it over the duration of the phase-detection recording, i.e., that an active site nucleating at a frequency smaller than 7 Hz might not get detected on a recording lasting about 140 ms.

The method shows some limitations. In particular, the value of $N_{\min}$ cannot get larger than the maximum number of footprints that can fit on the surface without overlapping one another. The upper-bound depends on the size of the heated surface and on the minimum bubble footprint that can be detected. In the case we presented in Figure 2.25 and 2.26, we cannot have more than 7,140 sites, considering an imaged surface of 338 pixels x 338 pixels and a minimum footprint of 4 pixels in diameter. The second limitation is that the method doesn't inform on the exact positions of the nucleation sites, but only on their number.

2.2.4. Image treatment for backlit shadowgraphy recordings

The processing of the backlit shadowgraphy is rather different than the one used for phase-detection. The shadowgraphy images are much more complicated by nature, as bubble migrating through the boiling cell obstruct light access to the bubbles of interest on the surface.

Due to the design of the experiment, the recording of the backlit shadowgraphy cannot be directly overlapped. The shadowgraphy is performed using a camera attached to the test-section and therefore always shows the same field of view as the inclination angle of the test-section is changed. However, the camera used for phase-detection is placed on tripod separated from the experiment, which is aligned each

time the test-section orientation is changed. Both cameras are synchronized in time, with a framerate for the phase-detection typically twice than for the shadowgraphy, 14 kHz and 7 kHz, respectively.

The heater does not have clear reference points which can be used to realign the shadowgraphy recording with its phase-detection counterpart. Instead, the recordings are realigned using the centroids of multiple bubbles as control point. The control points on the reference image on each recording are numbered such that a control point on the shadowgraphy image is paired with a point on the phase detection image. Among the 5 pairs of control points, 4 are used to calculate the mapping between the two reference images while the last pair is used to verify how well a point not used in the calculation is matched. Let's consider the following pairs of points on each reference image,

$$\{(x_1, y_1) \dots (x_5, y_5)\}_{\mathrm{BS}} \text{ and } \{(u_1, v_1) \dots (u_5, v_5)\}_{\mathrm{PIR}} \tag{2.2}$$

With BS standing for Backlit Shadowgraphy and PIR for Partial Internal Reflection (i.e., the phase-detection). Therefore, the point with coordinate (u_1, v_1) on the phase detection image corresponds to the point with coordinates (x_1, y_1) on the shadowgraphy image. The coordinates (x, y) and (u, v) are related by an affine transformation represented by a 3 x 3 matrix M such that,

$$MX = U \tag{2.3}$$

with

$$M = \begin{bmatrix} m_{11} & m_{12} & m_{13} \\ m_{21} & m_{22} & m_{23} \\ 0 & 0 & 1 \end{bmatrix}, \qquad X = \begin{bmatrix} x \\ y \\ 1 \end{bmatrix} \text{ and } U = \begin{bmatrix} u \\ v \\ 1 \end{bmatrix} \tag{2.4}$$

While the space of the image is only 2-dimensional, it is convenient to represent M as 3-dimensional. The coefficients m_{13} and m_{23} represent coordinate shifts along the u and v axis, respectively. However, the 3rd row of the matrix M can be ignored. Eq. 2.4 can be rewritten by transforming the matrix M into a vector, noted M_v and the vector X into a matrix X_M:

$$X_M M_v = U. \tag{2.5}$$

After extending the matrices to account for each control points,

$$X_M = \begin{bmatrix} x_1 & y_1 & 1 & 0 & 0 & 0 \\ 0 & 0 & 0 & x_1 & y_1 & 1 \\ & & \dots & \dots & & \\ & & \dots & \dots & & \\ x_4 & y_4 & 1 & 0 & 0 & 0 \\ 0 & 0 & 0 & x_4 & y_4 & 1 \end{bmatrix}, \qquad M_v = \begin{bmatrix} m_{11} \\ m_{12} \\ m_{13} \\ m_{21} \\ m_{22} \\ m_{23} \end{bmatrix} \text{ and } U = \begin{bmatrix} u_1 \\ v_1 \\ \dots \\ \dots \\ u_4 \\ v_4 \end{bmatrix} \tag{2.6}$$

Therefore, the coefficients m_{ij} of the affine transformation can be found by solving,

$$M_v = {X_M}^{+} U \tag{2.7}$$

${X_M}^{+}$ being the pseudo-inverse matrix of X_M.

An alternative method was later found to evaluate the affine transformation by simply using the function *fitgeotform2d* implemented in MatLab (R2022). The built-in function of MatLab uses a more complex form of the algorithm but gives nearly-identical results than obtained by using Eqs. 2.7 and 2.6 in the tested cases. The transformation is verified by inspecting the overlap between the shadowgraphy images and the phase-detection binary map. The error associated with the transformation is checked on the 5th pair of points, not used in the calculation of the transformation. The error should be below 1 pixel difference (in x and y coordinate), typically it is below ½ pixel. Figure 2.27 shows a schematic of the processing procedure to align phase-detection and shadowgraphy recording.

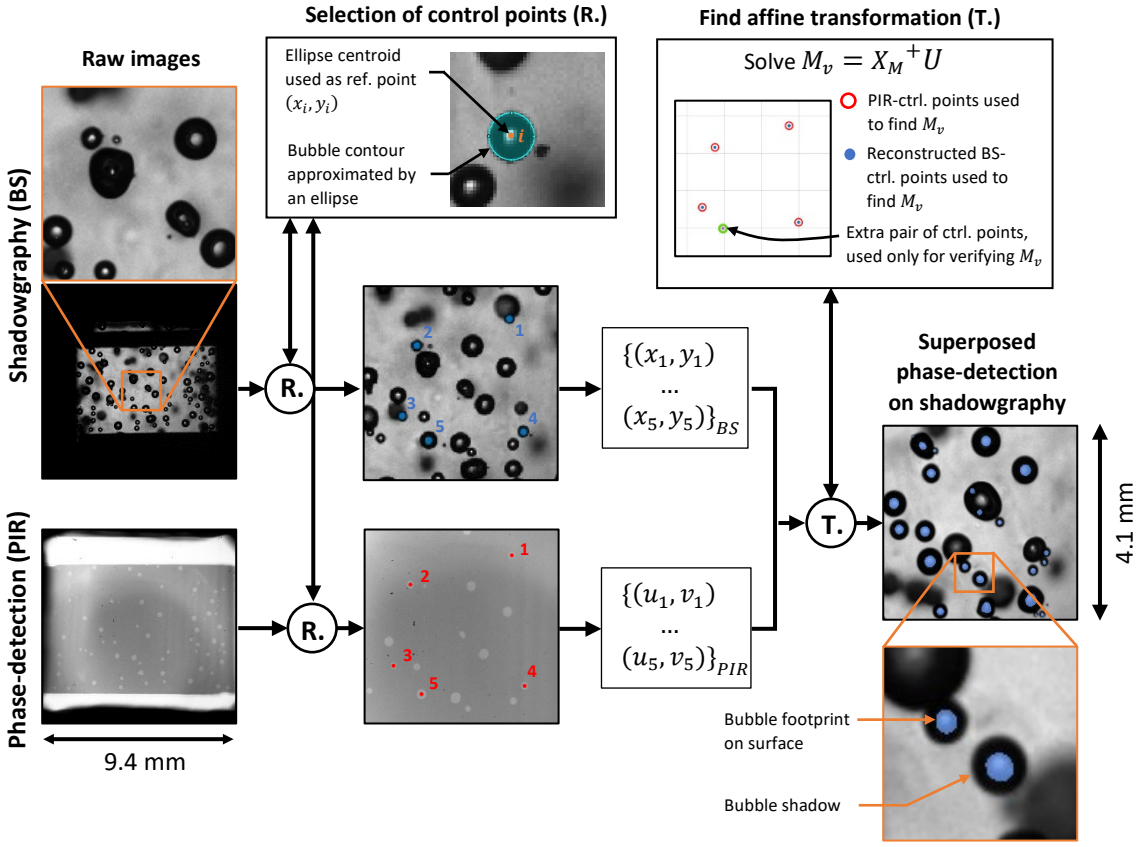

Figure 2.31. Image-processing used for superposing shadowgraphy and phase-detection recording.

A processing procedure is also required for segmenting the shadowgraphy recordings. A different method than proposed for phase-detection recordings is required. The shadowgraphy images are inherently more complicated due to depth perception, e.g., bubbles shadows can overlap or move out of focus after lifting-

off from the heated surface while still appearing on camera. Figure 2.28 shows a diagram of the procedure used to segment the shadowgraphy recordings.

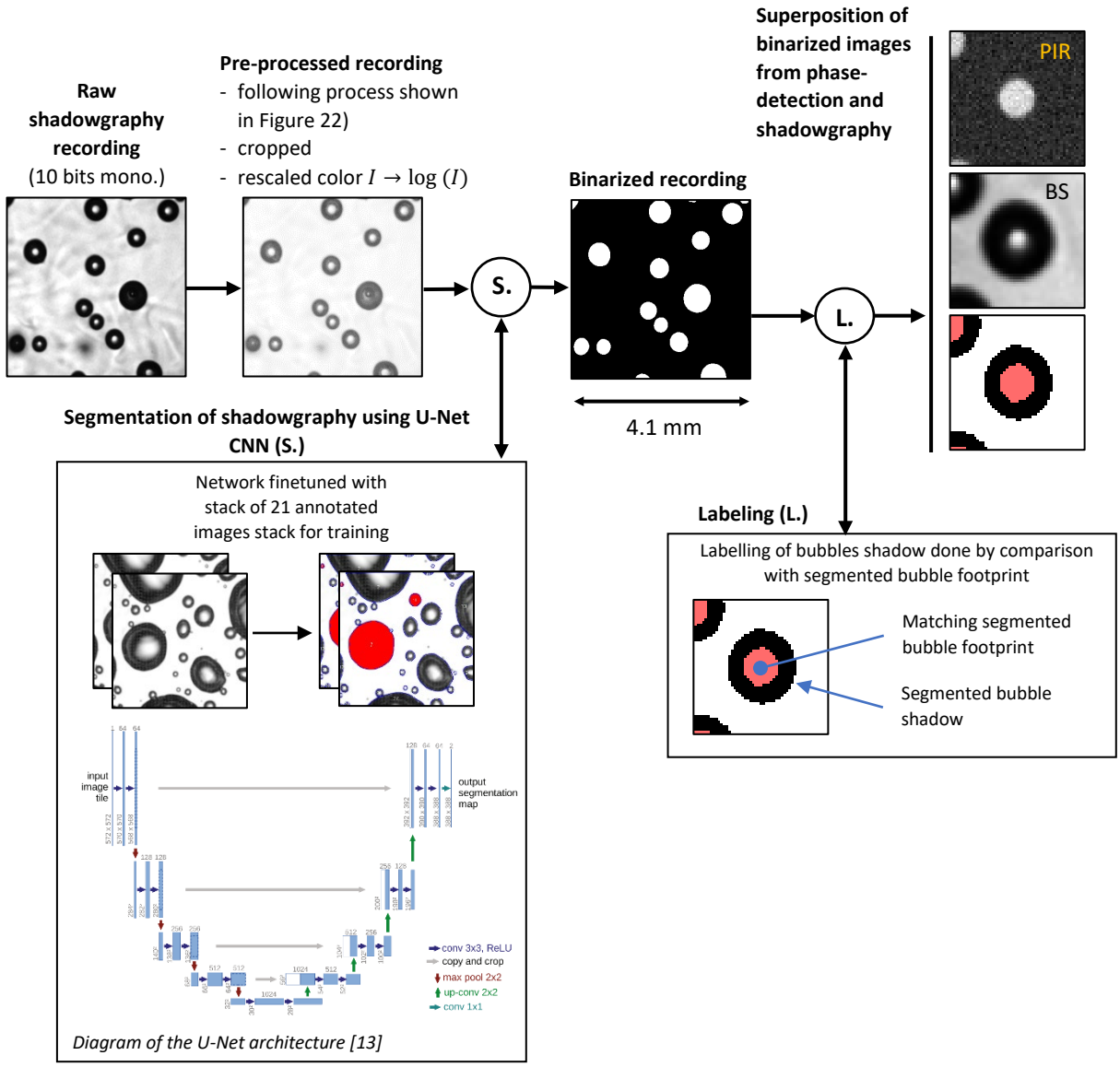

Figure 2.32. Overview of the image-processing used for segmenting the vapor phase from the liquid phase on phase-detection recordings.

The method shown in Figure 2.28 leverages our experience using convolutional neural network. Our laboratory recently develop method to use a U-net neural network, developed by the university of Freiburg [78], to segment shadowgraphy images obtained for nucleate boiling water [79]. The network has been fine-tuned for this study to segment shadowgraphy images of nitrogen boiling data. Despite the important improvement in segmenting bubbles in complicated images, only low heat flux with minimum bubbles

interactions can be post-processed and analyzed. Figure 2.29 shows shadowgraphy images with the segmented bubbles represented as green overlay. The labelling of bubbles on shadowgraphy recordings is straightforward since phase-detection and shadowgraphy recordings are synchronized and can be overlapped.

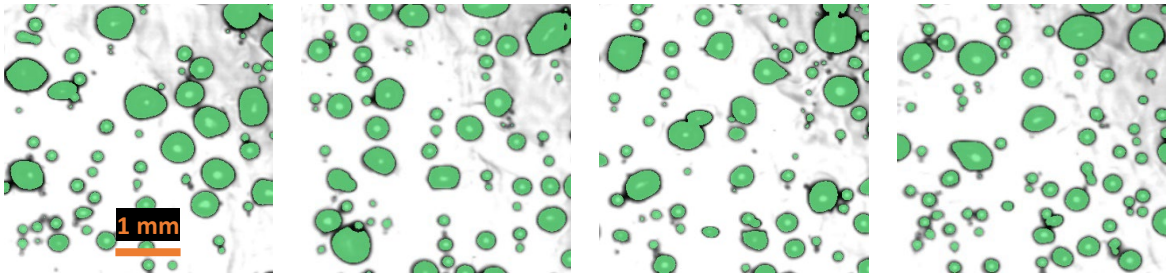

t = 0 (arb.) (A) +46.8 ms +96.6 ms +140.0 ms

Figure 2.33. Series of backlit shadowgraphy images with binary masks as overlay for a nitrogen boiling test on an inclined surface (α~60º). The average wall superheat is +1.2 K.

2.3. Measurement uncertainty and reproducibility

The measurement uncertainty on the heat input is ±1.5%. The uncertainty on temperature has a bias error common to all measurements and a random error. The RTDs are calibrated against 2 T-type thermocouples. At cryogenic temperature, the thermocouples had unacceptable biases, and therefore were recalibrated against the saturation temperature obtained from pressure measurement. The resulting bias on the RTD measurements is about ± 1 K. For each boiling step, heat input and temperature are measured over 1 second at 1 kHz. Only the averaged measured value is shown. The repeatability of the measurements indicative of our random error is lower than the bias error as shown by Figure 2.30, with a dispersion at ±2σ of 0.5 K. The error bars are omitted for clarity when plotting heat input and temperature measurement.

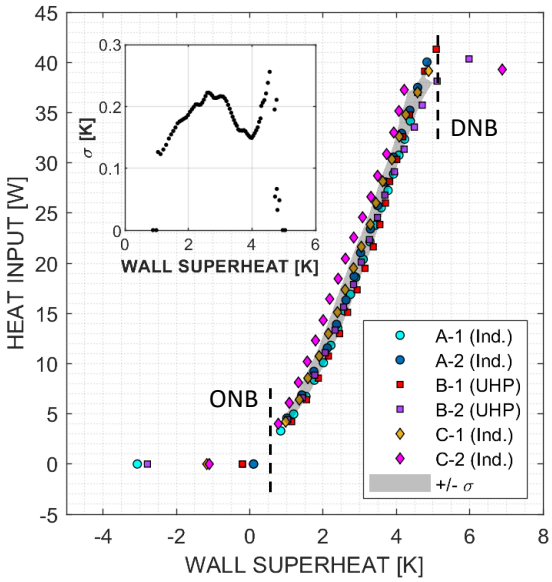

Figure 2.34. Reproducibility of boiling curves measurement for saturated pool boiling at 0.48 MPa. Each marker color indicates a distinct boiling test. Test named with the same letter (A, B or C) are performed the same day. The nitrogen grade used for each test is given in the legend. ONB and DNB stand for Onset of Nucleate Boiling and Departure from Nucleate Boiling, respectively.

2.4. Equilibrium contact-angle measurement

Wettability of the heating surface impacts the boiling heat transfer and should be taken into account when comparing experimental data. Since no published measurement of equilibrium contact angle have been found in our conditions, i.e., nitrogen on a sapphire-ITO surface, we performed our own measurements with sessile drops of liquid nitrogen at atmospheric pressure. To perform these measurements, a droplet of liquid nitrogen is formed at the tip of a 0.02" inner diameter needle and dropped on a sapphire substrate coated with ITO. Figure 2.31 shows the experimental set up used. The needle is cooled by surrounding it with liquid nitrogen. Droplet diameter ranges from 1 to 2 mm. The sapphire is kept between 0 and 3 K below saturation (i.e., between 74 and 77 K) and the temperature is monitored with a T-type thermocouple attached to the sapphire holder. After impact, the footprint of droplet of nitrogen on the surface spreads until it reaches a steady state. The entire process is recorded with a high-speed video at 4,000 fps and 18 µm of pixel resolution with side view slightly looking downward. The ITO-sapphire surface is cleaned with iso-propanol and dried with nitrogen before the series of tests, and the ITO is heated regularly between tests to remove frost forming on its surface from residual humidity present in the chamber. The testing cell is inside a moisture-free chamber to prevent frost to form on optical accesses. The height of the needle orifice from the substrate surface is kept short enough to prevent the droplet to break on impact. An estimate of maximum heigh ensuring that the droplet integrity can be obtained by enforcing the gravitational potential energy to be lower than the droplet's surface energy:

$$E_{\mathrm{p}}\left(=\rho_{\mathrm{l}}\frac{4\pi}{3}{R_{\mathrm{d}}}^{3}gh\right)<E_{\sigma}\left(=\sigma 4\pi {R_{\mathrm{d}}}^{2}\right) \tag{2.8}$$

where R_d is the droplet radius and h the height from which the droplet falls. Therefore, the condition on h is,

$$h<\frac{3\sigma}{R_{\mathrm{d}}\rho_{\mathrm{l}}g} \tag{2.9}$$

Using the nitrogen properties at saturation and atmospheric pressure, we get that the height should not exceed 2 and 4 mm, for a droplet radius between 1 and 2 mm, respectively.

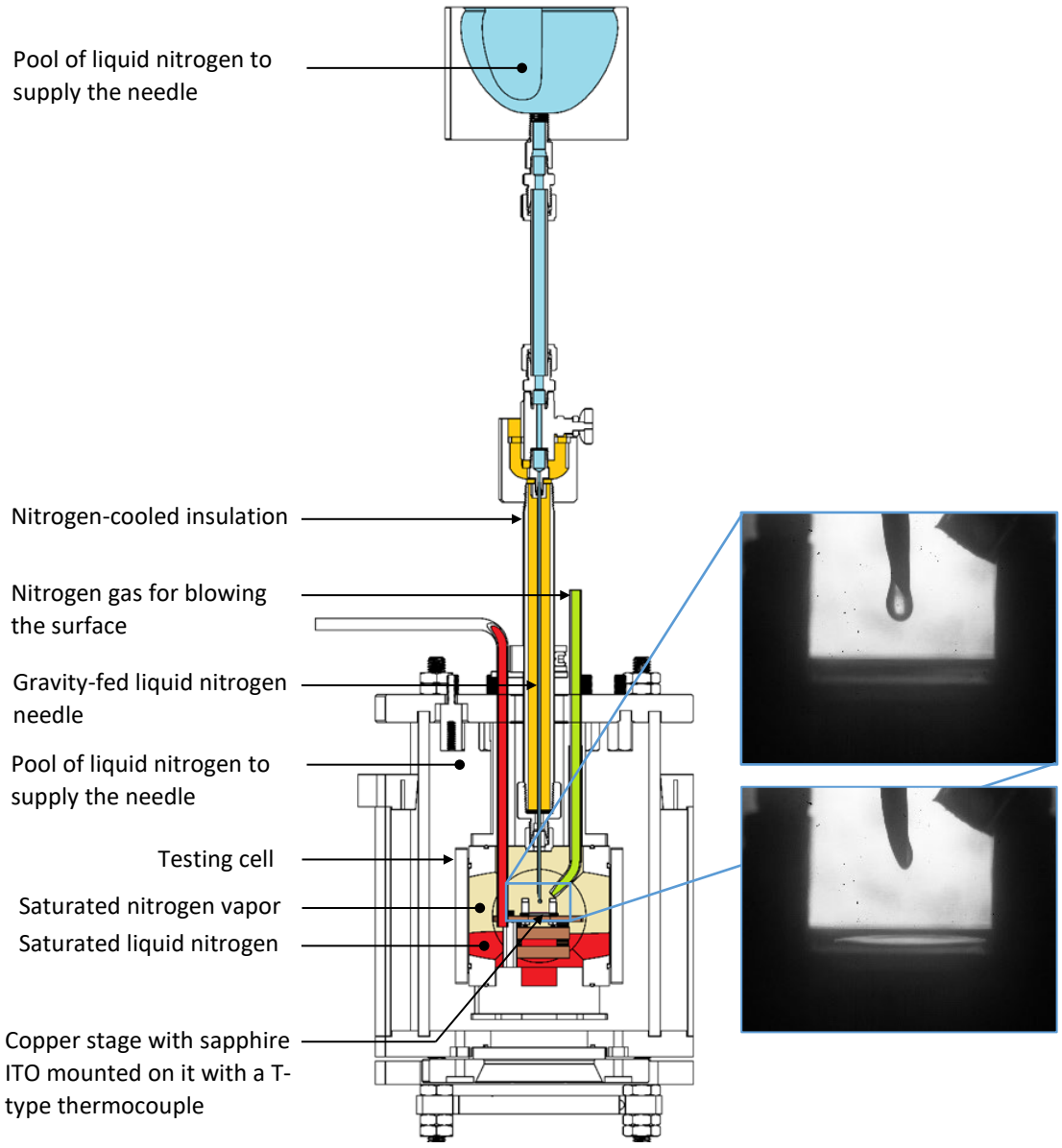

Figure 2.35. Schematics of the experimental setup used to measure the equilibrium contact angle of a nitrogen sessile droplet.

The droplet diameter is measured after leaving the needle, and by assuming sphericity, we can get its volume. Additionally, the diameter D_p of the puddle formed by the droplet on the surface can be evaluated, assuming that the puddle is axisymmetric after reaching a steady state. By assuming conservation of the droplet volume, we can estimate the static contact angle formed by the puddle.

The puddle cannot be modeled as a spherical cap as gravity forces are not insignificant compared to the surface tension,

$$R_f > \sqrt{\frac{\sigma}{\rho_l g}} \sim 1.1 \text{ mm} \tag{2.10}$$

where R_f is the radius of the puddle footprint. Instead, we solve the axisymmetric force balance for the droplet on the surface, including gravitational and surface tension effects,

$$\frac{z''}{(1+z'^2)^{3/2}} + \frac{z'}{x(1+z'^2)^{1/2}} = \frac{2}{b} + \frac{\rho g z}{\sigma} \tag{2.11}$$

z is the coordinate of the axis normal to the surface, pointing downward, with $z = 0$ at the apex of the droplet, x the radial distance of the interface from the center, b the curvature of the interface at the apex. z' and z'' corresponds the derivative and double derivative of z with respect to x.

This equation can be solved by parametrizing θ, where θ is the angle formed by the vertical and the radius passing by the point (x, z). The equation can also be split into 2 first-order differential equations and the system of equations can be solved using a numerical solver (e.g., MatLab's ode45 solver). The volume of the droplet, known experimentally, can be evaluated from,

$$v = \int_0^h \pi x^2 dz \tag{2.12}$$

h is equal to $z(\theta = \theta_{st})$ with θ_{st} the angle between the interface and the horizontal at the coordinate z The base radius of the droplet is given similarly by $x(\theta = \theta_{st})$. The equation requires to iterate on the volume v and the apex curvature b to get to the solution $x(z)$. Figure 2.32 shows images of the 2 droplets during measurement.

Example #4 *of LN_2 droplet on ITO/Sapphire – h~4.1 mm*

$t = 0$ +24 ms +37 ms +160 ms +1 s

Example #9 *of LN_2 droplet on ITO/Sapphire – h~2.3 mm*

$t = 0$ +40 ms +63 ms +113 ms +0.413 s

Figure 2.36. Images of liquid nitrogen droplets on ITO/Sapphire in a nitrogen gas atmosphere, with a space resolution of 18 µm/px.

Table 2.1 shows the results for all recorded droplets. An estimated measurement uncertainty of ± 10° should be considered.

Table *2.3.* Static contact angles measured for liquid nitrogen droplet close to saturation on ITO/sapphire.

Droplets	**Needle height [mm]**	**Diameter D_d [mm]**	**Footprint diameter D_f [mm]**	**Ratio D_f/D_d**	**Equilibrium contact angle θ_Y [°]**
#1	4.1	1.53	10.55	6.88	1.9
#2	4.1	1.59	> 10.7	> 6.75	< 2.0
#3	4.1	1.61	8.10	5.05	4.0
#4	4.1	1.82	9.29	5.09	4.3
#5	2.3	1.66	9.09	5.47	3.4
#6	2.3	1.61	8.74	5.44	3.4
#7	2.3	1.50	8.85	5.91	2.6
#8	2.3	1.70	9.49	5.59	3.3
#9	2.3	1.68	9.56	5.70	3.1
				Average:	3.2 ± 0.8 (1σ)

The equilibrium contact angle shown in Table 2.1 shows that liquid nitrogen has a super-hydrophilic behavior on our nano-smooth ITO-sapphire substrate, similar to typical all metallic surfaces with cryogens (e.g., see Ref. [80]).

Measurements on equilibrium contact angle of nitrogen on solid carbon dioxide were also carried out. To perform such measurement, the setup shown in Figure 2.31 was modified. The copper stage shown in Figure 2.31 was replaced by a hollow and sealed copper stage in which liquid nitrogen can be flown through. This allows the testing cell to stay dry during measurement, while keeping the stage at the saturation of nitrogen (i.e., 77 K at 1 atm). Figure 2.33 shows images of the setup with and without a solid carbon dioxide coating. No ITO-sapphire substrate is attached to the stage for these measurements. The top surface of the stage where the nitrogen droplets are dropped is mirror polished. Gaseous CO_2 can be introduced in the testing cell, which freezes at the contact of the cold stage forming a thick layer of CO_2 frost. The atmosphere of the testing cell is then replaced by dry nitrogen prior to the measurement. The thickness of CO_2 frost could not be measured. However, tests with different thicknesses did not show any different in the results.

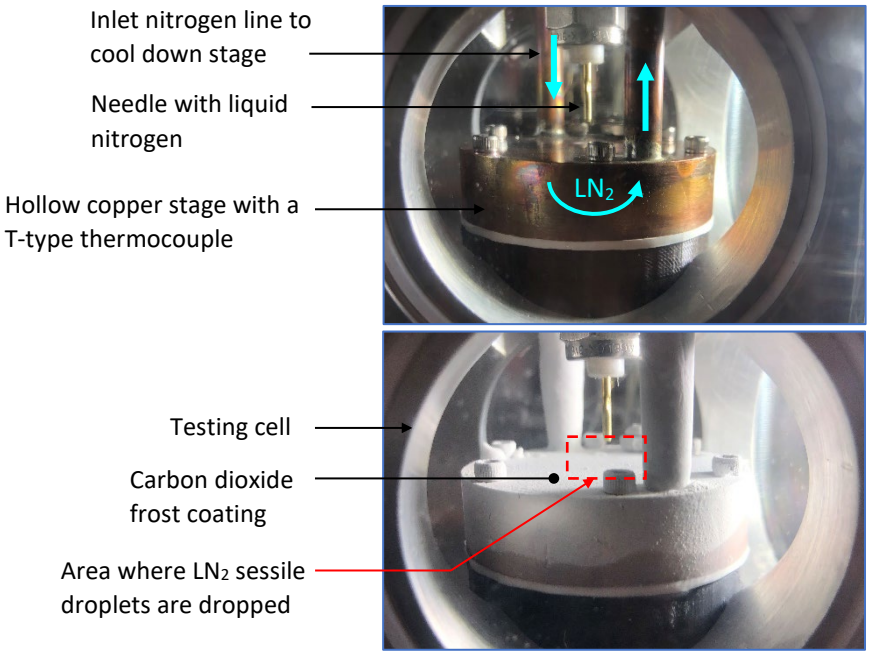

Figure 2.37. Images of the testing cell to measure the equilibrium contact angle of a nitrogen sessile droplet on solid carbon dioxide.

Table 2.2 shows the results for recorded droplets of nitrogen on a thin layer of solid carbon dioxide (before reaching a porous snow-like appearance). An estimated measurement uncertainty of ± 10° should be considered.

Table 2.4. Static contact angles measured for liquid nitrogen droplet close to saturation on solid carbon dioxide.

Droplets	Needle height [mm]	Diameter D_d [mm]	Footprint diameter D_f [mm]	Ratio D_f/D_d	Equilibrium contact angle θ_Y [°]
#1	4.8	1.97	9.38	4.75	5.3
#2	4.8	1.79	9.13	5.09	5.0
#3	4.8	1.77	9.01	5.09	5.0
				Average:	5.1 ± 0.2 (1σ)

An example of droplet measurement is shown in Figure 2.34 with droplet #3 of Table 2.2.

Example #3 *of LN_2 droplet on CO_2/Copper – h~4.8 mm*

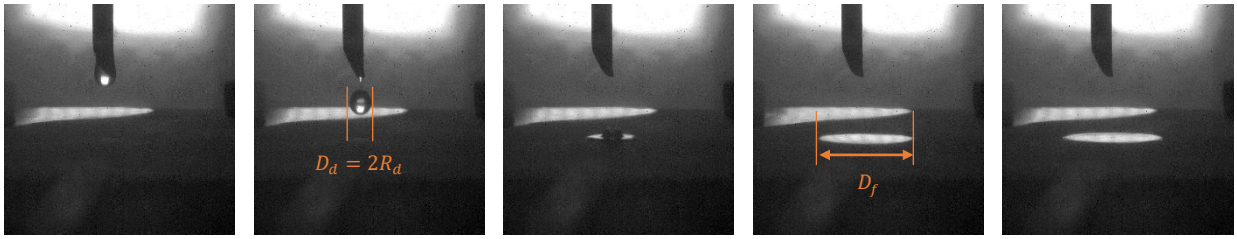

$t = 0$ +175 ms +192 ms +205 ms +670 ms

Figure 2.38. Images of liquid nitrogen droplets on ITO/Sapphire in a nitrogen gas atmosphere, with a space resolution of 23 µm/px.

2.5. Test-matrix

Table 2.3 summarizes operating conditions and the test-matrix that has been performed in order to answer the scientific question listed in Chapter 1.

Table 2.3. Test-matrix

Experimental parameters	**Values**	**Unit**
Heater design	ITO-coated monocrystalline sapphire slab	
Fluids	Industrial purity LN_2/GN_2	
Absolute pressure	0.492 ± 0.014 (~71.5 psi-a)	MPa
Bulk temperature	Saturated (i.e., 93.8 K)	K
Tilt angle of the heating surface	0 (heating surface horizontal upward facing), 30, 60, 90 (vertical), 120, 150, 165, 175, 179 (horizontal downward facing)	°
Heat flux direction	Steady-state increasing with pre-heating	

3. EXPERIMENTAL RESULTS ON INDIVIDUAL BUBBLES

In this chapter, we analyze the characteristics of uncoalesced nitrogen bubbles, i.e., bubbles which nucleate on the heating surface and disappear either by lifting-off or coalescing with other bubbles, therefore forming coalesced bubbles. Figure 3.1 shows a schematic of bubble growing on the surface, viewed from their footprint . Bubble #1 nucleates on the surface, grows, and eventually lift-off, or coalesce with bubble #2 to form a coalesced bubble, called bubble #3. In our analysis, bubbles #1, #2 and #3 will treated as distinct objects.

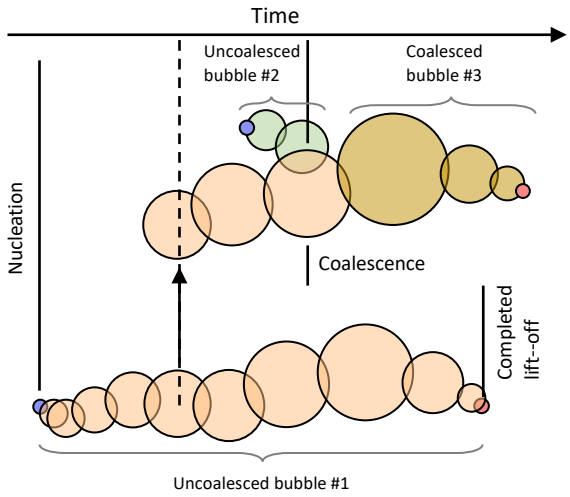

Figure 3.39. Schematics of growing and coalescing bubbles over time, represented by their footprint.

In the first part of this chapter, we focus on uncoalesced bubbles. This allows us to measure critical boiling parameters and identify evaporative mechanisms at play during growth which are necessary to the development of heat flux partitioning model. By the end of the chapter, we will discuss how to extend the analysis to bubbles which results from coalescence. An analysis of cryogenic boiling as a system of interacting bubbles will be given in the next chapter.

3.1. Bubble growth

3.1.1. Basic theory of bubble growth

The growth of bubbles has been extensively studied both experimentally and theoretically. Several authors, e.g., Scriven [81], and Plesset and Zwick [82] among others, have provided analytical solutions of the problem of bubble growth for idealized spherical bubbles growing in a uniformly superheated liquid. A

detailed derivation of such model has been nicely reported by Brennen [83]. We will provide an outline of the model and use some of the results.

The model considers a spherical bubble of radius $R(t)$ immersed in an infinite pool of liquid with uniform temperature. For growth to occur, the pool has to be superheated. The mass and momentum conservation equations in the liquid leads to the so-called Rayleigh-Plesset equation:

$$\frac{p_{\mathrm{v}}(T_\infty) - p_\infty}{\rho_{\mathrm{l}}} + \frac{p_{\mathrm{v}}(T_{\mathrm{B}}) - p_{\mathrm{v}}(T_\infty)}{\rho_{\mathrm{l}}} = R\ddot{R} + \frac{3}{2}\left(\dot{R}\right)^2 + \frac{4\vartheta_{\mathrm{l}}}{R}\dot{R} + \frac{2\sigma_{lv}}{\rho_{\mathrm{l}}R} \tag{3.1}$$

$p_{\mathrm{V}}(T)$ is the saturation pressure of nitrogen at the temperature T, ρ_l the density of the liquid, ϑ_{l} its kinematic viscosity and σ_{lv} the liquid-vapor surface tension. The left terms are the driving terms of the bubble growth or collapse due to liquid pressure (1st term) and temperature (2nd term). The right terms correspond to reaction of the system due to inertia (1st and 2nd terms), liquid viscosity (3rd term) and surface tension (4th term). Few non-condensable gases can be present in liquid nitrogen. Only neon, hydrogen and helium have a boiling point lower than nitrogen, and only traces of these gases are present in our nitrogen. Therefore, their presence during bubble growth can be safely neglected. Using this assumption, we get,

$$p_{\mathrm{B}}(t) \sim p_{\mathrm{v}}\left(T_{\mathrm{B}}(t)\right) \tag{3.2}$$

For analytical purpures, the second term can then be linearized using Clausius-Clapeyron relationship,

$$\frac{p_{\mathrm{v}}(T_B) - p_{\mathrm{v}}(T_\infty)}{\rho_l} \sim \frac{\rho_v(T_\infty)h_{\mathrm{lv}}(T_\infty)}{\rho_l(T_\infty)T_\infty}(T_B - T_\infty) \tag{3.3}$$

The energy conservation equation in the liquid is also necessary to close the problem. Assuming thermal diffusion only and by neglecting gravity and viscous related terms, the energy conservation becomes a one-dimensional non-linear heat conduction equation.

$$\frac{\partial T}{\partial t} + \frac{\dot{R}R^2}{r^2}\frac{\partial T}{\partial r} = \frac{\alpha_l}{r^2}\frac{\partial}{\partial \mathrm{r}}\left(r^2\frac{\partial T}{\partial r}\right) \tag{3.4}$$

Lastly, the energy balance at the bubble interface is required to close the problem. Assuming thermal equilibrium in the bubble such that all the heat supplied by the liquid is used as latent heat,

$$\dot{R} = \frac{k_l}{\rho_v h_{lv}}\frac{dT}{dr}_{|R} \tag{3.5}$$

The following approximate solution of the heat equation was proposed by Plesset and Zwick [82],

$$T_\infty - T_B = \frac{\rho_v h_{lv}}{\rho_l c_{p,l}\sqrt{\pi\alpha_l}} \int_0^t \frac{R(x)^2 \dot{R} dx}{\left[\int_x^t R(y)^4 dy\right]^{1/2}} \tag{3.6}$$

The main assumption behind the Plesset-Zwick approximation is considering the thermal boundary layer thin compared to the bubble radius, such that the bubble curvature can be neglected. An exact solution was later provided by Scriven [81]. It is worth mentioning that the popular Mikic et al.'s [31] formulation of bubble growth uses the Plesset-Zwick approximation. We will discuss the validity of this approximation for nitrogen bubble later on. The temperature difference, and consequently the second term of the Rayleigh-Plesset equation can simplified by assuming of a growth law for R, such as

$$R = R_0 t^n \tag{3.7}$$

This assumption leads to,

$$\frac{p_V(T_B) - p_V(T_\infty)}{\rho_l} \sim -\Sigma(T_\infty) C(n) R_0 t^{n-1/2} \tag{3.8}$$

where Σ is a parameter depending only on the fluid properties,

$$\Sigma(T_\infty) = \frac{{\rho_v}^2 {h_{fg}}^2}{{\rho_l}^2 c_{p,l} T_\infty \sqrt{\alpha_l}} \text{ in } [\text{m/s}^{3/2}] \tag{3.9}$$

And $C(n)$ a known function depending only on the value of the exponent n ($C(n) = n\sqrt{\frac{4n+1}{\pi}} \int_0^1 \frac{z^{3n-1} dz}{\sqrt{1-z^{4n+1}}}$).

Replacing Eq. 3.8 in Eq. 3.1 gives,

$$\frac{p_V(T_\infty) - p_\infty}{\rho_l} - \Sigma(T_\infty) C(n) R_0 t^{n-1/2} = R\ddot{R} + \frac{3}{2}\left(\dot{R}\right)^2 + \frac{4\vartheta_l}{R}\dot{R} + \frac{2\sigma_{lv}}{\rho_l R} \tag{3.10}$$

For the case where the viscous and surface tension terms can be neglected compared to the liquid inertia terms (i.e., the first and second right hand-side terms), Eq. 3.10 gives two asymptotic growth trends depending on the relative magnitude of the driving terms. At small time, the second left hand-side term is negligible with the assumption that $n > 1/2$. In this situation, the solution of the equation is given by,

$$R = t\sqrt{\frac{2}{3}\frac{p_V(T_\infty) - p_\infty}{\rho_l}} \tag{3.11}$$

The driving term is only balanced by the liquid inertia and therefore the solution corresponds to the so-called inertia-controlled growth. At large time, the importance of inertial term decreases compared to the second term, and the solution becomes,

$$R = \frac{p_V(T_\infty) - p_\infty}{\rho_l \Sigma(T_\infty) C(1/2)} \sqrt{t} \equiv \frac{Ja_{SH}}{2C(1/2)} (\alpha_l t)^{1/2} \tag{3.12}$$

$C(1/2)$ is equal to $\frac{1}{2}\sqrt{\frac{\pi}{3}}$. With the solution in Eq. 3.12, we can verify that the inertial terms are indeed decreasing with time ($\dot{R} \propto t^{-1/2}$). Here the Jakob number is defined as:

$$Ja_{SH} = \frac{\rho_l c_{p,l}(T_\infty - T_{sat})}{\rho_v h_{lv}} \tag{3.13}$$

$$\dot{R} = \frac{Ja_{SH}}{2C(1/2)} \left(\frac{\alpha_l}{2t}\right)^{1/2} \tag{3.14}$$

The term depending on the fluid properties, i.e., $Ja_{SH}\sqrt{\alpha_l}$, can be rewritten as $\varepsilon_l \Delta T_{sat}/\rho_v h_{lv}$. Figure 3.3 shows a plot $\varepsilon_l/\rho_v h_{lv}$ against pressure for different fluids.

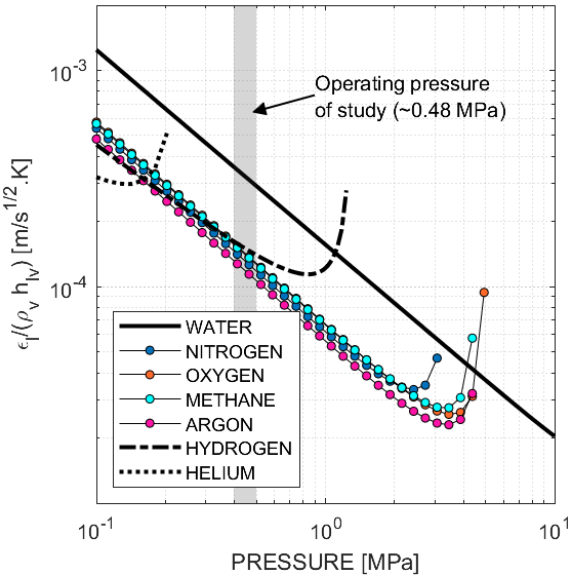

Figure 3.40. Plot of $\varepsilon_l/\rho_v h_{lv}$ vs. pressure for different fluids. The fluid properties are evaluated at saturation.

$\varepsilon_l/\rho_v h_{lv}$ is about 3 times higher in water than in cryogens at pressures far from their critical point. The typical liquid thermal effusivity of cryogens is about 3 to 6 times lower than for water. Instead, the vapor density is about 1 order of magnitude higher in cryogens, which balances with the order of magnitude

smaller latent heat. Hence, according to Eq. 3.14, the growth velocity during heat-transfer controlled growth in cryogens is expected to be lower compared to water for the same wall superheat.

An estimate of the time separating the inertia-controlled growth and thermal-controlled growth can be obtained by comparing the magnitude of the first and second terms of Eq. 3.1,

$$\frac{p_V(T_\infty) - p_\infty}{\rho_l} \sim \Sigma(T_\infty) C(1/2) R_0 {t_{i\to t}}^{1/2} \tag{3.15}$$

Using the R_0 found from the inertial controlled growth solution, it yields to,

$$t_{i\to t} \sim \frac{18}{\pi} \frac{p_V(T_\infty) - p_\infty}{\rho_l} \frac{1}{\Sigma(T_\infty)^2} \tag{3.16}$$

Or with the Jakob number after linearization of $p_V(T_\infty) - p_\infty \approx \frac{\rho_v h_{lv}}{T_{sat}}(T_\infty - T_{sat})$ around T_{sat},

$$t_{i\to t} \sim \frac{18}{\pi} Ja_{SH} \frac{{\rho_l}^2 \alpha_l {T_\infty}^2}{{\rho_v}^2 {h_{lv}}^2 T_{sat}} \tag{3.17}$$

From Eq. 3.16 and 3.17, we can see that the transition from inertia-controlled growth to thermal-controlled growth appears earlier with increasing Σ or decreasing Ja_{SH}. Figure 3.4 shows a plot of the Jakob number vs. pressure for different fluids, normalized per degree of wall superheat.

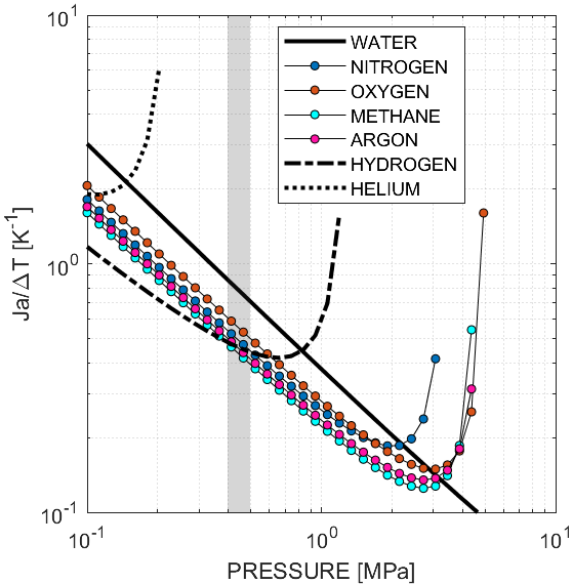

Figure 3.41. Plot of the normalized Jakob number $Ja/\Delta T$ vs. pressure for different fluids at saturation.

We will see later on that the typical range of wall superheat encountered for saturated nitrogen pool boiling is between 1 to 10 K on smooth surfaces, at pressure from 0.1 to 0.48 MPa. At the latter pressure, the Jakob

number is therefore quite low, ranging from 0.5 to 5. Figure 3.5 shows a plot $t_{i\to t}$ for different values of wall superheat and pressure for nitrogen. The transition time appears too small to be of any significance from the perspective of modeling boiling heat transfer. We will see experimentally that the typical time scale of bubble growth (e.g., the growth time corresponding to the time required after nucleation to reach the maximum bubble size) is in the order of 10^{-3} to 10^{-1} s for nitrogen at low pressure (in our case, around 0.48 MPa).

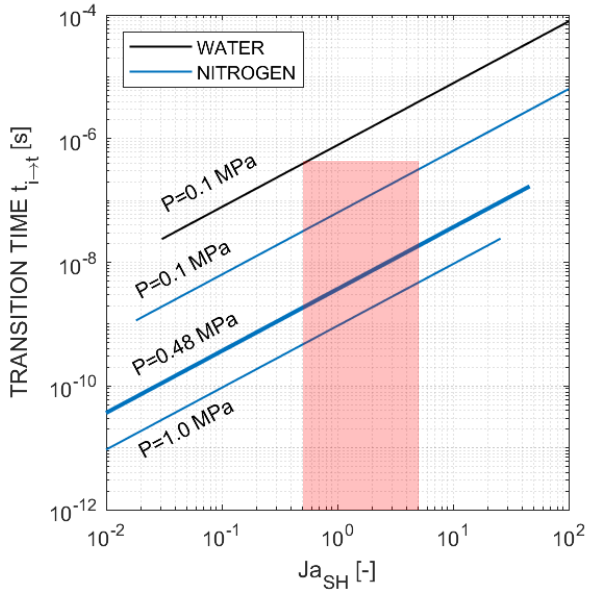

Figure 3.42. Plot of the transition time between inertia-controlled growth regime and heat-transfer-controlled growth regime (Eq. 3.17) against the Jakob number Ja_{SH} at different pressure for nitrogen and water. The red area corresponds to the range of Ja_{SH} of interest.

Riznic et al. (see Ref. [83]) showed that for Jakob number smaller than 2, the thin-boundary layer assumption considered by Plesset and Zwick becomes incorrect. The formulation of Scriven, i.e., without assumption on the boundary layer thickness, results in R having a lesser dependance to Ja_{SH} during the asymptotic heat-transfer controlled growth (comparing Eqs. 3.12, 3.14 and 3.18),

$$R = \sqrt{2Ja_{SH}\alpha_l t} \quad \text{and} \quad \dot{R} = t^{-\frac{1}{2}}\sqrt{\frac{1}{2}Ja_{SH}\alpha_l} \tag{3.18}$$

At a given pressure and wall superheat, Figure 3.4 shows that cryogens will give smaller values of Ja_{SH} than water, mainly due to the lower heat capacity and higher density ratio (ρ_v/ρ_l). For a given surface (i.e., given cavities of particular sizes), we can also estimate the wall superheat required for nucleation using Young-Laplace equation:

$$p_V(T_B) - p_\infty = \frac{2\sigma_{lv}}{R^*}. \tag{3.19}$$

Figure 3.6 shows a plot of Eq. 3.19. The wall superheat required for the nitrogen vapor embryo to grow outside the cavity is given by the smallest value taken by the embryo radius R^* during growth, such that mechanical equilibrium is always satisfied [47]. For simplification, let us assume that the equilibrium radius is always larger than the cavity radius. This is a crude assumption in the case of superwetting fluids, like cryogens. More rigorously, we should expect the minimum radius of the embryo to be smaller by a factor of 1-10, as for small equilibrium contact angle, the most restrictive condition (i.e., requiring the highest temperature) may be at the earlier stage of the vapor embryo growth, before even reaching the cavity mouth. Lorentz [84] proposed a method to evaluate the volume of the initial vapor embryo, from which we can deduce the embryo radius. However, the added complexity does not necessarily make the calculation more accurate from a physical point of view due to the numerous assumptions that need to be considered due to the lack of characterizations of the actual surface and fluid properties (e.g., the conical shape of the cavity with its opening angle or the lack of hysteresis in the contact angle when liquid is receding in the cavity during the growth of the embryo).

Then, using our assumption and given a cavity radius, Eq. 3.19 outputs the wall superheat expected at nucleation. From the plot of Figure 3.6, one can see that wall superheat expected when boiling cryogens is expected to be much smaller than with water in the same conditions (i.e., on the same cavities). Past experiments using similar sapphire substrates with boiling water at atmospheric pressure showed that micrometric cavities (i.e., radius ~ 1 μm) are typically at the origin of bubbles nucleation, with Jakob number between 50 and 150 (which correspond to the gray area in Figure 3.6). The corresponding range of Jakob numbers in liquid nitrogen (at atmospheric pressure on similar cavities) is shown green. In our pressurized tests (at ~480 kPa), the observed range of Jakob numbers (0.5-5) indicates that we likely nucleates on smaller cavities (~ 100 nm, shown in red in Figure 3.6)

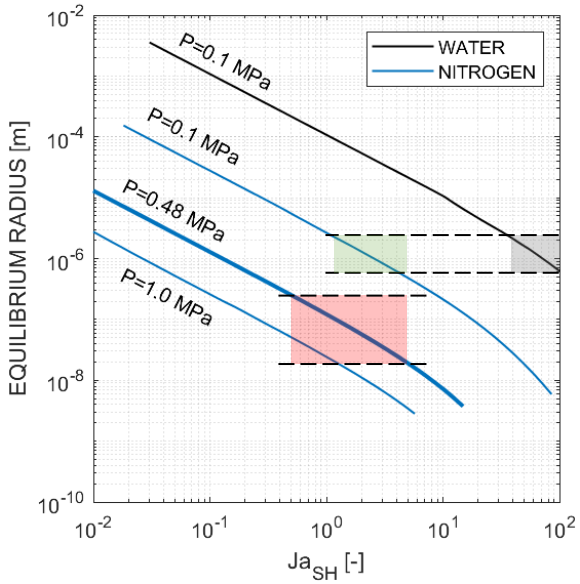

Figure 3.43. Plot of the embryo equilibrium radius R^* from the Young-Laplace equation (Eq. 3.19) against the Jakob number Ja_{SH} at different pressure for nitrogen and water. The red area corresponds to the range of Ja_{SH} of interest

The solid surface has not yet been considered. However, we should expect the same asymptotic behavior, i.e., a growth trend following a $\sqrt{t}$ for the bubble's radius. This is because the trend is characteristic of the heat diffusion process rather than the geometry of the problem. The problem is however not trivial when conduction is taken into account in the heating substrate.

3.1.2. Observations of nitrogen bubble growth

We carried out an analysis of individual bubbles using the experimental apparatus described in Chapter 2 with synchronized phase-detection and shadowgraphy recordings. Figure 3.7 illustrate the growth of a bubble captured simultaneously on shadowgraphy and phase-detection recordings (top and middle row, respectively). The superposition of the binary masks in shown the last row (see Chapter 2 for details on the procedure to obtain the binary masks). On the last row, the bubble footprint is shown in red and the shadow is in black. The images are centered on the bubble being tracked (indicated by the orange arrow om Figure 3.7). The initial time stamp ($t = 0$) corresponds to time of nucleation of the bubble, which is obtained by fitting the optical radius (obtained from shadowgraphy) and footprint radius (obtained phase-detection). The fitting method is described later on.

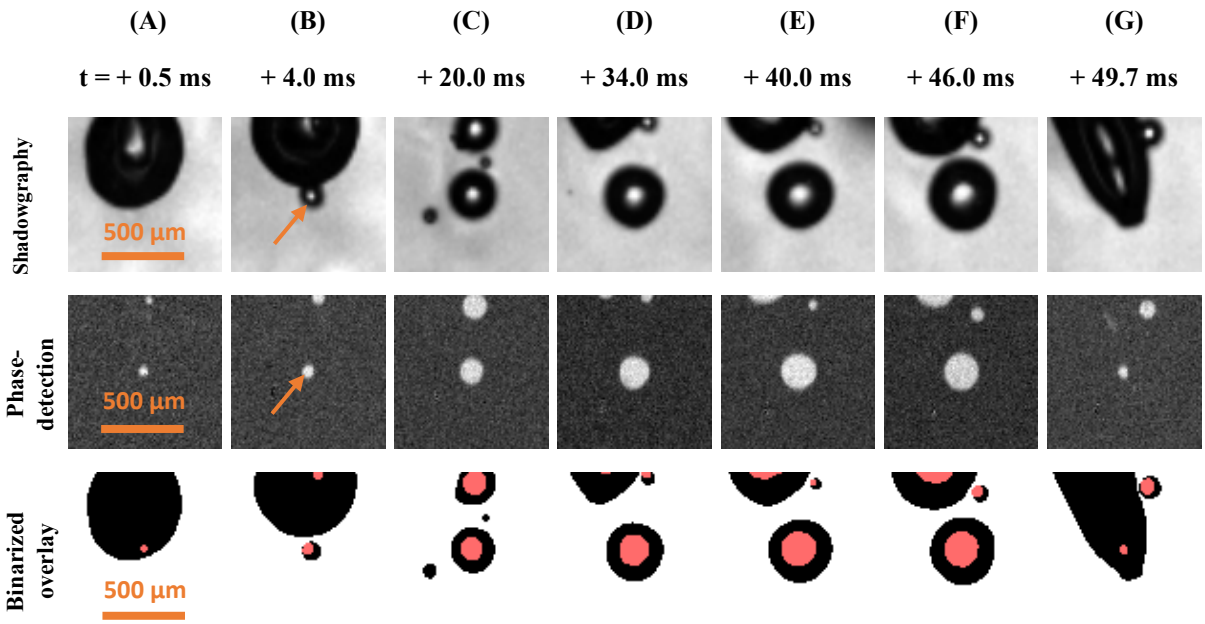

Figure 3.44. Superposed images of phase-detection and backlit shadowgraphy of nitrogen bubble growth (**bubble #1** in Table 3.3, shown later on).

To simplify the analysis of bubble growth, it is convenient to measure surface area A experimentally for either the bubbles optical shadow or the bubbles footprint and calculate equivalent diameters D_{eq} (or equivalent radii R_{eq}), defined as the diameter of a disk with the same area, i.e.,

$$D_{\mathrm{eq}} = 2R_{\mathrm{eq}} = \sqrt{\frac{4A}{\pi}} \tag{3.20}$$

The equivalent diameter is close but not equal to the average diameter, unless the shape is a circle. However, the difference is small, as discussed hereafter. Let's consider the bubble radius measured at the heated surface, i.e., $R_f(\varphi, t)$ with φ the angle of rotation around the normal to the surface. We can decompose $R_f(\varphi, t)$ into two components: an average radius $\overline{R_f}(t)$ and a small deviation $\varepsilon(\varphi, t)$,

$$R_f(\varphi, t) = \overline{R_f}(t) + \varepsilon(\varphi, t) \tag{3.21}$$

The equivalent radius is expressed as,

$$R_{f,eq} = \frac{1}{\sqrt{2\pi}} \int_0^{2\pi} R_f(\varphi, t)^2 d\varphi \tag{3.22}$$

Which gives,

$$R_{f,eq} = \overline{R_f}\left[1 + \frac{2}{\overline{R_f}}\int_0^{2\pi} \varepsilon d\varphi + o(\varepsilon^2)\right]^{1/2} \xrightarrow{small\ \varepsilon} \overline{R_f} + \int_0^{2\pi} \varepsilon d\varphi \ \ (\equiv \bar{\varepsilon}) \tag{3.23}$$

$\bar{\varepsilon}$ tends to be quite small as bubbles tends to take shapes that minimize the curvature. For example, if the contact line perimeter is constrained (imposing $\int_0^{2\pi} \varepsilon(\varphi, t)\, d\varphi = 0$), we can show that the difference between average radius and equivalent radius reduces further,

$$R_{f,eq} \xrightarrow{small\ \varepsilon} \overline{R_f} + o(\varepsilon^2) \tag{3.24}$$

To simplify the writing, we will omit the *eq* for equivalent radii and diameters.

Each of the bubble we will present can be characterize with several parameters of interest. We can define an average capillary number Ca to characterize the movement of the liquid-vapor interface, specifically the magnitude of viscous forces in the liquid relative the capillary forces at the interface,

$$Ca = \mu_l \langle \dot{R}_f \rangle / \sigma_{lv} \tag{3.25}$$

where μ_l is the dynamic viscosity in the liquid, σ_{lvlv} liquid-vapor surface tension and $\langle \dot{R}_f \rangle$ corresponds to a time-averaged growth velocity of the footprint.

We can also define a Bond number Bo characterizing the magnitude of buoyancy relative to the capillary forces,

$$Bo = \Delta\rho g \max(D_o)^2 / \sigma_{lvlv} \tag{3.26}$$

With $\Delta\rho$ the difference of density between liquid and vapor at saturation (i.e., $\rho_l - \rho_v$).

Finally, we can define an effective contact angle θ_{eff} by,

$$\theta_{eff} = \sin^{-1}\left(D_f / D_o\right) \tag{3.27}$$

with D_o and D_f being the equivalent diameters obtained from the bubble shadow area and the bubble footprint area. θ_{eff} is the contact angle that a bubble assumed as a spherical cap would form on a surface if its footprint and optical radius were D_f and D_o, respectively.

For a given uncoalesced bubble, based on our theoretical analysis, the measured radii (R_o and R_f) can be fitted with an expression following a $\sqrt{t}$ trend as in Eq. 3,12,

$$\begin{cases} R_o = B_o\sqrt{t + t_0} \\ R_f = B_f\sqrt{t + t_0} \end{cases} \tag{3.28}$$

With B_o and B_f the growth modulus measured from the optical and footprint radius, respectively, and t_0 the time of nucleation. t equal 0 correspond to the time of the first phase-detection frame on which the bubble appears. While the growth modulus differs depending on the radius being characterized, t_0 has to be the same in both fitting expressions. The fitting variables, i.e., B_o, B_f and t_0, are evaluated in 2 steps. First, t_0 is guessed. This allows us to evaluate the values of B_o and B_f which minimize the sum of the square residuals, noted S_o and S_f, associated to each fit. Second, we formulate a compound error S, that is minimized by iterating on the value of t_0. Naturally, B_o and B_f are re-evaluated at each iteration. The compound error S is simply given by a Euclidean distance between (0,0) and (S_o, S_f),

$$S \equiv \sqrt{{S_o}^2 + {S_f}^2} \tag{3.29}$$

Other definitions of S can be used as long as S is minimized when S_o and S_f are minimized. Figure 3.8 shows history plots of the equivalent radii R_o (in pink) and R_f (in cyan) using a nitrogen bubble at 491 kPa, growing on the horizontal upward facing heated surface with an average wall superheat of +1.6 K. The measurements of some of the bubble characteristics (Bo, Ca, etc.) are shown in Table 3.1 (as bubble #0-3). The fittings following Eq. 3.28 are shown with black dashed line. The time $t + t_0$ (with t_0 defined by Eq. 3.28) is represented on the x-axis. The bubble is expected to have nucleated at $t + t_0 = 0$, but is first observed only t_0 second after nucleation.

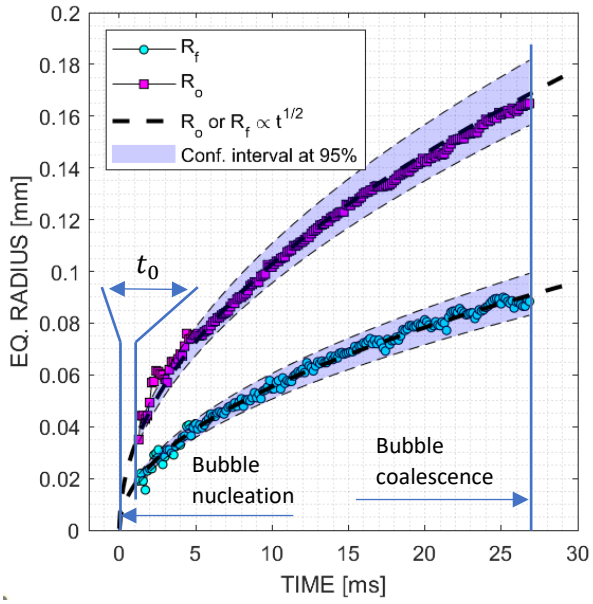

Figure 3.45. Plot of footprint and optical radii during growth for the bubble #0-3 given in Table 3.1. The bulk pressure is about 491 kPa, and the heating surface has a wall superheat of +1.6 K.

Both equivalent radii, from measured from shadow and footprint, follows closely a growth in $\sqrt{t}$ as shown in Figure 3.8. Similar growth trends can be seen for all bubbles. Figure 3.9 shows another clear example of such growth on a log-log plot. The wall superheat is about +1.2 K, everything else being the same as the bubble in Figure 3.8. The bubble shown in Figure 3.9. is listed as bubble #0-1 in Table 3.1. Visually, we can see from Figure 3.9 that the bubble footprint radius and optical radius share the same time dependence, which is equivalent to write that,

$$\frac{1}{R_o}\frac{dR_o}{dt} = \frac{1}{R_f}\frac{dR_f}{dt} \tag{3.30}$$

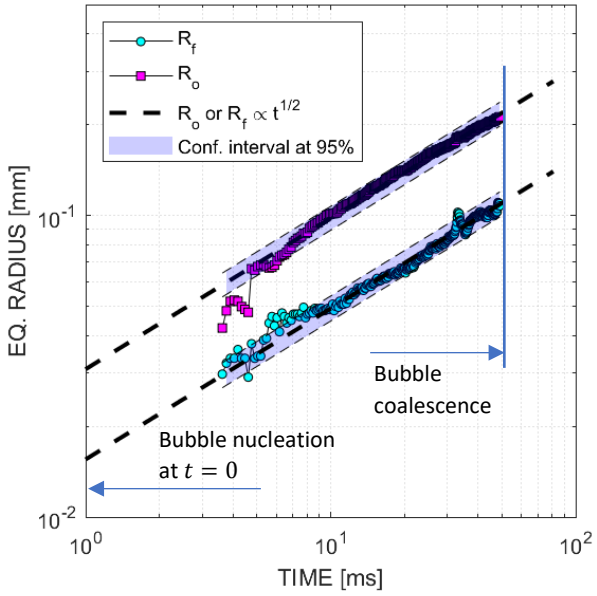

Figure 3.46. Log-log plot of footprint and optical radii during growth for the bubble #0-1 given in Table 3.1.

The systematic observation of proportionality between R_o and R_f during growth is important for understanding how the heat is removed by the nitrogen bubbles. It is indicative of two aspects. First, the triple-contact line is free to move and is not pinned by surface defects on our heated surface (nano-smooth sapphire). This is shown by the measurement of bubble radii (Figure 3.9) and the video recording of bubble growth (shown in Figure 3.7). Second, the proportionality between R_o and R_f suggests that the bubble interface follows a quasi-static growth, i.e., its free energy is minimized at any moment of the growth.We will see later on that this quasi-static growth hypothesis is particularly useful to evaluate the evaporation at the bubble interface. We can justify this hypothesis further byevaluating the relaxation time scale of the bubble interface after an initial hypothetical perturbation and compare it to the bubble growth time. A relaxation time scale much smaller than the growth time would indicates the bubble interface always minimized its energy throughout the growth. Figure 3.10 shows a schematic of a bubble during relaxation

after an initial perturbation at its interface. The perturbation can be the result of extremely strong evaporation at the bubble base inducing a rapid sliding of the triple contact line, a bubble coalescing ora mechanical disturbance due liquid movement, e.g., caused by surrounding bubbles lifting off from the heated surface. The perturbation considered in the calculation below is the rapid displacement of the triple contact line. Similar results can be obtained when the perturbation originates from a coalescence. As a matter of fact, we will observation of the relaxation time in the case of bubbles coalescence.

Irrespective of the origins of the bubble interface perturbation, the relaxation time scale should depend on how fast the perturbation propagates to the rest of the bubble interface (i.e., by capillary waves on the interface or by pressure wave through the vapor) and how fast the energy is dissipated in the liquid (i.e., by agitation). Let us start with estimating the time scales associated with the propagation of the perturbation.

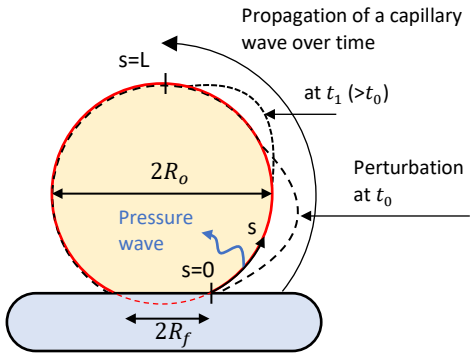

Figure 3.47. Schematics of a bubble interface relaxing after an initial perturbation.

We can estimate the propagation velocity v_c of a capillary wave assuming that the amplitude of the perturbation is small enough compared to the bubble radius such that the effect of curvature can be neglected. The formulation for this capillary wave velocity is given by (see Ref. [108]),

$$v_c = \sqrt{\frac{2\pi}{\lambda}\frac{\sigma_{lv}}{\rho_l + \rho_v}} \tag{3.31}$$

With λ the wavelength associated with the perturbation. Let's assume a wavelength close to the bubble radius R_o. Then, Eq. 3.31 yields,

$$v_c = \sqrt{\frac{2\pi}{R_o}\frac{\sigma_{lv}}{\rho_l + \rho_v}} \tag{3.32}$$

We assumed here that the perturbation and the bubble interface are axisymmetric, therefore the maximum distance L over which the wave propagates is half bubble contour, i.e., πR_o. The propagation time of a capillary wave is then given by,

$$t_{\mathrm{p,c}} = \frac{L}{v_c} = \sqrt{\frac{{R_o}^3(\rho_l + \rho_v)\pi}{2\sigma_{lv}}} \tag{3.33}$$

The information of the initial perturbation can also travel through the bubble vapor as pressure wave. Assuming that the vapor behaves as ideal gas, the velocity of the pressure wave v_p is given by,

$$v_p = \sqrt{\gamma r T_B} \tag{3.34}$$

With γ the ratio of heat capacity of nitrogen gas ($\equiv c_p/c_{\mathrm{v}}$), r its specific gas constant and T_{B} the vapor temperature inside the bubble (assumed as ~T_{SAT}). The propagation time scale of the pressure waves is given by,

$$t_{p,p} = \frac{2R_o}{v_p} = \frac{2R_o}{\sqrt{\gamma r T_{\mathrm{B}}}} \tag{3.35}$$

A last time scale related to how quick a perturbation is dissipated can be evaluated. Let's assume that the perturbation is related to a rapid sliding of the contact line. The length of the contact line displacement is given by $\dot{R}_f \Delta t$ (based on our assumption that the perturbation comes from the rapid evaporation at the triple contact line). The magnitude of the turbulent dissipation in the liquid, noted ε_t, is given by,

$$\varepsilon_t = \frac{\left(V_{eddy}\right)^3}{L_{eddy}} \sim \frac{\left(\dot{R}_o\right)^3}{\dot{R}_f \Delta t} \tag{3.36}$$

The energy scale Δe associated with the increase of surface energy due to the displacement of the contact line can be evaluated as,

$$\Delta e = \frac{\sigma_{lv} + \sigma_{sv} - \sigma_{sl}}{\dot{R}_f \Delta t} \sim \frac{\sigma_{lv}}{\dot{R}_f \Delta t} \tag{3.37}$$

Therefore, the time to dissipate the increase of surface energy by turbulent dissipation is given by,

$$t_d \sim \frac{\Delta e}{\varepsilon_t} = \frac{\sigma_{lv}}{\left(\dot{R}_o\right)^3} \tag{3.38}$$

Finally, we can evaluate a bubble time based on $\dot{R}_o$ and R_o appearing on the time scale previously formulated,

$$t_g \sim \frac{R_o}{\dot{R}_o} \tag{3.39}$$

Using characteristic values of R_o~10^{-4} m, $\dot{R}_o$~10^{-3} m/s, we get a characteristic growth time of t_g~10^{-1} s while the propagation time scales $t_{p,c}$ and $t_{p,p}$, as well as the energy diffusion time scale t_d, are orders of magnitude smaller ($t_{p,c}$~10^{-3} s, $t_{p,p}$~10^{-6} s and t_d~10^{-5} s). This comparison of time scale shows that if the triple contact line is not pinned to the heated the surface, any local perturbation of the bubble interface should be seen everywhere on the bubble, therefore the bubble interface should grow with some self similarity (with R_o then expected to be proportional to R_f).

The proportionality over time of R_o and R_f can be better represented by the effective contact angle θ_{eff} (defined in Eq. 3.27). Figure 3.11 shows the values of θ_{eff} during the growth of bubble #0-3 whose radii are shown in Figure 3.8. θ_{eff} is mostly constant during growth for all the bubble analyzed. Fluctuations can be observed at the very beginning of the growth, likely due to inaccuracy in the radii measurements, at the end of growth when the bubble lift-off from the heated surface or coalesces with surrounding bubbles, and during growth when the bubble interface is perturbed by liquid agitations.

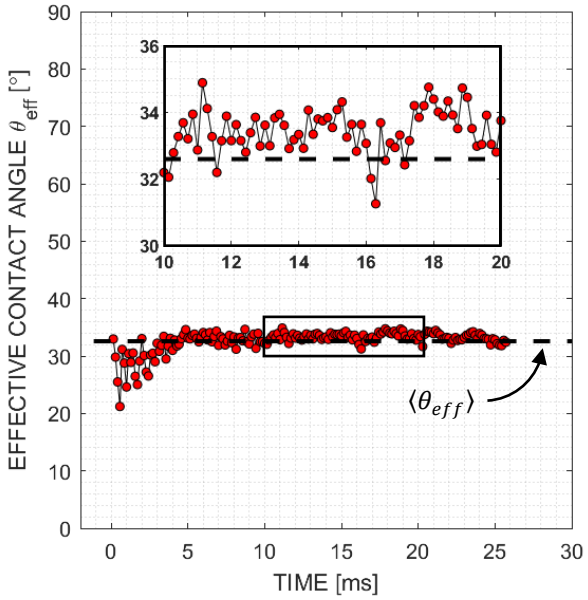

Figure 3.48. Plot of effective contact angle θ_{eff} during growth for the bubble with radii shown in Figure 3.8 (ΔT_{sat}~ +1.6 K, bubble #0-3 given in Table 3.1).

Unlike Figure 3.11, Figures 3.12 show the radii and effective contact angle of a coalesced bubbles. Each coalescence occurs with at least 2 bubbles involved. For simplification only one bubble is tracked at each

coalescence. The fitting of the radii applies only between the 1st and 2nd coalescence event. The time represented corresponds to a shifted time scale $t - t_0$, with t_0 obtained from the fitting procedure. Since the fitting is performed on a coalesced bubble, t_0 does not correspond to the time of nucleation of the initial bubble.

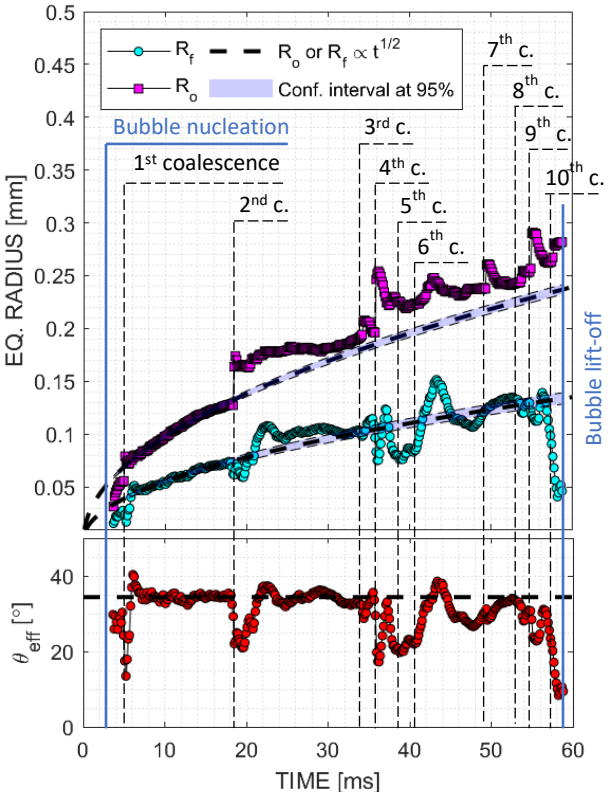

Figure 3.49. Plot of the footprint, optical radii and effective contact angle during growth of successively coalescing bubbles. Only the largest of the coalescing bubbles is tracked for simplification for each coalescence event.

Figure 3.12 (bottom) shows that a bubble formed by coalescence also has a constant effective contact angle given enough time for the interface to relax, which is particularly clear between the 2nd and 3rd coalescence. Together with Figure 3.11, we can see that more generally the effective contact angle is independent from bubble radii and consequently its volume. Figure 3.12 also shows that after a perturbation, bubble radius rapidly recover, within few milliseconds for R_o and about 10 ms for R_f, and follows again a $\sqrt{t}$ trend, see for instance the 2nd coalescence. This perturbation is not small as it corresponds to a rapid increase of roughly 25% of the radius. Intuitively, this shows that, at least at low wall superheat, bubble growth is not too sensitive to perturbations of the liquid-vapor interface or perturbation in the liquid bulk, as we expected from the analysis of time scales above..

In both cases shown in Figure 3.11 and 3.12, we can see that the effective contact angle (i.e., 30°-35°) is larger than the equilibrium contact, typically below 10° for nitrogen on most surfaces, including nano-smooth sapphire-ITO (see details in Chapter 2).

While the above analysis was done on couple selected bubbles, some of the observations can be generalized to a larger number of bubbles. The typical values of effective contact angle can be seen on superpositions of shadowgraphy and phase detection images at low wall superheat (+1.21 K) with a field of view allowing to see multiple bubbles. Figure 3.13 shows such images. The three images differ only by their time stamp. An effective contact angle of 30° to 40° means that the ratio R_f/R_o is between 0.5 and 0.64. Visually, it is fairly clear from Figure 3.13 that the effective contact angle of most bubbles at low wall superheat falls in that range, which consistent with the measurements shown in Figure 3.11 and 3.12.

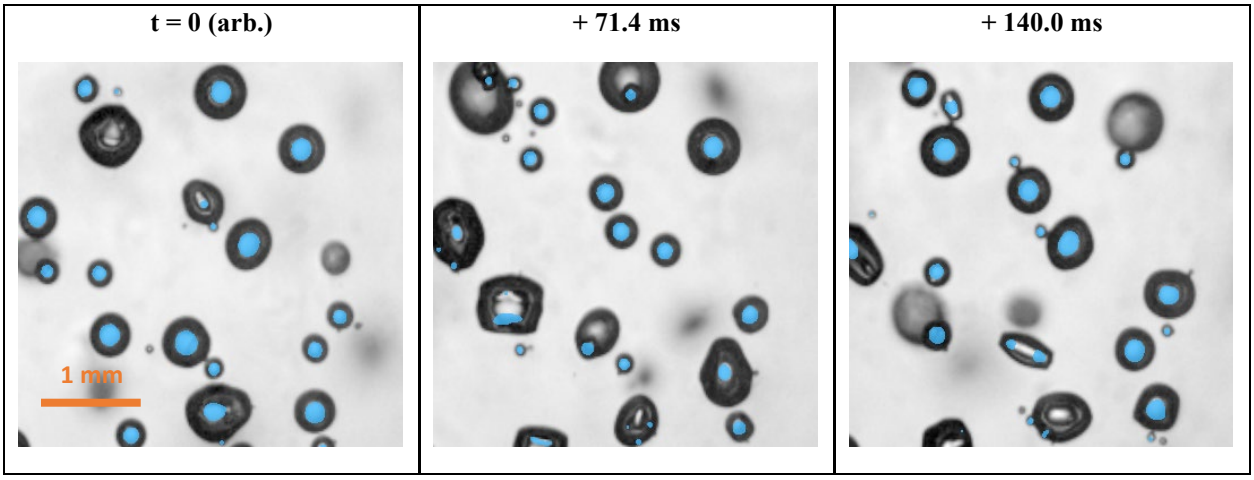

Figure 3.50. General view of the ratio of bubble footprint (in blue) to bubble shadow (in black) for nitrogen pool-boiling on horizontal surface, ΔT_{sat}~ + 1.2 K, P~ 491 kPa.

Figure 3.14 shows similar images at a slightly higher wall superheat (+1.6 K), still on a horizontal upward facing heating surface. We can see from Figure 3.14 that the ratio of footprint radius over optical radius slightly increases. We will confirm that observation with a quantitative analysis later on.

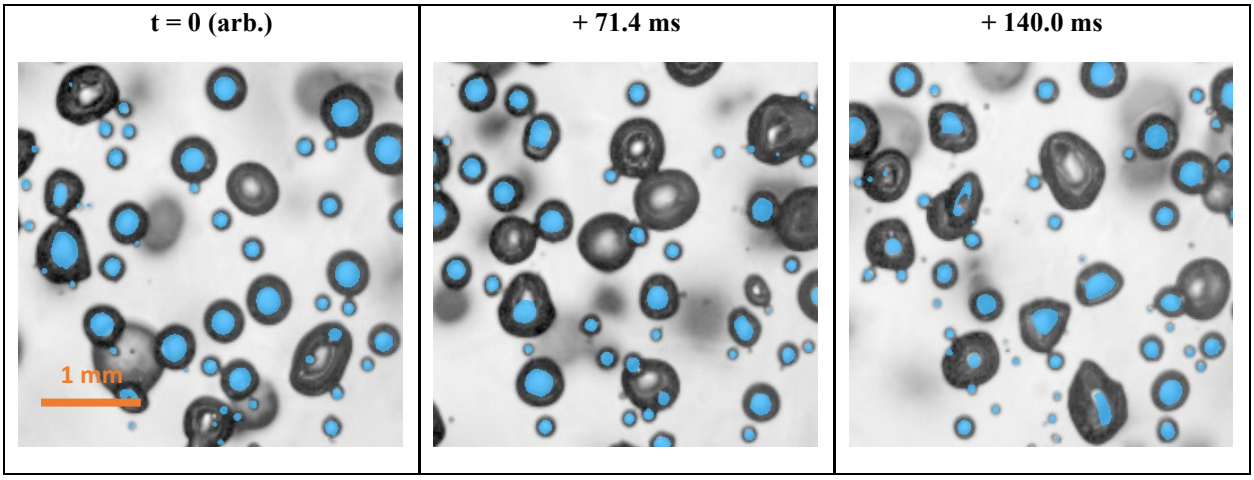

Figure 3.51. General view of the ratio of bubble footprint (in blue) to bubble shadow (in black) for nitrogen pool-boiling on horizontal surface, ΔT_{sat}~ +1.6 K, P~491 kPa.

Another observation that can be generalized is the growth trend of the bubble footprint radius. Figures 3.8 and 3.9 presented very clear $\sqrt{t}$ growth trend, while in general, small deviation of the analytical trend can be observed. Several causes can explain it, such as important gradient of temperature near the heated surface, local change of temperature in the substrate or perturbations in the liquid. At higher wall superheat, we can analyze bubbles growth focusing on the phase-detection data. Bubbles are no longer isolated, interacts frequently with each other, making the growth of a given bubble less predictable. However, we can still analyze bubble growth from a statistical point of view. Figure 3.15 shows an experimental measurement of the probability $P(D_f, t)$ of finding a bubble footprint of diameter D_f at a time t (t=0 corresponds to the time of nucleation), at different wall superheat for horizontal saturated nitrogen pool boiling. The x-axis gives the elapsed time from nucleation. The colormap indicates the value of $P(D_f, t)$ for different values of footprint diameter and elapsed time. The expected value of footprint diameter is shown for each time with continuous red curve. The error bars indicate the standard deviations. Only data of bubbles prior a coalescence are considered.

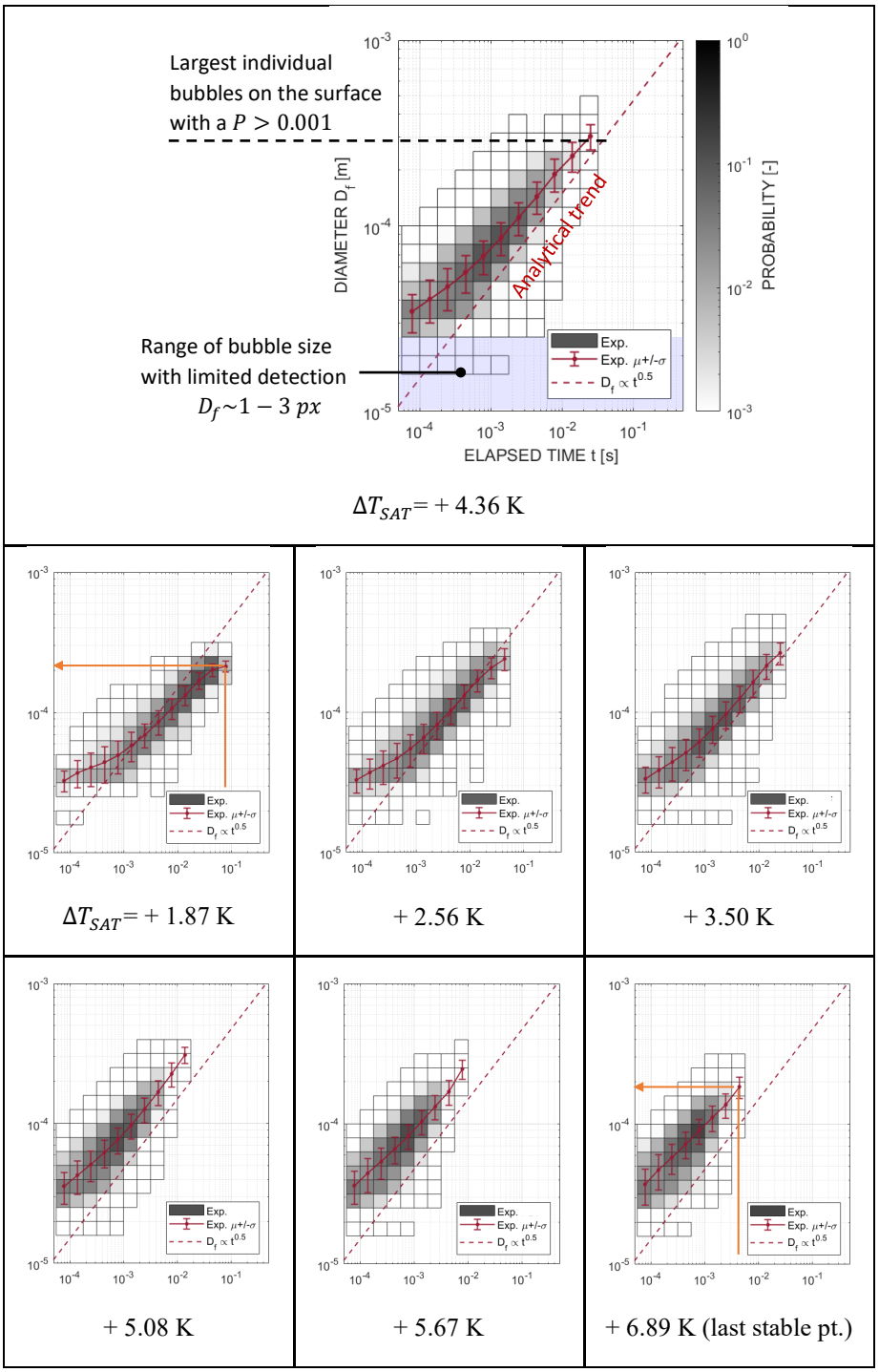

Figure 3.52. Plot of the probability for a bubble footprint to be observed t-second after nucleation with a diameter D_f. The wall superheat varies between each plot. All plots share the same x- and y-axis, as well as the same colormap.

The footprint diameter arguably follows the expected trend in $\sqrt{t}$ (shown in Figure 3.15 by a red dashed line), irrespective of the wall superheat. Figure 3.15 also shows that uncoalesced bubbles footprint hardly

exceeds ~300 μm in diameter with growth as long as ~50 ms, at low wall superheat (e.g., at +1.87 K). The range of diameters and times shrink slightly as the wall superheat increases (shown by orange arrow), i.e., the likelihood of a bubble growing to a large diameter (and equivalently growing during a long period of time) reduces. This is indicative of an increase of the probability of coalescence.

3.1.3. Effect of buoyancy during bubble growth

In the analysis done in Section 3.1.2., we let aside the effect of buoyancy on bubble growth. Buoyancy can modify the bubble growth in more than one way. The most direct effect is by inducing a pressure gradient in the liquid, thus deforming the bubble interface. A less direct effect is by modifying the thickness of the thermal boundary layer or more generally by inducing convective movement in the liquid.

Judging the effect of buoyancy on the bubbles interface is relatively straightforward and can be done by comparing the magnitude of gravitational potential energy and bubble surface energy (see Ref. [85] for more details). This ratio is expressed by the Bond number Bo (similar to the Eq. 3.26),

$$Bo = (R/\lambda_c)^2 \text{ with } \lambda_c = \sqrt{\sigma_{lv}/(\rho_l - \rho_g)g} \tag{3.40}$$

λ_c is the so-called capillary length. σ_{lv} is the liquid-vapor surface tension. When the Bo is much below 1 (i.e., $R \ll \lambda_c$), then gravity has negligible impact of the shape of the bubble interface.

Figure 3.16 shows a plot of capillary length for nitrogen and other fluids as a function of pressure. At the tested pressure (~ 480 kPa), the capillary length of nitrogen is about 0.9 mm. We can see all cryogens show lower capillary length than water due to their lower surface tension, and therefore cryogens bubbles could be expected to be more sensitive to gravitational forces than water vapor bubbles.

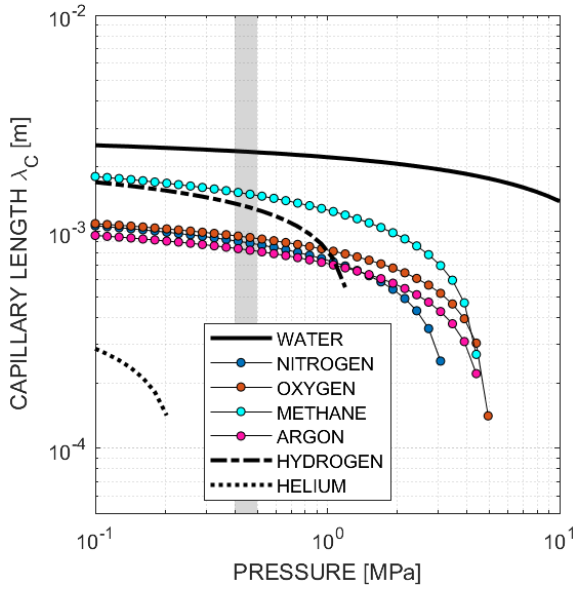

Figure 3.53. Capillary length vs. pressure for different fluids

However, in our experimental conditions, we can show that the Bond number associated with uncoalesced bubbles is in the order of 10^{-1} for saturated nitrogen boiling with an upward-facing horizontal heating surface (based on the results shown in Figure 3.13, showing images of nitrogen bubbles with optical radius typ. below 0.25 mm, and the capillary length of nitrogen shown in Figure 3.16). In order to have more complete picture of the bubble size on the heating surface, we can evaluate their footprint area spectra for various wall superheat. Figure 3.17 shows cumulative distribution functions (CDFs) of the Bond number associated with the footprint radius, noted Bo_{R_f}, in horizontal nitrogen pool boiling. Only uncoalesced bubbles are considered. The lines represent the CDFs obtained at each boiling step with constant heat input between the Onset of Nucleate Boiling (ONB) and the Departure from the Nucleate Boiling (DNB). The lines are colored from blue to red as the heat input is increased from ONB to DNB, respectively. As the wall superheat increase, Figure 3.17 shows that the CDFs generally shift towards smaller Bo_{R_f}, indicating that uncoalesced bubbles tends to be smaller as the likelihood of coalescing becomes greater. For Bo_{R_f}>2.10^{-2}, we observe an inversion of the trend in the last few percent of the CDFs with uncoalesced bubbles getting larger as the wall superheat increases. This might be an artefact in the procedure to identify uncoalesced bubbles on phase-detection recordings resulting in coalesced bubbles mistakenly considered as uncoalesced. Nonetheless, Figure 3.17 shows that uncoalesced bubbles have typically a value for Bo_{R_f} below or around 10^{-1}, irrespective of the heat input, and therefore showing that the bubbles surface energy is at least an order of magnitude above the potential energy from buoyancy. The Bond number based on R_f

is smaller than the more common expression, based on the optical radius R_o. Both Bo_{R_f} and Bo_{R_o} are related by,

$$Bo_{R_o} = \frac{1}{[\sin\theta_{\text{eff}}]^2} Bo_{R_f} \tag{3.41}$$

Assuming conservatively a value of θ_{eff} equal to 25° (i.e., a lower bound of our measurements of effective contact angle), we get Bo_{R_o}~5.6Bo_{R_f} which still indicates negligible buoyancy effect on the interface of uncoalesced bubble.

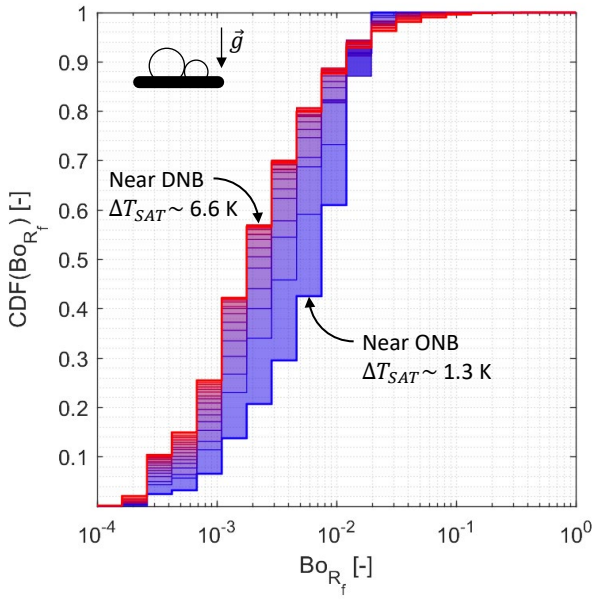

Figure 3.54. Cumulative distribution functions of the Bond number Bo_{R_f} based on the bubble footprint radius, R_f, during nitrogen pool boiling on a horizontal surface. Each line represents a boiling step from near-ONB (in blue) to near-DNB (in red).

Similar observations can be made for the vertical heating surface tests. Figure 3.18 shows the CDF of Bo_{R_f} for uncoalesced bubbles on a vertical heating surface.

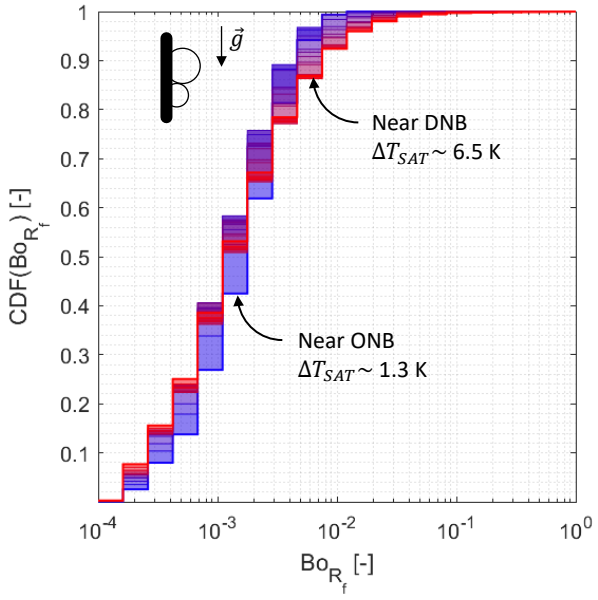

Figure 3.55. Cumulative distribution functions of the Bond number Bo_{R_f} based on the bubble footprint radius, R_f, during nitrogen pool boiling on a vertical surface. Each line represents a boiling step from near-ONB (in blue) to near-DNB (in red).

Figures 3.19 shows shadowgraphy and phase-detection images of bubble growing on an inclined surface at 150° with a wall superheat of +1.2 K (bubble #150-3 in Table 3.4). The bubble which is tracked is circled in red and centered on each image. Figure 3.20 shows the measurement of the optical radius R_o (in pink) and footprint radius R_f (in blue) and the effective contact angle θ_{eff} measured during growth (shown in red). In both Figures 3.19 and 3.20, the time shown corresponds to the time elapsed from nucleation. The time from nucleation t_0 is obtained by fitting Eq. 3.28. The measurements stop once the bubble coalesces (~26 ms after nucleation).

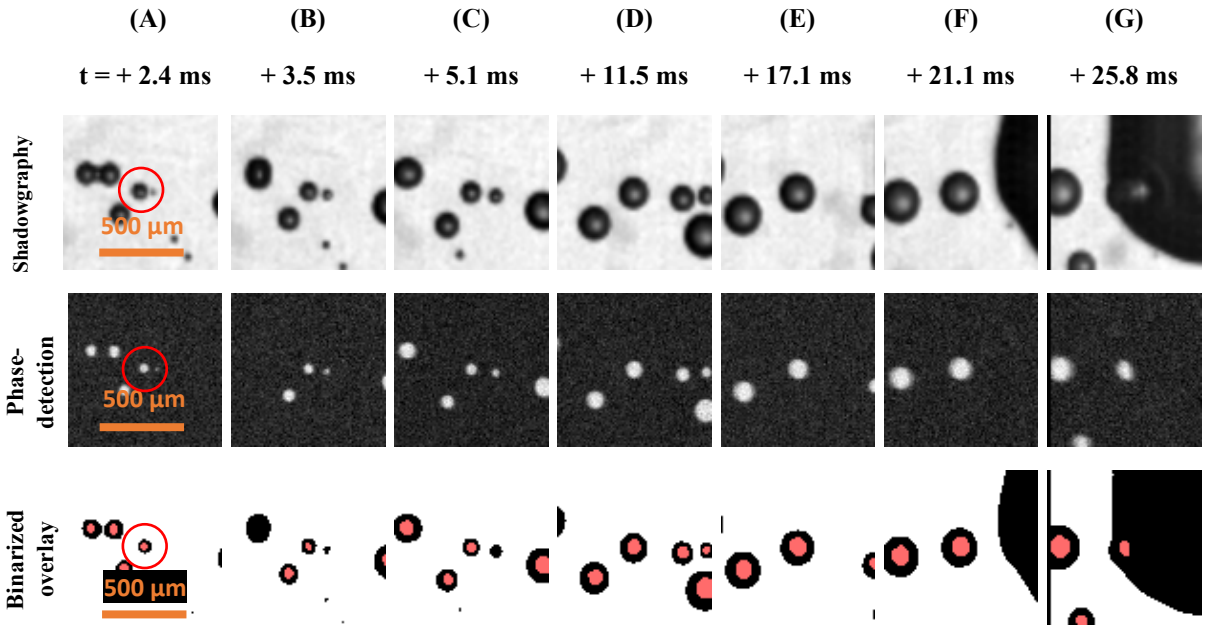

Figure 3.56. Superposed images of phase-detection and backlit shadowgraphy of nitrogen bubble growth for bubble #150-1 (see Table 3.2).

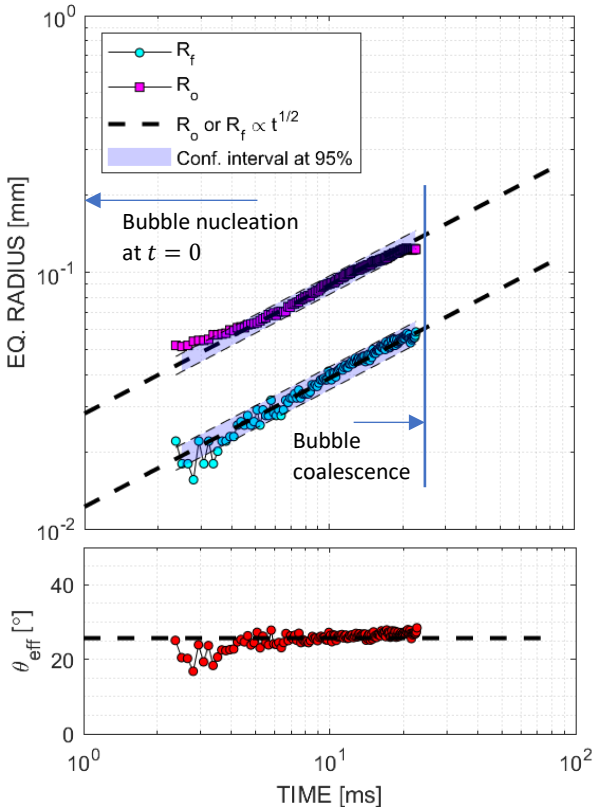

Figure 3.57. Plot of the footprint, optical radii effective contact angle during growth on an inclined surface (150°) at low wall superheat (+1.23 K) for bubble #150-3 in Table 3.2.

Figure 3.20 shows that both radii grow with the same time dependance, which is typical of any uncoalesced bubbles, irrespective of the surface inclination. The radii increase still with $\sqrt{t}$. Naturally, the effective contact angle is then roughly constant during growth. Its average value tends to be around 20° to 30° along the growth. A more in-depth analysis of the values of effective angles with wall superheat and inclination angle will be given in the following section. For the moment, we note that no major effect of the heating surface inclination is seen when comparing the radii of a bubble growing on a horizontal surface (see Figure 3.9) or an inclined, almost upside-down surface at 150° (see Figure 3.20), both performed at the same temperature and pressure.

We can generalize the growth trend of the bubble footprint to most uncoalesced bubbles irrespective of the surface inclination angle. Figure 3.21 shows growth of uncoalesced bubbles from a statistical point of view. However, instead of showing the probability $P(r,t)$ (defined by Eq. 3.27) for different values of wall superheat on a horizontal surface as done in Figure 3.13, Figure 3.21 shows it at fixed wall superheat and different surface inclination angles. The different plots of Figure 3.21 as well as the plot presented at similar superheat in Figure 3.13 (i.e., ~ 3 K) shows great similarity despite the variation of surface inclination. The growth rate in $\sim\sqrt{t}$, the typical maximum growth time and maximum footprint diameter are nearly identical in all the tests. These results suggest that in our boiling conditions, uncoalesced bubbles never reaches the size for buoyancy to start playing a role. The data also suggest that the contribution of buoyancy to the growth of uncoalesced bubbles by other means (e.g., the thickening of the thermal boundary layer on surface inclined at more than 90°) is also minimal.

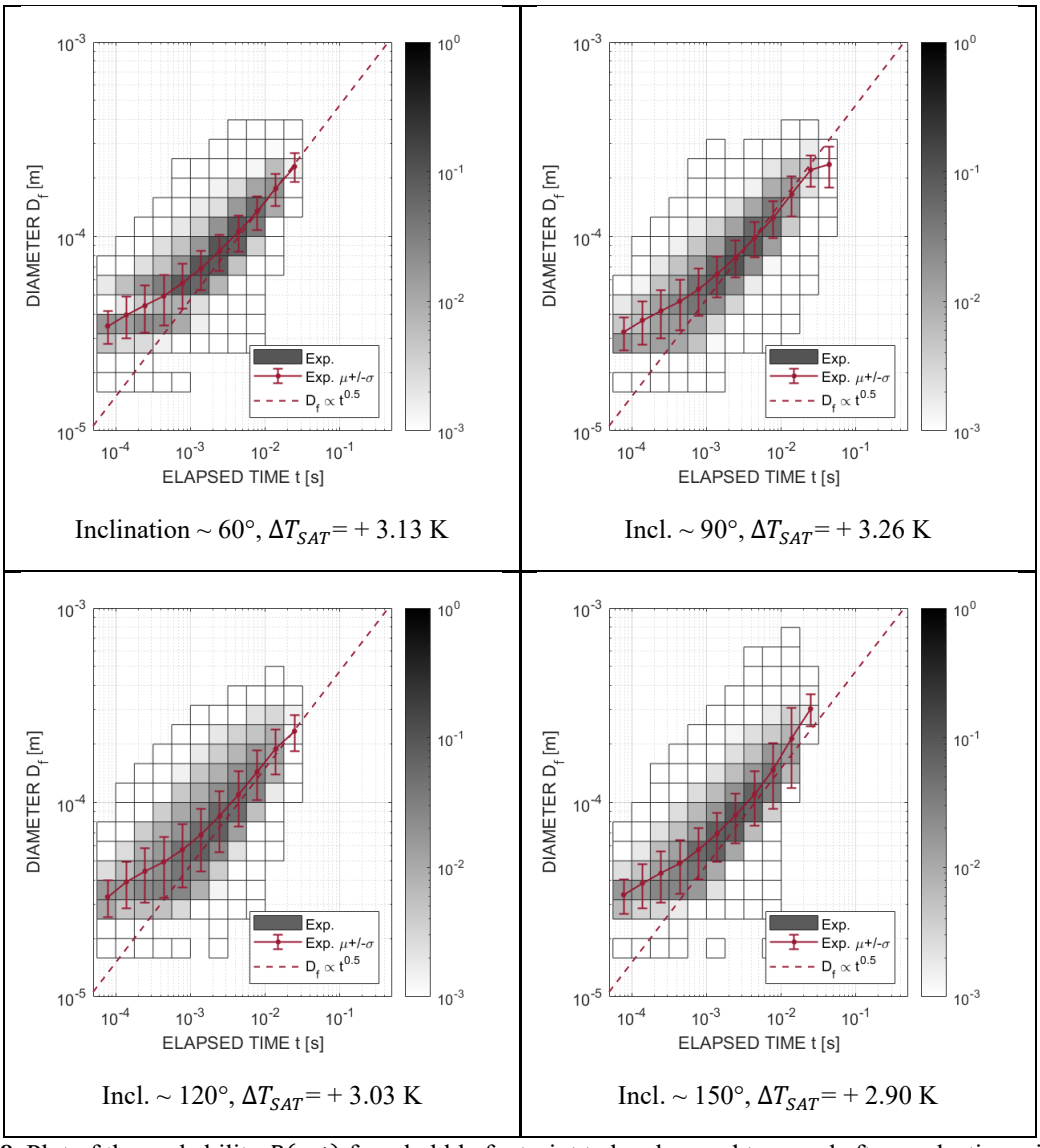

Figure 3.58. Plot of the probability $P(r,t)$ for a bubble footprint to be observed t-second after nucleation with a diameter D_f. The inclination angle of the heating surface varies between each plot. All plots share the same x- and y-axis, as well as the same colormap.

3.1.4. Bubble sliding

So far, we set aside the movement of bubbles on the surface. While buoyancy does not affect significantly the bubble interface, it allows bubble to slide on an inclined surface. Figures 3.22 and 3.23 shows illustrative cases with a bubble sliding on a surface inclined at 60° and 150°, respectively. The images consist of a superposition of shadowgraphy images with the bubbles' footprint as blue overlay. The initial position of the bubble is shown by a blue circular marker, while the last position on the heated surface is shown by a red marker. The current position of the bubble (using the centroid of its footprint) is shown for each image by a pink marker and the trajectory of the bubble over time is indicated by a red line. The black arrow is

the projection of the gravity vector on the inclined heated surface (from left to right in these figures). In both cases shown in Figures 3.22 and 3.23, the bubble slides a significant distance, above 10 times its average diameter due to buoyancy. As we will see more in details, the sliding distance depends on multiple factors including the bubble density, the magnitude of $\vec{g}_t$ (which is related to the magnitude of $\vec{g}$ and the inclination angle of the heating surface), potential convective movement in the surrounding liquid, heating surface conditions promoting either sliding or pinning of the triple contact line and other factors related to the bubble growth and its lift-off diameter (e.g., the wall superheat).

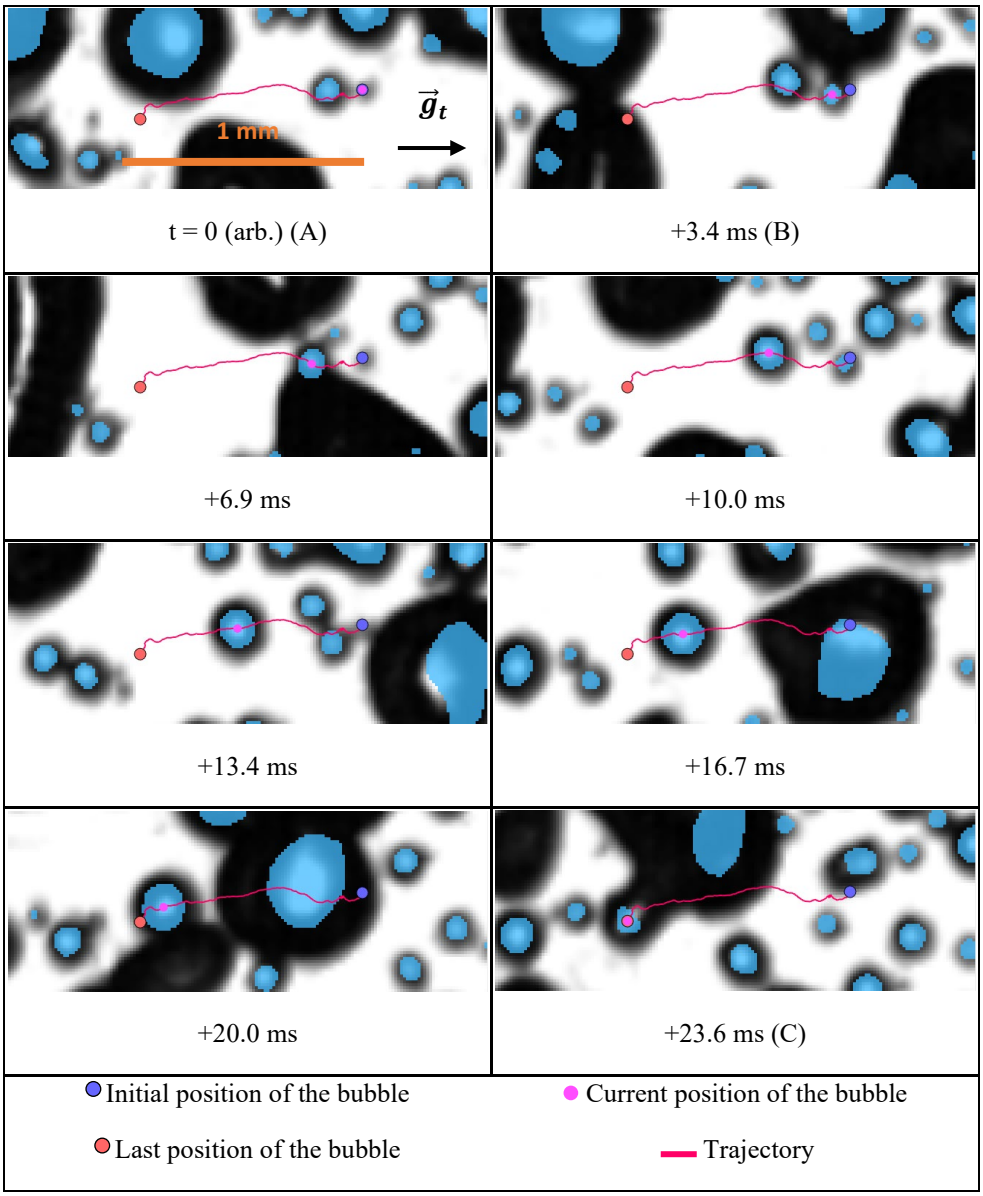

Figure 3.59. Example of trajectory for a nitrogen bubble nucleating in pool boiling on the heating surface with an inclination angle of 60°. The average surface wall superheat is +2.06 K. $\vec{g}_t$ is the gravity vector projected on the heated surface. The footprint is shown in blue.

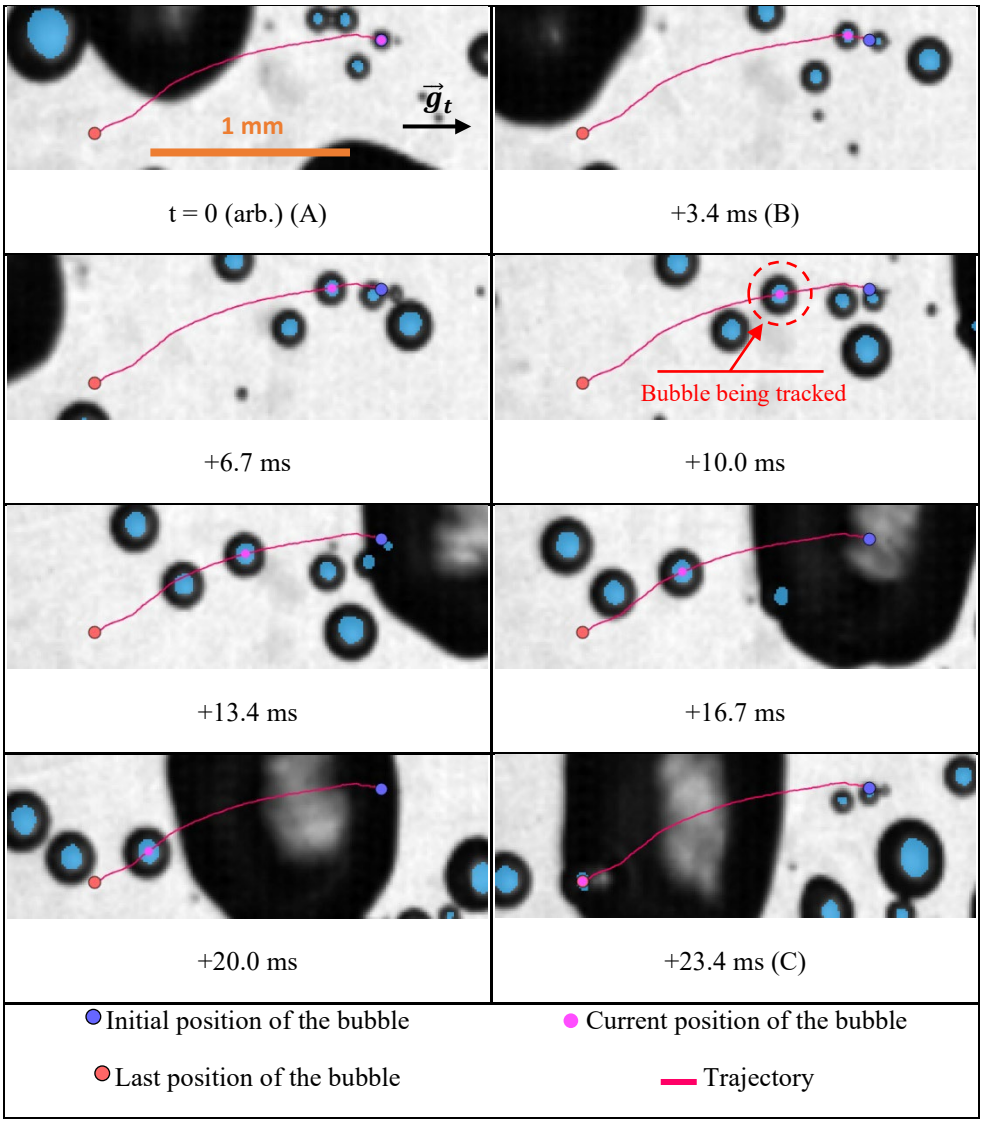

Figure 3.60. Example of trajectory for a nitrogen bubble nucleating in pool boiling on the heating surface with an inclination angle of 150°. The average surface wall superheat is +1.23 K. $\vec{g}_t$ is the gravity vector projected on the heated surface. The footprint is shown in blue.

Bubble sliding on the surface can also be observed from a statistical analysis by looking how distant bubble centroids are from their respective nucleation sites. Figure 3.24 shows the probability distribution functions (PDFs) of the last location $p(x, y)$, i.e., at $t = t_e$, of an uncoalesced bubble, indicated by its footprint centroid in the case of horizontal upward facing nitrogen pool boiling. The PDFs are represented in log-scale. The reference (0,0) corresponds to the location of the bubble initial bubble footprint centroid (indicative of its nucleation site). All PDFs naturally peaks at the origin. In horizontal pool boiling, the distributions are centered on (0,0), with a relatively low dispersion compared to the bubble footprint diameter. Plots B and C shows slightly non-symmetric distribution which might be due to some residual flow within the boiling cell. Plot A appears scattered due to the low number of bubbles available at that

lowest wall superheat to build significant statistics. How far each distribution extends from the origin indicate how far bubbles slide on the surface before lift-off or coalescing. We can see from Figure 3.24 that the distributions do not extend more than twice the average bubble footprint diameter $\langle D_f \rangle$ () irrespective of the wall superheat in horizontal pool boiling.

Figure 3.25 shows the measurements of PDFs on an inclined surface at 150°. The scale over x and y is twice larger than in Figure 3.24. Buoyancy breaks the point symmetry of the distribution by imposing a preferred direction of sliding, along $-\vec{g}_t$, producing an off-set tail. The size of the tail depends on the wall superheat with the length of the tail decreasing for increasing wall superheat.

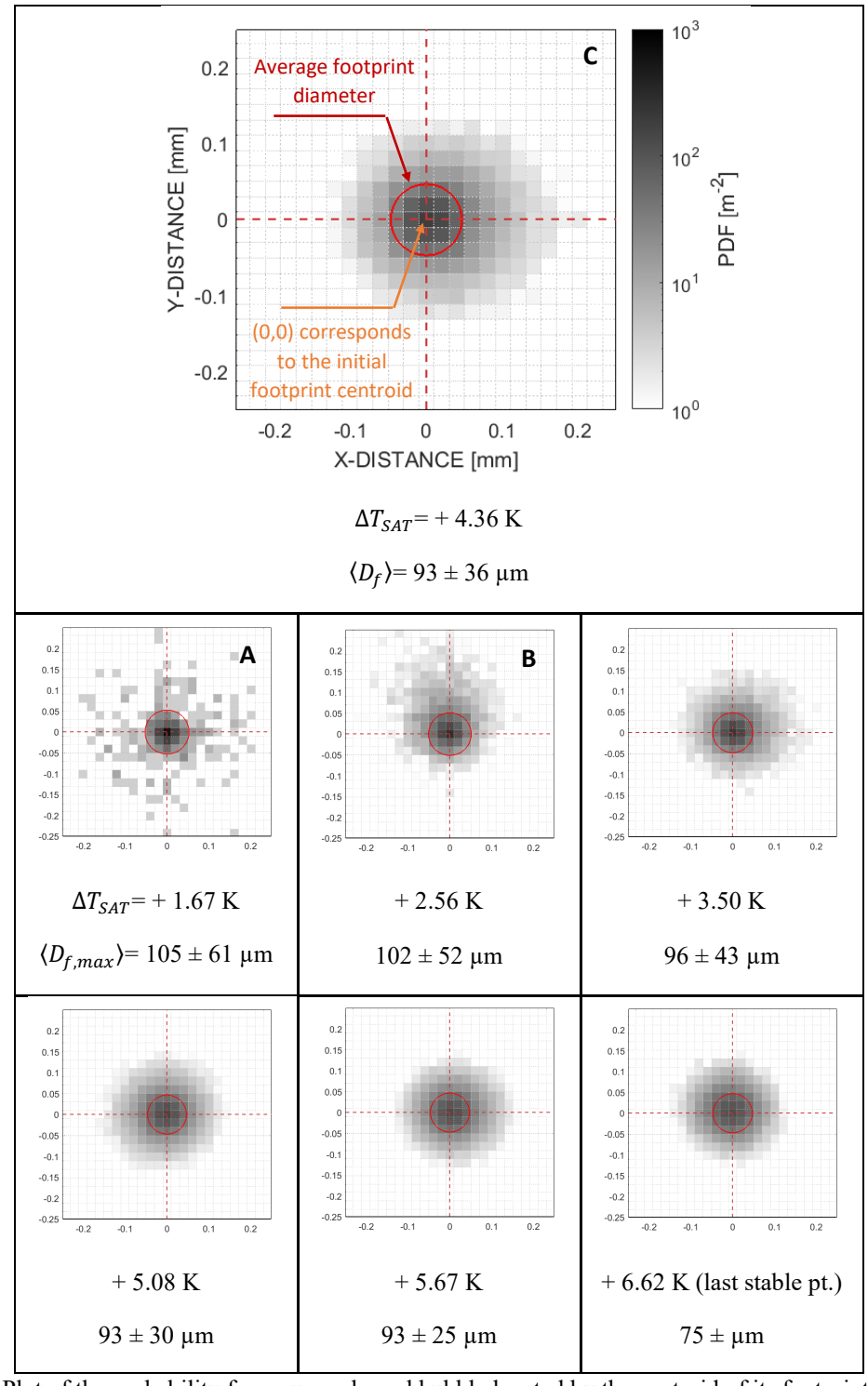

Figure 3.61. Plot of the probability for an uncoalesced bubble located by the centroid of its footprint to be observed at certain distance from its initial position on a horizontal upward facing boiling surface. The wall superheat varies between each plot. The average equivalent bubble footprint diameter is represented by a red circle for each wall superheat. All plots share the same x- and y-axis, as well as the same colormap.

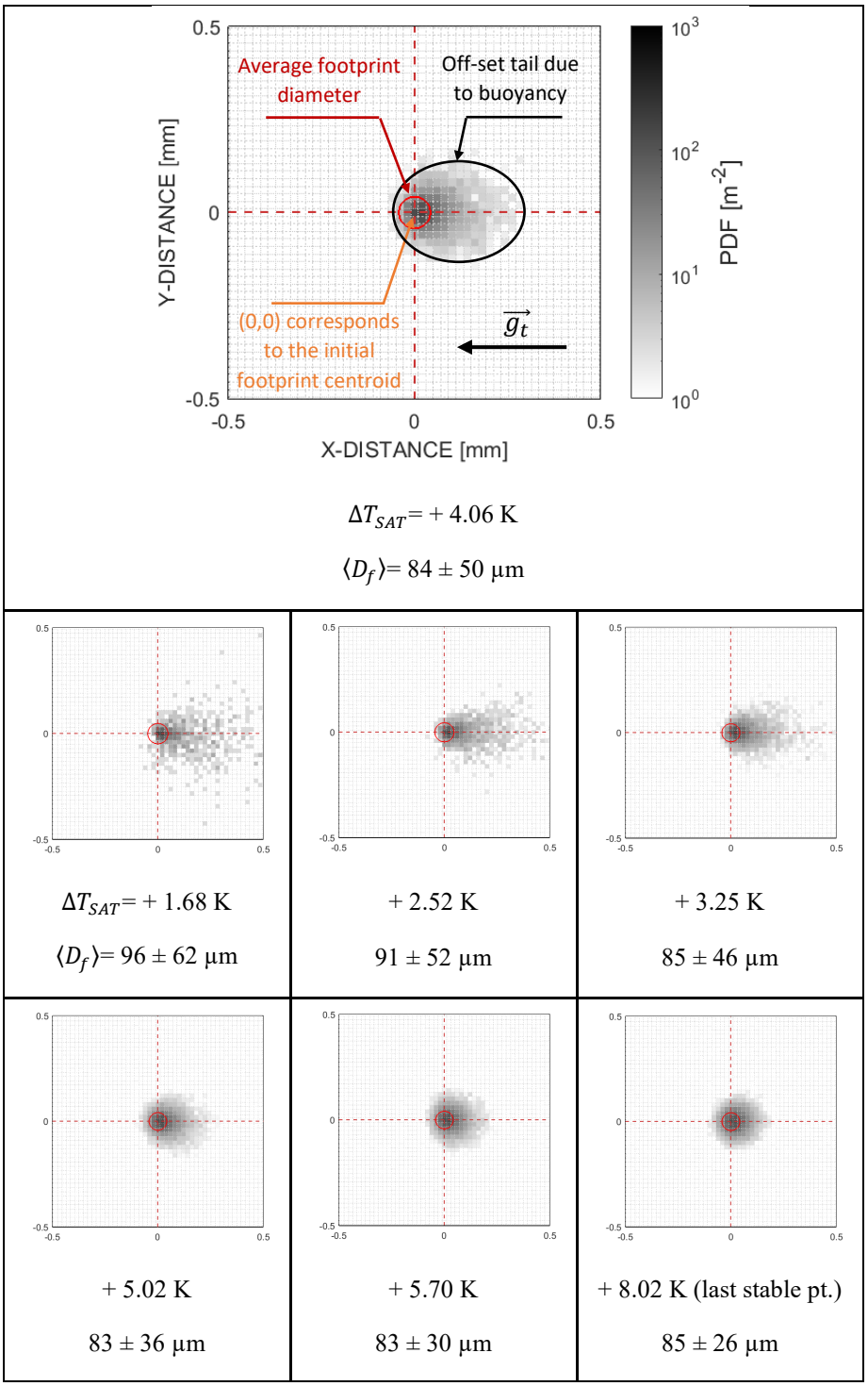

Figure 3.62. Plot of the probability for an uncoalesced bubble located by the centroid of its footprint to be observed at certain distance from its initial position on a 150°-angle inclined boiling surface. The wall superheat varies between each plot. The average equivalent bubble footprint diameter is represented by a red circle for each wall superheat. All plots share the same x- and y-axis, as well as the same colormap.

We saw in Section 3.1.3 that bubble growth time is independent from the inclination angle, and a trend in $\sqrt{t}$ can be seen for any angle. These observations can be made despite bubble sliding being more prominent on inclined surface which is shown by comparing Figure 3.24 and 3.25. Therefore, this suggests that the evaporation mechanism responsible for bubbles growth is independent of the bubbles sliding. However, bubble sliding is still expected to impact the amount of heat removed from the surface by quenching. We can naturally have 2 asymptotic behaviors in path of sliding bubbles depending on the magnitude of $\vec{g}_t$. Figure 3.26 shows a schematic of these behaviors. For low values of $\|\vec{g}_t\|$, we expect the bubbles movement on the surface to be dominated by week convective effects (not induced by buoyancy) in the surrounding liquid. When $\|\vec{g}_t\|$ increases, the sliding distance increases and the trajectory of the bubble becomes more predictable, aligning with $-\vec{g}_t$. The case with the bubble pinned to the surface (i.e., preventing the bubbles to slide) is not shown here, as it does not seem to occur in our testing conditions with nitrogen bubbles on nano-smooth sapphire-ITO.

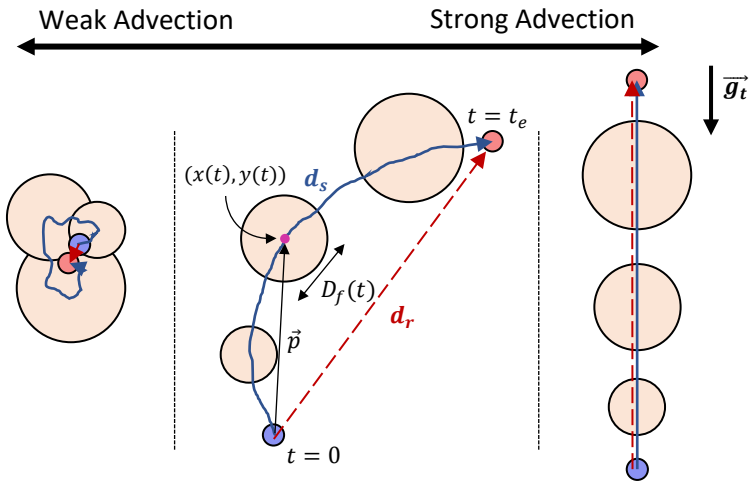

Figure 3.63. Schematics of sliding bubble.

In order to quantify and analyze bubbles sliding, we define two metrics of interest. The first metric is the distance d_s traveled by the bubble centroid,

$$d_s = \int_{t=0}^{t_e} \left\| \frac{d\vec{p}}{dt} \right\|_2 dt \tag{3.42}$$

With $\vec{p}(t)$ the position vector of the bubble footprint. The bubble nucleation occurs at $t = 0$ with $\vec{p}(0) = 0$. d_s is related the surface area swiped by the bubble and therefore quenched by the liquid. $\| \ \|_2$ is the Euclidean norm.

The second metric of interest is the "flight" distance of the bubble, noted d_r and defined by,

$$d_r = \|\vec{p}(t_e) - \vec{p}(0)\|_2 \tag{3.43}$$

d_r corresponds to how far from the nucleation site the bubble has traveled. Intuitively, we expect d_r to be much smaller than d_s when $\|\vec{g}_t\|_2$ is small and convective effects (e.g., generated by surrounding bubbles) are weak. Instead, when $\|\vec{g}_t\|_2$ is large, we expect d_r to be in the same order of magnitude as d_s. The distance $\langle d_r \rangle$, averaged over all bubbles nucleating on the surface with d_r defined by Eq. 3.43, corresponds to the expectation of $p(x, y)$ given by,

$$\langle d_r \rangle = \int_0^{2\pi} \int_0^{\infty} p(r, \theta) r dr d\theta \text{ with } p(r, \theta) dr d\theta = p(x, y) dx dy \tag{3.44}$$

It is clear that the average distance traveled by bubbles (whether it is measured by d_r or d_s) is expected to be different if bubbles mostly coalesce or lift-off. Bubbles nucleating on the boiling surface predominantly end up coalescing. Therefore we restrict the analysis of the bubble traveled distance to bubble nucleating of the surface and then coalescing. We note $d_{r,co}$ the flying distance between nucleation and the location of the heated surface of first coalescence. Figure 3.27 shows the probability distribution $p(d_{r,co})$ for different values of inclination angles (0°, 90° and 150°) and wall superheat (~1.8 K, 3.5 K and 5 K).

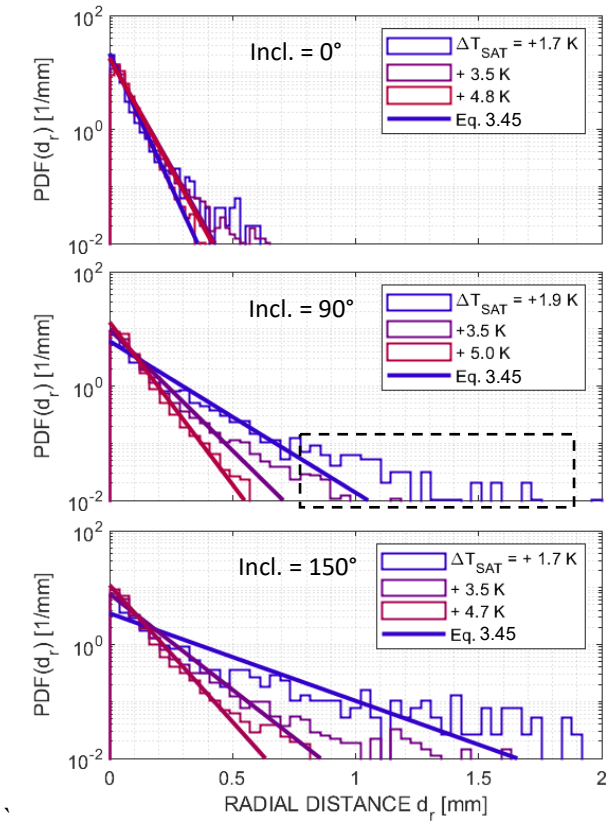

Figure 3.64. Probability distribution function of $d_{r,co}$ for different inclination angles and wall superheat.

$$p(d_{r,co}) = \frac{1}{K} e^{-d_r/K} \tag{3.45}$$

With K is a constant corresponding to a mean free path. Using Eq. 3.45, we can deduce that K is equal to $\langle d_{r,co} \rangle$. The exponentially damped distribution fails to fit well the experimental data for low wall superheat and high inclination angles (see, the black dashed frame in Figure 3.27). That might be due to a lack of bubbles to be statistically converged.

From the plots of Figure 3.27, we can then see that K decreases when the wall superheat increases (which is consistent with an increase of the bubble density and the high probability of coalescence between bubbles). Figure 3.28 shows the values of mean flying distance $\langle d_{r,co} \rangle$ before coalescence for bubbles on a horizontal surface (inclination at 0°) and inclined surface (at 90° and 150°).

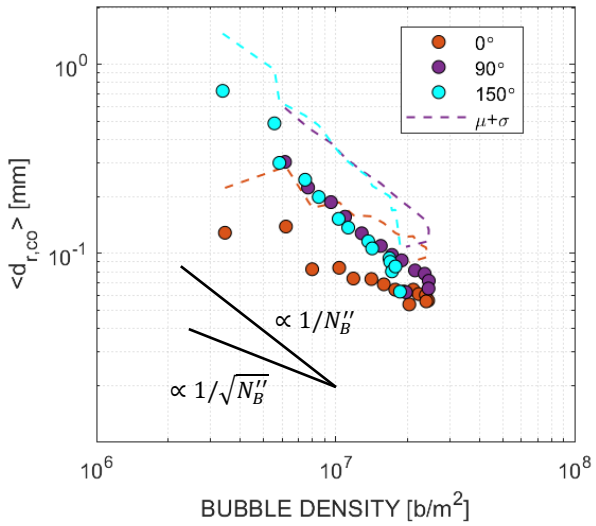

Figure 3.65. Flying distance $\langle d_{r,co} \rangle$ traveled by bubbles between nucleation and coalescence against the average bubble density on the heated surface N_B'' and for different values of surface inclination angle. The dashed line represents the value of $d_{r,co}$ at 1 standard deviation from the average.

Two trends are noticeable in Figure 3.28. On a horizontal surface (shown in orange), the mean free path of the bubbles ($\langle d_{r,co} \rangle$) is proportional to the average distance between 2 bubbles which is approximated by $1/\sqrt{N_B''}$ for bubbles uniformly dispersed on the surface. However, when the surface is inclined (shown in purple and blue), it appears that a steeper reduction of the mean free path with the bubble density occurs, and $\langle d_{r,co} \rangle \propto 1/N_B''$. For a high enough heat flux and therefore large bubble density, the mean free path $\langle d_{r,co} \rangle$ becomes independent of the inclination angle, which is consistent with the distribution of $d_{r,co}$ plotted in Figure 3.27 (all red lines showing the highest surface wall superheat, ~ +5 K, are similar, irrespective of the inclination angle).

d_r indicates how far bubbles can slide on the surface without coalescing. However, one can see from the sketch in Figure 3.26 that unless strong advection is present, d_r does not characterize correctly the surface swiped by the bubbles and the heat removed when the heated surface is rewetted in the wake of the sliding bubbles. Instead, the distance traveled by bubbles d_s introduced in Eq. 3.42 appear more appropriate. Figure 3.29 shows a plot of $\langle d_s/d_r \rangle$ for different values of inclination angle (0º, 90º and 150º) and wall superheat. Knowing the relationship between d_s and d_r (e.g., from the ratio $\langle d_s/d_r \rangle$) is useful from a modeling point of view, as d_r is easier to estimate in most cases (e.g., from the bubble density as shown in Figure 3.28), while d_s is necessary to estimate the quenching component of the boiling heat flux. Figure 3.29 shows that the ratio $\langle d_s/d_r \rangle$ is mostly constant irrespective of the wall superheat and irrespective of the inclination angle. $\langle d_s/d_r \rangle$ is about 2 in all cases. The exception is seen at low wall superheat for a horizontal surface

(i.e., 0º), in which case, larger values of $\langle d_s/d_r \rangle$ are found. This appears consistent from what we expected and illustrated in Figure 3.26. In the absence of gravitational force tangent to the heating surface (i.e., at 0º), bubbles sliding is dictated by convective effects induced by other bubbles in boiling cell and potentially some residual liquid flow, e.g., due to the venting and supply of the nitrogen as the liquid boils (see Chapter 2 for the description of the boiling cell). This results in bubbles having more chaotic trajectory on the surface, and therefore d_s can be significantly larger than d_r. As the wall superheat increases, the ratio $\langle d_{ss}/d_r \rangle$ decreases for bubbles on a horizontal surface and the asymptotic value matches with the cases on inclined surface (at 90º and 150º). That behavior might be explained by the higher probability for bubbles to coalesce at higher wall superheat (as the surface is more crowded with neighboring bubbles), resulting in smaller traveled distance d_s. However, this argument is cannot be complete since we all also saw that d_r decreases as well as wall superheat increases (see Figure 3.28). We suspect that the increase of turbulence due the higher bubble density reduces the distance d_s more than it affects d_r, until the ratio reaches it asymptotic value.

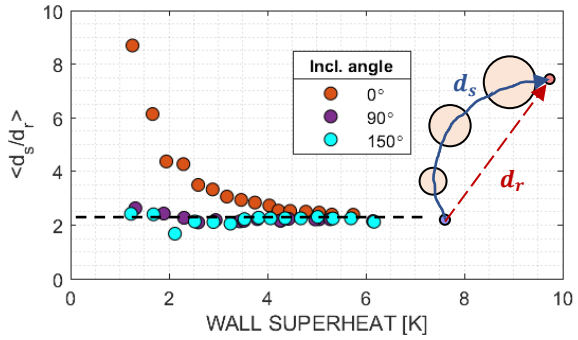

Figure 3.66. Average ratio between the traveled distance d_s and the flying distance d_r for uncoalesced bubbles against wall superheat at difference values of surface inclination.

3.1.5. Bubble departure and lift-off

The bubble departure footprint diameter corresponds to the equivalent diameter of the bubble footprint at the moment the footprint no longer overlaps with the nucleation site where it has started to grow. Bubble lift-off occurs when the bubble reaches its maximum size, and then rapidly separate from the heated surface. The bubble footprint diameter at lift-off is defined as its maximum value. Along with $\langle d_s \rangle$, lift-off and departure diameter allow to estimate the surface area of the heated surface that has been swiped by the bubbles, and therefore potentially cooled down by quenching. We saw from Figure 3.27-3.29 that bubbles are mobile on the surface even when the heated surface is horizontal. Naturally from this observation we can see in Figure 3.30 that the average bubble departure footprint diameter $\langle D_{f,\mathrm{d}} \rangle$ is small, around 40 µm. The error bars show the standard deviation of each of the data sets for a given inclination angle and wall

superheat. The measurement related to the segmentation procedure gives $D_{f,\mathrm{d}}$ ± 2 px (i.e., ~ ± 24 µm), which is roughly equivalent to having an uncertain of ± 1 px all around the bubble footprint.

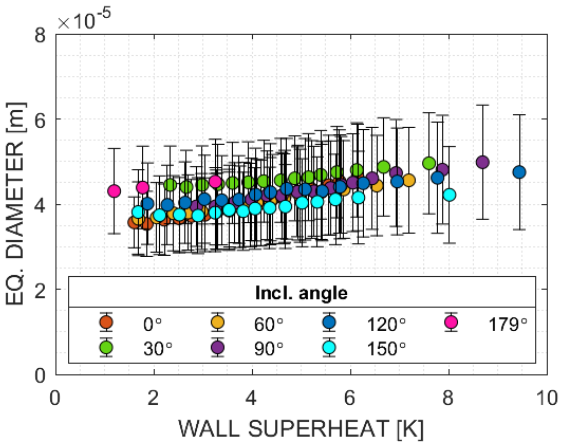

Figure 3.67. Plot of the average departure diameter $\langle D_{f,d} \rangle$ measured on uncoalesced bubbles for different inclination angles and wall superheat.

The lift-off diameter is evaluated by measuring the maximum footprint diameter of the bubble over its growth. Figure 3.31 shows the probability distribution functions of the lift-off diameter of nitrogen bubbles for the heating surface with no inclination (i.e., horizontal upward facing). Only bubbles crossing the border of the image are excluded. On each of the plots, the PDF shown with light color shade accounts for all segmented bubbles regardless their origin (nucleation or coalescence), while the darker shade PDF excludes bubbles which result from coalescence. The uncertainty band corresponds to the uncertainty related to the segmentation procedure, $D_{f,lo}$ ± 2 px (i.e., ~ ± 24 µm). Two regions, noted A and B, can be distinguished on each of the PDFs shown in Figure 3.31, irrespective of the wall superheat, and splitting each curve at their maximum. The average value of each PDFs lies within the region B in all cases. Region A shows an increase of the likelihood for small bubbles to lift-off when their size increases. This behavior corresponds to what we should expect from basic bubble force balance. The magnitude of forces responsible for bubbles to lift-off grows faster (for lift and drag forces, $\propto D^2$, for buoyancy $\propto D^3$) than the surface tension keeping the bubble attached to the surface (i.e., $\propto D$). However, we should point out that the uncertainty in region A is significant as the associated range of bubble size is not far from the space resolution (~12 µm/px) and our capability to accurately segment the bubble footprint. Therefore, a more details analysis of region A, e.g., of the slope of the distribution, would not be useful. Region B shows a different trend: the likelihood of observing bubbles with large lift-off diameter decreases as the diameter increases. The trends observed show a decrease of the probability in ${D_{f,lo}}^{-n}$ with n equal or larger than 2. The apparent probability of

observing a bubble reaching a given lift-off diameter is lower when only uncoalesced bubbles (i.e., bubbles originating from a nucleation on the heated surface) are considered (shown by darker shade lines).

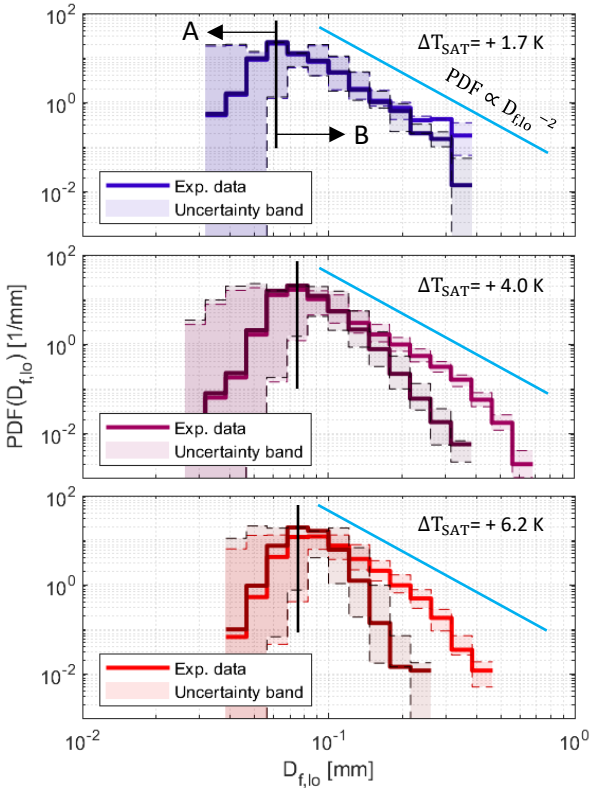

Figure 3.68. Plot of the probability distribution function associated with the lift-off diameter for horizontal nitrogen pool boiling. The wall superheat is increased from top to bottom. The lines with a brighter shade are the PDFs accounting for all bubbles, while the darker shade account only for bubbles which did not coalesce before lift-off.

The difference between the distribution of uncoalesced bubbles (plotted in dark shades) and all bubbles (plotted in light shades) also increases as the wall superheat increases. This observation is consistent with the fact that the probability of bubble coalescing increases with the bubble density at the surface (and therefore, with the wall superheat). The probability for a discrete bubble to nucleate and reach large lift-off diameter necessarily decreases with the increasing probability of coalescing.

In existing heat flux partitioning frameworks, only the average value of the lift-off diameter distributions matter. Figure 3.32 shows the average lift-off diameter measured for different inclination angles of the heating surface and wall superheat from ONB to DNB. Only uncoalesced bubble are considered. The error bars indicate the standard deviations of the data. The measurement uncertainty is equal to +/- 24 µm over the diameter (i.e., 2 px). As we could expect from the distribution plotted in Figure 3.32, the average value

of lift-off diameter is mostly constant with the wall superheat. The average value also remains unchanged when the angle of surface inclination is increased from 0° to 179°.

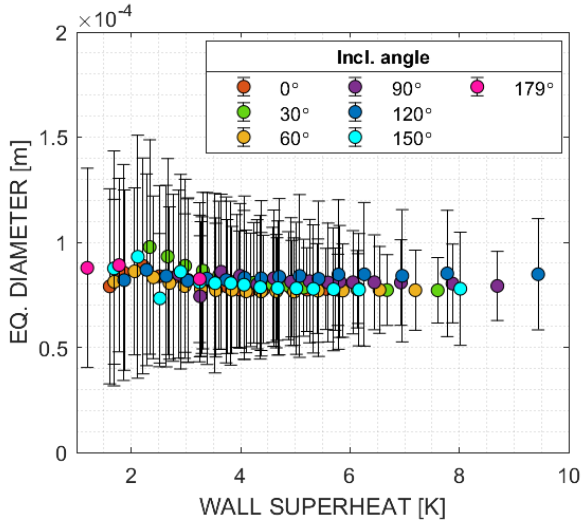

Figure 3.69. Plot of the lift-off diameter measured on uncoalesced bubbles for different inclination angles and wall superheat.

3.1.6. Relationships between growth moduli, effective contact angle and wall superheat

We saw that bubble growth follows a characteristic $\sqrt{t}$ trend, irrespective of the inclination angle of the heating surface. We also showed that bubbles seemingly have larger bubble footprint than expected from the low equilibrium contact of nitrogen on sapphire-ITO. Finally, we also showed that sliding does not modify the growth rate of the bubbles. Here, we analyze how the growth moduli and the effective contact angle of a larger set of bubbles changes with wall superheat. Bubbles are collected using data at different inclination angles as well to highlight any effect of buoyancy on the bubbles' growth.

The measurements of the effective contact angle and growth modulus has been performed on 14 different bubbles at various wall superheat on a horizontal heating surface and are shown in Table 3.1, and the measurements of 28 additional bubble are given in Table 3.2 with different inclination angles.

Table 3.4. Growth conditions of selected individual nitrogen bubbles in horizontal pool boiling

Bubble	Inclination angle	Pressure	Saturation temp.	Average wall superheat	Average heat flux	Average Ca $\mu_l\langle\dot{R}_f\rangle/\sigma_{lv}$	Maximum Bo $\Delta\rho g D_o^2/\sigma_{lv}$	Average θ_{eff} $\langle\sin^{-1} D_f/D_o\rangle$
#	[°]	[kPa]	[K]	[K]	[kW/m^2]	[-] (10^{-5})	[-]	[°]
0-1	0	491.8	93.8	1.21	23.55	2.9 ± 4.4	0.25	29.5 ± 1.2
0-2	0	491.8	93.8	1.21	23.55	1.0 ± 1.4	0.34	25.7 ± 1.0
0-3	0	491.8	93.8	1.61	40.76	4.6 ± 3.7	0.14	33.3 ± 0.8
0-4	0	491.8	93.8	1.61	40.76	4.8 ± 4.2	0.12	36.7 ± 2.6
0-5	0	481.9	93.5	1.02	19.20	1.2 ± 1.4	0.17	30.7 ± 0.9
0-6	0	481.9	93.5	1.02	19.20	0.7 ± 1.6	0.34	27.4 ± 0.9
0-7	0	481.9	93.5	1.02	19.20	0.7 ± 1.4	0.30	26.4 ± 1.4
0-8	0	481.9	93.5	1.47	32.75	4.5 ± 2.4	0.037	38.8 ± 0.8
0-9	0	481.9	93.5	1.47	32.75	4.1 ± 3.0	0.087	37.5 ± 1.0
0-10	0	481.9	93.5	1.79	49.88	2.0 ± 2.1	0.25	35.8 ± 1.0
0-11	0	481.9	93.5	1.79	49.88	4.0 ± 4.1	0.088	42.5 ± 1.9
0-12	0	481.9	93.5	1.79	49.88	5.2 ± 4.7	0.13	38.6 ± 2.0
0-13	0	481.9	93.5	2.07	63.68	4.6 ± 3.0	0.082	43.1 ± 2.2
0-14	0	481.9	93.8	2.07	63.68	7.5 ± 6.0	0.091	43.1 ± 1.6

Table 3.5. Growth conditions of selected individual nitrogen bubbles on an inclined surface.

Bubble	Inclination angle	Pressure	Saturation temp.	Average wall superheat	Average heat flux	Average Ca $\mu_l\langle\dot{R}_{f,eq}\rangle/\sigma_{lv}$	Maximum Bo $\Delta\rho g D^2_{o,max}/\sigma_{lv}$	Average θ_{eff} $\langle\sin^{-1} D_f/D_o\rangle$
#	[°]	[kPa]	[K]	[K]	[kW/m^2]	(10^{-5}) [-]	[-]	[°]
30-1	30	487.7	93.7	1.89	23.54	3.5 ± 3.8	0.12	34.5 ± 1.3
30-2	30	487.7	93.7	1.89	23.54	4.7 ± 3.4	0.074	33.0 ± 2.0
30-3	30	487.7	93.7	2.34	40.75	4.0 ± 4.7	0.28	36.6 ± 1.5
30-4	30	487.7	93.7	2.67	40.75	8.0 ± 3.3	0.054	41.4 ± 2.1
60-1	60	478.6	93.4	1.23	26.94	2.1 ± 2.5	0.078	29.6 ± 1.0
60-2	60	478.6	93.4	1.23	26.94	2.9 ± 3.8	0.14	26.4 ± 0.8
60-3	60	478.6	93.4	1.69	45.47	4.4 ± 3.2	0.054	31.7 ± 2.1
60-4	60	478.6	93.4	1.69	66.07	3.1 ± 3.6	0.093	33.9 ± 1.1
90-1	90	504.1	94.1	1.06	24.90	3.5 ± 3.8	0.11	31.4 ± 1.6
90-2	90	504.1	94.1	1.59	24.90	6.5 ± 8.9	0.053	34.1 ± 4.1
90-3	90	504.1	94.1	1.99	43.23	6.0 ± 6.8	0.059	37.4 ± 2.3
90-4	90	504.1	94.1	2.26	43.23	5.8 ± 8.1	0.075	42.8 ± 4.8
120-1	120	519.9	94.4	1.46	27.80	3.0 ± 5.1	0.14	33.5 ± 1.9
120-2	120	519.9	94.4	1.87	46.80	5.1 ± 6.2	0.053	38.3 ± 2.8
120-3	120	519.9	94.4	2.28	70.49	6.3 ± 3.2	0.081	39.3 ± 1.5
120-4	120	519.9	94.4	2.64	92.92	10.5 ± 4.6	0.032	45.3 ± 1.9
150-1	150	496.8	93.9	1.23	22.35	3.3 ± 2.6	0.067	30.0 ± 0.8
150-2	150	496.8	93.9	2.52	37.18	6.4 ± 4.9	0.053	37.2 ± 1.3
150-3	150	496.8	93.9	4.36	53.26	10.8 ± 5.2	0.031	51.6 ± 2.3
150-4	150	496.8	93.9	5.70	68.42	10.9 ± 5.0	0.031	57.5 ± 2.2
165-1	165	479.0	93.4	0.49	18.30	1.7 ± 2.7	0.13	28.0 ± 1.3
165-2	165	479.0	93.4	1.53	53.70	4.5 ± 2.6	0.083	34.2 ± 0.8
165-3	165	479.0	93.4	2.43	129.23	7.8 ± 6.5	0.12	38.7 ± 2.6
165-4	165	479.0	93.4	3.09	170.67	10.6 ± 3.8	0.032	38.7 ±2.6
179-1	179	444.5	92.5	2.56	17.01	6.3 ± 6.0	0.21	42.3 ± 1.2
179-2	179	444.5	92.5	2.56	50.23	5.2 ± 4.0	0.14	42.3 ± 0.9
179-3	179	444.5	92.5	3.11	83.37	6.1 ± 11.6	0.47	45.6 ± 3.2
179-4	179	444.5	92.5	3.11	117.62	7.7 ± 3.7	0.061	46.6 ± 1.7

All the bubbles listed in Tables 3.1 and 3.2 follow similar trend than shown in Figures 3.8 and 3.9, irrespective of the inclination angle with footprint radius and optical radius growing with $\sqrt{t}$ and an effective contact angle remaining constant throughout the growth. We can therefore evaluate the growth moduli B_f and B_o for each of these bubbles. B_f and B_o are defined using Eq. 3.28 and are related to one another by the effective contact angle θ_{eff}. Figure 3.33 shows a plot of B_f and B_o for each of the bubbles listed in Tables 3.1-3.2. Different values of growth modulus are obtained depending on the explored wall superheat. All data points align on a line with $B_o \propto {B_f}^{1/2}$. The trend appears independent of the inclination angle (represented here by different colors in Figure 3.33).

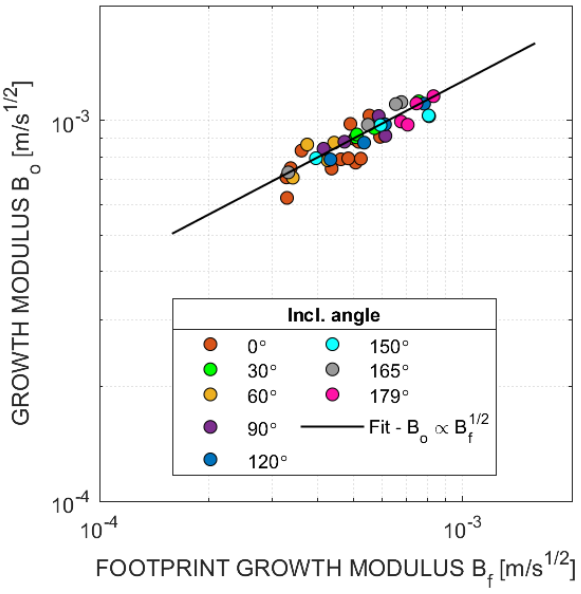

Figure 3.70. Plot of the growth modulus evaluated from the optical radius (B_o) against the growth modulus evaluated from the bubble footprint B_f.

This well-defined trend seen between B_f and B_o captures the regularity observed in the bubbles shape. If the bubble footprint grows slightly faster, we can then predict simply how faster the bubble size (estimated by its optical radius) will grow. Note that the relationship ($B_o \propto {B_f}^{1/2}$) implies that the effective contact angle (equal to $\sin^{-1}(B_f/B_o)$) depends on the wall superheat as we will show below. Figure 3.34 shows the variation of B_f with the wall superheat. As the wall superheat increases, the growth modulus B_f increases. The observed trend is relatively unclear but lies between $B_f \propto \Delta T_{SAT}^{1/2}$ and $B_f \propto \Delta T_{SAT}$. The data points obtained on a horizontal downward heating surface (i.e., with an inclination angle of ~179°) are disregarded to assess the fitting trends. At this inclination angle, nucleate boiling is very unstable, as we

will discuss later on, and therefore the space- and time-averaged wall superheat measured might not represents well enough the effective wall superheat at the time of the bubble growth.

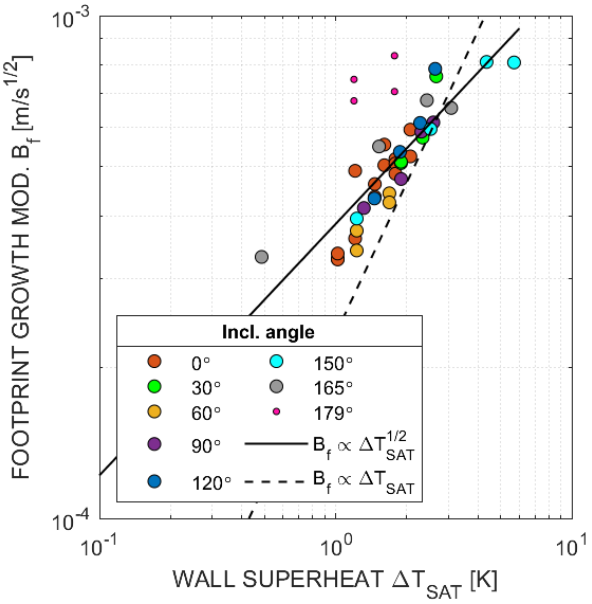

Figure 3.71. Plot of the growth modulus evaluated from the footprint radius (B_f) against the wall superheat.

It is not obvious if a direct comparison between the experimental data and Scriven or Plesset-Zwick's model is reasonable due several model assumptions. In particular Scriven or Plesset-Zwick's model assumes the growth to occur in an infinite pool of superheated liquid. However, the bubble wait times typically observed in our test conditions appear small (t_w~10^{-3}-10^{-2} s) resulting in small boundary layer (~$\sqrt{\alpha_l t_w}$, i.e., 10-30 μm) much thinner than the typical bubble size (up to D_f~200 μm for uncoalesced bubbles, see Figure 3.15). Also, in the theory developed in Section 3.1.1, the change in bubble radius R is a measure of how much liquid is evaporated at the liquid-vapor interface with the assumption of spherical symmetry. Experimentally, this is not clear, as neither the optical radius nor the footprint radius characterizes fully the vapor content of the bubble. To circumvent this issue, we define a spherical equivalent bubble radius which should better match in principle the radius R used in the analytic model,

$$R_v = \left(\frac{3V}{4\pi}\right)^{1/3} \tag{3.46}$$

V can be evaluated by assuming that the bubble is a spherical cap,

$$V = \frac{\pi}{3} {R_f}^3 F(\theta_{eff}) \tag{3.47}$$

where R_f is the footprint radius and

$$F(\theta_{eff}) = \frac{(2-\cos\theta_{eff})(1+\cos\theta_{eff})^2}{\sin(\theta_{eff})^3} \tag{3.48}$$

Therefore,

$$R_v = R_f\left(\frac{F(\theta_{eff})}{4}\right)^{1/3} \tag{3.49}$$

We can define a growth modulus B_v associated with R_v using a similar expression than in Eq. 3.28,

$$R_v = B_v\sqrt{t+t_0} \tag{3.50}$$

A relationship between R_v and R_o can be simply derived from Eq. 3.27 and Eq. 3.48,

$$R_v = R_o G(\theta_{eff}) \text{ with } G = \left(\frac{(2-\cos\theta_{eff})(1+\cos\theta_{eff})^2}{4}\right)^{1/3} \tag{3.51}$$

B_v characterizes the volumetric growth rate of bubbles (and therefore the evaporative heat transfer),

$$\frac{dV}{dt} = 2\pi {B_v}^3\sqrt{t+t_0} \tag{3.52}$$

$G(\theta_{eff})$ is between 0 and 1 for θ_{eff} between 180° and 0°. For θ_{eff} small, below 50°, $G(\theta_{eff})$ is approximately equal to 1, getting down to ~0.97 for θ_{eff} equal to 50°. Figure 3.35 shows a plot of B_v against the bubble growth modulus B_o for the different bubbles listed in Table 3.1 and Table 3.2. As a consequence of the relatively low effective angle observed in nitrogen boiling, we can observe that B_v is well approximated by B_o.

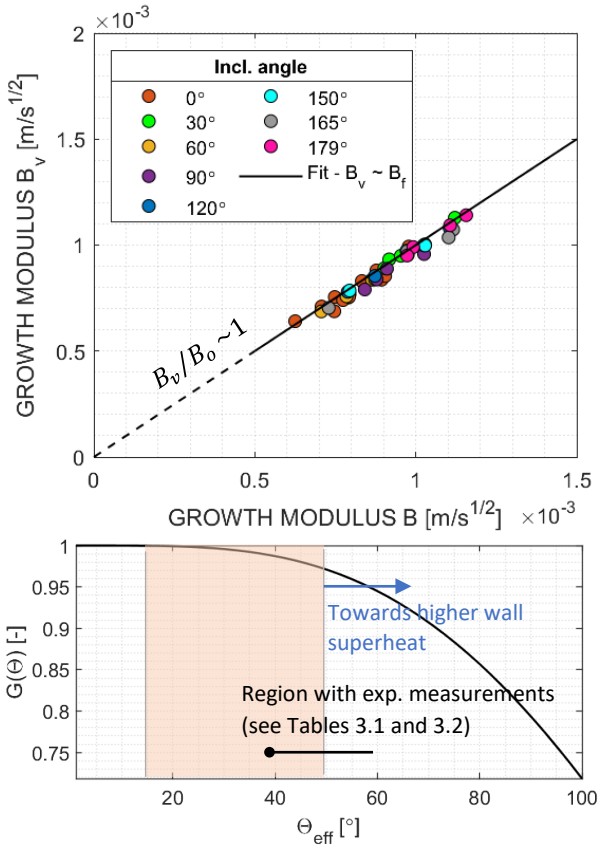

Figure 3.72. Plot of the growth modulus associated with volume growth (B_v) against the growth modulus evaluated from the optical radius B_o.

Since B_o and B_v are roughly equal, the modulus B_o should well characterize the evaporative heat transfer during bubble growth. We can compare the trend of B_o with wall superheat and the growth modulus obtained from theoretical analysis, developed in Section 3.1.1. From the relationship found in Figure 3.33 ($B_o \propto {B_f}^{1/2}$), we can then deduce that the trend of B_o with the wall superheat is between $B_o \propto \Delta T_{SAT}$ and $B_o \propto \Delta T_{SAT}^2$.

More about the evaporative heat transfer can be understood by analyzing the effective contact angle. Figure 3.36 shows a plot of the values of effective contact angle measured experimentally for different inclination angles and wall superheat, previously given in Tables 3.1 and 3.2. Markers plotted with a same color are data measured with the same surface inclination angle. The measurements of effective contact angle plotted in Figure 3.36 supports the previous observation: the effective contact is fairly large compared to the equilibrium contact angle (<10° for nitrogen on our surface), between 25° and 50° depending on the wall superheat.

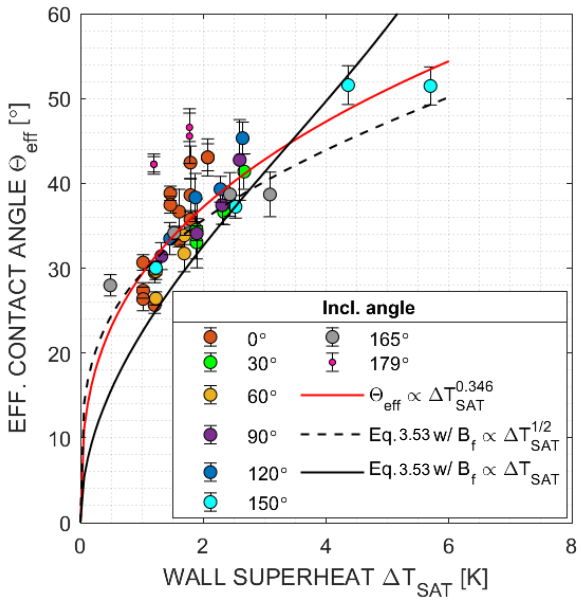

Figure 3.73. Plot of the effective contact angle defined by Eq. 3.27 (i.e., defined as $\sin^{-1} R_f/R_o$) against wall superheat for different inclination angles.

Leveraging the apparent relationship between the growth moduli evaluated from the footprint and optical radius (see Figure 3.33), we can derive a relationship between B_f and the effective contact angle θ_{eff},

$$\theta_{eff} = \left(\sin^{-1}\frac{1}{K}\sqrt{B_f}\right) \tag{3.53}$$

With K~0.04 $s^{1/4}/m^{1/2}$ obtained from the fitting shown in Figure 3.34. This is particularly interesting, because it allows to extrapolate the estimation θ_{eff} toward higher wall superheat by leveraging only the phase-detection recordings. The black line in Figure 3.36 corresponds to Eq. 3.53, while the red line corresponds to a fitting power law. A clear increase of the effective contact angle θ_{eff} with increasing wall superheat is visible from Figure 3.36, irrespective of the inclination angle, which is consistent with our previous observations (Figures 3.33 and 3.34). No measurement is available for very low wall superheat, close to saturation. We can expect the effective contact angle to match the equilibrium contact angle near saturation for small enough bubbles such that the bubbles are spherical. The equilibrium contact angle was measured around 5° for nitrogen at 1 atm on an ITO-sapphire surface (see Chapter 2). However, for simplification, we assumed in Figure 3.36 that the effective contact angle goes to 0 as the wall temperature goes to the saturation temperature ($\Delta T_{SAT} \rightarrow 0$).

3.2. Evaporative heat transfer during bubble growth

3.2.1. Absence of microlayer during nitrogen bubble growth

Under the boiling conditions tested in this study, no microlayer have been observed during bubble growth. The absence of microlayer might be the result of a combined effect of low growth velocity related to cryogens physical properties (about ~ 1 mm/s for our case with nitrogen) and the high thermal effusivity of our substrate. Figure 3.37 shows a plot of sapphire thermal effusivity against temperature from the published data of Ref. [12].

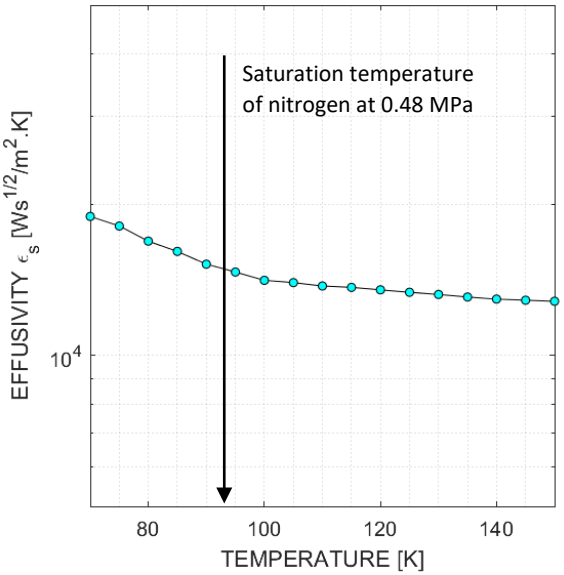

Figure 3.74. Plot of the thermal effusivity of sapphire against temperature.

The role of surface properties and fluids properties on the absence of microlayer is not clear yet. Further analysis and potentially more boiling data on surface with different thermos-physical properties would be necessary before we would draw clear conclusions. On-going cryogenic boiling studies in our laboratory have shown that with lower effusivity materials, like borosilicate, microlayer formation can form during bubble growth with liquid nitrogen . This suggests that the microlayer is evaporated as soon as it forms, and that evaporation mostly occur near thetriple contact line. In particular, we will show in the following section that prediction of models of triple contact line evaporation well matches our experimental observation.

3.2.2. Triple contact line evaporation

3.2.2.1. Experimental inference

The lack of space resolved temperature measurement limits the analysis we can provide to understand how heat is removed by nitrogen bubbles. We know from visual observation that microlayer doesn't form in the

tested conditions. The analysis done in Section 3.1.2 shows that the variations over time of bubble shape are expected to be minimal as indicated by constant effective contact angle. We also know that buoyancy does not significantly deform uncoalesced bubbles due to low Bond numbers (~10^{-2}-10^{-1}), which was shown in Figure 3.18 and 3.17. Therefore, in absence of additional forces, the bubbles should be close to spherical caps. We can use these 2 observations (bubble sphericity and constant effective contact angle throughout growth) to estimate the evaporative heat transfer associated with the growth of a single nitrogen bubble. We will assume at first that all the heat is removed at the triple contact line, and then we will discuss this assumption. Let's consider the axisymmetric bubble described in Figure 3.40.

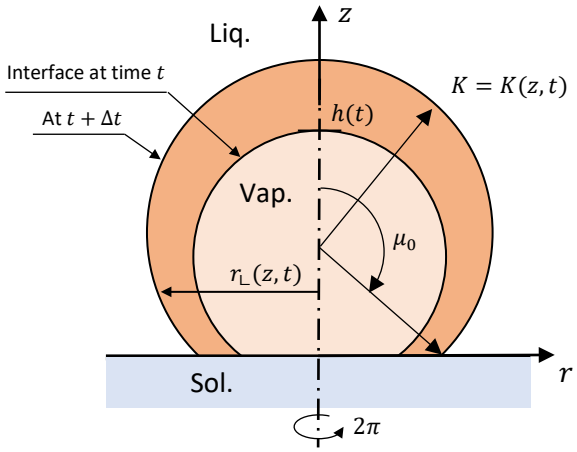

Figure 3.75. Schematics of growing axisymmetric bubble.

The volume of the bubble is given in cylindrical coordinate by,

$$V = \pi \int_0^h r_L{}^2 dz \tag{3.55}$$

With h the height of the bubble at a certain time t and r_L the distance with the axis of symmetry and the interface measured on plane parallel to the wall. The axis $\hat{z}$ is defined normal to wall. We can normalize the coordinate z by dividing it by h,

$$z^* = z/h \tag{3.56}$$

Therefore,

$$V = \pi h \int_0^1 r_L{}^2 dz^* \tag{3.57}$$

The bubble footprint perimeter, i.e., the triple contact line length, can be written as,

$$P = 2\pi r_{\llcorner}(z^* = 0) \tag{3.58}$$

The mass rate of liquid evaporated is given by,

$$\dot{m}_{ev} = \rho_v \frac{dV}{dt} \tag{3.59}$$

Using the assumption that the heat used evaporate the superheated liquid is removed near the triple contact line, we then get,

$$\dot{m}_{ev} = \dot{q}' \frac{P}{h_{lv}} \tag{3.60}$$

where $\dot{q}'$ is the heat transfer rate per unit length of triple contact line.

Combining Eqs. 3.34 to 3.35, we can derive the following expression for $\dot{q}'$,

$$\dot{q}' = \frac{\rho_v h_{lv}}{P} \frac{dV}{dt} \tag{3.61}$$

Using Leibniz integral rule to expand dV/dt, it yields the general expression of $\dot{q}'$ for an axisymmetric bubble:

$$\dot{q}' = \rho_v h_{lv} \frac{1}{r_{\llcorner}(z^* = 0)} \left[h \int_0^1 r_{\llcorner} \frac{\partial r_{\llcorner}}{\partial t}_{z^*} dz^* + \frac{1}{2} \frac{dh}{dt} \int_0^1 {r_{\llcorner}}^2 dz^* \right] \tag{3.62}$$

If the bubble volume is well described by a spherical cap of radius R and opening angle μ_0, and its footprint perimeter by a circle for radius R_f, we have,

$$V = \frac{\pi}{3} R^3 (2 + \cos\mu_0)(1 - \cos\mu_0)^2 \tag{3.63}$$

And,

$$P = 2\pi R_f \tag{3.64}$$

Since we are assuming a spherical cap, we can replace μ_0 by the effective contact angle θ_{eff} ($= \pi - \mu_0$). It is also convenient to replace R by R_f using Eq. 3.27. Then, with Eq. 3.61, we get the $\dot{q}'$ for a spherical cap bubble:

$$\dot{q}' = \frac{1}{2}\rho_v h_{lv} F\left(\theta_{eff}\right) R_f \frac{dR_f}{dt} \tag{3.65}$$

Eq. 3.65 gives a relationship between the movement of the triple-contact line and the evaporation rate. $F\left(\theta_{eff}\right)$ is given in Eq. 3.48. Figure 3.41 shows a plot of F for reference.

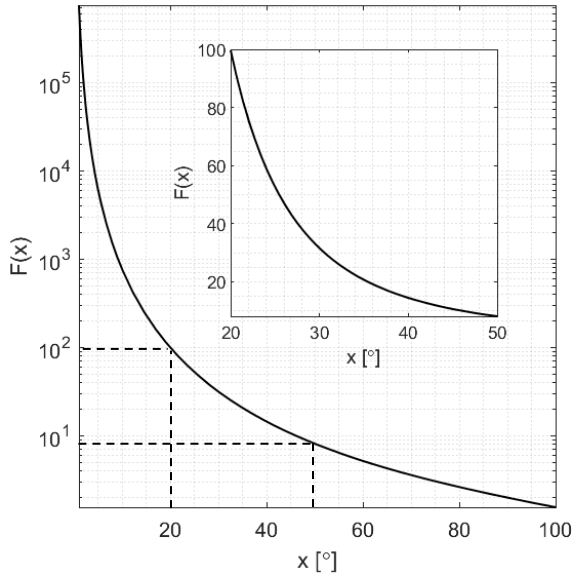

Figure 3.76. Plot of $F(x)$ for x between 0° and 100° using Eq. 3.48. The inner plot shows $F(x)$ with linear axes.

Interestingly, when the bubble growth follows the asymptotic trend dictated by heat-transfer controlled growth, i.e., $R_f = B_f\sqrt{t}$, then $\dot{q}'$ becomes time-independent since:

$$R_f \frac{dR_f}{dt} = \frac{{B_f}^2}{2} \neq f(t) \tag{3.66}$$

It is important to note that Eq. 3.65 provides an estimate of the evaporative heat removal rate, but does not tell where along the bubble interface the vaporization occurs. Temperature measurements at the bubble triple contact line or some elements of analysis could justify the assumption of the triple contact line evaporation considered here (in Eq. 3.60). In this work, we use an analysis done by other research groups to explain and justify this assumption of triple contact line evaporation.

From a modeling perspective that we will develop later on, it is convenient to consider the time-averaged of $\dot{q}'$ during the bubble growth. By integrating Eq. 3.65 between the time of nucleation ($t = 0$) and the time required to reach the maximum bubble radius (i.e., the growth time $t = t_g$), we get,

$$\langle \dot{q}' \rangle = \frac{1}{2}\rho_v h_{lv} \frac{1}{t_g} \int_0^{t_g} F(\theta_{eff}) R_f \frac{dR_f}{dt} dt \tag{3.67}$$

We saw that θ_{eff} stays relatively constant during the growth, and therefore $F(\theta_{eff})$ can be removed from the integral, so we have,

$$\langle \dot{q}' \rangle = \frac{1}{4}\rho_v h_{lv} F(\theta_{eff}) \frac{{R_{f,lo}}^2}{t_g} \tag{3.68}$$

Eq. 3.68 gives a relationship between the triple contact line evaporation $\langle \dot{q}' \rangle$, the bubble footprint radius at lift-off $R_{f,lo}$, the growth time t_g and the effective contact angle θ_{eff} during growth. $\langle \dot{q}' \rangle$ does not depend on the expression of $R_f(t)$, but only on its last point $R_{f,lo} = R_f(t_g)$. In the specific case of $R_f = B_f\sqrt{t}$, $\dot{q}'$ is time-independent (see Eq. 3.66), and therefore is equal to $\langle \dot{q}' \rangle$ at any time.

Figure 3.42 shows the values of $\dot{q}'$ ($= \langle \dot{q}' \rangle$) using Eq. 3.65 and 3.66 for each of the bubbles listed in Tables 3.1 and 3.2. $\dot{q}'$ does not appear to depend on the wall superheat over the range of temperature for which data is available. No effect of the inclination angle is visible either. The measured average value is about ~4.9 W/m with a scattering of ± 0.9 at 1-σ.

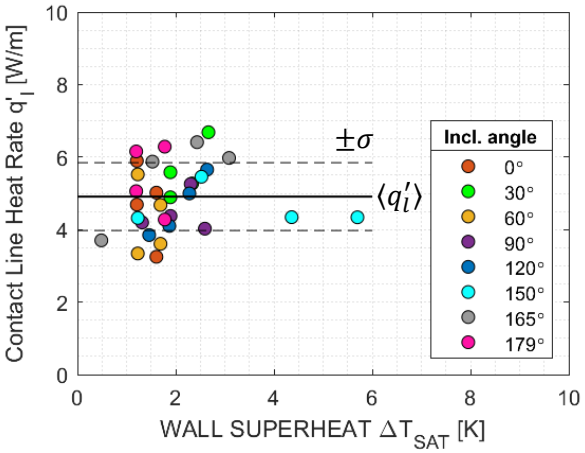

Figure 3.77. Contact line evaporation evaluated based on Eqs. 3.65 and 3.66 and the bubbles analyzed in Table 3.1 and 3.2.

Figure 3.43 shows another representation of the data shown in Figure 3.42, with $\dot{q}'$ plotted against the volumetric growth modulus B_v. Using Eqs. 3.28, 3.52 and 3.65, we can show that introducing B_v in the expression of $\dot{q}'$ yields to the following expression,

$$\dot{q}' \propto \frac{1}{P}\frac{dV}{dt} = \frac{B_v^3}{B_f} \tag{3.69}$$

With P the triple contact line length and V the volume of the bubble. Figure 3.43 shows that accounting only for the change in B_v between the different bubbles analyzed allows to grasp most of the difference in the values of $\dot{q}'$. The black highlight shows a fitting power law trend as $\dot{q}' \propto {B_v}^2$. We can reasonably expect $\dot{q}'$ to go to 0 for an infinitely small growth rate, i.e., when dV/dt goes to 0. The growth of the footprint should also get infinitely small, i.e., B_f goes to 0 as well, but we can see that with the difference of exponents between the numerator and denominator, $\dot{q}'$ then goes to 0.

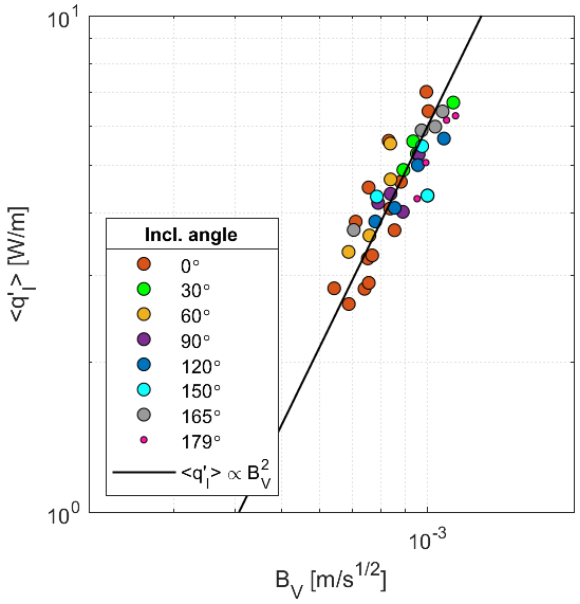

Figure 3.78. Plot of the triple-contact line evaporation rate $\dot{q}'$ against the volumetric growth modulus (B_v).

The formulation proposed in Eqs. 3.65 and 3.68 provides a convenient way to estimate the triple contact line evaporation, however it doesn't provide a physical explanation for such evaporative heat transfer. The proposed formulations leverage experimental observation from which we could make some reasonable assumptions. Namely, we assumed that:

- Most of the evaporative heat transfer occurs near the contact line based on the observations of effective angle consistently much larger than the equilibrium contact angle expected from nitrogen on sapphire-ITO;
- The shape of uncoalesced bubbles appears self-similar during growth based on the observation of constant effective angle throughout bubble growth;

Uncoalesced bubble stays mostly spherical, based on the evaluation of the Bond and Weber number and the observation of constant effective contact angle.

3.2.2.2. Macroscopic justification

Several authors have proposed analytical estimate of the evaporative heat transfer at the triple-contact line while studying highly wetting fluids. Nikolayev and Beysens [86] proposed a macroscopic model which evaluate the deformation of the bubble interface resulting from vapor recoil through a surface minimization calculation. Stephan and Hammer [67] and later on Raj et al. [68] proposed another model, microscopically relating the evaporation heat rate at the triple contact line to the apparent contact angle of the bubble. The model introduces a slightly more complex mechanism, in which the strong evaporation at the triple contact line is permitted by a capillary flow on a microscopic scale at contact line of the bubble. Both studies deal with superwetting fluid, high pressure water in the case of Nikolayev and Beysens, and R-114 for Stephan and Hammer. While both studies have different approach to the problem and leads to different results, they both relate the large bubble footprint found underneath bubbles of superwetting fluid to a strong evaporation occurring near the triple contact line. The two models are presented below and some of their outputs arecompared to our experimental data in nitrogen boiling.

The model of Nikolayev and Beysens [86] is particularly interesting as it proposes a simple explanation to the movement of the triple contact line, allowing to reconciliate the observations of large dry spot underneath bubbles in normally superwetting fluids (i.e., $\theta_{eff} \gg \theta_Y$). Figure 3.44 shows a schematic of the modeled bubble used by these authors.

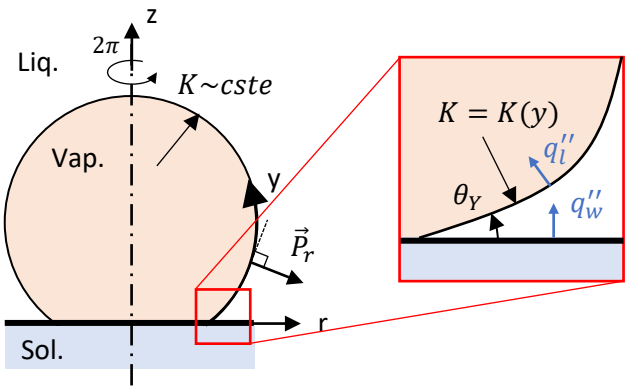

Figure 3.79. Schematics of bubble growth following Nikolayev et Beysens [19] vapor recoil model.

The bubble is assumed in mechanical equilibrium, i.e., that the free energy associated with the bubble interface is minimized at any time (and values of bubble volume), throughout the growth. Using this assumption, the authors deduced two relationships leveraging the work of Finn [85]. The first relationship corresponds to the mechanical equilibrium at the liquid-vapor interface,

$$K\sigma_{lv} = \lambda + P_r(y) \tag{3.70}$$

With $P_r(y)$ the pressure recoil at the curvilinear coordinate y, K the mean curvature of the interface and λ the Lagrange multiplier. The Lagrange multiplier λ is introduced mathematically to find the solution of the free energy minimization problem. In this particular problem, λ corresponds physically to the bubble internal overpressure in absence of the vapor recoil term. The second relationship gives the Young's equation, which corresponds to the mechanical equilibrium condition at the triple contact line.

The recoil pressure P_r is directly related to the rate of liquid evaporation at the bubble interface and therefore the heat-flux at the interface with the assumption that only latent heat is transferred across the liquid-vapor interface. From mass and momentum conservation at the liquid-vapor interface, the recoil pressure is given by,

$$P_r = \left(\frac{q_l''}{h_{lv}}\right)^2 \nu_{lv} \tag{3.71}$$

With $\nu_{lv} = \rho_v^{-1} - \rho_l^{-1}$. A major difficulty is to evaluate q_l'' from q_w''. The final solution proposed by Nikolayev and Beysens [19] is given by,

$$P_r = -C * \ln\left(\frac{y}{L}\right) \exp\left(-\left(\frac{y}{aL}\right)^2\right) \tag{3.72}$$

With,

$$C = \frac{4N_r}{aL\sqrt{\pi}} * \frac{1}{\gamma + \ln 4/a^2} \tag{3.73}$$

And,

$$N_r \sim \frac{{q_w''}^2 R}{a\rho_v {h_{lv}}^2 \sigma_{lv}} \tag{3.74}$$

γ is the Euler's constant, aL is a distance from the interface from the triple contact line to the curvilinear coordinate where most of the heat transfer is occurring. L is half contour of the bubble, i.e., the distance between the contact line and the apex, and N_r is a quantity which scales the overall vapor recoil (see Ref. [86] for additional details). This solution comes from solving the steady-state temperature field, assuming

conduction only, in the liquid represented as a two-dimensional semi-infinite domain where the solid interface is normal to the liquid-vapor interface with imposed wall heat flux.

Figure 3.45 shows the solution of Eq. 3.70 for different values of N_r. Since N_r is imposed, the bubble shape doesn't depend on its size. In Figure 3.45, each bubble has a volume equal to 1. As N_r increases, the bubble footprint radius also increases, while maintaining a contact angle equal to θ_Y. A value of ½ for N_r corresponds to an effective contact angle θ_{eff} of roughly 30°, typ. of our experimental observation at low wall superheat. Figure 3.46 shows the capillary pressure along the bubble interface for a value of N_r of ½. The strong evaporation near the contact line results in the local overpressure shown in Figure 3.46 and the local change of curvature as shown in Figure 3.45.

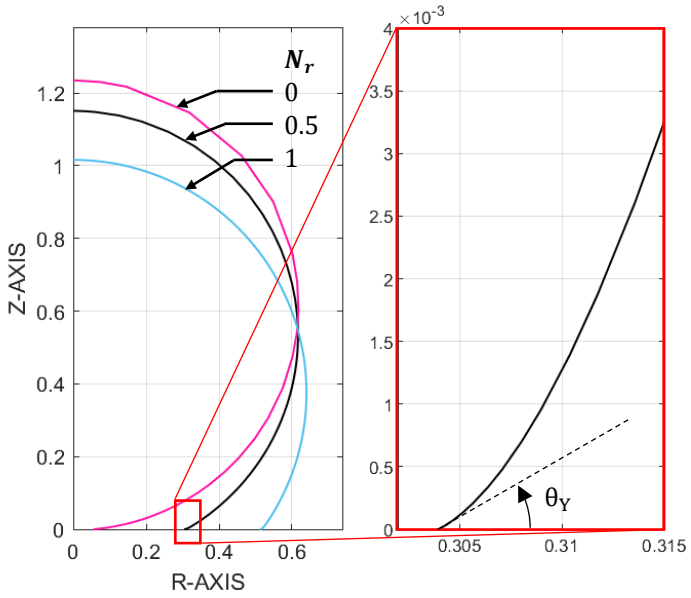

Figure 3.80. Plot of the bubbles contour, solution of Eq. 3.70 with N_r equal to 0, 0.5 and 1, θ_Y equal 5°, a equal 10^{-2} and nitrogen properties at 480 kPa. All bubbles have the same volume, equal to 1.

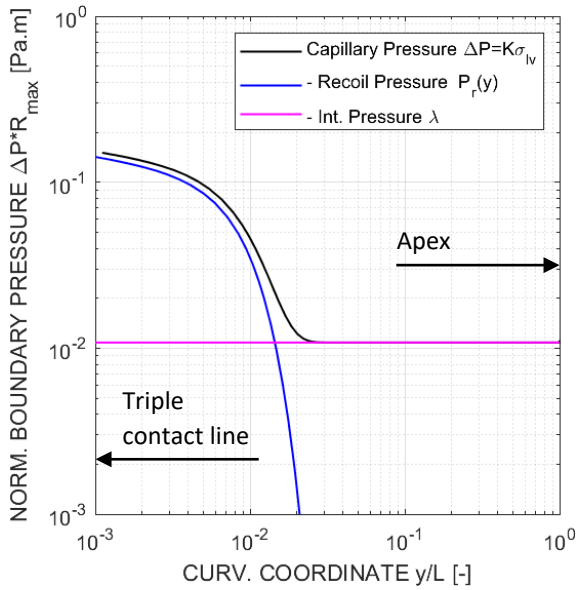

Figure 3.81. Plot of the pressure terms from Eq. for N_r equal to 0.5, with the same properties and parameters than used in Figure 3.45.

The value of a was fixed to 0.01 by Nikolayev and Beysens [86]. Experimentally, we don't really know the exact bubble shape as we measure only R_o and R_f. The knowledge of these radii is not sufficient to evaluate $\dot{q}'$, which is why we had to assume a spherical cap bubble in the estimation of $\dot{q}'$ using experimental data. Nikolayev et Beysens introduced the parameter a to determine how fast along the curvilinear coordinate y the evaporation heat flux decays spatially to circumvent the need to use more complicated analytical expressions of the evaporative heat flux at the interface $q_l''(y)$. Without drastic assumption, the problem of finding the heat flux at the wall and at the bubble interface is not trivial as the heat transfer at the bubble interface depends on its shape and vice-versa. We can note that a is expected to depend on the thermal properties required to solve the heat transfer problem, i.e., at least the thermal diffusivity of the liquid as well as its effusivity. Later on, Nikolayev et al. [21] proposed a numerical solution of the heat transfer problem of relating $q_w''(r)$ and $q_l''(y)$ with some approximations. This problem is beyond the scope of this study and will not be detailed furthermore as it. However, we can show that the spherical cap approximation is fairly good even at large values of a.

Equation 3.65 can be written differently by separating the factors depending on time and the factors depending on the bubble geometry. This can be done using the assumption previously made that bubble shape is self-similar during growth, i.e.,

$$V = F(t)^3 * V^* \text{ and } P = F(t) * P^* \tag{3.75}$$

Then, Eq. 3.65 becomes,

$$\dot{q}' = 3\rho_v h_{lv} F \frac{dF}{dt} * \frac{V^*}{P^*} \tag{3.76}$$

Figure 3.47 shows the values of V^*/P^* of a bubble satisfying Eq. 3.43 and 3.45 with the constraint of θ_{eff} equal 30° (i.e., R_f/R_o equal ½) and R_o equal 1 for different values of a. Figure 3.48 shows the contours of the bubble for the different value of a. The values of V^*/P^* are compared to the value V^*/P^* given by spherical cap assumption,

$$V^*/P^* = \frac{1}{6} {R_f}^2 F(\theta_{eff}) \sim 1.316 \tag{3.77}$$

With F given by Eq. 3.41.

Figure 3.47 shows that V^*/P^* stays within few percent of the value given by the spherical cap assumption for values of a up to 1. By propagating the uncertainty of a within Eq. 3.76, we get that the uncertainty on $\dot{q}'$ from the assumption on the parameter a (i.e., on the sphericity of the bubble) is at most 10%, according to the model of Nikolayev and Beysens.

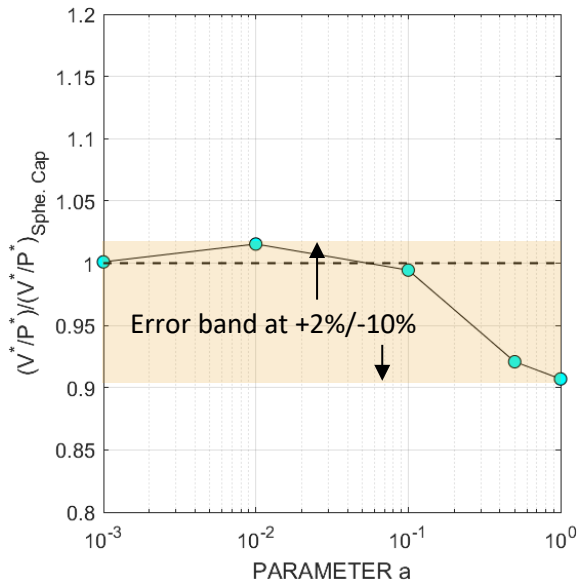

Figure 3.82. Plot of V^*/P^* for different value of a. The value at a equal to 10^{-3} corresponds to the spherical cap ($N_r = 0$, $\theta_Y = 30°$).

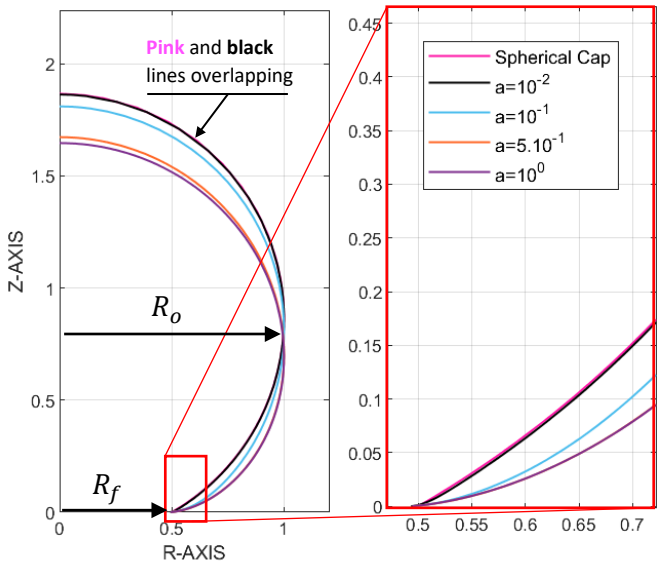

Figure 3.83. Plot of the bubbles contour, solution of Eq. 3.43 for different value of a with the constraints θ_Y equal 5° and θ_{eff} equal 30°, and nitrogen properties at 480 kPa. All bubbles have the same radii R_o and R_f, equal to 1 and ½ respectively.

Using Eq. 3.74, and the value of N_r required to match our observation of effective contact angle, we can estimate the evaporative heat rate at the triple contact line. The relationship between q''_w and $\dot{q}'$ is given by,

$$\dot{q}' = q''_w aL \cos\theta_Y \sim q''_w aL \tag{3.78}$$

Therefore,

$$\dot{q}' \sim \sqrt{N_r a^3 R \pi^2 \rho_v {h_{lv}}^2 \sigma_{lv}} \tag{3.79}$$

Using numerical values proposed by Nikolayev (a~10^{-2}), the value of Nr necessary to have an effective contact angle observed experimentally (N_r~0.5 for having θ_{eff}~30°), a typical bubble radius of 100 µm, and the physical properties of nitrogen, we obtain $\dot{q}'$ of about 1.3 W/m. This result matches in order of magnitude the values calculated from experimental measured.

3.2.2.3. Microscopic justification

The contact line evaporation modeled by Nikolayev et al. and presented in Section 3.2.2.2 explains the large values of effective contact angle through the presence of a vapor recoil force due to strong evaporation at

the triple contact line. The interface shape is evaluated by minimizing the surface energy of the entire bubble. However, the model proposed by Nikolayev does not resolve the evaporation near the triple contact line. The solution of the heat equation should naturally diverge as we go closer and closer to the contact line (see Eq. 3.72 with $\lim_{y\to 0} \ln y/L \to -\infty$).

Several research groups have proposed a microscopic description on the evaporative heat transfer at the triple contact line with some variations (see Refs. [67, 68, 87 and 88]). In this section, we will leverage the model reported by Raj et al. [68] as the model was successfully tested on a FC-72, a superwetting fluid with physical and thermal properties not far from liquid nitrogen. . Figure 3.49 shows the schematics of the model proposed by Raj et al. [68]. Three distinct regions are theorized in the model: an absorbed film region, a micro-region and a macro-region. Underneath the bubble ($\xi < 0$), Van der Waals forces increases locally the pressure in the surrounding nitrogen molecules forming a nanometric layer, which is maintained in liquid state. This nanometric layer of liquid is called the absorbed film. As the we move further to the edge of the bubble footprint and enter the microregion ($\xi \in [0, \xi_s]$), the increase in curvature results in an increase of the liquid thickness underneath the bubble. The decrease of the adhesive pressure as the liquid layer thickens allows the liquid of the evaporate, while the liquid remains thin enough to produce a significant heat transfer. Further away, the larger and larger thickness of the liquid layer results in a drop of the heat transfer through the liquid layer. This last region is called the macro-region. Unlike the model shown in Section 3.2.2.2, the model presented here focus on solving the heat transfer (in particular the heat flux at the wall near the triple contact line, q''_w) and the bubble interface shape only in the micro-region (i.e., ξ_s which corresponds to the size of the region with strong liquid evaporation and the apparent contact angle θ_{app}). Both absorbed film and macro-region are introduced in the model as boundary conditions.

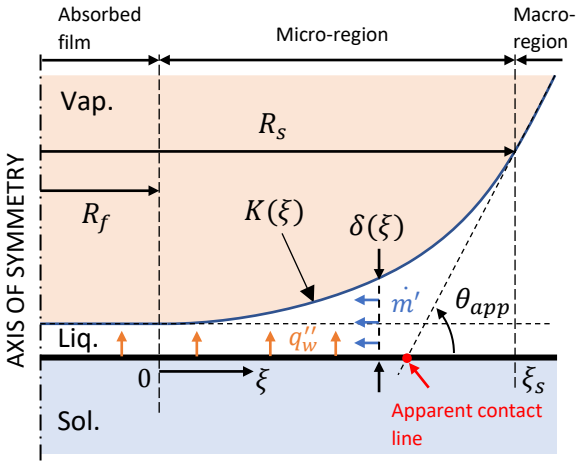

Figure 3.84. Schematics of Raj's [68] triple contact line evaporation model.

To obtain the wall heat flux in the microregion q''_w, Raj et al. [68] solved the 1-D heat equation in the liquid layer of the microregion, taking into account the conduction in the liquid layer (with a thermal resistance δ/k_l with k_l the conductivity of liquid nitrogen) and the interfacial resistance R_i. The difference of temperature across the liquid layer is equal to the wall superheat (ΔT_{SAT}) with the addition superheating due to the curved liquid-vapor interface ($\frac{T_{SAT} p_c}{h_{lv}\rho_l}$) with p_c the capillary pressure. The heat flux q''_w, is then given by,

$$q''_w = \frac{T_w - T_{SAT}\left(1 + \frac{p_c}{h_{lv}\rho_l}\right)}{\frac{\delta}{k_l} + R_i} \tag{3.80}$$

With the interfacial resistance R_i given by,

$$R_i = \frac{T_{SAT}\sqrt{2\pi R T_{SAT}}}{\rho_v {h_{lv}}^2}\frac{2-f}{f} \tag{3.81}$$

And p_c given by,

$$p_c = \sigma_{lv} K + \frac{A}{\delta^3} - \left(\frac{q''_w}{h_{lv}}\right)^2 \left(\frac{1}{\rho_v} - \frac{1}{\rho_l}\right) \tag{3.82}$$

With K the curvature at the liquid vapor interface which can be written using differential geometry results as a function of δ and $\frac{d\delta}{d\xi}$. Finally, an equation models the inward flow within the liquid layer of the microregion assuming that the liquid flow behaves like a laminar boundary layer with no stress at liquid-vapor interface,

$$\dot{m}'' = \frac{\partial \dot{m}'}{\partial \xi} = -\frac{1}{3\nu_l}\frac{d}{d\xi}\left(\delta^3 \frac{dp_c}{d\xi}\right)\left(= \frac{q''_w}{h_{lv}}\right) \tag{3.83}$$

A last equation is formulated by relating the mass flow rate $\dot{m}''$ to q''_w by assuming that all the heat transferred from the heated wall is used for liquid evaporation. Note that the apostrophe of $\dot{m}'$ corresponds to the derivative along the dimension not accounted for in the model, i.e., tangential to the triple contact line.

The problem yields a fourth order differential equation that can be recast into a system of 4 coupled differential equations of 1st order with δ, $d\delta/d\xi$, p_c and Q (defined as $\int_0^\xi q''_w\, d\xi$) as unknown. The final equations are given in the publication of Raj et al [68]. The solution of the problem is obtained numerically using a finite difference discretization with a 4th order Runge-Kutta method. More details on the resolutions

of the equations are given in their paper. The initial conditions were slightly modified compared to the original conditions to facilitate the convergence of the solution. The initial condition of $d\delta/d\xi$ is normally 0, as the absorbed film is expected to have a constant thickness. Such condition often makes the solution to diverge toward an unphysical solution, in particular with $d\delta/d\xi$ becoming negative. Instead, we force $d\delta/d\xi$ to stay positive by applying a positive initial condition. The initial condition is then replaced by,

$$\left.\frac{d\delta}{d\xi}\right|_{\xi=0} = 0.1 \tag{3.84}$$

Lower values (i.e., below ~0.08) or larger values (above ~0.2) prevents the numerical solution to converge. Figure 3.50 shows a comparison between Raj et al.'s solution (in red) and our numerical solution (in black) for the heat flux q''_w in the micro-region with FC-72. A slight shift of the heat flux peak toward the left (i.e., toward the absorbed film) can be seen. This is likely due to the change in the initial condition of $d\delta/d\xi$.

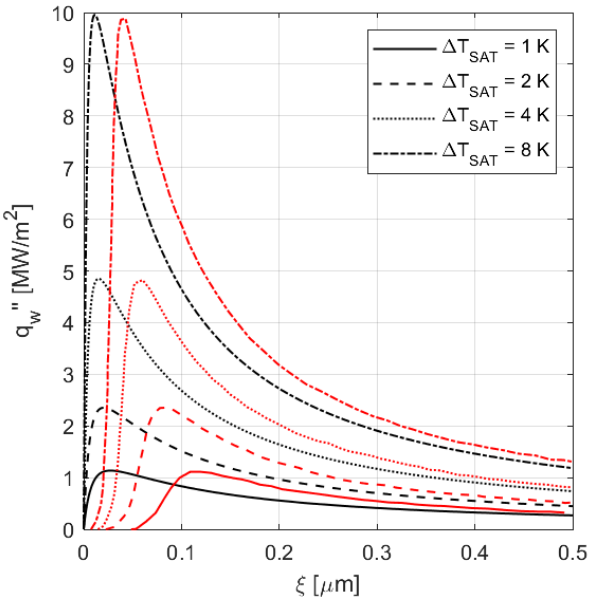

Figure 3.85. Comparison between the solution of q''_w obtained for FC-72 from Ref. [22] (in red) and our numerical solution (in black). Each line style corresponds to a different value of ΔT_{SAT}.

The model of Raj et al. [68] can be used to evaluate the apparent contact angle. Figure 3.51 shows a comparison between the apparent contact angle from our numerical solutions (shown by black markers), and Raj's solution (shown by the red line). Again, there is a slight difference between our numerical solution and the results published by Raj et al. [68]. However, the trend of θ_{app} with the wall superheat ΔT_{sat} is the same and the values differs only by couple degrees.

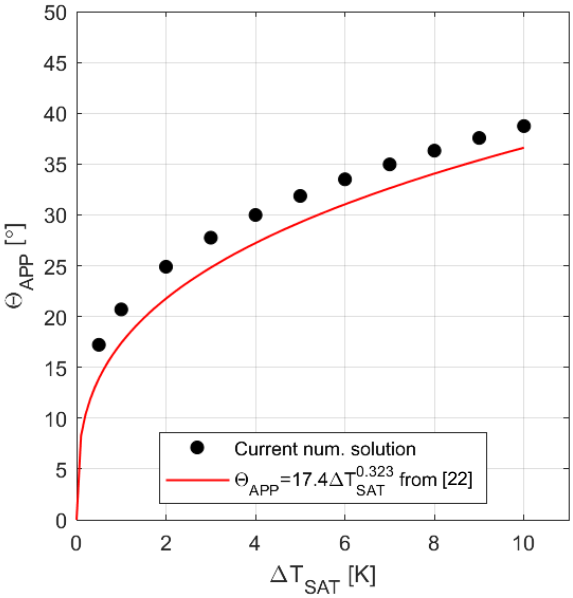

Figure 3.86. Comparison between the solution of θ_{app} obtained for FC-72 at different values of wall superheat from Ref. [68] (in black) and our numerical solution (in red).

The model can also be used to evaluate the effective contact angle, which was done in the original paper. The effective contact angle θ_{eff} can be evaluated using Eq. 3.27 and the following geometrical relationship,

$$R_f = R_s - \xi_s \tag{3.85}$$

With ξ_s the length of the microregion and R_s defined in Figure 3.49 and evaluated using,

$$R_s = R_o \sin\left(\tan^{-1}\left(\delta'(\xi_s)\right)\right) \tag{3.86}$$

R_o is the optical radius of the bubble, defined in the model by the bubble curvature in the macro-region, which is used as a boundary condition at $\xi = \xi_s$,

$$R_o = \frac{2}{K(\xi_s)} \tag{3.87}$$

Figure 3.52 shows the effective contact angle solution of the Raj et al.'s model for liquid nitrogen for a wall superheat of 2 K and 4 K and different values of bubble optical radius R_o. The Hamaker constant is set to the same value than FC-72 (i.e., $2*10^{-21}$) and the accommodation coefficient associated with the interface thermal resistance is set to 1 for simplification. The model prediction shows that the effective contact angle

is relatively insensitive to the bubble size, evaluated by R_o, which is consistent with our observations that the effective contact angle doesn't change significantly during the growth of bubbles.

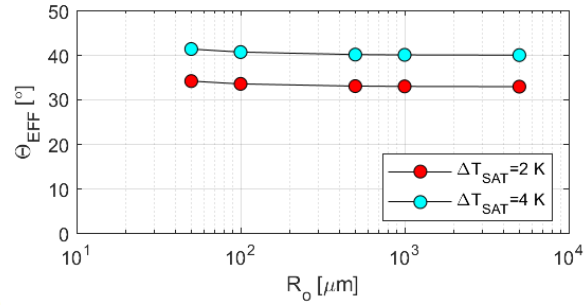

Figure 3.87. Plot of the effective angles for different values of bubble radius (equiv. to the interface curvature in the macro-region) at a wall superheat of 2 K and 4 K.

Figure 3.53 shows a plot of effective contact angle measured for bubbles listed in Tables 3.1-.3.2 with colored markers and compare it to the numerical solution obtained from Raj et al.'s model (in black). The best fit of our experimental data is shown by a red line. As previously, the contact angles measured on a surface inclined at 179° (shown by smaller markers) are excluded from the fit as boiling does not appear to reach a steady-state behavior, and therefore the measured average wall superheat might by off by few degrees from the superheat when the bubbles are observed.

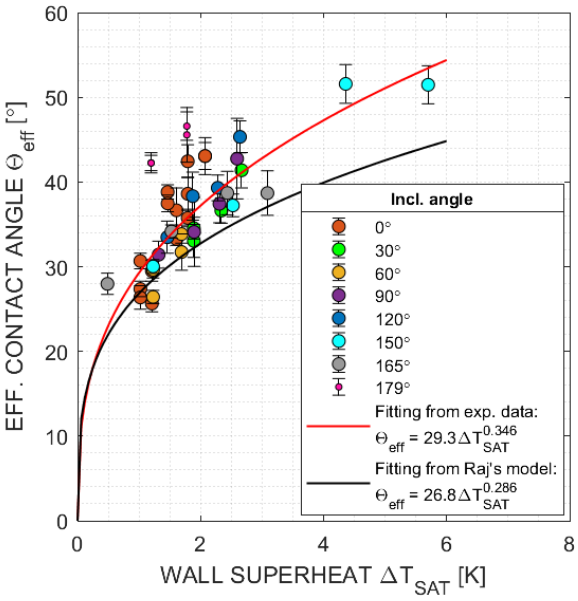

Figure 3.88. Comparison between the effective angle measured for each bubble listed in Tables 3.1-3.2 (in colored markers), the best fit (in red) and the numerical solution of Raj et al.'s model (in black).

The value of effective contact angles and its trend with wall superheat observed experimentally (shown by markers and the red line) and obtained from the numerical solution of Raj et al.'s model (black line) are similar. Both numerical and experimental data show a dependance as $\theta_{eff} \propto \Delta T_{sat}{}^{n}$ with an exponent n around 0.3, and values of θ_{eff} ranging between 25° to 50° for a wall superheat between 1 K and 6 K. However, the numerical solution appears to underestimate the values of θ_{eff} measured experimentally. This underestimation is larger at higher wall superheat due to lower exponent n given by the numerical solution.

Figure 3.54 shows the wall heat flux in the micro-region for liquid nitrogen at wall superheat of 2, 4 and 6 K. The profile of heat flux along the coordinate is similar to the results obtained in FC-72. The adhesive pressure decreases for increasing ξ resulting in more and more liquid evaporating at the bubble interface, visible by the increasing trend of q''_w. When the thickness of liquid layer δ gets larger, the thermal resistance between the heated wall and the bubble interface increases resulting in a decrease of the evaporative heat flux (seen by the decreasing slope of q''_w in Figure 3.54). However, for a same wall superheat, significantly larger values of heat flux are found in liquid nitrogen (~4.7 MW/m^2 in FC-72 compared to ~ 73 MW/m^2 in LN_2 at 4 K). FC-72 and LN_2 are remarkably similar in terms of physical and thermal properties. It is not clear yet why there should be such a large difference in the micro-region heat flux.

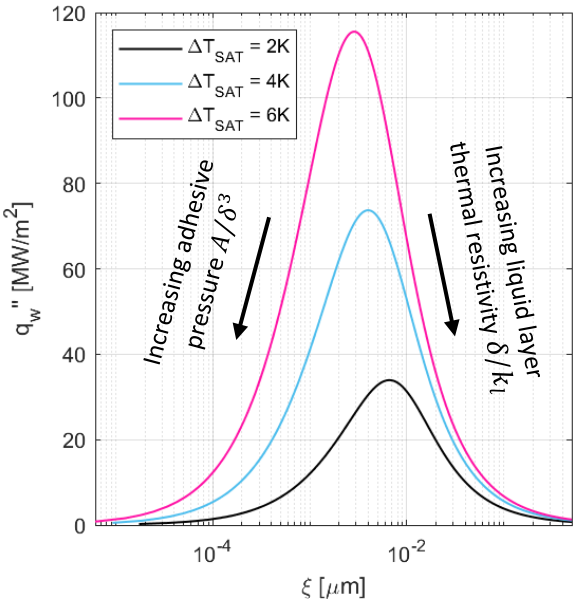

Figure 3.89. Plot of the numerical solution of the wall heat flux $q''_w(\xi)$ for different wall superheat by solving Eqs. 3.80 to 3.83 with nitrogen thermal properties.

Figure 3.55 shows the integral Q of the q''_w along ξ, i.e., $\int_0^{\xi} q''_w(\xi')d\xi'$. The asymptotic value of Q corresponds to evaporation heat rate $\dot{q}'$ at the triple contact line that we evaluated experimentally at different values of wall superheat. Both the numerical solution and the experimental data show similar order of magnitude, i.e., 1-10 W/m, with a slight underestimation of $\dot{q}'$ from the numerical solution. The numerical solutions show an increase of $\dot{q}'$ with temperature, which was not seen in the experimental data. However, it would be difficult to draw conclusion due to the relatively small batch of experimental bubbles that were analyzed (i.e., 42 bubbles) and the uncertainty on the actual local wall temperature when each of the bubble grows, which have approximated by the surface-averaged wall temperature.

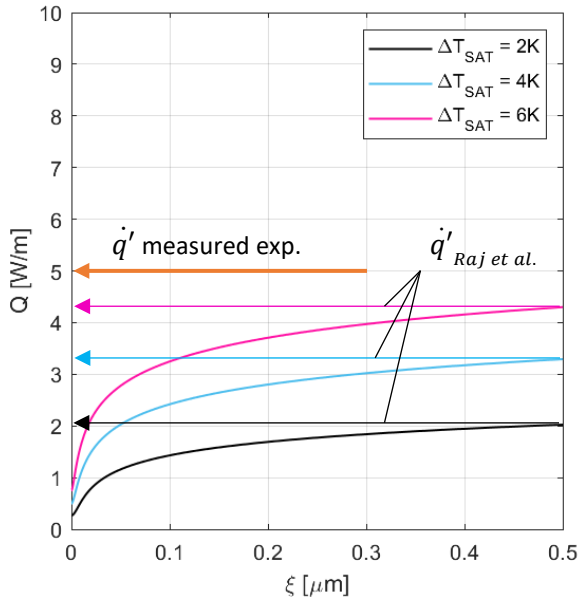

Figure 3.90. Integral contact line evaporation heat rate obtained from numerical solution of Raj et al.'s model for different values of wall superheat shown in black (2 K), blue (4 K) and pink (6 K). The average value of evaporative heat found experimentally from the data plotted in Figure 3.42 is shown in orange.

3.3. Summary of the chapter

In this chapter we analyzed the characteristics of individual nitrogen bubbles on an inclined heating surface at various wall superheat.

We showed that bubbles grow in a heat transfer controlled regime. A characteristic trend of radius growth in $\sqrt{t}$ was shown on the analysis of the optical and footprint radii of 42 selected individual bubbles as well as the statistical analysis of footprint radii of all uncoalesced bubbles detected on the heated surface from phase-detection. From the analysis of the 42 selected bubbles, a proportional relationship between the footprint radius and optical radius was found throughout their growth. The proportionality was

mathematically represented as an effective contact angle, corresponding to the contact angle that the bubbles would have if they were spherical caps. The proportionality between the footprint radius and optical radius leads a constant effective contact angle during the bubble growth. Effective contact angles range from 20° to 50°, and depend on the wall superheat. No effect of the inclination angle was found. The values of effective contact angle were significantly larger than the observed equilibrium contact (<10°, see Chapter 2) resulting in larger bubble footprint than expected. However, the values of effective contact angle, its stability during bubble growth, and its trend with temperature can be all explained by a strong evaporation at the triple contact line according to the model developed by Raj et al. [68].

We showed that bubbles do not reach significant size before coalescing resulting in buoyancy being negligible in determining their shape. In other words, uncoalesced bubbles are expected to have the shape of a spherical cap. This was shown by the measurement of size distribution of bubbles (>10^4 bubbles) before they coalesce, and by comparing the growth modulus associated with footprint and optical radii of 42 bubbles obtained for different inclination angles of the heating surface. After comparing the trajectory of bubbles and their growth moduli measured at different surface inclination angles, we could show that the effect of sliding on bubble growth is negligible if existing at all.

4. SYSTEMIC EFFECT OF BUOYANCY ON NUCLEATE BOILING HEAT TRANSFER

In the Chapter 3, we analyzed the characteristics of uncoalesced bubbles. In this chapter we will focus our analysis on how the collective behavior of bubbles on the boiling surface relate to the boiling heat transfer coefficient. From a modelling point of view, the interest is to provide measurement and understanding of several boiling parameters, e.g., nucleation site density, nucleation frequency, dry area fraction and liquid-vapor-solid triple contact line density. These boiling parameters depends on numerous variables, but foremost on how all bubbles on the heated surface interact with each other. We will see that bubbles coalescence plays a critical role in the degradation of boiling heat transfer on inclined surfaces. Using our experimental data, we will provide estimates of the heat flux partitioning, in particular between quenching heat transfer and evaporative heat transfer. Finally, we will discuss how critical heat flux depends on the angle of inclination of the surface.

4.1. Boiling curves

Figure 4.1 shows the boiling curves corresponding to the different cases given in the test-matrix in Chapter 2. The wall temperature and heat flux are averaged over a 5 mm-side square at the center of the active ITO area. All the boiling curves are performed ramping up the heat input up to CHF after preheating for 3 seconds (see Section 2.1.4. for details). The slightly higher initial subcooling on certain curves (e.g., 0º in orange and 60º in yellow) has no influence on the nucleate boiling heat transfer. The boiling curves shows 3 distinct regimes: a single-phase heat transfer regime, a nucleate boiling regime, and a post-DNB regime. Our data points do not cover the single-phase regime and only at the zero-power step (i.e., at zero heat flux), the heated surface is not boiling. The nucleate boiling regime spans at most over 6-7 K, e.g., on a horizontal upward-facing surface (incl. at 0º, shown in orange). All boiling overlaps within a 1 K band during the nucleate boiling regime, and before the inflections of the curves approaching DNB, irrespective of the inclination angle. This observation suggests that the buoyancy is not a dominant factor determining the boiling heat transfer coefficient, at least far enough from DNB. For larger inclinations, in particular past 90º, DNB occurs at lower wall superheat (e.g., see the case at 179º, in pink). These observations trigger two important questions that we will discuss in this chapter: why boiling heat transfer does not appear to be sensitive to buoyancy unless very close to DNB? And why DNB is instead sensitive to the inclination angle, and therefore to buoyancy?

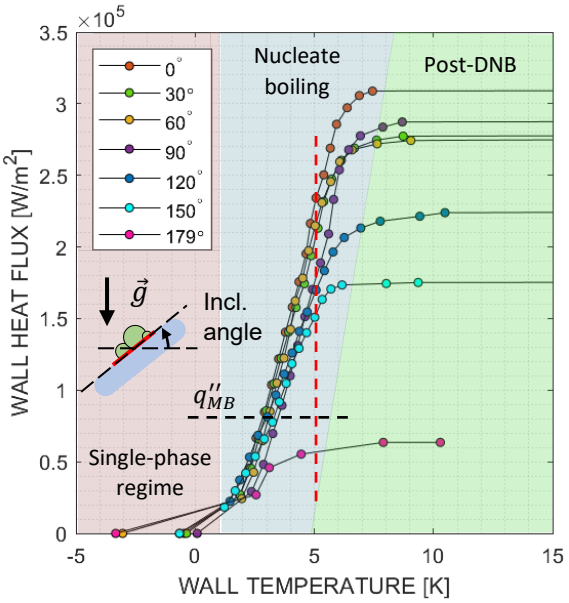

Figure 4.91. Plot of the boiling curves for different inclination angles. The uncertainties on heat-flux and wall temperature are omitted for clarity but are given in Section 2.3.

In pool boiling water at atmospheric pressure, the boiling heat transfer coefficient has been found to be dependent on the inclination angle at sufficiently low heat flux, with the heat transfer improving as the inclination angle increase from 0° (horizontal upward facing) to 175° (see review from Ref. [47]). Above a certain heat flux (corresponding to the so-called Moissis-Berenson transition), the effect disappears. An empirical formulation of this heat flux is given by Moissis and Berenson [89].

$$q''_{MB} = 0.11\rho_v h_{lv}\sqrt{\theta_{eq}}\left(\frac{\sigma_{lv}g}{\rho_l - \rho_v}\right)^{1/4} \tag{4.1}$$

In the case of nitrogen (at 480 kPa, corresponding to our operating conditions), q''_{MB} is about 79.0 kW/m^2 assuming an equilibrium contact angle of 5°, based on our measurement on a sessile droplet (see Chapter 2).

4.2. General aspect of boiling with varying surface inclination angle

A general overview of how nitrogen look like on horizontal and inclined surface is presented below with illustrative phase-detection images. Figure 4.2 shows post-processed images from the phase-detection recordings acquired for different inclination angles of the heating surface and at different wall superheat. As usual, the vapor phase appears in light gray while the liquid appears in dark gray. Below 90°, the phase-detection images appear quite similar in terms of void fraction and bubble diameters. This corroborates the

observation of similarity between the boiling curve in that range of inclination angles. Above 90°, the phase-detection images show the presence of large vapor patches on surface at relatively low wall superheat (e.g., at ΔT_{sat}= ~3 K for an inclination angle of 150°). The presence of vapor patches is even clearer as the inclination angle gets close to 180° (see ΔT_{sat} = ~2 K for an inclination angle of 179°). Several observations can be made from these recordings. Large vapor patches are formed from an agglomeration of smaller bubbles on the heating surface, and typically grow larger at higher inclination angle. These patches are typically mobile, i.e., often slide away from the surface. Qualitatively, the average size of the footprint of bubbles looks visually similar across all inclination angles, which is consistent with our observations done on uncoalesced bubbles in previous chapter (see Chapter 3). Also, as the inclination angle increases past 90°, some boiling instabilities tend to appear, with large vapor patches intermittently forming and swiping the heated surface. An occurrence of it will be analyzed in detail later in this chapter. Due to these instabilities on inclined surface, instantaneous snapshots of the heated surface, as shown in Figure 4.2, do not give necessarily an accurate representation of the boiling heat transfer at all times.

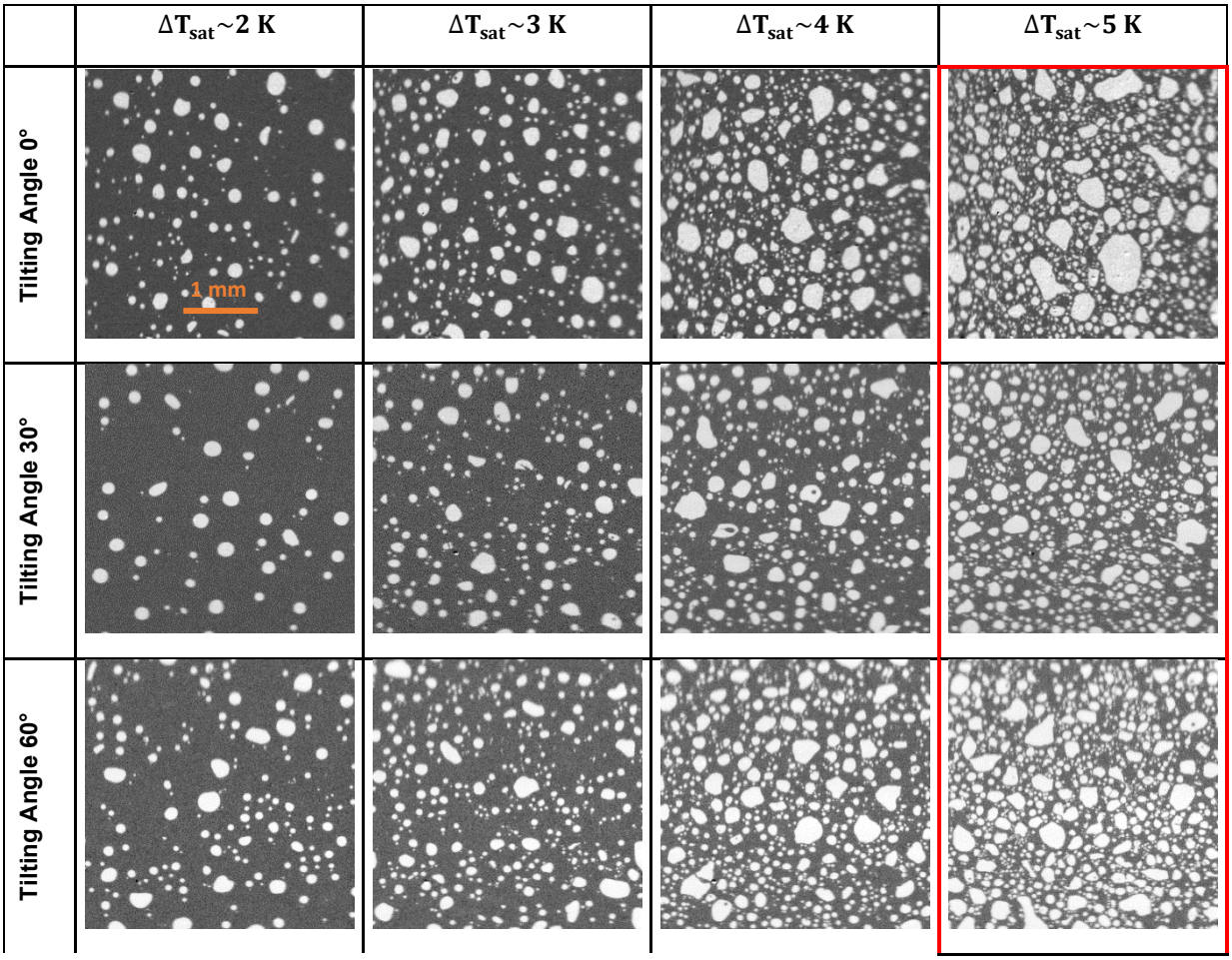

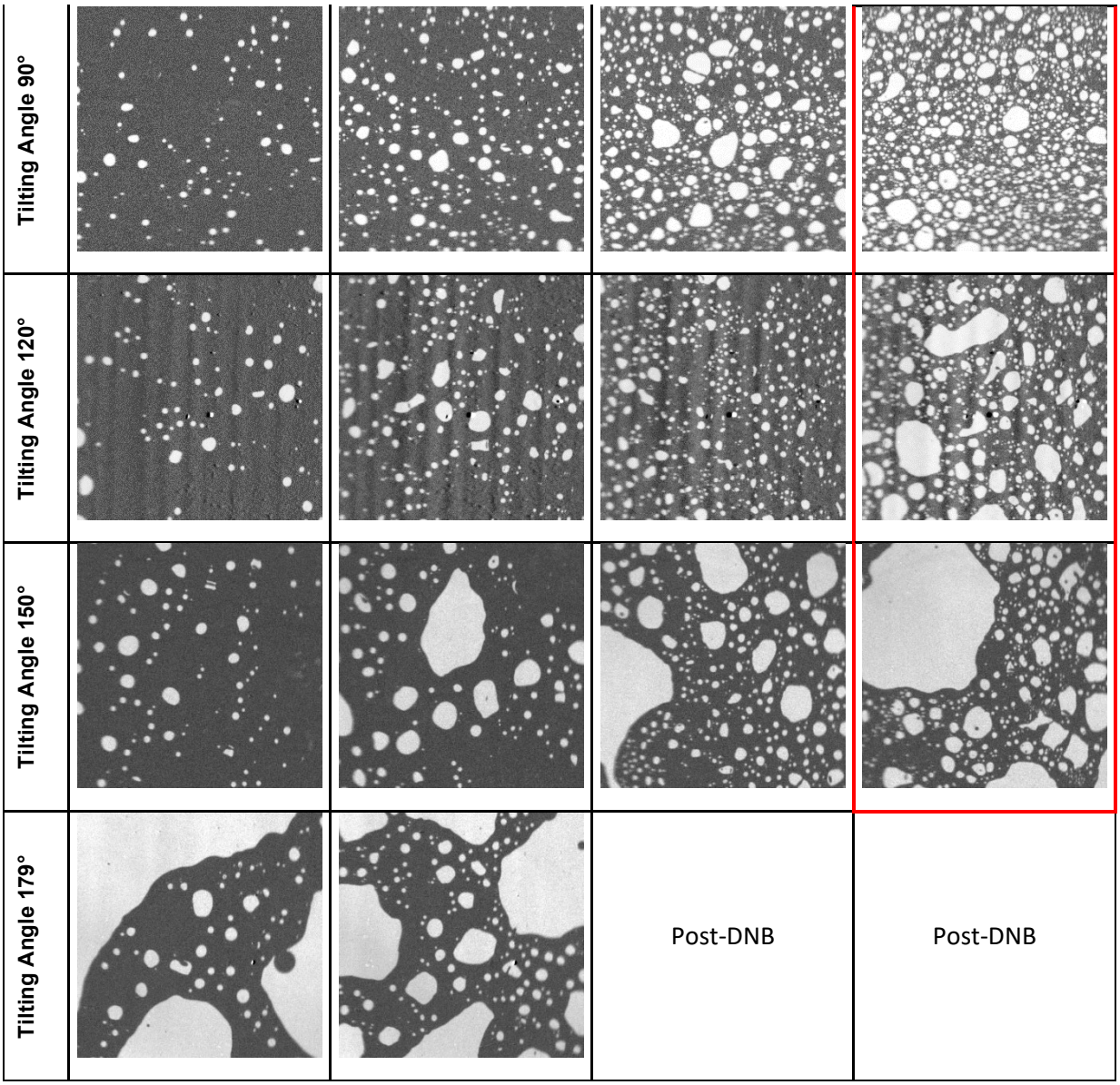

Figure 4.92. Phase-detection images of the boiling surface for different angles of inclination and wall superheat in liquid nitrogen. Liquid nitrogen appears dark grey, while nitrogen vapor appears light grey. All recordings have been acquired at 14,000 fps.

4.3. Contact line density and dry area fraction analysis

The triple contact line density and dry area fraction are critical macroscopic parameters determining in large part the boiling heat transfer. The dry area fraction, noted α_v, is the fraction of the heated surface covered by vapor, and correlates with several aspects of boiling heat transfer, e.g., the number of active nucleation sites or the quenching heat flux, as we will discuss in Chapter 6. It also appears to be a good measure of how far the boiling heat transfer is from DNB [90]. The dry area fraction appears to increase as the inclination angle increases at constant wall superheat. Qualitatively, one can see it by comparing phase-

detection images at a wall superheat of +5 K in Figure 4.2 (framed in red). The red line in Figure 4.1 shows the corresponding iso-temperature of 5 K. This line crosses each the boiling curve closer and closer to the critical heat flux as the inclination angle increases. The triple contact line density, noted l_3'', corresponds to the length of triple contact line (i.e., the apparent line of contact between liquid, vapor and solid) observed per unit surface area of heated surface (note that the triple contact line is measured in m/m^2). The analysis performed in Chapter 3 suggests that most of the evaporative heat transfer occurs at the triple contact line for nitrogen boiling (and in our operating conditions), i.e., $q_{\mathrm{ev}}'' \sim \dot{q}_3' l_3''$. We also showed that the heat rate of evaporation at the triple contact line per unit length of contact line (i.e., $\dot{q}_3'$) does not depend on the wall superheat. Therefore, we expect a proportionality between the evaporative heat flux and the triple contact line density to hold throughout the boiling curves.

Figure 4.3 shows plot of the time-averaged triple contact line density l_3'', on the left and dry area fraction α_v, against the boiling heat flux on the right for the boiling curves shown in Figure 4.1. For each data point represented in Figure 4.3, the dry area fraction and the triple contact line density are measured based on 2000 successive phase-detection images (recorded at 14 kHz) and then averaged. Dots of same color are performed at the same heated surface inclination angle. The error bars indicate the standard deviation observed over the set of 2000 images. The last point shown in the l_3'' plot corresponds the last stable point before DNB. Dry area fraction above ~0.55 and up to 1 are indicative of transition to film boiling. The spreading in the data among tests performed at different inclination angles does not seem to be related to the angle but could be the results of some contaminations of the boiling surfaces or small variations in the processing of the data.

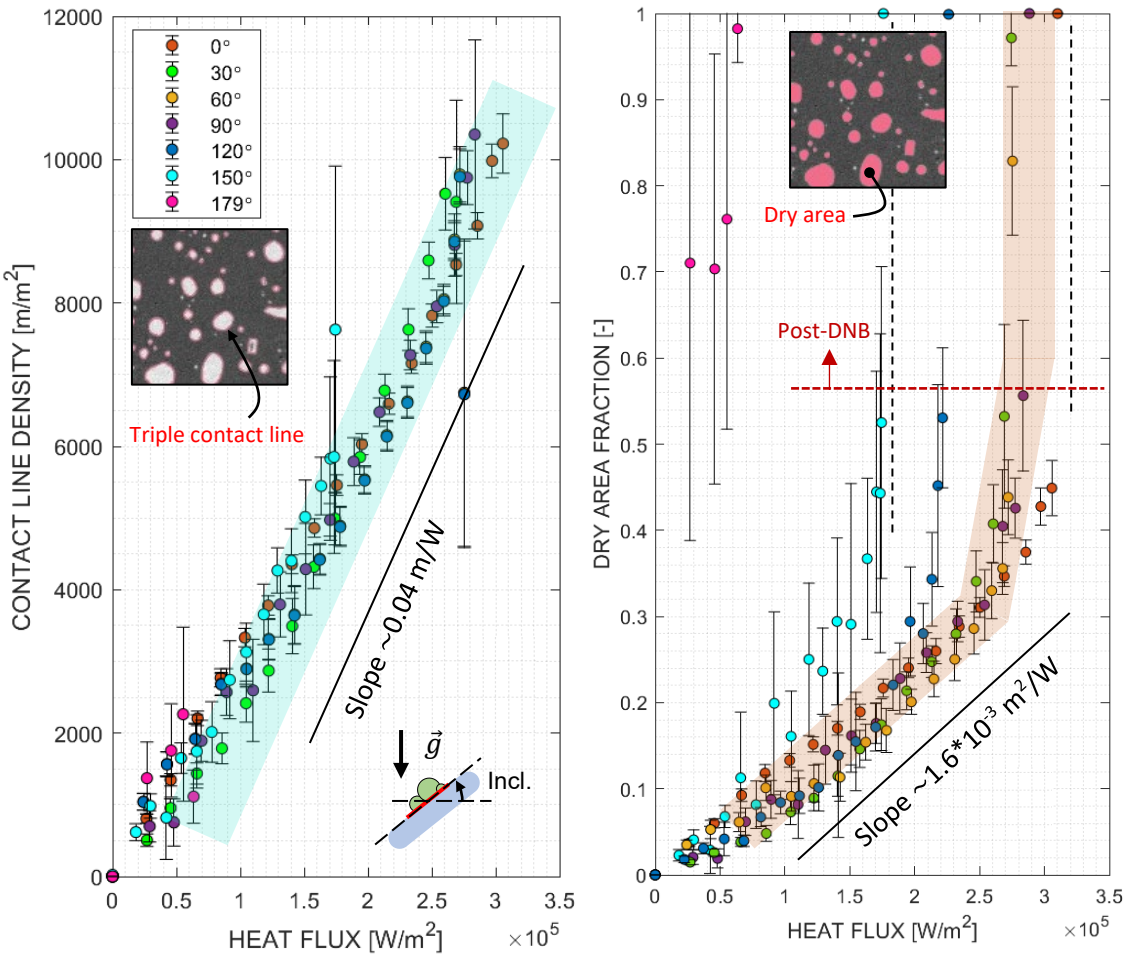

Figure 4.93. Plot of average triple contact line density l_3'' (left) and dry area fraction α_v (right) vs. the total boiling heat flux measured at the ITO.

The poor detection of small bubbles (see discussion in Section 3.3.4) likely results in an underestimation of l_3''. Presently, we cannot precisely estimate this measurement error. However, a comparison between measurement of contact line density with a segmentation using U-Net convolutional neural network have revealed that the underprediction can be as high as 30%. The dry area fraction should be relatively unaffected by this issue, as large bubbles footprint that contribute the most to the dry area fraction are well detected. Figure 4.3 shows that both the tiple contact line density l_3'' and the dry area fraction α_v increases as the boiling heat flux is increased as one can expect from the phase-detection images shown in Figure 4.2. Triple contact line density reaches about 10^4 m/m^2, while the dry area fraction reaches about ~0.5 near DNB, irrespective of the heat flux. Figure 4.4 shows the triple contact line density (left plot) and the dry area fraction (right plot) at DNB for the different angles of surface inclination.

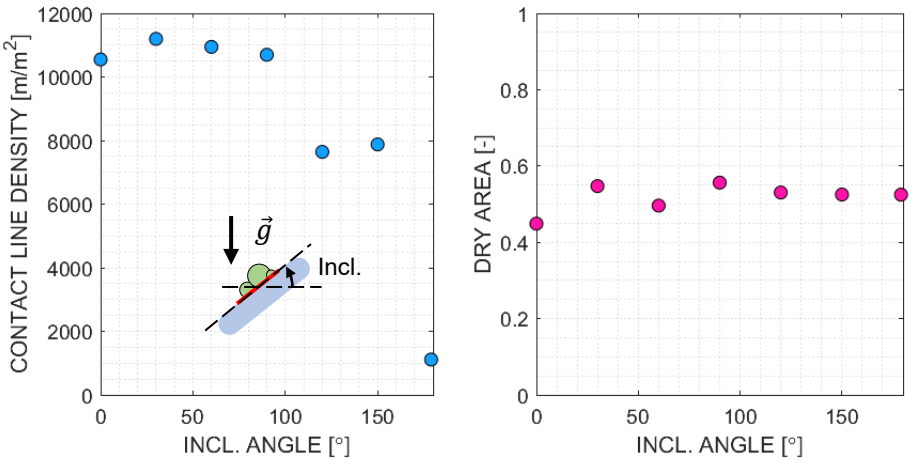

Figure 4.4. Plot of average triple contact line density l_3'' (left) and dry area fraction α_v (right) for different angle of surface inclination at DNB. The standard deviations (shown in Figure 4.3) are omitted.

In Figure 4.3, l_3'' also appears to linearly correlate with the wall heat flux anywhere along the boiling curves. Interestingly, this observation suggests that the mechanisms responsible for removing a dominant part of the heat from the surface depend linearly with the contact line density, which includes at least the triple contact line evaporation studied in Chapter 3. However, the heat removed by triple contact line evaporation alone cannot explain the measured boiling heat transfer coefficient (e.g., in Figure 4.1). The fraction of heat removed by triple contact line evaporation is given by the product of linear evaporation heat rate $\dot{q}_3'$ evaluated in Chapter 3 and l_3''/q_w'', which is the slope shown in Figure 4.3. Based on an average value for $\dot{q}_3'$ of 5 W/m, we estimate that ~20% ($= \dot{q}_3' \, l_3''/q_w''$) is removed by triple contact line evaporation. Therefore, a second heat transfer mechanism depending on l_3'' might well explain the linearity between boiling heat flux and l_3'' all the way to DNB. The dry area fraction also follows a linear trend, at least for low enough heat flux values. The heat flux up to which this observation is true depends on the inclination angle of the surface. For a surface between 0° (i.e., horizontal upward-facing) and 90° (i.e., vertical), the linearity between dry fraction and heat flux is observed up to ~250 kW/m^2. As the inclination increases, this heat flux value decreases. Below this heat flux value, the triple contact line density and the dry area fraction are proportional, since both l_3'' and α_v are linearly related to the heat flux. Figure 4.5 highlights the proportionality between l_3'' and α_v, by plotting l_3'' against α_v. The solid black line fits well the data with a coefficient C (defined as α_v/l_3'') equal to ~37.5 µm.

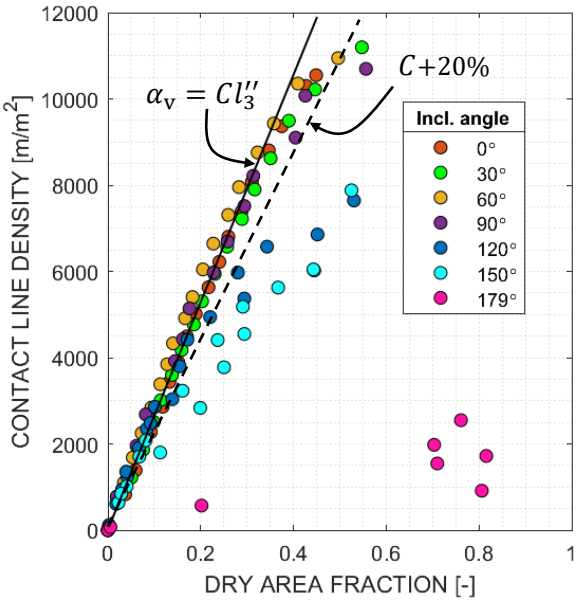

Figure 4.5. Plot of the triple contact line density l_3'' against dry area fraction α_v for different angles of surface inclination.

It is rather clear that the damping of the boiling curves when approaching DNB and the lower CHF values observed on inclined surfaces (in particular above 90°) observed in Figure 4.1 must be related to the observations of Figure 4.5. Based on the phase-detection images shown in Figure 4.2, we can reasonably expect the increase of bubbles coalescence at high heat flux and high inclination angle to cause the damping of the contact line density at high heat flux for increasing dry area fraction. The boiling curves overlap irrespective of the inclination angle when the contact line density and dry area fraction of the respective tests follows the trend $\alpha_v = Cl_3''$. Based on this observation, we can analyze the cause of the deviation of the linear trend between α_v and l_3'' to understand the behaviors of the boiling curves with respect to the heat flux and inclination angle.

We can first show that α_v and l_3'' are both related to the bubble footprint distribution, and more importantly that C is related to the bubble footprint distribution. Given the bubble density on the heated surface N_B'' (i.e., a number of bubbles per unit surface), the dry area fraction scales as,

$$\alpha_v = N_B'' A_f = N_B'' \pi \langle {R_f}^2 \rangle \tag{4.2}$$

where $\pi \langle {R_f}^2 \rangle$ is the average bubble footprint area observed on the surface. We can write a similar scaling formula for the triple contact line density,

$$l_3'' = N_B''\langle P\rangle \sim N_B'' 2\pi\langle R_f\rangle \tag{4.3}$$

where $\langle P\rangle$ is the average contact line perimeter observed of a bubble footprint. When the boiling surface is only covered with small bubbles, such that their footprint remains circular, $\langle P\rangle$ can be approximated by $2\pi\langle R_f\rangle$. Using Eqs. 4.1 and 4.2, we can deduce that the coefficient C shown in Figure 4.5 is given by,

$$C = \frac{\alpha_v}{l_3''} = \frac{\pi\langle {R_f}^2\rangle}{\langle P\rangle} = \frac{1}{2}\left(\frac{2\pi\langle R_f\rangle}{\langle P\rangle}\right)\left(\frac{\langle {R_f}^2\rangle}{\langle R_f\rangle}\right) \sim \frac{\langle {R_f}^2\rangle}{2\langle R_f\rangle} \tag{4.4}$$

C has indeed the dimension of a length and is related to the size of the bubbles' footprints. The relationship between $\langle R_f\rangle$ and $\langle {R_f}^2\rangle$ depends on the distribution of R_f. In the simple case of a Dirac distribution (i.e., all bubbles have the same footprint area), then the relationship is straightforward,

$$\sqrt{\langle {R_f}^2\rangle} = \sqrt{\langle R_f\rangle^2} = \langle R_f\rangle \tag{4.5}$$

In that case,

$$C = \frac{1}{2}\langle R_f\rangle \tag{4.6}$$

Experimentally, the increase of C shown in Figure 4.5 (note that l_3'' is plotted on the y-axis of Figure 4.5, so slope shown is equal to $1/C$) when the heated surface is inclined to 150°, and in a lesser extent at 120°, cannot be explain by the variations of $\langle R_f\rangle$. Instead, other contributions related to the shape of the bubble footprint radius distribution have to be considered to explain the increase of C for large angle of surface inclination. In particular we show hereafter that $\langle {R_f}^2\rangle$ getting larger and larger than $\langle R_f\rangle^2$ (indicating an increasing number of large bubble footprints present on the surface) can partially explain why the linearity between the contact line density and the dry area fraction breaks down with increasing wall superheat.$\langle R_f\rangle$ changes slightly throughout the boiling curves. For instance, it increases by about 20% between a wall superheat of 2 K to 6 K. However this increases can be seen irrespective of the surface inclination angle, whereas the damping of the contact line density for increasing dry area fraction is only seen for larger angles (120° and 150° in Figure 4.5). Instead, other contributors to the observed deviation from $\alpha_v \propto l_3''$ for sufficiently high heat flux in Figure 4.5 may come from one of two assumptions we made to write that $C = \langle R_f\rangle/2$, i.e., $\langle P\rangle \sim 2\pi\langle R_f\rangle$ (which is an assumption on the circularity of the bubble footprints), and $\langle R_f\rangle \sim \sqrt{\langle {R_f}^2\rangle}$ (which is an assumption of the bubble footprint radius distribution).

The first assumption cannot explain the higher dry area fraction for a given triple contact line density since $2\pi\langle R_f\rangle$ is always equal (for circular footprint) or smaller than $\langle P\rangle$ (i.e., C would decrease with increasing $\langle P\rangle$). However, the distribution of R_f (or equivalently A_f) is of course more complex than a Dirac distribution as we will see in more details in the next Section. As a consequence, $\sqrt{\langle {R_f}^2\rangle}$ is not exactly equal to $\langle R_f\rangle$. Figure 4.6 shows the ratio $\sqrt{\langle {R_f}^2\rangle}/\langle R_f\rangle$ against wall superheat during nitrogen pool boiling on a horizontal surface and inclined surfaces. The ratio $\sqrt{\langle {R_f}^2\rangle}/\langle R_f\rangle$ increases by about 10% as the wall superheat increases, resulting in another increase of C by about 20% with increasing wall superheat ($C \propto \langle {R_f}^2\rangle/\langle R_f\rangle^2$). The black dashed line plotted in Figure 4.5 shows l_3'' as a function of α_v (assuming $\alpha_v = Cl_3''$) with a value of C 20% higher than initially. It is clear that we still miss at least another contributor to explain the deviation of linearity between l_3'' and α_v when the heated surface is inclined past 120°. A more thorough analysis of the probability distribution function of both R_f and ${R_f}^2$ seems necessary to explain the results of Figure 4.5.

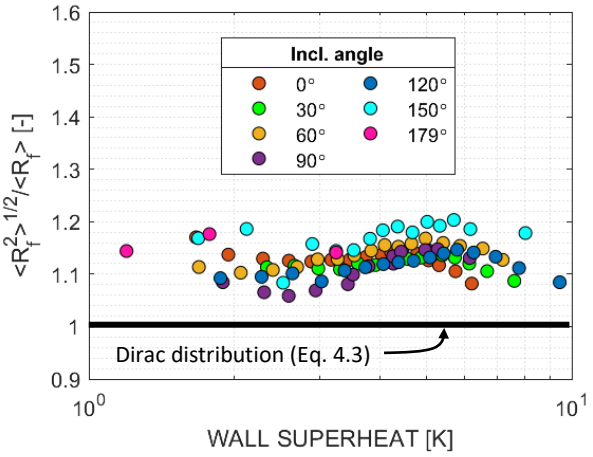

Figure 4.6. Plot of ratio $\sqrt{\langle {R_f}^2\rangle}/\langle R_f\rangle$ against the wall superheat for nitrogen boiling for different inclination angle of the heating surface.

4.4. Probability distribution function of bubbles footprints

The analysis of uncoalesced bubbles in Chapter 3 showed little to no effect of buoyancy on bubble growth in terms of trend, maximum diameter or growth time. The boiling curves plotted in Figure 4.1 shows also very little change in boiling heat transfer for different angles of heated surface inclination for sufficiently low heat flux. On the other hand, buoyancy does affect the boiling heat transfer at higher heat flux, and in

particular near DNB. The visualization of the surface also shows the increasing presence of larger vapor patches when the inclination angle is increased for a given wall superheat (see Figure 4.2), which also seemingly causes the damping of the triple contact line density for increasing dry area fraction (shown in Figure 4.5). Therefore, the effect of buoyancy observed on the boiling heat transfer must be related to the change in the size distribution of bubbles when the heat flux is increased (larger bubbles being naturally more affected by buoyancy).

A quantitative analysis of the footprint area distribution of the nitrogen bubbles was performed. Figure 4.7 shows the probability distribution function (PDF) of the nitrogen bubbles' footprint area A_f on a horizontal upward facing surface. The PDF is shown at 2 different heat fluxes, at 45 kW/m^2 near the onset of nucleate boiling (plotted in blue) and at 310 kW/m^2 near the departure from nucleate boiling (in red). In the latter case, the data come from the last stable boiling step before reaching DNB. The areas of all visible bubble footprints are measured for each phase-detection frame (typ. about 2000 frames) of a given boiling step to construct these PDFs. Uncoalesced and coalesced bubbles are included without distinction in the calculation of the PDFs. Phase-detection images are shown on the right of Figure 4.7 for illustration (the vapor appears white and the liquid appears dark grey). Both PDF curves shows that the probability of finding a bubble with footprint area A_f decreases with increasing A_f, irrespective of the heat flux. However, the rate of decrease of the PDFs with increasing A_f changes with the heat flux. When bubbles are isolated such that no significant number of coalescence events occur (e.g., near ONB), the probability of having a large bubble depends on the probability that the bubble lifts off from the surface or slide out of the heating surface during growth. As the bubble gets larger and larger with time ($R_f \propto \sqrt{t}$ from Chapter 3), the probability of the bubble leaving the surface increases (buoyant forces, lift and drag forces all increase with the increasing size of the bubble faster than capillary forces retaining the bubble). When coalescence increases, as the number of bubbles increases on the surface, the probability of finding large bubble naturally increases (e.g., shown by the PDF plotted in red for q''_w~310 kW/m^2). While there is no universal law to fit the PDF at all heat flux, asymptotic fittings have been previously proposed based on boiling water studies, e.g., by Zhang et al. [91]. At low heat flux the PDF can be approximated with an exponentially damped function (i.e., $p(A_\mathrm{f}) \sim ce^{-cA_\mathrm{f}}$ with c a constant equal to $1/\langle A_\mathrm{f} \rangle$, which then depends on the boiling conditions). When the heat flux is increases and approaches the critical heat flux, the PDF tends to a power law (i.e., $p(A_\mathrm{f}) \propto {A_\mathrm{f}}^{\gamma}$, here with an exponent γ of -2). This power law will be discussed in more details at the end of the Chapter along with the measurements of critical heat flux. Both fittings capture well the PDF of the bubble footprint area for nitrogen boiling at low heat flux and at DNB.

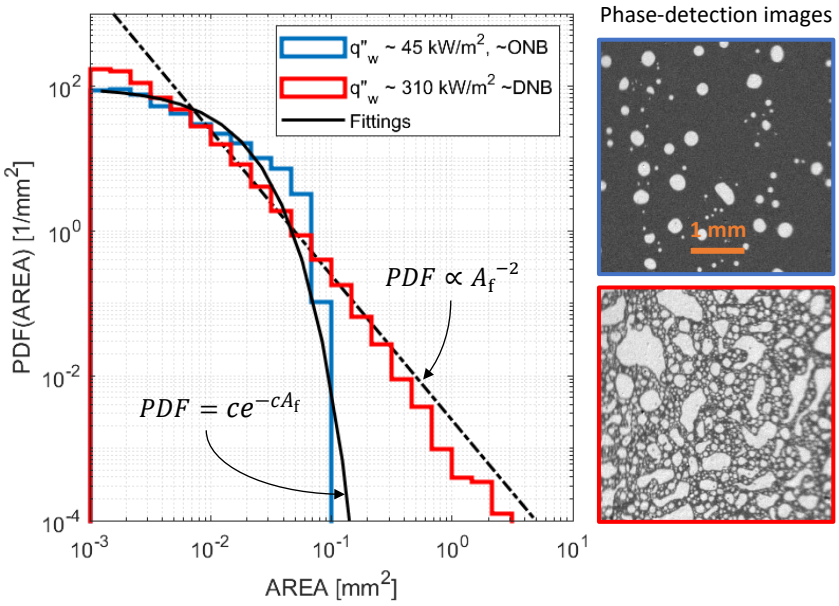

Figure 4.7. Plot of the PDF of the bubbles' footprint near ONB (in blue) and near DNB (in red) for saturated nitrogen pool boiling on horizontal upward-facing surface.

The shape of the PDFs shown in Figure 4.7 is the result of a competition between the rate of formation of bubbles, the rate at which they grow, the rate at which they coalesce to form larger bubbles, and the rate at which they are removed from the surface, with most of mechanisms depending on the bubbles size. By inclining the heating surface, we modify the magnitude of the buoyant force components (i.e., normal and tangential to the surface) acting the bubbles. The norm of the buoyancy force component normal to the heating surface is given by $g\cos\alpha$ with α the inclination angle, while the norm of the tangential component is given by $g\sin\alpha$. In particular, as the inclination angle is increased from 0º to ~90º (i.e., vertical surface), buoyancy contributes more and more to bubbles sliding rather than lifting-off from the surface. At higher inclination angle, i.e., between 90º and 180º, the tangential component of buoyancy will decrease, while the normal component will change sign such that buoyancy will tend to keep large bubbles attached to the heated surface. Hence, increasing the surface inclination angle modifies the bubbles removal mechanisms, but more importantly increases the probability of forming large bubble by coalescence. Figure 4.8 shows the effect of the heated surface inclination angle on the probability distribution functions (PDF) of the bubbles' footprint. Unlike in Figure 4.7, the PDFs in Figure 4.8 are plotted for surface inclination between 0° (horizontal upward-facing) to 179° (~ horizontal downward-facing) for 3 values of heat fluxes (50, 150 and 250 kW/m^2).

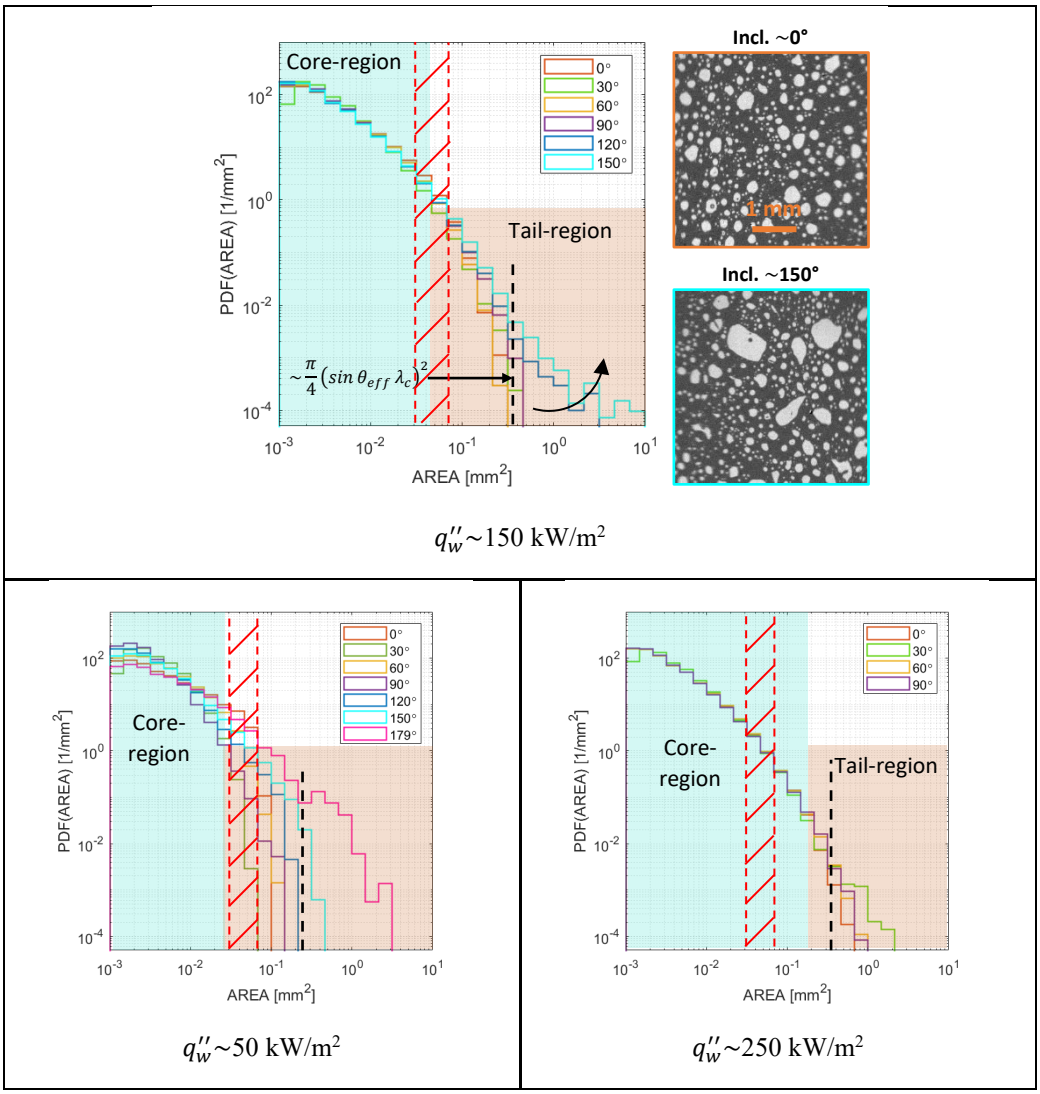

Figure 4.8. Plot of the PDF of the bubbles' footprint for different boiling heat-fluxes and values of inclination angle for saturated nitrogen pool boiling.

Two regions can be distinguished on the PDFs, a core region and a tail region, based on the effect of surface inclination angle. For small enough footprint area (corresponding to the core region), the bubble footprint area distribution appears independent of the inclination angle. For larger footprint area, corresponding to the tail region, the distribution appears highly dependent on the inclination angle. This distinction is particularly clear for a high enough heat-flux (e.g., 150 and 250 kW/m^2). One can notice that the PDFs don't perfectly overlap in the core region at the lowest heat flux (i.e., 50 kW/m^2). Since the order of the PDFs doesn't seem to correlate with the inclination angle, the observed spreading might be related to the limited number of bubbles used to draw the PDFs.

The area with red diagonal stripes shown in Figure 4.8 corresponds to the maximum footprint area we expect for uncoalesced bubbles based on the results of Figure 3.21 in Chapter 3 (~3-7.10^{-2} mm^2, i.e., an equivalent footprint diameter between 2 and 3.10^{-1} mm). Uncoalesced bubbles (found on the PDFs on the left side of the red striped area) are mostly found in the core region, which is independent of the inclination angle. Again, this is in agreement with our previous analysis in Chapter 3, where we showed that the characteristics of uncoalesced bubble do not dependent on the inclination angle of the heated surface. The bubbles with footprint area on the right side of the red striped area consist mostly of coalesced bubbles. These bubbles form the tail region of the PDFs, which tends to depend on the inclination angle. At low heat flux and small inclination angle (e.g., at 0° and ~50 kW/m^2 plotted in orange in Figure 4.8) only a very small fraction of bubbles has footprints larger due to the limited number of coalescence events. The characteristic footprint area of bubbles affected by buoyancy can found by considering the bubbles with diameter roughly equal to the capillary length λ_c. By noting $A_{f,c}$ the footprint area of a bubble whose diameter would be equal to λ_c, one gets

$$A_f = \frac{\pi}{4} {D_f}^2 \sim \frac{\pi}{4} \left(\sin \theta_{eff}\right)^2 D^2 \xrightarrow{D \sim \lambda_c} A_{f,c} \sim \frac{\pi}{4} (\sin \theta_{eff})^2 \lambda_c^2 \tag{4.7}$$

With the assumption that $D_f/D = \sin \theta_{eff}$. $A_{f,c}$ is highlighted in Figure 4.8 by a black dashed line. A plot of $A_{f,c}$ with wall superheat is given in Figure 4.9. The effective contact angle θ_{eff} is increasing with wall superheat as we have seen in Chapter 3. In order to calculate $A_{f,c}$, θ_{eff} is evaluated using the fit of our experimental data ($\theta_{eff}[°] = 29.3 \Delta T_{SAT}^{0.346}$, shown in Figure 3.36).

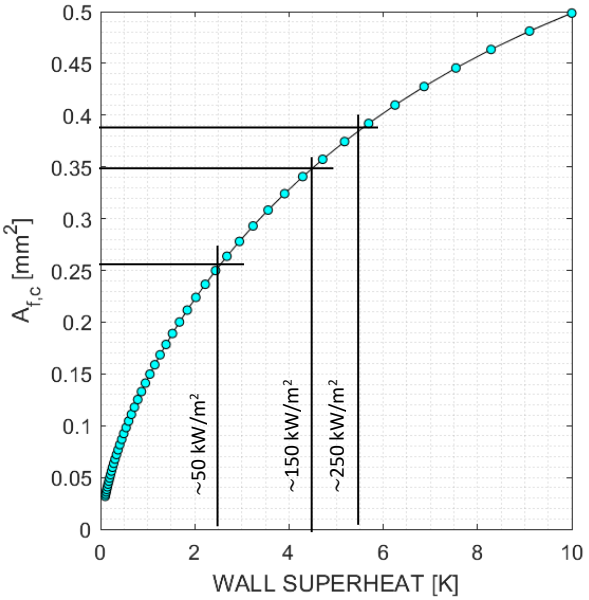

Figure 4.9. Plot of $A_{f,c}$ given by Eq. 4.1 in nitrogen at 0.48 MPa.

One can see that the tail of the bubbles' footprint area distribution lifts up for increasing inclination angle. Physically, the PDFs tail lifting means an increase in the likelihood of finding large bubbles. Since we saw that uncoalesced bubbles do not grow to sizes corresponding to the tail region, the lift of the PDFs tails must be the consequence of an increasing number of coalescence events when the inclination angle is increased.

The triple contact line density plotted against the boiling heat flux, shown in Figure 4.3, appeared independent of the heated surface inclination at any heat flux. We can show that this is the consequence of small bubbles being unaffected by changes of buoyancy (corresponding to bubbles within the core region of the PDFs plotted in Figure 4.8).

Figure 4.10 shows a plot of the contribution of the bubbles with a footprint perimeter below or equal P_f to the triple contact line density l_3'' for nitrogen bubbles on a surface inclined at 150°. We note this contribution $S_\mathrm{P}(P_\mathrm{f})$. The contribution is evaluated for 3 heat flux values, from low heat flux to near DNB (given by the last stable boiling point, here at 174.7 kW/m^2). Each colored line corresponds to a different heat flux value. $S_\mathrm{P}(P_\mathrm{f})$ has the same dimension than l_3''. The contribution to the triple contact line density l_3'' of bubbles with footprint perimeter exactly equal to P_f can be calculated by $N_B'' p(P_\mathrm{f}) P_\mathrm{f}$ with $p(P_\mathrm{f})$ the probability distribution function of the bubble footprint perimeter evaluated at P_f, and N_B'' the average number density of bubbles on the surface at any given time. $N_B'' p(P_\mathrm{f})$ is the average number density of bubbles' footprint of perimeter P_f found on the boiling surface. $S(P_\mathrm{f})$ is given by,

$$S_\mathrm{P}(P_\mathrm{f}) = \int_0^{P_\mathrm{f}} N_B'' p(P_\mathrm{f}') P_\mathrm{f}' dP_\mathrm{f}' \tag{4.8}$$

When P_f goes to infinity $S_\mathrm{P}(P_\mathrm{f})$ tends to the triple contact line density l_3''. In Figure 4.10, $S(P_\mathrm{f})$ is normalized by l_3'' and therefore the ratio tends to 1 for P_f going to infinity. A similar calculation can be made for the dry area fraction. We can define the contribution $S_\mathrm{A}(P_\mathrm{f})$ of the bubbles with a footprint area below or equal A_f to the dry area fraction α_V,

$$S_\mathrm{A}(A_\mathrm{f}) = \int_0^{A_\mathrm{f}} N_B'' p(A_\mathrm{f}') A_\mathrm{f}' dA_\mathrm{f}' \tag{4.9}$$

Both x-axis of Figure 4.10 is shown as bubble footprint equivalent radius. When $S_\mathrm{P}(P_\mathrm{f})$ is plotted, the equivalent radius is based on the footprint perimeter ($P_\mathrm{f}/2\pi$), while it is based on the footprint area (i.e., $\sqrt{A_\mathrm{f}/\pi}$ for the plot of $S_\mathrm{A}(A_\mathrm{f})$. Figure 4.10 shows that distribution of bubbles size that contribute to the triple contact line density does not change significantly with increasing heat flux. This is consistent with the

bubble footprint distributions shown in Figure 4.8. Most of the triple contact line ($S_{\mathrm{P}}(P_{\mathrm{f}})$ above 70%) is made by small bubbles (typ. below an equivalent diameter of 1-2.10^{-4} m). This is consistent with the PDF of bubbles footprint area that are not changing with increasing heat flux for small bubbles (i.e., within the core region shown in Figure 4.8). Since these bubbles are not affected by change in buoyancy, the triple contact line density becomes mostly independent from the inclination angle as shown in Figure 4.2.

On the other hand, the plot of spectral contribution of bubble footprint area to the dry area fraction $S_{\mathrm{A}}(A_{\mathrm{f}})/\alpha_{\mathrm{v}}$ shows the impact of larger coalesced bubbles forming as the heat flux is increased. At low heat flux (i.e., the blue curve at a heat flux of ~53.7 kW/m^2) the dry area fraction consists mostly of small bubbles due to the lack of coalescence. As the heat flux is increased (see the purple and red lines), the plot of $S_{\mathrm{A}}(A_{\mathrm{f}})/\alpha_{\mathrm{v}}$ shows the increasing contributionof large coalesced bubbles ($\sqrt{A_{\mathrm{f}}/\pi}$>2.$10^{-4}$ m) to the dry area fraction (see black arrow).

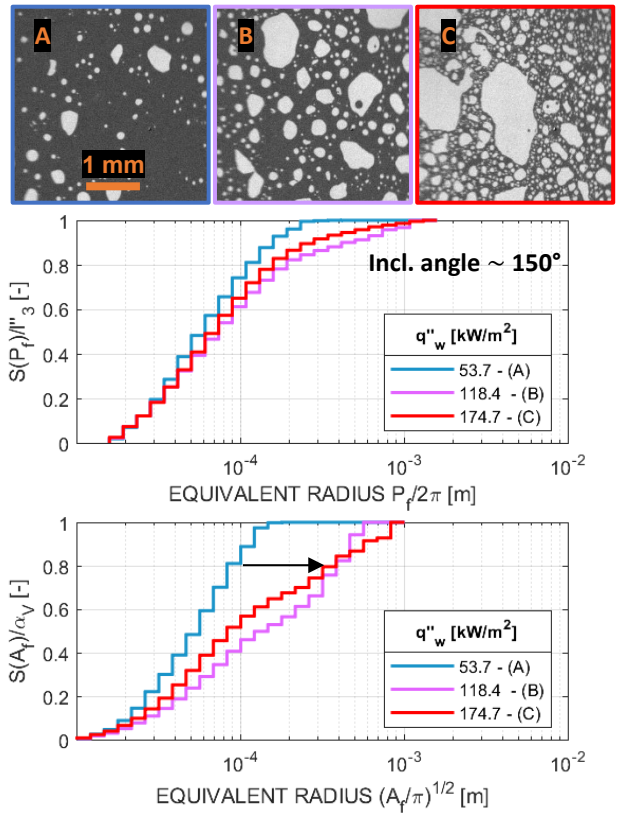

Figure 4.10. Plot of the contribution of bubble footprint of perimeter P_f to the overall triple contact line density l_3'', and the contribution of bubble footprint area A_f to the dry area fraction α_V, given by $S_P(P_f)$ and $S_A(A_f)$, respectively. The heated surface is inclined at 150°. The different curves show the $S_P(P_f)$ and $S_A(A_f)$ at low (in blue), intermediate (in purple) and high heat flux (in red). Phase-detection images A, B and C are shown for illustration.

Figure 4.11 shows plots of $S_{\mathrm{P}}(P_{\mathrm{f}})$ and $S_{\mathrm{A}}(P_{\mathrm{f}})$ for the same heat fluxes than shown in previously (i.e., in Figure 4.10), but on a horizontal upward-facing heated surface. Both $S_{\mathrm{P}}(P_{\mathrm{f}})$ and $S_{\mathrm{A}}(P_{\mathrm{f}})$ remain unchanged for the heat fluxes plotted, translating that the bubbles size distribution also remains unchanged, as the lack of bubble sliding limit the formation of large patches. The fact that both $S_{\mathrm{P}}(P_{\mathrm{f}})$ and $S_{\mathrm{A}}(P_{\mathrm{f}})$ remaining unchanged at the heat flux values presented (up to ~174.9 kW/m^2) explains the linearity observed between l_3'' and α_V, unlike in the case at 150° presented in Figure 4.10.

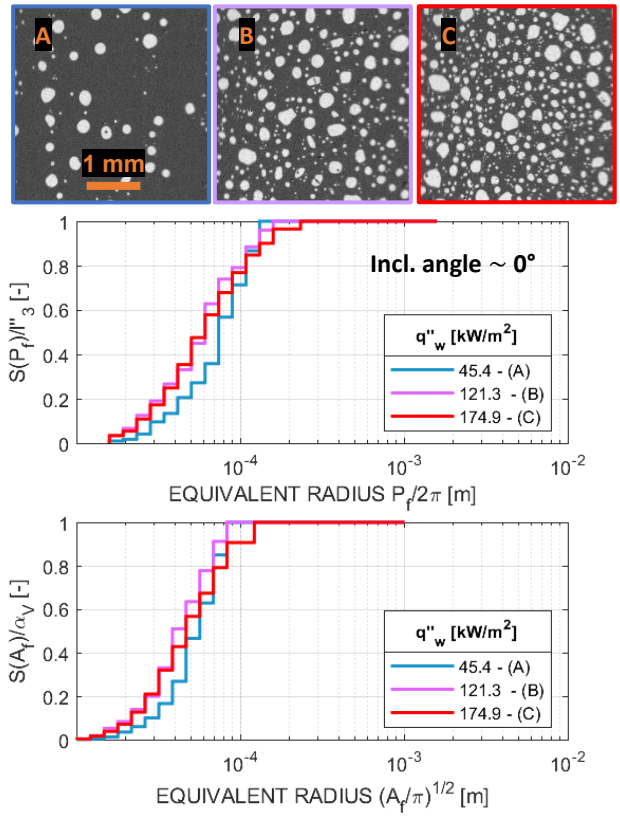

Figure 4.94. Plot of the contribution of bubble footprint of perimeter P_f to the overall triple contact line density l_3'', and the contribution of bubble footprint area A_f to the dry area fraction α_V, given by $S_P(P_f)$ and $S_A(A_f)$, respectively. The heated surface is horizontal upward facing. The different curves show the $S_P(P_f)$ and $S_A(A_f)$ at low (in blue), intermediate (in purple) and high heat flux (in red). Phase-detection images A, B and C are shown for illustration.

4.5. Bubble surface density and active nucleation site density

The instantaneous bubble density N_{B}'' (simply called bubble density) is a critical boiling parameter to know in order evaluate the triple contact line density, dry area fraction and more generally the boiling heat fluxes in a heat flux partitioning model. The parameter appears in the expression of l_3'' and α_{v} in Eq. 4.2 and 4.3. The linearity between the triple contact line density l_3'' and the boiling heat flux (shown in Figure 4.3) and

the lack of change of the bubble size distribution with the core region for increasing heat flux and inclination angle (shown in Figure 4.8) suggests that the bubble density N_B'' is proportional to the boiling heat flux and is also independent of the inclination angle (for a given heat flux). We can show from measurement that this is indeed the case. Figure 4.12 shows the bubble density against the boiling heat flux for different values of heated surface inclination angle. The bubble density is given by the average number of bubbles in contact with the heated surface per unit area. As previously, each colored dot corresponds to a measurement done at a boiling step, i.e., using 2000 phase-detection images recorded at 14 kfps. Dots of same color are for the same surface inclination angle. The error bars indicate the standard deviation after evaluating all the phase-detection frames of each boiling steps. The values of bubble density ranges from $2*10^6$ bubbles/m^2 near ONB to a maximum value of bubble density of about $2*10^7$ bubbles/m^2 near DNB. Experimentally the detection of bubbles with footprints smaller than 30-40 µm in diameter is fairly poor. Therefore, the values bubble density shown in Figure 4.12 are lower bounds. The true value, estimated by counting bubbles manually on selected images, can range up to twice more. Since all recordings are post-processed similarly, and the PDF of bubble footprint are also similar, then the error on the bubble density should be roughly equal on all the tests presented.

Naturally, the bubbles density increases with increasing heat flux, irrespective of the inclination angle. More specifically, N_B'' increases linearly with the boiling heat flux q_w'', which is then consistent with our previous observation that $l_3'' \propto q_w''$.

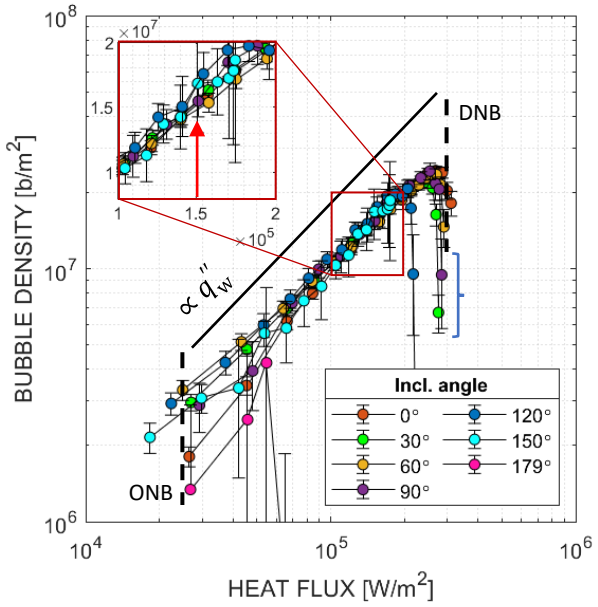

Figure 4.1295. Plot of the bubble density N_B'' against boiling heat flux for different angles of surface inclination.

The drop in bubble density at the largest heat fluxes is caused by the proximity with DNB, and the presence of large lasting vapor patches. The last points shown in Figure 4.12 are stable over the duration of the boiling step (i.e., 3 seconds). However, the drop of the bubble density might be the sign that a transition to film boiling could have occurred if the boiling step lasted longer.

Interestingly, one can see that even at high flux (slightly before DNB) the bubble density N_B'' is the same for an inclination angle of 0° or 150° (e.g., at ~150 kW/m^2), despite almost twice larger dry area fraction (see Figure 4.3 and the additional presence of bubbles with large footprint area (> 2-3.10^{-1} mm^2, see Figure 4.8) when the heated surface is inclined at 150°. We could have expected a reduction of the bubble density on the inclined surface simply due to the lack of free space to generate bubbles. Instead, the heating surface becomes sightly overheated on the inclined surface, therefore generating more bubbles on surface regions not covered by large patches and compensating for the larger dry area fraction. Figure 4.13 shows the measurement of bubble density plotted against the wall superheat. At a constant heat flux (here shown by arrows for 150 kW/m^2), we measure about the same bubble density, but the surface temperature appears slightly higher by about 1 K on the surface inclined at 150° compared to the horizontal surface (i.e., 0°). From a heat transfer perspective, this observation suggests that the heat is removed from the surface by a large number of small bubbles rather than fewer bubbles with the larger footprint.

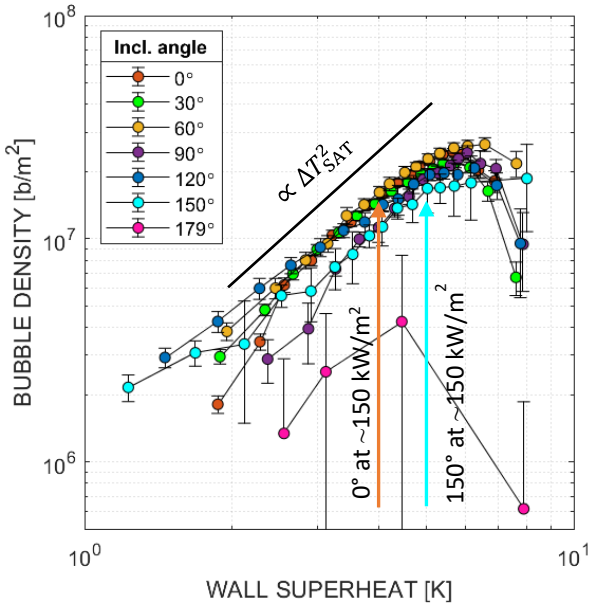

Figure 4.13. Plot of the bubble density N_B'' against wall superheat for different angles of surface inclination.

4.6. Bubble nucleation site density and nucleation frequency

From a model perspective, the bubble density is often decomposed as the product of the nucleation site density N''_{A}, the nucleation frequency f and the bubble growth time t_{g}. The nucleation frequency is critical in the evaluation of the quenching heat transfer as well. As we will see, f is a particularly challenging boiling parameters to measure and model. While f is typically defined for a given nucleation site, it also depends largely on the interaction with sliding bubbles and neighboring nucleation sites in the case of nitrogen boiling. Figure 4.14 shows the active nucleation sites density (NSD), noted N''_{A}, against wall superheat, evaluated using the method described in Section 2.2.3. Using this method the value of N''_{A} is only a strict lower bound of the true nucleation site density. In Figure 4.14, we can see that the NSD increases with the wall superheat, at the exception of the last point before DNB, following a similar overall trend than shown for N''_B in Figure 4.13. Near ONB, the active nucleation site density increases rapidly with the wall superheat ($N''_A \propto \Delta T_{SAT}^5$) before reaching a slower rate of increase ($N''_A \propto \Delta T_{SAT}^{1.8}$). The exponent around 1.8 (2 would provide an equally satisfactory fit with our data) through the region of fully developed nucleate boiling is consistent with typical trend found experimentally (e.g., as shown by the popular Lemmard-Chawla's correlation [47]). Values of N''_{A} ranges from 10^7 site/m^2 to $5*10^8$ s/m^2. The spreading between measurements performed at different inclination angles is small for a given wall superheat. This is consistent as the nucleation site density shouldn't depend on buoyancy, but only on the wall superheat. For the upside-down surface (179º), we suspect that the duration of the recordings (~140 ms) are too short to spot at least a nucleation in all the activated sites due the large dry area fraction.

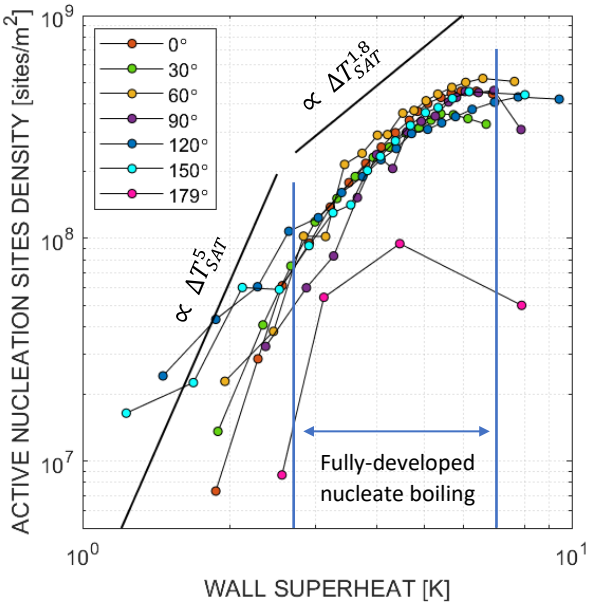

Figure 4.14. Plot of the active nucleation sites against wall superheat for different angles of inclination.

Turbulence, bubble-bubble interaction and the low surface tension of nitrogen make bubbles to slide very easily, and make the nucleation frequency a challenging quantity to measure. Also, the distance between nucleation sites (~$(N_A'')^{-1/2}$ i.e., 10^{-4} m for N_A''~10^8 s/m^2) is similar than the average bubble radius making interaction between active sites common, even at low heat flux. Figure 4.15 presents a simple case of interaction between nucleation sites in boiling nitrogen. Three nucleation sites are close enough such that the bubbles generated by the different nucleation sites coalesce during their growth triggering a premature lift-off of the bubbles from the surface. In this case, we should expect higher nucleation frequencies associated with the nucleation sites due to the interaction than if the sites were isolated from each other.

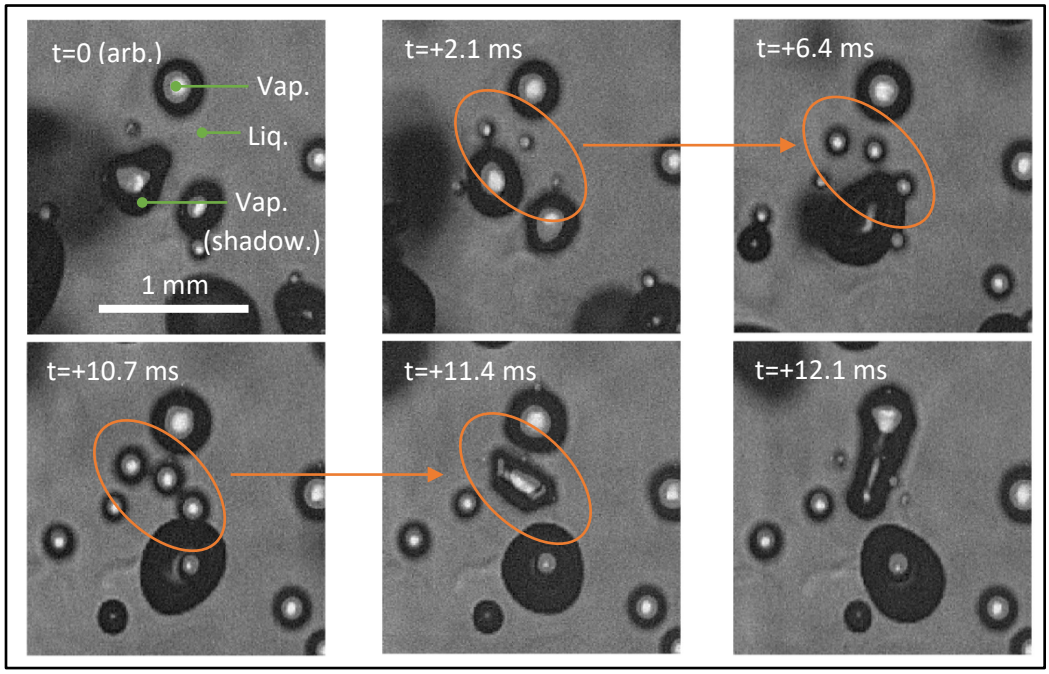

Figure 4.15. Example of nucleation site interactions in nitrogen boiling seen from a superposition of phase-detection and backlit shadowgraphy imaging, with saturated nitrogen pool boiling. The black area shows the bubble as seen from the shadowgraphy, while the light gray indicates the interface between vapor and the heated surface.

It is therefore convenient to evaluate an average nucleation frequency $\tilde{f}$ from the measurement of the bubble nucleation flux $\dot{N}_N''$ (i.e., the number of bubble nucleating per second and per unit surface area) and the active nucleation site density N_A'',

$$\tilde{f} = \dot{N}_N''/N_A'' \ (= \langle f_i \rangle_{all\ sites}) \tag{4.10}$$

$\tilde{f}$ is a surface averaged quantity and does not characterize a particular active nucleation site and f_i is the nucleation frequency of a site arbitrary labeled i. However, we will see in Section 6 that evaluating $\tilde{f}$ is

particularly interesting from a modelling point of view, as the boiling heat flux depends on $\dot{N}_N''$ rather than N_A'' alone. Figure 4.16 shows a plot $\dot{N}_N''$ against N_A''. Each color corresponds to a test with particular inclination angle. At a given inclination angle, both $\dot{N}_N''$ and N_A'' increase as the wall superheat increases. The measurements show a clear trend as $\dot{N}_{\mathrm{N}}'' \propto (N_{\mathrm{A}}'')^{3/2}$, irrespective of the inclination angle. It is not clear whether this 3/2 exponent is universal for different operating conditions, e.g., when the pressure is changed. Both $\dot{N}_{\mathrm{N}}''$ and N_{A}'' depends on multiple variables in addition to the wall superheat. We can easily imagine the size of the bubbles' footprint, or whether bubbles are sliding on the surface, to impact the amount of bubble coalescence events and therefore the relationship between $\dot{N}_{\mathrm{N}}''$ and N_{A}''.

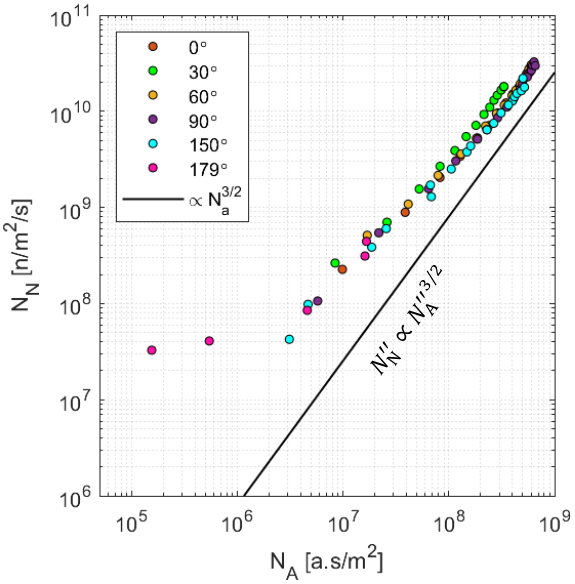

Figure 4.16. Plot of the bubble nucleation flux $\dot{N}_N''$ against the active nucleation site density N_A'' for different inclination angles of the boiling surface.

Figure 4.17 shows a plot of $\tilde{f}$ against wall superheat using the data shown in Figure 4.15 and 4.16. The frequency $\tilde{f}$ ranges from 20 to 60 Hz. Slightly lower frequencies for increasing inclination angle are visible for angle superior to 90°. $\tilde{f}$ increases with increasing wall superheat. The typical nucleation frequency f is expressed as $1/(t_{\mathrm{w}} + t_{\mathrm{g}})$. While $\tilde{f}$ is different than f in the sense that it includes the effect of bubble coalescence and sliding to describe how frequent bubbles nucleate from the surface, $\tilde{f}$ should also behave similar to f with respect to the wait time t_{w} and the growth time t_{g}. According to Hsu's criterion from nucleation theory [92], the wait time necessary to reform the thermal boundary layer before nucleation decreases with increasing heat flux (and therefore wall superheat). Moreover, the bubble growth rate increases with the wall superheat as we have seen in Chapter 3, while the lift-off diameter is fairly constant,

therefore the growth time decreases with increasing wall superheat. Finally, coalescence tends to reduce the bubble growth time and promote bubble lift-off (for inclination angle below 90°) or sliding (for inclination angle above 90°). All these effects tend to increase the nucleation frequency $\tilde{f}$ with increasing wall superheat, which what is observed in Figure 4.17. From the relationship between $\dot{N}_N''$ and N_A'' (shown in Figure 4.15, i.e., $N_{\mathrm{N}}'' \propto {N_{\mathrm{A}}''}^{3/2}$), and the relationship between N_{A}'' and ΔT_{sat} (shown in Figure 4.14 for fully developed nucleate boiling), we can deduce that $\tilde{f} \propto \sqrt{N_A''} \propto \Delta T_{sat}$.

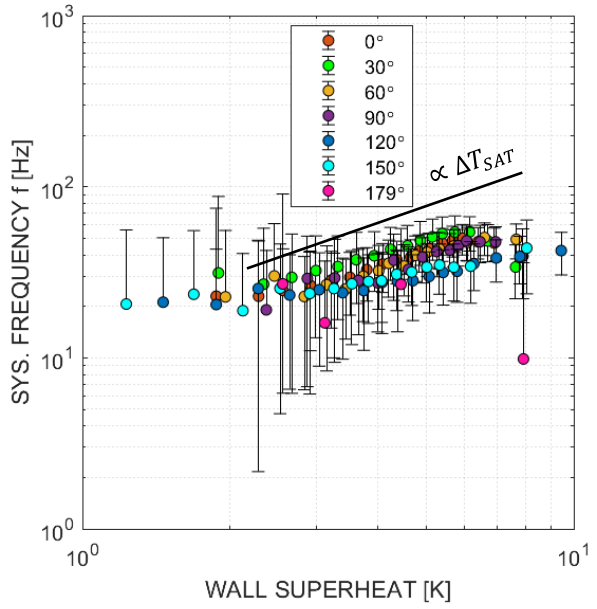

Figure 4.17. Plot of $\tilde{f}$ using Eq. 4.10 for different inclination angles of the boiling surface in nitrogen pool boiling.

The reduction or absence of efficient departure mechanism for large bubbles on inclined surface past 90º result in a lack of stability in the boiling process, which might be the cause of the lower boiling frequency observed in Figure 4.17 (data plotted in blue, cyan and pink). This is particularly evident on the upside-down boiling case (i.e., ~179º in our case). Figure 4.18 shows superposed phase-detection and shadowgraphy images illustrating 200 ms of boiling with an inclination angle of 179º and a wall superheat of + 3.1 K. In this case, we can observe the movement of the very large vapor patches sliding on the surface. The process is relatively slow because the inclination angle is close to 180º. Numerous nucleation events can be observed on the trailing edge of the vapor patch when the surface gets rewetted. The trail of the vapor patch is relatively small (the footprint almost covering the shadow). On the other hand, at the receding triple line during the dry-out phase, liquid gets enveloped by the vapor and even more nucleation can be spotted. Therefore, in this case, the nucleation frequency $\tilde{f}$ is strongly connected to the dynamics of the large vapor patches on the surface.

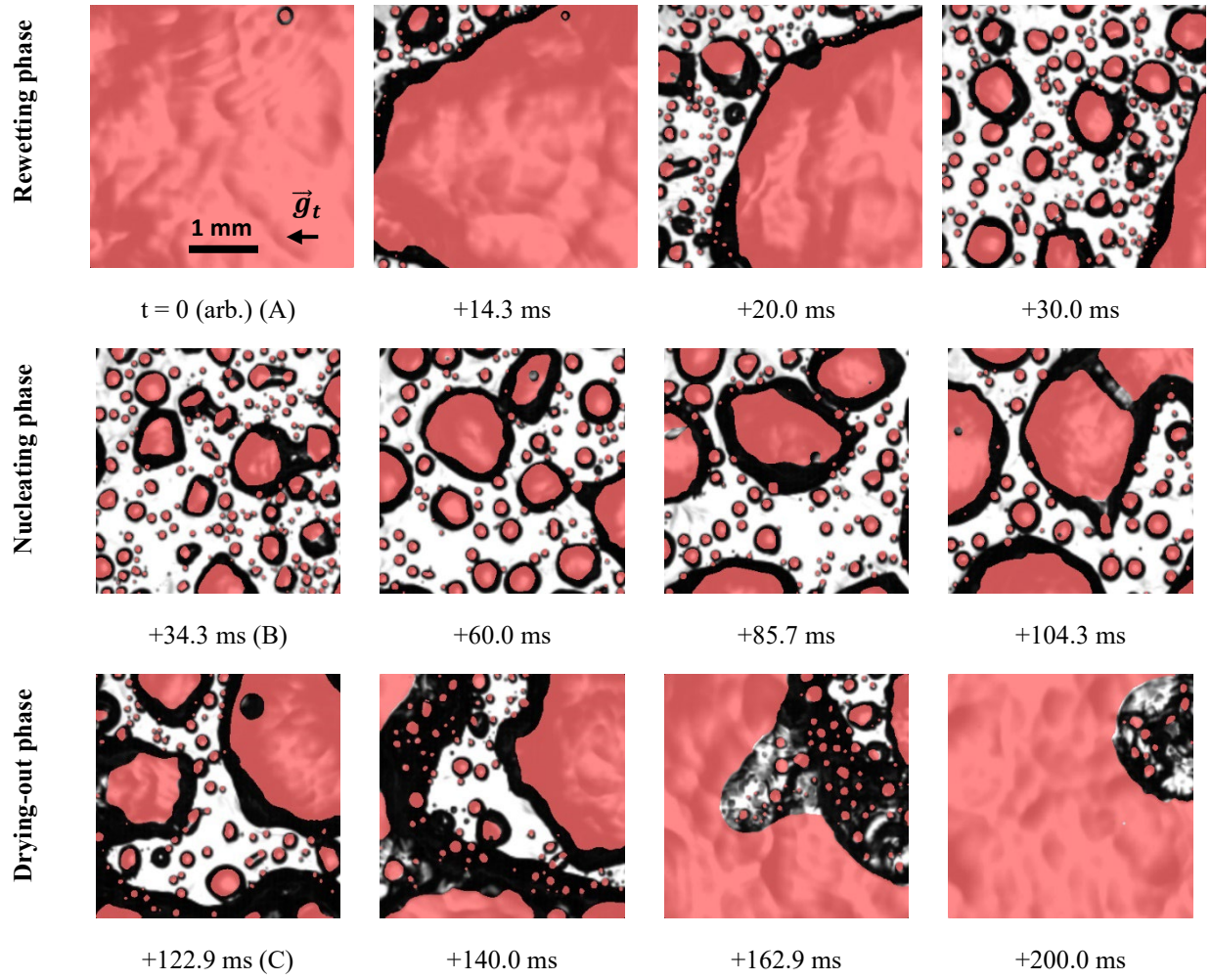

Figure 4.18. Temporary dry-out phase during nucleate boiling with upside-down heated surface (α~179º). The bubbles shadow appear black, while their footprint measured from phase-detection is shown as red overlay.

Figure 4.19 shows the temperature measured by the RTDs during the 200 ms shown in Figure 4.18. The temperature signals show large temperature oscillations (about 1 K peak-to-peak) caused by the movement of the large vapor patches. The temperature of the substrates decreases during the rewetting phase (in blue overlay in Figure 4.19), is minimum during the nucleation phase (in orange) and increases during the dry-out phase (in yellow). These oscillations have a low frequency, about ~3 Hz (i.e., an order of magnitude smaller than $\tilde{f}$, ~20-60 Hz, shown in Figure 4.17) and therefore will tend to the overall nucleation frequency of the system $\tilde{f}$. Figure 4.20 shows the oscillation in the associated instantaneous dry area fraction and contact line density. The peak of temperature observed in Figure 4.19 (at -0.1 s and +0.3 s) corresponds to large increase of the dry area fraction and decrease of the triple contact line density as shown in Figure 4.20. Inversely, the rapid increase of the contact line density and decrease

of the dry area fraction, resulting from small bubbles nucleating on the surface, allows the substrate temperature to decrease by increasing the boiling heat transfer.

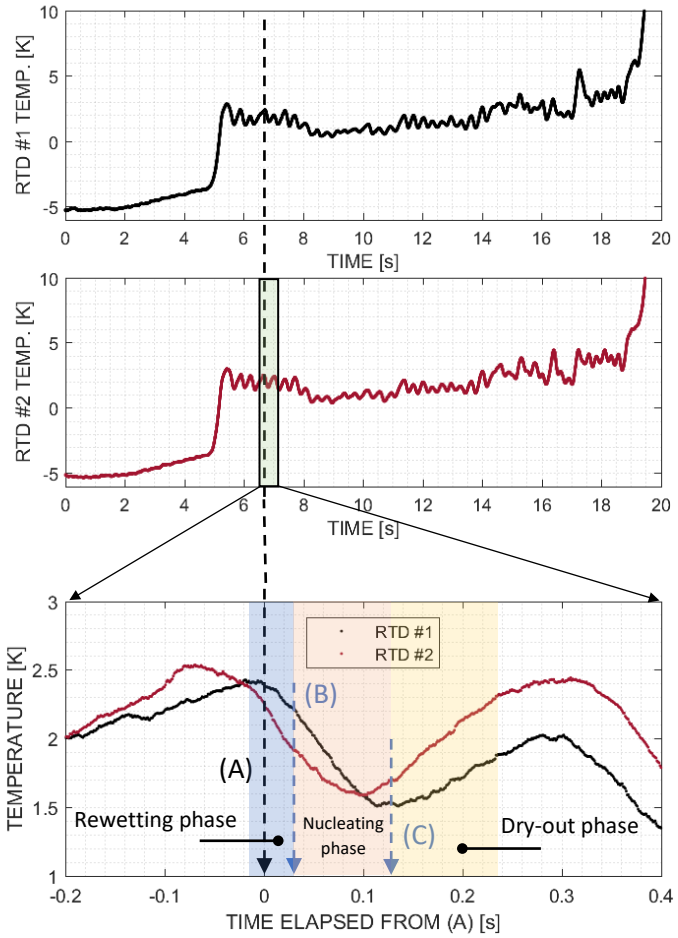

Figure 4.19. Plot of the temperature oscillations associated with the drying and rewetting cycle shown in Figure 4.18 for an inclination angle of 179º. The time is at 0 when the test begins on top and middle plot, and is shifted on the bottom plot such that it matches with the time scale shown in Figure 4.18.

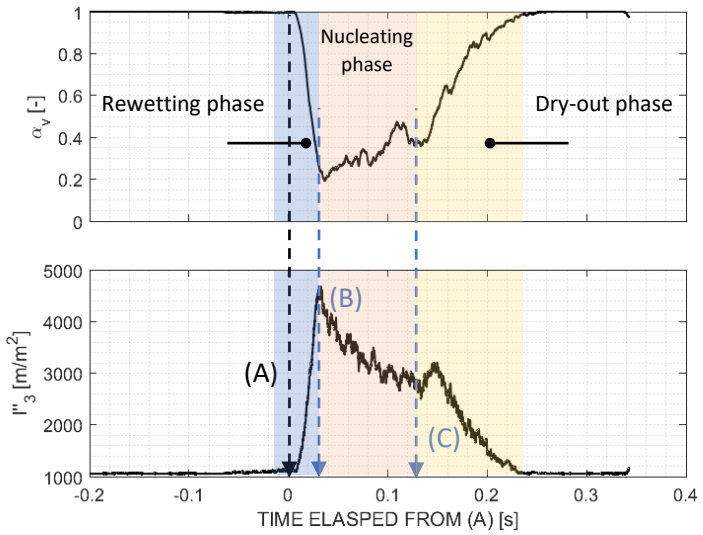

Figure 4.20. Plot of the dry area α_v and contact line density l_3'' during the drying and rewetting cycle shown in Figures 4.18 and 4.19 for an inclination angle of 179º. The time is at 0 when the test begins on top and middle plot, and is shifted on the bottom plot such that it matches with the time scale shown in Figure 4.18.

We present below another case where the dynamics of the vapor impact the nucleation frequency. In this case, the presence of a large vapor cloth near the wall is inhibiting bubble nucleation, while leaving the heating surface locally wetted. Figure 4.21 shows an example of such situation, observed on a surface inclined at 150°. The shadow of bubbles is seen in black, while the bubble footprint is highlighted by a blue overlay. One can see that large vapor patches hoovering on the heating surface show no or limited contact with the surface), and almost no bubble nucleation can be spotted underneath (normally visible on the phase-detection blue overlay). This situation is thought to be possible because the velocity of the hoovering vapor cloth is sufficiently high compared to the thermal conduction through the liquid layer present between the heated surface and the cloth, and the vapor cloth are sufficiently small to still allow proper cooling of the heating surface. While the thickness of the liquid film cannot be measured, we expect it to be well above the micron range as no interference pattern is visible on the phase-detection recordings. As we have seen in the previous case with a dry-out-rewetting cycle (see Figure 4.18), the presence of hoovering vapor cloth inhibiting bubbles nucleation reduces the nucleation frequency of the system. If the vapor clothes would be hoovering slower on the surface and reach large size, it could lead to a drying of the liquid film. Figure 4.22 shows such case where a vapor cloth inhibiting bubble nucleation is slow and large enough for the liquid trapped underneath it to warm up and produce an uncontrolled growth a dry patch (highlighted by orange circles from images A to B). Eventually, the movement of the vapor cloth allowed the dry patch to shrink and the heated surface to eventually rewet (from image B to the last image).

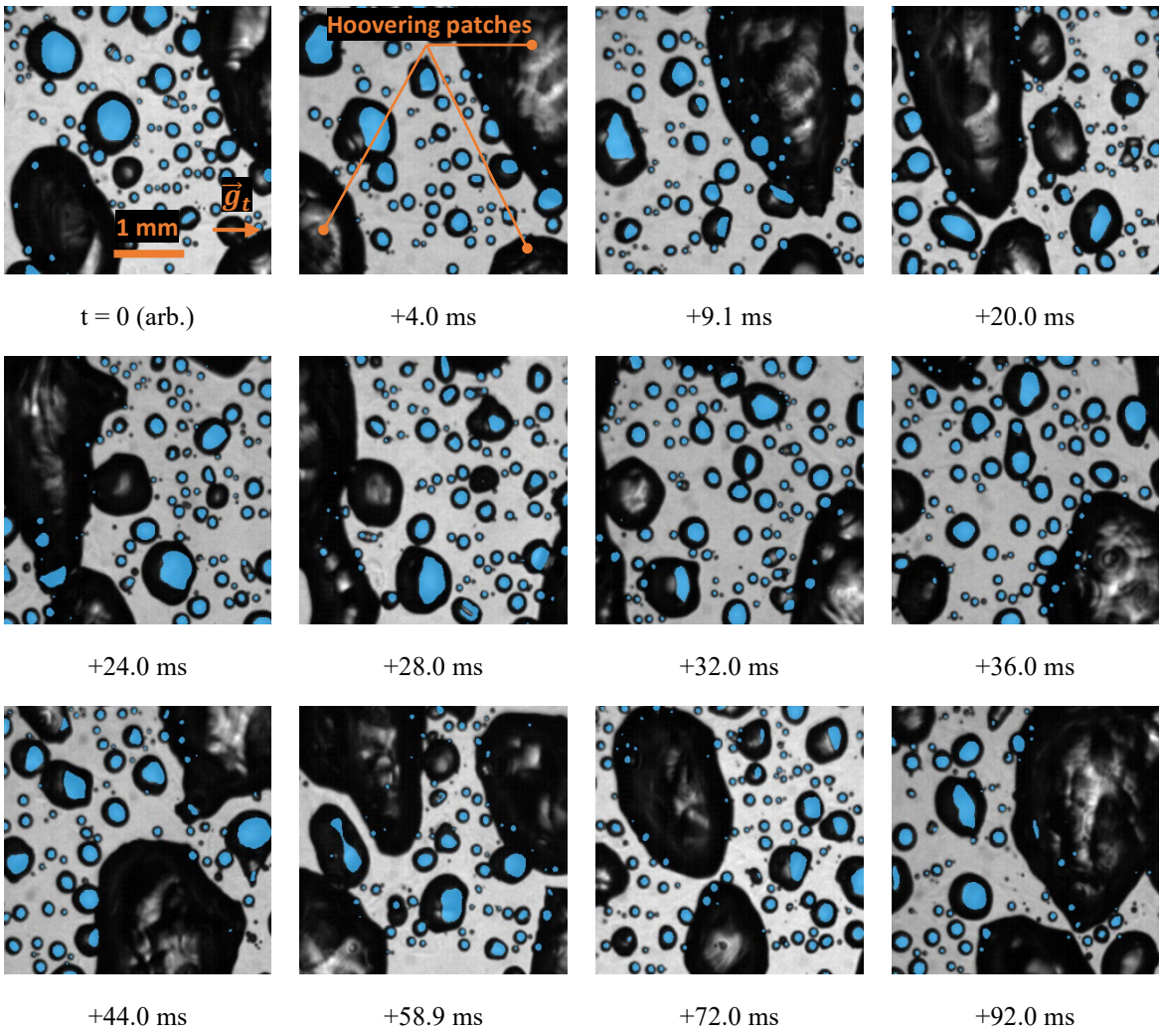

Figure 4.21. Example of nucleation inhibition by the presence of a vapor cloth hoovering on the surface during nucleate boiling with inclined heated surface (~150º). The average wall superheat is +2.5 K. The bubbles shadow appear black, while their footprint measured from phase-detection is shown as blue overlay.

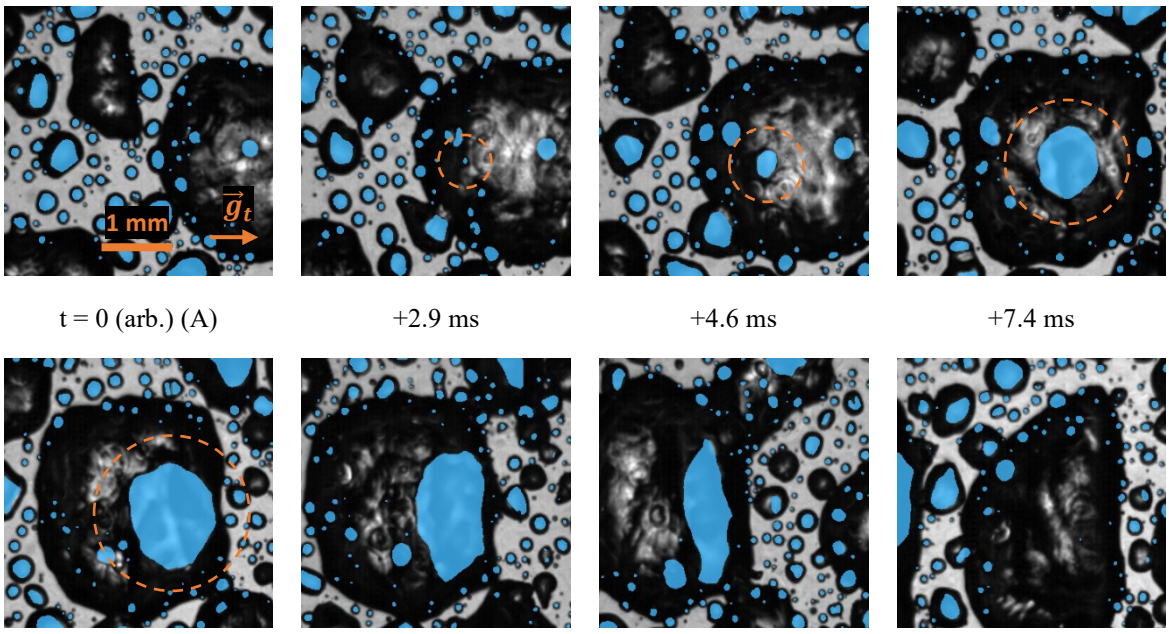

Figure 4.22. Uncontrolled vapor patch growth during nucleate boiling with inclined heated surface (α~150º). The average wall superheat is +3.2 K. The bubbles shadow appear black, while their footprint measured from phase-detection is shown as blue overlay.

4.7. Experimental estimation of heat flux partitioning

In this section, we propose an estimation of the heat flux partitioning based on the wall superheat temperature measurement and the data extracted from phase-detection recordings.

4.7.1. Single-phase heat transfer

Published partitioning model commonly distinguish between single-phase convective heat transfer and quenching heat transfer (e.g., see Ref. [35]). Both heat transfers correspond to the cooling of the heated surface by bringing cooler liquid from the bulk in contact with it. However, a major distinction between single-phase heat transfer and quenching is the location on the heated surface where the cooling occurs. In the case quenching, the cold liquid of the bulk comes in contact with the surface when bubbles lift-off. Initially, the heat transfer process is limited by transient thermal diffusion. As a thermal boundary layer grows in the liquid layer near the surface, liquid convective movement further away from the heated surface, either due to natural circulation, or bubbles-induced turbulence can start contributing to the quenching heat transfer. The process is inherently transient as it depends on the frequency at which the vapor covered the surface and on the duration of each wetting phases. In case of conduction this duration also impacts the heat transfer coefficient itself as it decays over time as the thermal boundary layer gets thicker. In the case single-phase convective heat transfer, the situation is simpler, as the affected portion of the heated surface is by

assumption never covered by vapor. Therefore, the single-phase convective heat transfer is often assumed steady-state and dominated by liquid convective movements formed by temperature gradient (in the case of natural circulation). In reality, a far-field turbulence induced by the bubbles can contribute to the heat transfer on regions of the heated surface deprived from bubble nucleation (e.g., see Ref. [93] for a model accounting for such effect).

However, we can show in the case of liquid nitrogen pool boiling that the entire heated surface is swept by vapor rapidly after the heat flux is increased, even when observed on a relatively short amount of time (corresponding to the recording time, i.e., ~140 ms). As consequence, the heat removed by liquid is better described by quenching heat transfer, which has implications for the formulation of the partitioning model. Figure 4.23 shows the cumulative dry area fraction evaluated for the boiling curve previously studied with different inclination angles. The cumulative dry area fraction is the fraction of the surface area that has been covered by vapor at least once during the duration of the recording. Figure 4.23 shows the cumulative dry area naturally increasing with increasing heat flux.

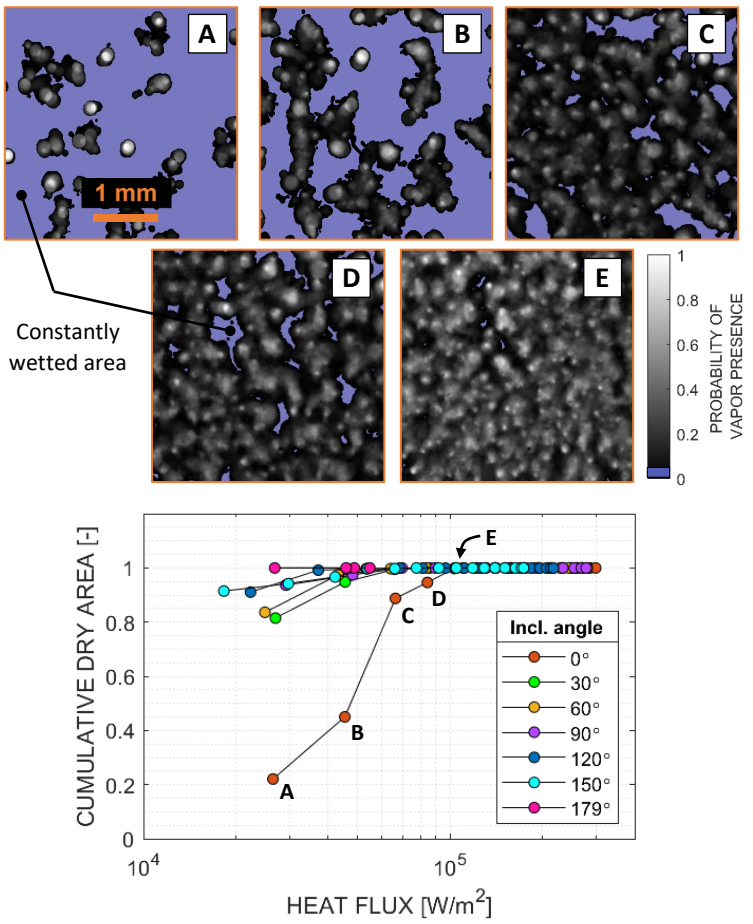

Figure 4.23. Plot of cumulative dry area fraction for different inclination angles of the boiling surface in nitrogen pool boiling. Phase-detection recordings with 2000 images (at 14,000 fps) are used to evaluate each data points on the plot.

A cumulative dry area fraction equal to 1 indicates that the entire surface is subject to quenching at a certain time. The heat flux at which it occurs depends on the bubble density and the bubble movement on the surface. Unless the surface is horizontal (i.e., at 0°), bubble sliding results in the cumulative dry area fraction being close to 1 for heat fluxes as low as 40 kW/m^2 (see plot of all colors but orange in Figure 4.23). When the heated surface is horizontal, the cumulative dry area fraction is initially lower due to bubbles staying about their nucleation site. Maps showing the probability of vapor presence (shown as gray scale) on the heated surface on the horizontal surface are also shown in Figure 4.23. A probability of 0.5 indicates that there is 50% chance of finding vapor at a random location of heated surface at any time. The portion of the surface where this probability is equal to 0 is highlighted by a purple overlay. One can see that initially the low bubble density and the lack of bubble movement on the surface results in a large portion of the surface overlayed in purple (see image A). However, the overlayed portion of the surface shrinks rapidly with the

rapid increase of bubble density, and disappears past 100 kW/m^2 in the case of horizontal pool boiling (see image E). This could have been expected by noting that as such heat flux, we have $(N''_A)^{-1/2} < \langle D_f \rangle$.

4.7.2. Quenching heat flux

Leveraging phase-detection measurement performed in nitrogen pool boiling, we can evaluate the magnitude of the heat removed by each mechanism. First, let us evaluate the quenching heat flux. We can provide an estimate of the quenching heat flux using the experimental phase-map assuming purely thermal conductive heat transfer. The liquid can be considered semi-infinite 1-dimensional because the width of the heating surface is much larger that the conduction length scale normal to the wall. Note that on the other hand, the sapphire has a high thermal diffusivity and therefore lateral conduction cannot be neglected, e.g., during the reconstruction of boiling heat flux (see Section 2.2.1). Figure 4.24 shows the thermal conduction length scale in liquid nitrogen and sapphire for a time scale of 1 and 10 ms, i.e., a time scale to quantify how long a surface stays wet during boiling. These time scale will be justified from experimental measurements later in the section.

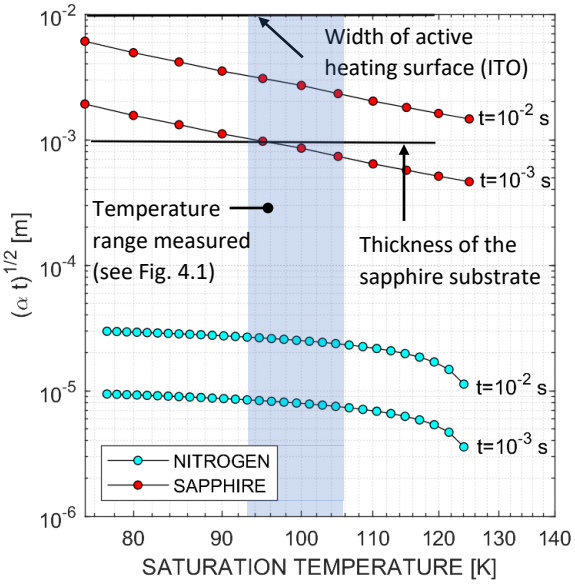

Figure 4.24. Plot of the heat diffusion length scale in sapphire and liquid nitrogen at saturation temperature.

The experiment is performed with imposed heat input. From a heat transfer point of view, this is equivalent to imposing the wall heat flux. The solution of the transient conduction problem through a semi-infinite slab of liquid using a 1-D approximation with imposed heat flux can be found in Kakac et al. [94],

$$q_q''(\vec{x},t) = \frac{\sqrt{\pi}\varepsilon_l}{2\sqrt{(t-t_r)}}(T_w - T_{sat}) \text{ for } t - t_0 > 0 \tag{4.11}$$

With the liquid being initially at uniform temperature T_{sat} and t_r the start of the quenching process. In our case t_r corresponds to the last time (compared to *t*) when the surface gets locally rewetted. t_r can be evaluated using phase-detection recording on each pixel. The surface-averaged quenching heat flux can be rewritten as:

$$q_q'' = \frac{1}{M}\sum_{all\ pixels} \frac{\varepsilon_l\sqrt{\pi}}{2}(T_w - T_{sat}) * g(\vec{x},t) \tag{4.12}$$

With M the number of pixels on each frame and g a function of the time t and the position of the pixel $\vec{x}$ on the heating surface such that:

$$\mathrm{g}(\vec{x},t) = \begin{cases} \dfrac{1}{\sqrt{t-t_r}} \text{ if liquid is present in } \vec{x} \\ 0 \text{ if vapor is present in } \vec{x} \end{cases} \tag{4.13}$$

With t_r the time at which the surface element (i.e., defined by the pixel) has been rewetted for the last time.

Figure 4.25 shows the phase (i.e., liquid or vapor) measured at a pixel evolving over time along with the result of Eq. 4.11 ($q_q''(\vec{x},t)$, at the bottom), Eq. 4.13 ($\mathrm{g}(\vec{x},t)$, in the middle). A blue overlay is shown when the heated surface at the pixel location is wet, and a red overlay when it is dry (i.e., covered by vapor). Sample phase-detection images are shown for two cases, where the pixel being analyzed is at the center of the white cross. At each rewetting phase, one can see the decrease $\mathrm{g}(\vec{x},t)$ with time in $(t-t_r)^{-1/2}$, characteristic of the transient thermal diffusion.

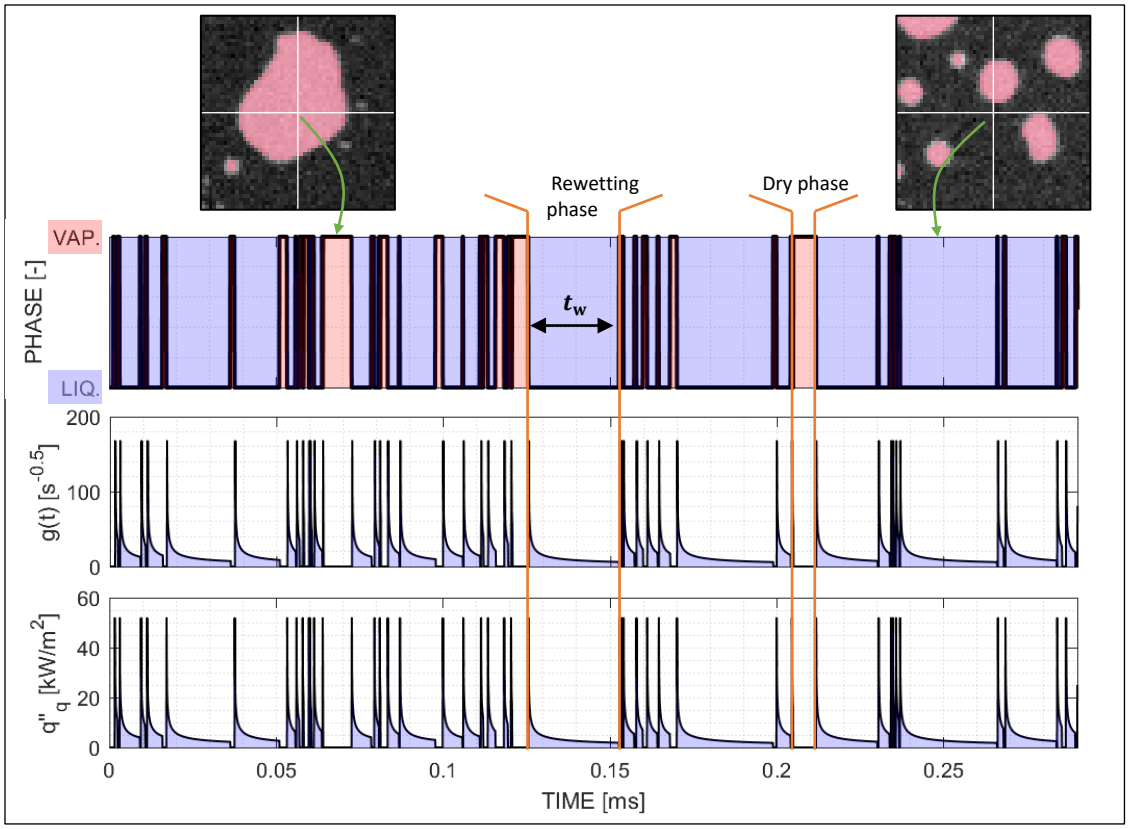

Figure 4.25. Evolution of the phase index (1 for vapor and 0 for liquid) and $g(t)$ from Eq. 4.13 and q_q'' at an arbitrary pixel during nitrogen boiling on a horizontal surface at +2.3 K of wall superheat. Red overlays indicate that vapor is in contact with the surface at the pixel location and blue overlays indicate liquid. The pixel is at the intersection of the white line on the phase-detection images.

Two time-scales are playing the role in the amount removed during quenching. On one hand, we have a time scale associated with how frequent rewetting events happen on the surface. The associated frequency is noted f_w. On the other, quenching will depend on how long each on these rewetting phases are. This duration is noted t_w. Both time scales emerge when averaging over a long period of time Eq. 4.11 (i.e., over multiple cycling of drying and rewetting phases),

$$\langle q_q'' \rangle = \boldsymbol{f_w} \langle \Delta E_q \rangle \tag{4.14}$$

With f_w the frequency of rewetting that the heated surface experience locally and $\langle \Delta E_q \rangle$ the average amount of heat removed by quenching during a rewetting. Assuming $\langle \sqrt{t_w} \rangle \sim \sqrt{\langle t_w \rangle}$, we get,

$$\langle \Delta E_q \rangle \sim \sqrt{\pi} \varepsilon_l \sqrt{\langle \boldsymbol{t_w} \rangle} (T_w - T_{sat}) \tag{4.15}$$

where $\langle t_w \rangle$ is the average time that liquid stays in contact with the heated surface. Figure 4.25 shows a plot of $\langle t_w \rangle$ against wall superheat for different inclination angle. $\langle t_w \rangle$ is computed by averaging the duration

of wetting phase t_w over time for each pixel of the phase-detection recording (i.e., 340 x 340 px). The distribution of t_w is shown in Figure 4.26 as well at different value of wall superheat, at low, medium and high heat flux and on a horizontal surface and inclined surface at 150°. The duration of the wetting phase reduces significantly when the wall superheat is increased following a trend in $\Delta T_{sat}{}^{-5/2}$, with a typical range of values between 10^{-2} and 10^{-3} s.

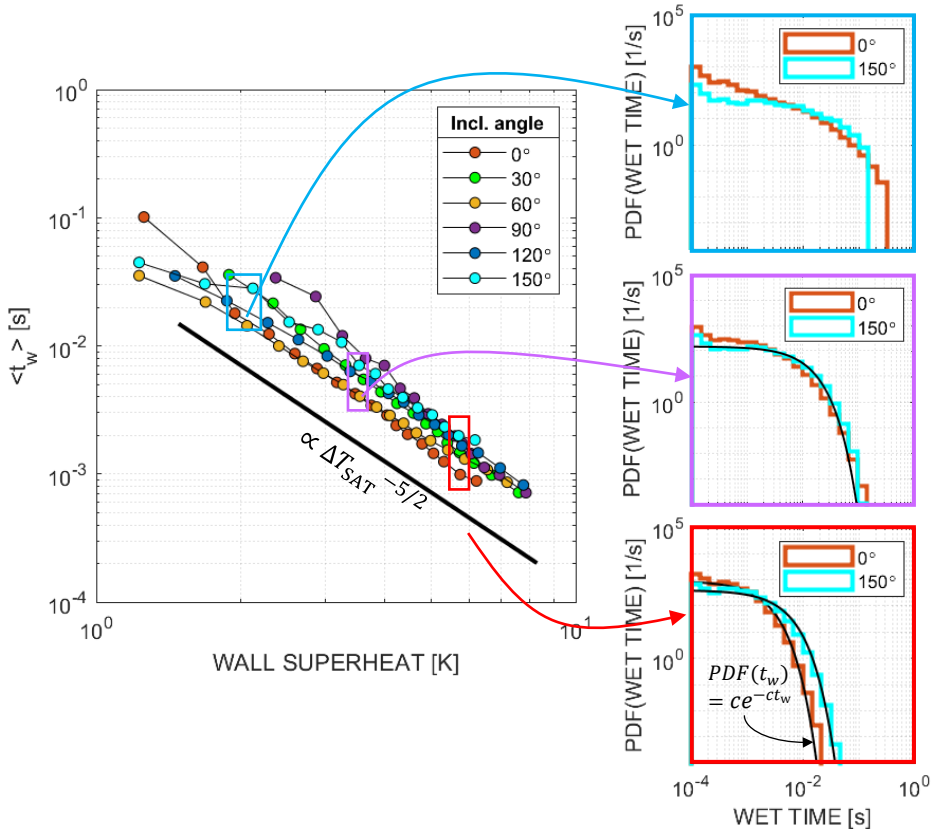

Figure 4.26. Plot of $\langle t_w \rangle$ against wall superheat for different inclination angles of the boiling surface in nitrogen pool boiling.

One can note that the average wetting time appears slightly reduced for lower inclination angle (e.g., by comparing orange markers, at 0° with the other colored markers). Even if the differences are too small to draw definite conclusion, we could have expected the opposite trend (i.e., smaller wait time on an inclined surface with a maximum at 90°). We saw that bubbles sliding is more prominent on inclined surface while the bubble density and bubbles size stays similar, therefore inclined surface far from horizontal should promote more frequent rewetting of the surface and a decrease of $\langle t_w \rangle$.

Interestingly, for a sufficiently high wall superheat (>2 K), the distribution of t_w can be well approximated by exponentially damped functions (ce^{-ct_w}) with a coefficient c increasing with increasing wall superheat. An evaluation of $\langle t_w \rangle$ shows that the coefficient c is simply equal to $1/\langle t_w \rangle$, and therefore varies as $\Delta T_{sat}{}^{5/2}$.

The wetting frequency f_w and the average wetting duration $\langle t_w \rangle$ are both related to the probability of finding vapor at certain time instant and certain location on the heating surface. Therefore, a relationship between f_w and $\langle t_w \rangle$ is expected. Figure 4.27 shows a plot of $1/f_w$ against $\langle t_w \rangle$ for the cases with horizontal heated surface and inclined at 150º. In this plot, the data points measured at the highest heat flux at in the bottom left corner, as both $\langle t_w \rangle$ and $1/f_w$ decrease with increasing heat flux.

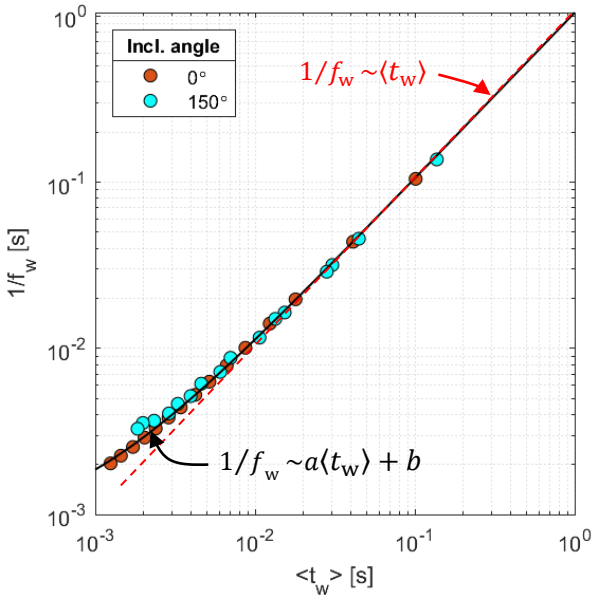

Figure 4.27. Plot of $\langle t_w \rangle$ against wall superheat for different inclination angles of the boiling surface in nitrogen pool boiling.

$\langle t_w \rangle$ and $1/f_w$ are nearly equal for large values of $\langle t_w \rangle$ (which corresponds to the low heat flux end of the boiling curves). As the heat flux increases and $\langle t_w \rangle$ reduces, the duration that the heated surface is dry becomes non-negligeable compared to $\langle t_w \rangle$ and $1/f_w$ becomes larger than $\langle t_w \rangle$. A simple affine fitting allows to capture the trend for small values of $\langle t_w \rangle$ (here, with $a = 1.051$ and $b = 0.81$ ms). Using this formulation, we can deduce that the average quenching heat flux can be evaluated as,

$$\langle q_q'' \rangle \sim \frac{2\varepsilon_l}{\sqrt{\pi}} \frac{\sqrt{\langle \boldsymbol{t_w} \rangle}}{a\langle \boldsymbol{t_w} \rangle + b} (T_w - T_{sat}) \tag{4.16}$$

With a and b fitting parameter independent of the inclination angle and the wall superheat. We foresee that $\langle t_w \rangle$ could be expressed as a function of the bubble density N_B'', the average velocity of bubbles sliding on the surface as well as their average footprint radius. From a modeling perspective, this formulation can be interesting as these 3 quantities are much easier to measure experimentally than the active nucleation sites density and bubble nucleation frequency used typically to model $\langle q_q'' \rangle$.With Eq. 4.12, we can evaluate the quenching heat flux q_q'' directly leveraging the phase-detecting recordings. Figure 4.28 shows the local and instantaneous quenching heat flux map using Eq. 4.11 on all the pixels of the phase-detection images. As bubbles move on the heating surface, cold liquid rewets previously dried areas producing the large quenching heat flux, appearing in red in Figure 4.28. The bubble circled in red highlight the quenching heat flux at the receding triple contact line during bubble lift-off.

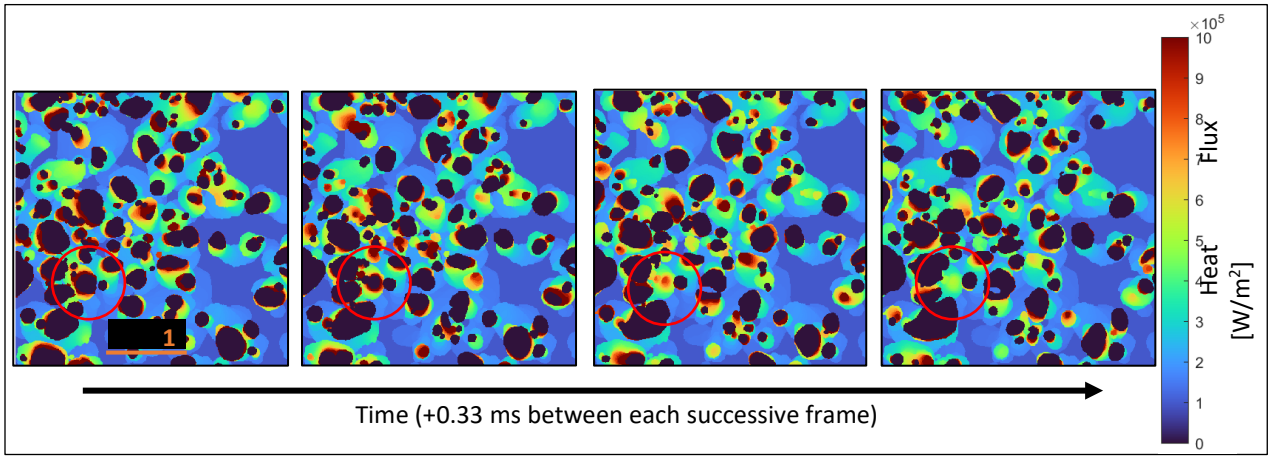

Figure 4.28. Quenching heat flux evaluated using Eq. 4.11 seen at different frames during pool boiling of liquid nitrogen with + 4.4 K of wall superheat. The red circle shows a zone where the quenching front is visible due to a bubble lifting-off.

The quenching heat flux calculated using Eq. 4.11 can be evaluated for different values of wall superheat and angles of inclination. The contribution of the quenching heat flux to the total heat flux (i.e., $\langle q_q'' \rangle / q_w''$) is shown in Figure 4.29 against wall superheat. Figure 4.29 shows that at most, the quenching heat flux should account for roughly 20% of the total heat flux. The contribution of the quenching heat flux appears to increase slightly on inclined surface between 0° and 150° which is consistent with more bubbles sliding and larger dry area fraction.

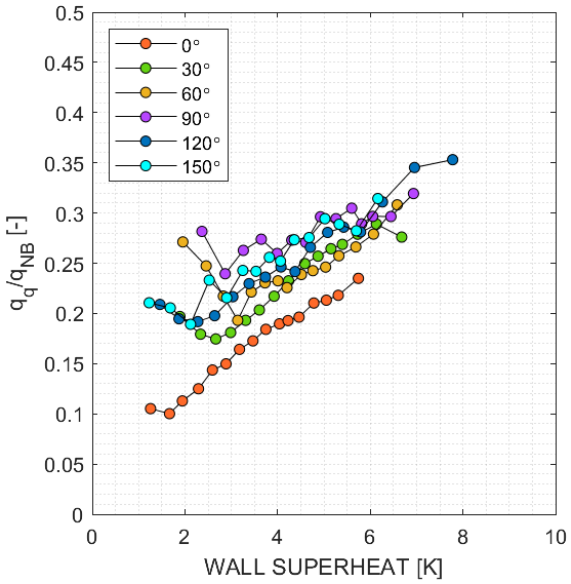

Figure 4.29. Plot of the contribution of transient conduction to the boiling heat flux.

So far, we assume no effect of convective heat transfer in the calculation of the quenching term, which means that no minimum heat transfer coefficient was assumed to plateau the quenching heat flux when time gets large. Physically, we could expect that some natural circulation to occur in the boiling cell due the temperature gradients or some convective liquid movement induced by the bubbles growing, sliding or lifting off the heated surface. In particular, we will see in the next section, that triple contact evaporation alone cannot explain the remaining heat to be removed, but only a fraction of it (about 20% of the remaining heat transferred).

Eqs. 4.11 and 4.13 can be modified to incorporate the effect of liquid convection using a heat transfer coefficient. A way of modelling is by adding the convective heat transfer coefficient as a lower bound of the transient heat transfer coefficient. Therefore, the instantaneous quenching heat flux is given by,

$$q_q'' = \begin{cases} \dfrac{\sqrt{\pi}\varepsilon_l}{2\sqrt{(t-t_0)}}(T_w - T_{sat}) \text{ for } t - t_0 > 0 \text{ and } \dfrac{\sqrt{\pi}\varepsilon_l}{2\sqrt{(t-t_0)}} > h_c \\ h_c(T_w - T_{sat}) \text{ otherwise} \end{cases} \tag{4.17}$$

Figure 4.30 shows of the quenching heat transfer coefficient h_q evaluated at the same pixel than shown in Figure 4.25, with and without a convective heat transfer coefficient h_c. The blue overlay indicates the period that liquid is in contact with the heated surface at the pixel location. For illustration a value for h_c of 2 kW/m^2/K is considered and is shown by the red dashed line. In the case of pure conduction, the quenching heat transfer falls below h_c after a certain time, given by $(t - t_0)$ equal to $\left(\frac{\sqrt{\pi}\varepsilon_l}{2h_c}\right)^2$.

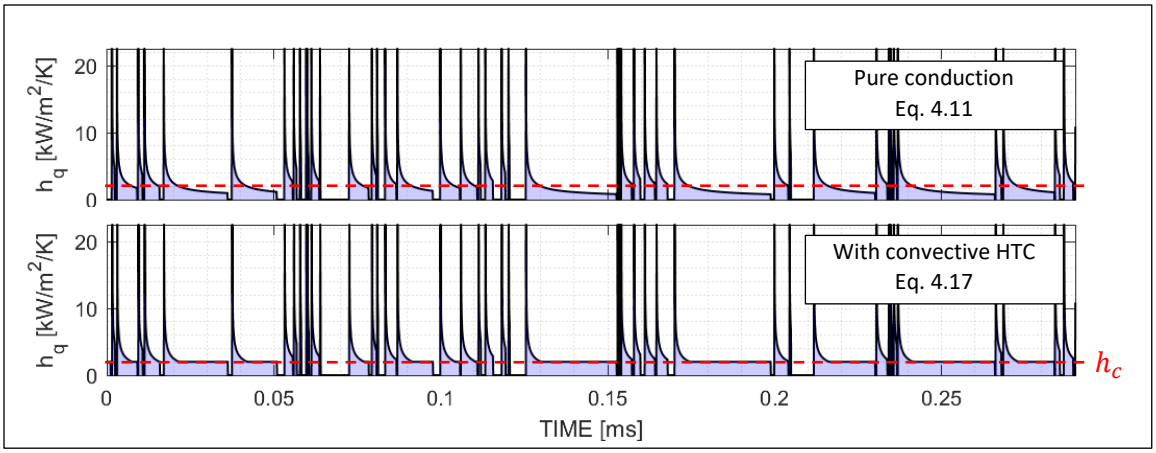

Figure 4.30. Evolution of the quenching heat transfer coefficient without (on top) and with (on bottom) a minimum convective coefficient using the same data than shown in Figure 4.25.

Figure 4.31 shows plots of the quenching heat flux (in purple) against wall superheat and compare it the total boiling heat flux (in cyan) for different values of convective heat transfer coefficient h_c (0, 10 and 20 kW/m^2/K).

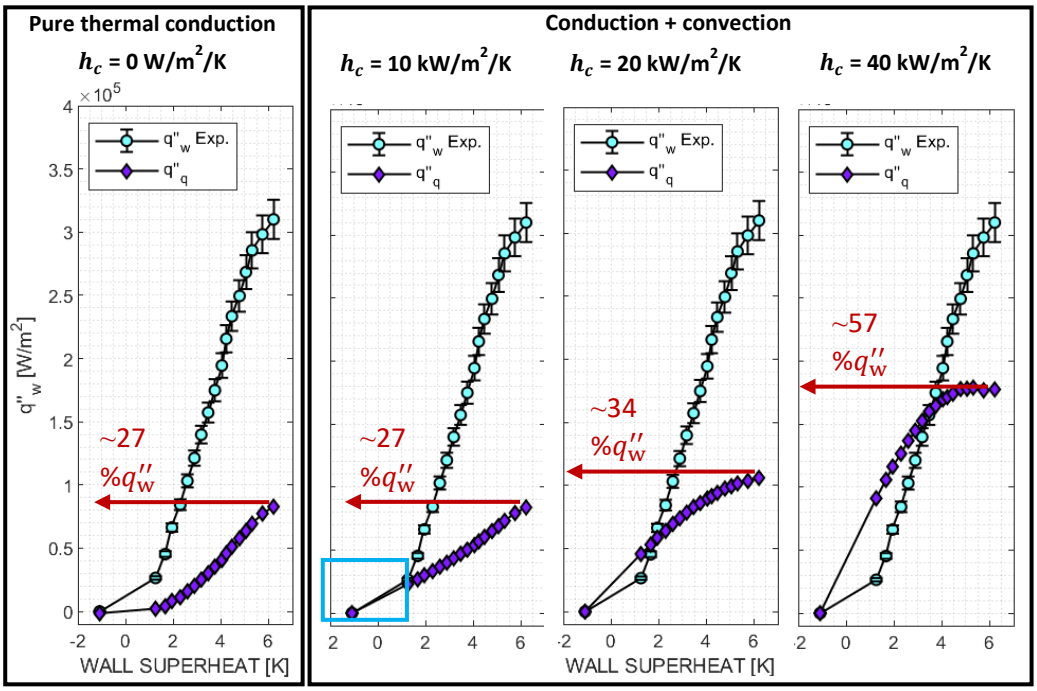

Figure 4.31. Estimate of the quenching heat flux for different values of h_c on the nitrogen pool boiling case with horizontal heated surface.

The quenching heat flux shown (in purple) is evaluated using Eq. 4.15.The quenching heat flux nominally (i.e., with h_c=0) accounts for at most 27% of the total boiling heat flux. As h_c increases, the fraction of heat

flux removed by quenching increases as well. A h_c equal to 10 kW/m^2/K corresponds to the upper estimate of the natural circulation in the boiling cell before boiling (shown in blue frame in Figure 4.30), but results in similar fraction of quenching in the boiling heat flux. For the convective effect to be significant, h_c has to be much larger than $\pi\varepsilon_l/2\sqrt{\langle t_\mathrm{w}\rangle}$ (which is about 11.8 kW/m^2/K for the minimum value of $\langle t_\mathrm{w}\rangle$ measured, ~1 ms from Figure 4.26). For such value of h_c, the quenching heat flux tends to be linear with the heat flux at low wall superheat,

$$\langle q_q''\rangle \sim h_c(T_w - T_{sat})\langle t_\mathrm{w}\rangle f_\mathrm{w} \tag{4.18}$$

With $\langle t_\mathrm{w}\rangle f_\mathrm{w}$ corresponding to the proportion in time that liquid stays in contact with the heated surface anywhere on it. At low heat flux, the product $\langle t_\mathrm{w}\rangle f_\mathrm{w}$ does not depend on the wall superheat (as shown in Figure 4.27, therefore $\langle q_q''\rangle \propto (T_w - T_{sat})$. At higher heat flux, the proportionality between $\langle t_\mathrm{w}\rangle$ and f_w breaks resulting in the quenching heat flux $\langle q_q''\rangle$ to plateau (e.g., see boiling curve with h_c at 40 kW/m^2/K in Figure 4.31). A value of h_c larger than 40 kW/m^2/K would be necessary to recover the total boiling heat flux after including the triple contact line evaporation (which accounts for ~20% of the total heat flux near DNB). One can see that in this case the quenching heat flux would be necessarily higher than the measured boiling heat flux at lower wall superheat (as it is the case for h_c at 40 kW/m^2/K in Figure 4.31). This simply shows that a temperature-independent convective heat transfer coefficient cannot be used to resolve the discrepancy between the boiling heat flux measured, and the heat fluxes from triple contact line evaporation and quenching. The presence of convective liquid movement induced by bubbles could provide a reasonable explanation, as h_c would be a function of at least the bubble density N_B''. More recent investigations using the same experimental setup than described in this thesis suggest that the wall superheat during nucleate boiling may be by a couple degrees higher than the measurement shown here. This would would increase the quenching heat flux, potentially removing the part of the heat flux that is left unexplained, while keeping the estimate of heat removed by triple contact line evaporation the same than shown in Chapter 3 (e.g., in Figure 3.42). Further research effect is necessary to evaluate these hypothesis.

4.8. Experimental estimate of the evaporation heat flux

We saw in Section 3.2.2.1 that about 2-8 W/m is removed at the triple contact line during bubble growth. We also measured the triple contact line density (shown in Figure 3.42). Therefore, we can evaluate the contribution of the triple contact line evaporation to the total boiling heat transfer. Assuming that the triple contact line evaporation explains the boiling heat discounted of its quenching component, we can write that,

$$q_{cl}'' = q_\mathrm{w}'' - q_\mathrm{q}'' \text{ and } \dot{q}' = q_{cl}''/l_3'' \tag{4.19}$$

With q_3'' the heat flux associated with triple contact line evaporation and $\dot{q}'$ the linear evaporation rate at the contact line. Only conduction is considered in the calculation of the quenching heat flux q_q''.

Figures 4.32 shows a plot of $(q_w'' - q_q'')/l_3''$ against the wall superheat for different angle of heated surface inclination. $(q_w'' - q_q'')/l_3''$ corresponds the linear heat rate at the triple contact line $\dot{q}'$ that should be measured in order to explain the fraction of the boiling heat flux through only quenching with pure thermal conduction heat transfer and triple contact line evaporation. Figure 4.32 shows that $\dot{q}'$ should be in the order of 20-30 W/m, irrespective of the angle of inclination. While the order of magnitude matches with our evaluation of $\dot{q}'$ based on single bubble analysis in Chapter 3. (~5 W/m), the difference is still significant.

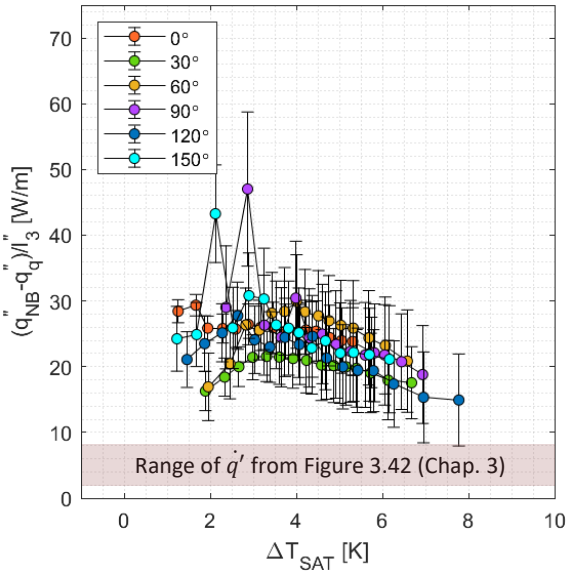

Figure 4.32. Estimated evaporative heat transfer at the triple-contact line from the measurement of boiling heat flux and temperature.

Interestingly, Figure 4.32 also shows that $(q_w'' - q_q'')/l_3''$ is quite independent from the wall superheat and inclination angle, which matches with the results of the single bubble analysis shown in Chapter 3. The independence from the wall superheat also appears to be an unusual characteristic of triple contact line evaporation. One can write q_3'' from equation by introducing the heat transfer coefficient h_3 related to the triple contact line evaporation,

$$q_3'' = \dot{q}' l_3'' = h_3 l_3'' (T_w - T_{sat}) \tag{4.19}$$

With h_3 in W/m/K. Since q' does not depend on $(T_w - T_{sat})$, then the heat transfer coefficient h_3 is proportional to $(T_w - T_{sat})^{-1}$. Therefore h_3 appears to increase as the wall superheat decreases, which is a surprising result making sense in the case of triple contact line evaporation once we know that $\dot{q}'$ is temperature independent. The discrepancy between the measured evaporation heat rate from $\left(q''_w - q''_q\right)/l''_3$ and measured from single bubble analysis (c.f. Chapter 3) might be explained in different ways. The lack of spatial resolution in our phase-detection recording results in small bubbles being missed and therefore an underestimation of l''_3. While a factor 2 is possible, it seems unlikely that the underestimation of l''_3 could explain the totality of the discrepancy which would require l''_3 to be ~5 times larger. An underestimation of the quenching heat flux q''_q is also possible as previously discussed. Such underestimation would bring closer $\left(q''_w - q''_q\right)/l''_3$ and the value of $\dot{q}'$ based on single bubble analysis. Further investigation is necessary to clear out this discrepancy.

4.9. Peculiarities of bubbles coalescence for low surface tension fluid

Schweizer [96] reported observation of liquid droplet trapped inside vapor bubble during coalescence in reduced gravity. The droplets quickly evaporate resulting locally in a high heat transfer in FC-72. We report similar observation for liquid nitrogen on different surface inclinations. Figure 4.33 to 4.35 shows different occurrence of droplet trapping during bubble coalescence in boiling liquid nitrogen from superposed phase-detection (the colored area indicates vapor in contact with the boiling surface) and shadowgraphy recordings (with a gray colormap).

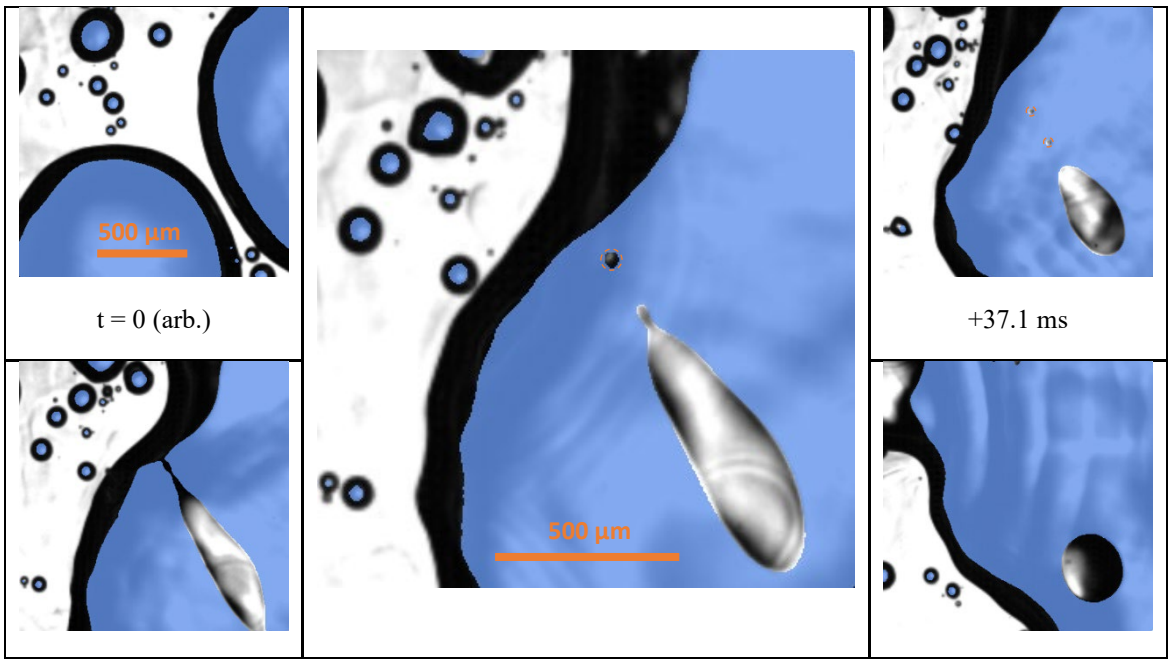

+30.0 ms	+32.9 ms	+70.0 ms

Figure 4.96. Formation of a large droplet trapped during coalescence in pool boiling nitrogen with upside-down heated surface (α~179º), viewed on shadowgraphy images with phase-detection as overlay (the blue overlay corresponds to vapor in contact with the heated surface).

In Figure 4.35, the droplet is trapped during the coalescence of 2 bubbles. However, rather than the droplet evaporating (as in Figure 4.33 and 4.34), one can see that the triple contact line breaks and pass around the droplet as the coalesced bubble slides on the surface.

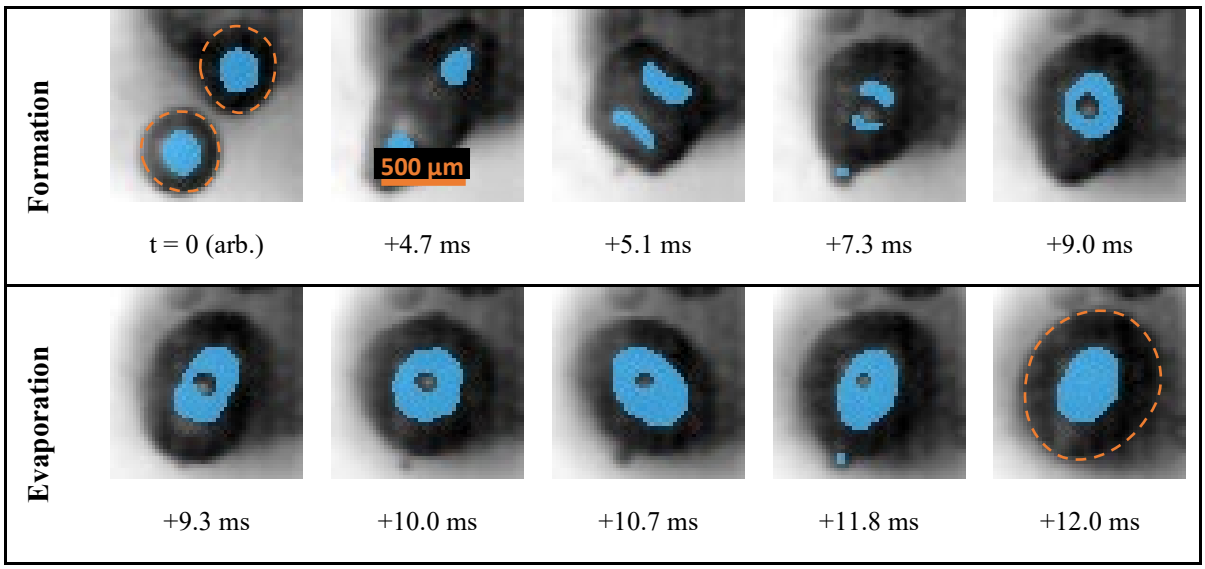

Figure 4.97. Droplet trapping during coalescence in horizontal pool boiling nitrogen (α~0º) followed by its evaporation, viewed on shadowgraphy images with phase-detection as overlay (the blue overlay corresponds to vapor in contact with the heated surface).

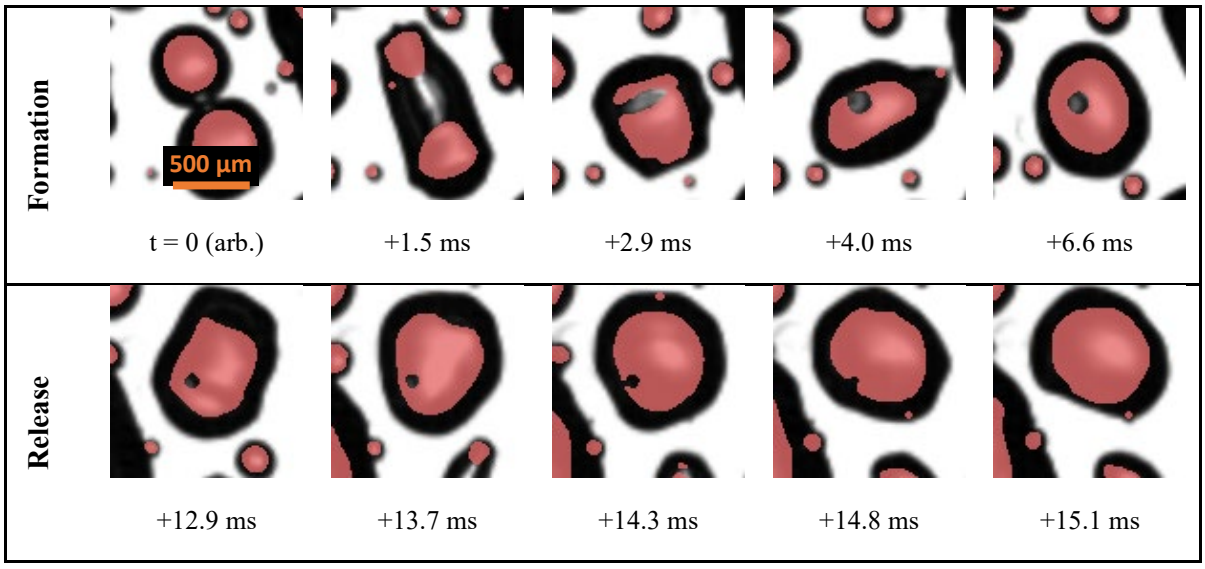

Figure 4.98. Escape of a droplet trapped during coalescence in upside-down horizontal pool boiling nitrogen (α~179º), viewed on shadowgraphy images with phase-detection as overlay (the red overlay corresponds to vapor in contact with the heated surface).

As suggest by Schweizer [96], low surface tension seems to be the key to explain this phenomenon and liquid nitrogen has a surface tension comparable to FC-72. Unfortunately, we cannot precisely evaluate the heat transfer associated with these trapped droplets. However, while this phenomenon is not difficulty to spot due to the large of number of coalescence events, its probability of occurrence seems low. Therefore, it should not affect the boiling heat transfer coefficient.

4.10. Effect of buoyancy on the critical heat flux

We saw from the boiling curves performed for nitrogen boiling that the effect of inclination of the heated surface appears mostly at high heat flux, in particular near DNB. In particular, the lack of efficient mechanism for large coalesced bubbles (or vapor patches) to lift-off from the heated surface when inclined past 90° (i.e., with the heated surface facing downward) results in a premature increase of the dry area fraction and a degradation of the boiling heat transfer. For the same reason, the critical heat flux (CHF) also reduces with increasing inclination angle, above 90°. Figure 4.36 shows a plot of the critical heat input against the angle of inclination. The highest CHF value was measured for the heated surface being horizontal upward facing. However, for an inclination angle up to 90º, the variations of critical heat flux are small enough, within few percent, and the CHF values can be considered independent of the inclination angle. A significant degradation of the critical heat flux is observed for increasing inclination angle past 90° with a minimum found close to 180°. As the inclination angle of the heating surface is getting closer to 180°, we find a higher variability (not shown) on when DNB occurs and at which heat flux. This variability is consequence of the dry-out and rewetting phases discussed in Section 4.3, which is particularly prominent when the heated surface is upside-down. The model of Brusstar and Merte [97] is shown in Figure 4.36. This resulting formulation of the CHF as a function of the inclination angle is followed,

$$q''_{\mathrm{CHF}}(\beta) = \begin{cases} q''_{\mathrm{CHF}}(\beta = 0)\ for\ \beta \leq \pi/2 \\ q''_{\mathrm{CHF}}(\beta = 0)\sqrt{|\sin\beta|}\ for\ \beta > \pi/2 \end{cases} \tag{4.20}$$

With β the inclination angle of the heating surface in radian and $q''_{\mathrm{CHF}}(\beta = 0)$ the critical heat flux when the heated surface is horizontal facing upward. This simple model is based on the idea that CHF scales with the velocity at which cold liquid is supplied to the heated surface. For a surface inclined at more than 90°, the rewetting of the surface is limited by the velocity of large vapor patches sliding on the surface. Brusstar and Merte [97] derived the characteristic velocity of the vapor patches and assumed that this velocity

equates the flow velocity of the liquid rewetting after sliding of the patches. The derivation was done by equating the drag force, limiting the movement of the patches on the surface and the buoyancy tangential to the heated surface, promoting sliding of the patches. The model proposed by Brusstar and Merte's model tends to underpredict the value of critical heat flux measured, in particular for inclination angle near 180°. Despite the model predicting the correct trend of CHF with the inclination angle. It is rather clear that DNB on inclined surfaces is more complex than described. A more physically accurate depiction of DNB might come from the stochastic bubble percolation model proposed by Zhang et al. [91]. An important outcome of the work of Zhang et al. [91] is the evidence that, at the triggering moment of DNB, due to coalescence, the bubble footprint area distribution becomes scale-free (i.e, a power law with an exponent lower between -1 and -3).

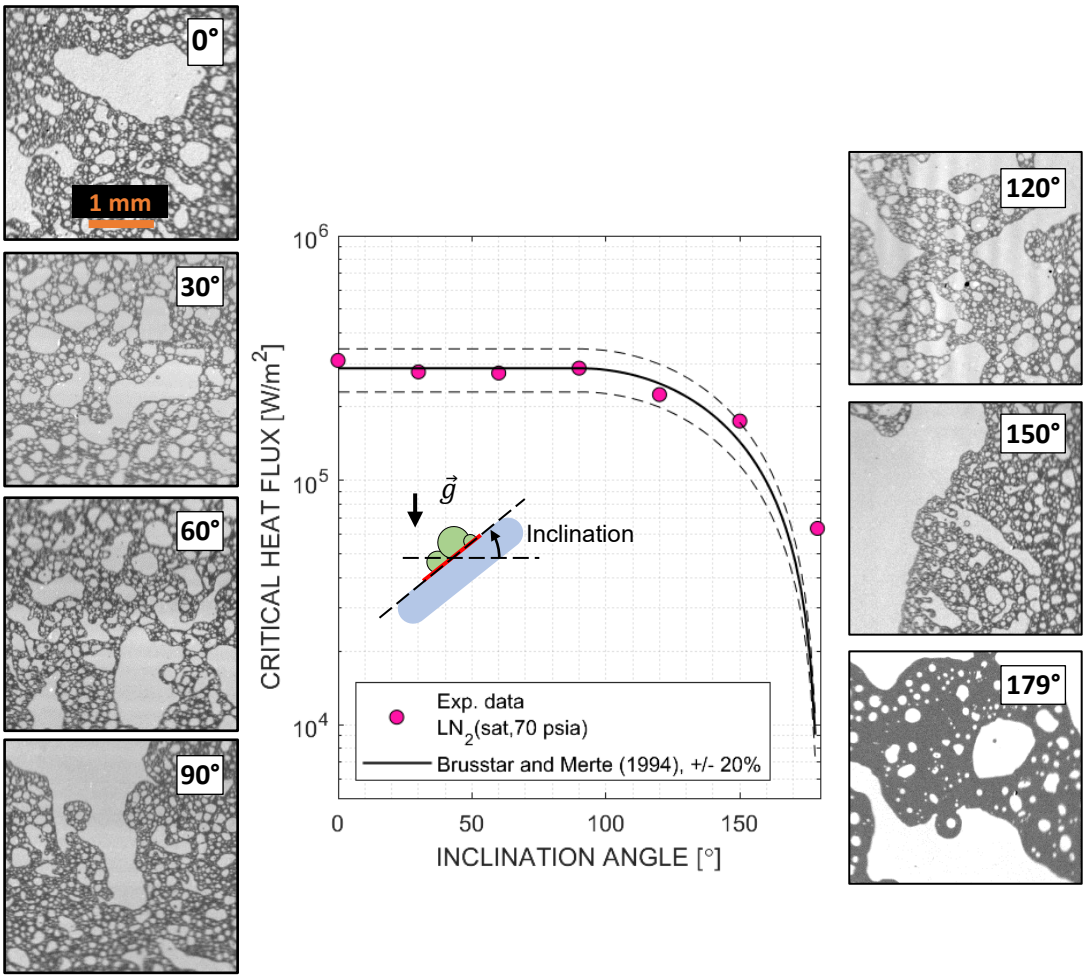

Figure 4.99. Plot of the critical heat flux for different inclination angles of the heating surface with phase-detection images of the last recorded boiling step.

Figure 4.37 shows the distribution of bubbles footprint area measured at the last boiling step before reaching DNB for different inclination angles. Despite different values of heat flux, all the distribution are well fitted by power law distribution. As a reminder from Figure 4.6, for lower heat flux, the footprint area distribution tends to an exponentially damped function rather than a power law. At DNB, all power law distributions appear to have an exponent close to -2. The case with an inclination angle of 179° appears supercritical (i.e., with a distribution tail lifting up above the power law distribution) which is characteristic of post-DNB conditions. The percolation model presented by Zhang et al. [91] assumes the boiling heat transfer is in equilibrium, i.e., that the boiling parameters (e.g., the bubble density) oscillates only slightly over time around an average value. When boiling upside-down, this equilibrium is broken at least on short time scale as we saw with the presence drying and rewetting phases in Section 4.4. From a model point of view, it may be useful to see whether the percolation model proposed by Zhang et al. [91] can be leveraged to treat such situations, where sliding of bubbles and vapor patches impacts the boiling crisis.

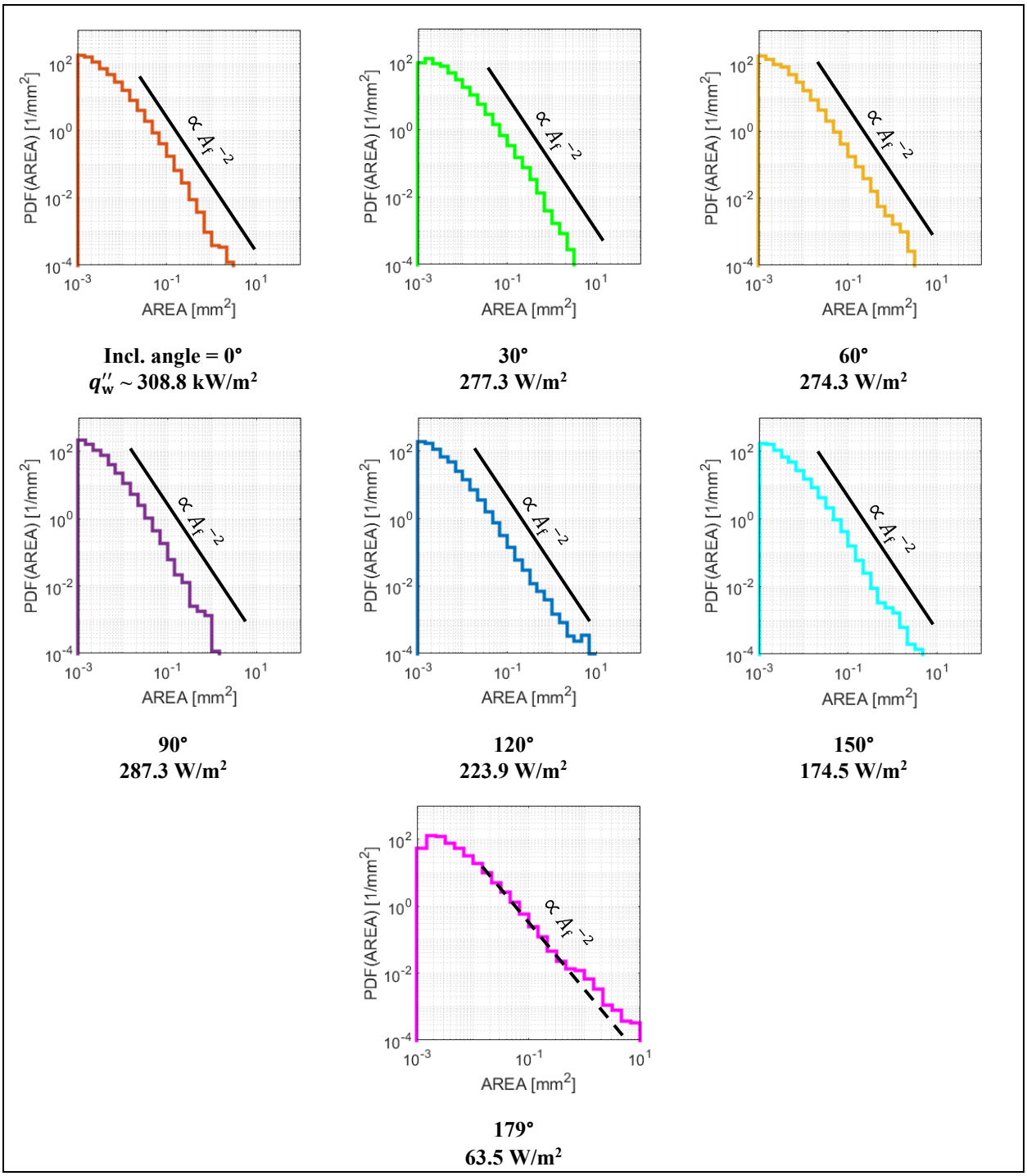

Figure 4.100. Probability distribution function of the bubbles' footprint area at the last recorded boiling step before reaching DNB, for nitrogen boiling on an inclined heated surface from 0° (horizontal upward-facing) to 179° (horizontal downward-facing).

4.11. Summary of the section

In this section we showed the results collected during the experimental campaign for nitrogen pool boiling on inclined surface with the angle ranging from 0º to 179º. We showed that the boiling heat transfer can be decomposed between an evaporation term, likely resulting from triple contact line evaporation, and a quenching term associated with transient conduction in the liquid. We showed that buoyancy doesn't play a role in the nucleate boiling process except near and at DNB. We showed that the triple contact line density increases linearly with the heat flux up to DNB and doesn't appear to be affected by the surface inclination. This suggests that nucleate boiling heat transfer is dominated by heat transfer mechanism whose heat flux depends linearly on the triple contact line density. However, we showed that the triple contact line evaporation cannot explain more 20% of the total boiling heat flux. Estimates of the quenching heat flux leveraging the phase-detection recordings shows that quenching also accounts for 10-20 % of the boiling heat flux when only transient conduction is consider, leaving roughly 60% of the boiling heat flux unexplained. This led us to suspect that a convective heat transfer component due to liquid agitation from bubble induced turbulence might significantly increase the quenching heat flux. Finally, the most significant impact of buoyancy appears at DNB. Our measurements showed that the critical heat flux decreases rapidly with the increasing inclination angle past 90º, from ~310 kW/m2 on a horizontal upward facing heated surface to ~65 kW/m^2 for an inclination angle of ~179°. The decrease in the critical heat flux is seemingly connected to the fact the rate of coalescence appears to increase with increasing angle of inclination. All bubble footprint area distributions tend a power law with an exponent -2 at DNB, irrespective of the value of critical heat flux and the inclination angle, corroborating the findings of Zhang et al. [91]

5. EFFECT OF CRYOGENIC FOULING ON THE BOILING HEAT TRANSFER

We present in this Chapter new insights on the effect of boiling surface contamination from carbon dioxide dissolved in liquid nitrogen. We showed that initial contamination of industrial-grade liquid nitrogen of does not appear to impact the boiling process when the surface is boiled for less than a minute, even at high heat flux (see comparison between boiling curves with industrial and high-purity grade liquid nitrogen in Figure 2.30). However, cryogenic fouling appears to be a major source of repeatability issues in cryogenic boiling measurement published in literature, as discussed in Chapter 1. The presence fouling is mostly speculative due to the lack of detection capabilities of most published studies. When does cryogenic fouling appear and how it impacts the boiling process are currently opened questions that needs to be answer to mitigate issues of repeatability in cryogenic experiment, and allow data comparisons between studies that potentially suffer from surface contamination. To probe the effect of cryogenic fouling, we produced highly contaminated liquid nitrogen by saturating industrial liquid nitrogen with CO_2. We show in this Chapter that CO_2 fouling can drastically change the boiling process (in particular in terms of active nucleation site density and bubble size), and more surprisingly improve the boiling heat transfer.

The procedure to produce CO_2-saturated liquid nitrogen consisted in slowly injecting about 2 Sm^3 of industrial gaseous CO_2 inside our 120 L liquid nitrogen cylinder over 24 hours. The nitrogen cylinder was then left pressurized for about 12 hours close to the operating pressure of 480 kPa. The concentration of CO_2 at saturation was estimated by using the data published by Rest et al. [50], about 13 ppm(mol) at 480 kPa (i.e., about 9.5 ppm(vol)). We suspect that boiling industrial liquid nitrogen without artificially increasing dissolved CO_2 in industrial-grade liquid nitrogen for longer period of time (i.e., much more than 1 min, typically use for our boiling curve) would have yield similar observations of cryogenic fouling than shown in this Chapter, but we would not be able to assess the initial CO_2 concentration in the nitrogen as we lack the capability of measuring it. Note that CO_2 is not the only dissolved contaminant that could be found in liquid nitrogen. A very common dissolvable contaminant is water that can easily be picked up from the humidity in the air in unsealed systems. In fluids with lower boiling point such as hydrogen, one might deal as well with presence of dissolved nitrogen or oxygen as potential foulant.

5.1. Experimental observations

5.1.1. Visual observation of cryogenic fouling

When using liquid nitrogen saturated with CO_2, it suffices to boil it at high heat flux to observe formation of a solid deposit on the surface. Figure 5.4 shows phase detection images obtained during boiling with a constant heat input using liquid nitrogen saturated with CO_2. The heated surface is initially free of contamination, which is ensured by bringing it to film boiling and letting it reach a sufficiently high

temperature. In this test, the nitrogen is boiled during 60 seconds at a constant heat input of 25.6 ± 0.4 W (for which we can estimate that the boiling heat flux is ~232.3 kW/m^2 when the surface is initially free of contamination). The presented test was performed at 480.3 ± 7.9 kPa. The solid deposits of CO_2, i.e., dry ice, appears as black dots on the snapshots presented in Figure 5.4. The black appearance of the deposits indicate low reflection from the phase-detection LED light. This low reflection is due to the index of refraction of dry ice (~1.45 from the measurements of Tempelmeyer and Mills [98]) being much closer to sapphire's (~1.7 from Ref. [77]) than the index of refraction of liquid and gas nitrogen (1.2 and ~1, respectively). The vapor and liquid nitrogen appear white and dark gray on the phase-detection recordings, respectively. The test shows a clear buildup of deposits at highly preferential locations as more nitrogen is boiled. The deposits get as large as 20 to 50 micrometers in diameter (i.e., 2 to 4 px) at the end of the test (i.e., at t+63.5 s). While the size of CO_2 deposits increases over time, it is clear from the recording that the number of deposition sites is roughly constant during the length of the test.

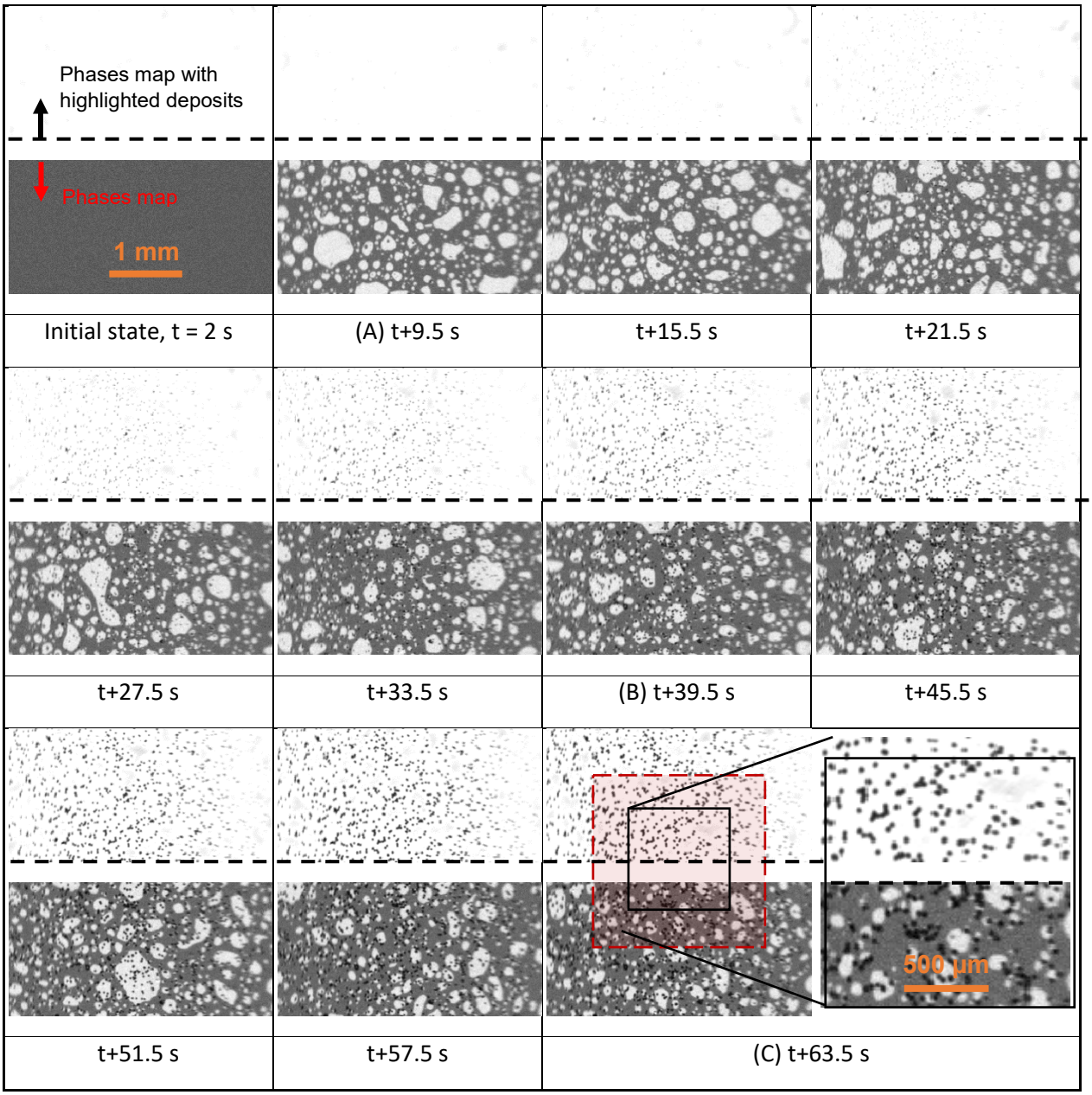

Figure 5.101. Successive phase-detection images of the heated surface during CO_2-saturated liquid nitrogen boiling. Each image is divided into two parts. The bottom part shows an instant map of all phases ($N_{2,Liq}$, $N_{2,Vap}$ and $CO_{2,Sol}$) in contact with the heated substrate, while the top part shows the solid CO_2 deposits only.

5.1.2. Connection between nucleation events and deposits formation

We can show that the preferential locations of CO_2 deposits seen in Figure 5.4 correspond to actives nucleation sites. Figure 5.5 shows a comparison between the locations of the deposits and active sites on the heated surface. Figure 5.5 (left) shows the contour of the deposits after significant build up taken roughly after boiling for 1 minute (corresponding to image C in Figure 5.4). Figure 5.5 (right) shows a superposition between the map of nucleation activity evaluated when no deposits is detected (i.e., at A in Figure 5.4) and

the contour of the deposits observed after 1 minute of boiling. Note that the exact locations of active nucleation sites are difficult to find. Instead, we give the nucleation activity per pixel, i.e., the number of nucleation events N that each pixel sees per second. To do so, we sum over time the binary maps which only contain the first visible footprint of every bubble (see Chapter 2 for more details).

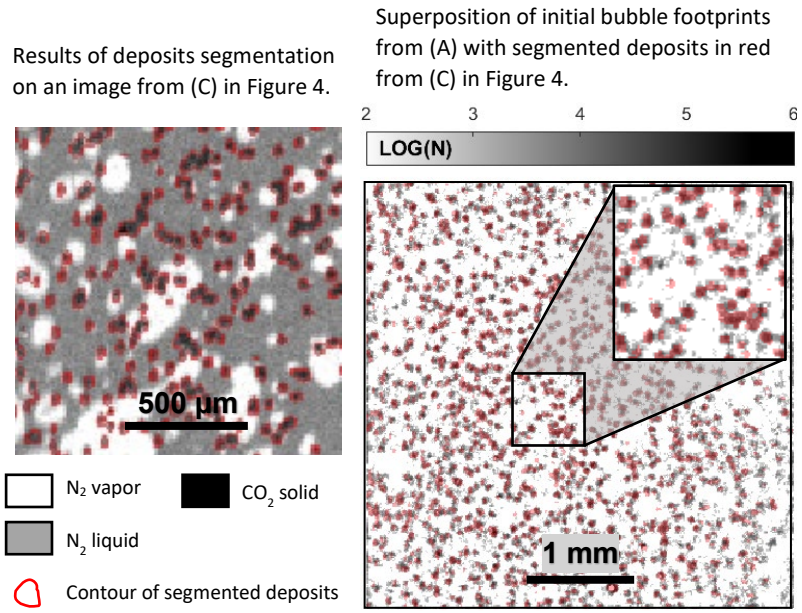

Figure 5.102. Carbon dioxide segmentation using phase-detection from last recorded video ((C) in Figure 5.4) (left) and comparison between the positions of deposits and the nucleation activity shown as $ln\,N$ with N in [nucleation events /s] obtained at the beginning of the experiment ((A) in Figure 5.4) (right).

The deposits later observed (in red) in the boiling tests overlap very well with the locations where high number of nucleation events (colored in black in Figure 5.5 (right)) are observed early in the test, before any deposit becomes apparent. With the observation of highly punctual deposits, the overlapping between nucleation activity and deposits supports the idea that the deposits forms upon evaporation of the liquid nitrogen by precipitating carbon dioxide. The deposition phenomenon is a particular case of surface crystallization fouling, also found in boiling studies with water (e.g., see Ref. [99]). The quasi-fixed number of deposition sites observed throughout the duration of the constant-heat input test along with the observation of Figure 5.5 suggests that the fouling does not increase the nucleation sites density for constant heat input.

The highly punctual shape of the deposits is rather interesting and is seemingly the consequence of where the nitrogen is warmed up and evaporated during bubble growth, which therefore suggests a rapid initial growth. Some ring-like depositions, typical of microlayer evaporation in water (e.g., see Ref. [100]), were

rarely found on fouled surface in nitrogen. An example of such deposits is visible on the test cases shown in Appendix B (Figure 5.24) and Figure 5.19. Instead, the more prevalent punctual appearance of the deposits contradicts the more dispersed deposition we expect from the observation of nitrogen bubble growth. Figure 5.6 shows the typical growth of a nitrogen bubble on a clean surface at low wall superheat. No microlayer, normally visible with phase-detection, was observed in the tested conditions with or without contamination. The top images in Figure 5.6 show the bubble shadow with an overlay of the segmented shadow (in pink) and footprint (in blue) used to evaluate the bubble equivalent radiuses. The equivalent bubble and footprint radiuses, noted R and R_f, are derived from surface areas of bubble shadow and bubble footprint as $\sqrt{A/\pi}$, respectively. A plot of the equivalent radiuses of our example bubble in clean nitrogen is shown in Figure 5.6 (bottom).

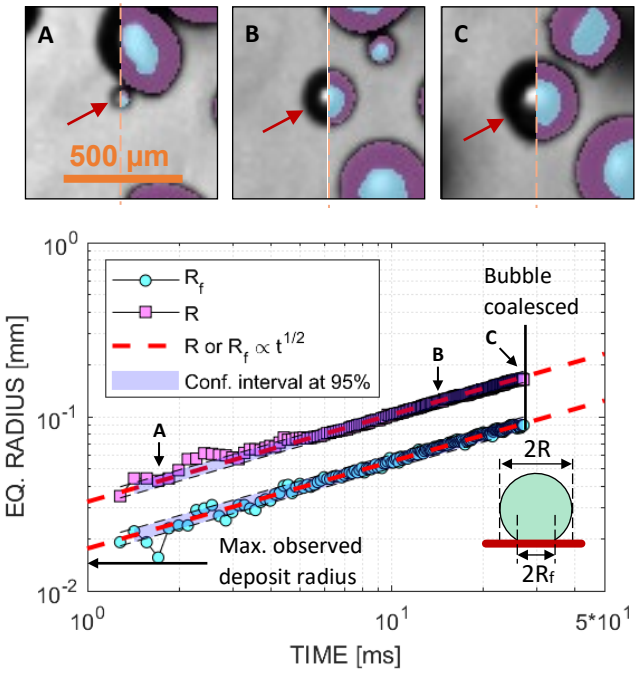

Figure 5.103. Typical equivalent bubble radiuses ($R \equiv \sqrt{A/\pi}$) during growth with clean nitrogen pressurized at 491.8 kPa on a heating surface at ~1.8 K wall superheat. The bubble marked by a red arrow is analyzed.

One can see that the optical radius (i.e., the equivalent radius of the shadow) and the footprint radius are proportional ($R \propto R_f$), both growing as $\sqrt{t}$, typical of a heat diffusion-controlled growth regime. This observation allows us to evaluate where the deposits are expected to precipitate. The volume of the bubble V and therefore the evaporated mass of liquid needed to sustain the bubble growth scales as R^3. The liquid evaporation rate is given by the time-derivative of the evaporated mass (i.e., $\sim dV/dt$), which then scales

as $R^2\dot{R}$. In order to crystalize at the surface, the dissolved CO_2 has to come out of solution near the surface, i.e., likely near the triple contact line. Therefore, the area on which the CO_2 will precipitate should correspond to the surface area swiped by the triple contact line. During a time dt, this area dA is given by $2\pi R_f \dot{R}_f dt$. Using the proportionality between R_f and R, dA can be rewritten as $2\pi R\dot{R}dt$. The mass of CO_2 deposited per unit surface area is then given by dV/dA which scales with R (or equiv. with R_f). Using this reasoning, we should have expected the thickness of the deposited CO_2 layer to increase as the bubble footprint grows, producing a wedge thickening radially outward. However, much smaller deposits than the bubbles footprints are systematically found on the heating surface. We don't have an explanation for this apparent oddity.

5.1.3. Sublimation temperature of the deposits

Solid deposits can be easily identified on phase-detection images as shown on Figure 5.4. However, it is much more complicated to confirm their composition. Since liquid nitrogen is saturated with CO_2, it is clear that it should be at least one of the foulants, if not the main one. Ex-situ analyses are not feasible as the deposits disappears when the temperature of the boiling surface is brought back to room temperature. Instead, we could estimate the temperature of sublimation of the deposits from phase-detection recording by bringing the heated surface to film boiling. The deposits completely disappeared when the temperature measured by the RTDs reached a temperature between 132.7 ± 3 and 139.6 ± 3 K, which was consistent among multiple measurements. The corresponding temperature at the heated wall can be evaluated assuming that most of the heat generated by ITO is conducted in the sapphire rather than dissipated by the vapor blanket. Then, the problem consists in solving the three-dimensional transient temperature field in the substrate under constant heat input with temperature-dependent properties and adiabatic boundary conditions. According to this reasoning, we deduced that sublimation is occurring at the heated wall temperature between 144 ± 3 and 154 ± 3 K. The temperature observed is lower than the sublimation temperature of bulk CO_2 at the operating pressure (about 220 K at 480 kPa). Instead, the low sublimation temperature band of the CO_2 deposits appears to be consistent with an under-saturated sublimation process limited by molecular diffusion of carbon dioxide gas in nitrogen gas. The model used to evaluate this process is detailed in Appendix A along with phase-detection observations of the process and the temperature measurements. Figure 5.7 shows the modeled deposit mass (primary y axis) or sublimation mass flux (secondary y axis) vs. temperature for an initial deposit mass of 2.1 ng of CO_2, corresponding to a cylindrical deposit with a radius of 15 μm, and 2 μm thick (shown with a thick solid black line).

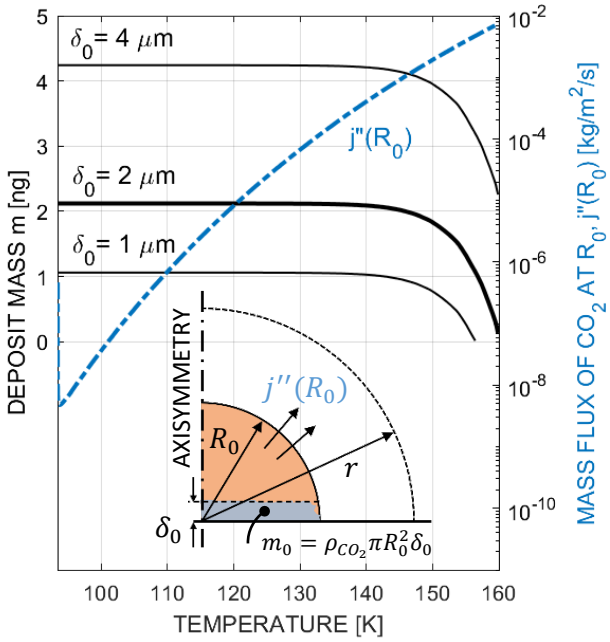

Figure 5.104. Plot of modeled mass deposit and sublimation mass flux against temperature during the sublimation transient shown in Figure 5.17 (Appendix A). The mass of the deposit m is plotted as solid black lines for different initial thicknesses (1, 2 and 4 μm), while the sublimation mass flux at the solid gas interface (i.e., at $r = R_0$) is shown with the dashed blue line.

The actual geometry and thickness of the deposits remains uncertain. However, their thickness is expected to be in the order of a few microns based on bubbles size, nucleation frequency, concentration of carbon dioxide dissolved in nitrogen and duration of the test. We assumed a baseline case of 2 microns in Figure 5.5, but also included results for thicker (i.e., 4 μm) and thinner (i.e., 1 μm) deposits. The solutions plotted in Figure 5.5 shows a rapid decrease of the deposit mass (shown by solid black lines) above ~140 K, no matter the initial deposit thickness. This is a direct consequence of the rapid increase of the CO_2 vapor pressure with temperature, which results in a rapid increase of the sublimation mass flux of CO_2, $J''(R_0)$ (plotted as blue dashed line). Despite its simplicity, the model allows us to explain the sublimation of the CO_2 deposits at temperatures much lower than the CO_2 saturation temperature. However, we can categorically exclude that the deposits consist of water.

5.2. Consequences of carbon dioxide deposits on boiling heat transfer

5.2.1. Case of boiling heat transfer at constant heat input

Signs of changes in the boiling dynamics due to the deposits are not immediately apparent in the tests conducted at constant heat flux (see Figure 5.4), but can be elucidated by estimating the surface area occupied by each phase throughout the test. Figure 5.8 shows the fraction of the heated surface covered with CO_2 deposits, noted α_S. The colored gray overlay shows the uncertainty associated with the segmentation of the deposits. During the first 25 seconds, the deposits are too small to be properly segmented and are therefore excluded from the plot. The border of the phase-detection images may be slightly out of focus, rendering the deposits blurry. Thus, only the central part of the images is analyzed (shown by red overlay in Figure 5.4, image (C)) to avoid introducing estimation errors. α_S increases throughout the test as more and more nitrogen is boiling on the heated surface, reaching about 17.8 % after 60 seconds of boiling.

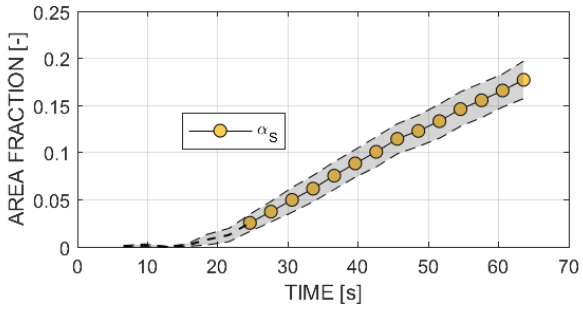

Figure 5.105. Measurement of the area fraction of the heated surface covered by carbon dioxide deposits during boiling of contaminated nitrogen at constant heat input. The gray overlay gives the measurement uncertainty due to the segmentation accuracy.

The fluid phase present on top of the CO_2 deposits cannot be evaluated from the phase-detection images. Therefore, it is necessary to evaluate dry and wetted area fractions based on the data only where the fluid phase is resolved. To do so, we note Σ_V, Σ_L and Σ_S the portions of the boiling surface visibly covered with vapor, liquid and solid, respectively, and Σ_T defined as the total surface (i.e., $\Sigma_V \cup \Sigma_L \cup \Sigma_S$). See Figure 5.7 for an illustration of the notation used.

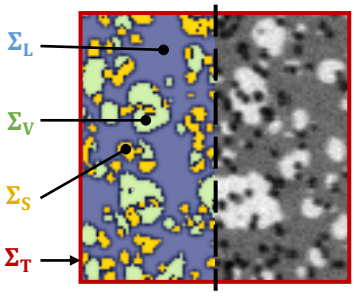

Figure 5.106. Illustration of the notation used to describe each portion of the heated surface. The left part of the phase-detection image is colorized for annotation.

Figure 5.8 shows plots of $\beta_L$and β_V, defined as $A(\Sigma_L)/A(\Sigma_V \cup \Sigma_L)$ and $A(\Sigma_V)/A(\Sigma_V \cup \Sigma_L)$, respectively, with the errors bar indicating the standard deviation of the variations over time. The surface $\Sigma_V \cup \Sigma_L$ is simply obtained by excluding Σ_S from Σ_T. As Σ_S changes over time (as shown in Figure 5.6), in order to limit our analysis to the surface that is never covered by the CO_2 deposits, the values of β_V and β_L shown in Figure 5.8 are calculated on the portion of the surface $\Sigma_V \cup \Sigma_L$ at the latest time (i.e., image C in Figure 5.2). This choice ensures that the surface eventually covered by the deposits is excluded from the analysis to avoid introducing uncertainties related to the segmentation of the deposits, since, as mentioned before, we cannot determine if the deposits are covered by the liquid or vapor. A value of α_V defined as $A(\Sigma_V)/A(\Sigma_T)$ and measured before formation of the deposits is also shown in Figure 5.8. As shown, the initial α_V and β_V are close, within a difference of 3%, indicating that the measurements over $\Sigma_L \cup \Sigma_V$ (i.e., β_V) are fairly representative of the overall α_V (i.e., the vapor fraction measured over Σ_T). The small difference may come from the higher probability of finding vapor over Σ_S than over $\Sigma_L \cup \Sigma_V$, as Σ_S covers the locations of active nucleation sites (as discussed in Section 5.1.2.). Finally, the average substrate temperature measured by the RTDs is shown at the bottom of Figure 5.8. A band of ± 0.25 K indicating the typical repeatability variation at 1-σ (as shown in Chapter 2 Figure 2.30) is also plotted.

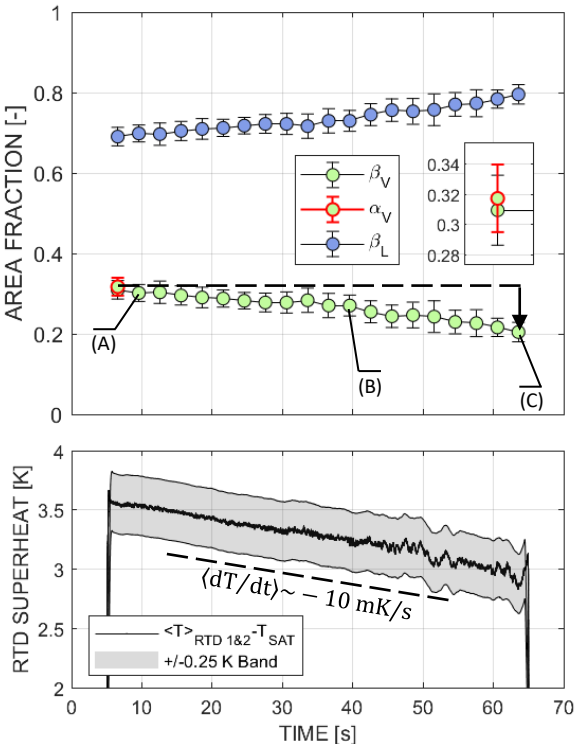

Figure 5.107. Measurements of wetted and dry area fractions, and substrate temperature during boiling of contaminated nitrogen at constant heat input. The x-axis is common to both plots.

The results shown in Figure 5.8 hint to changes in the boiling dynamics as carbon dioxide precipitates on the surface. The substrate temperature, measured by the 2 RTDs, decreases at a rate of -0.6 K/min, indicating an increase of the boiling heat transfer coefficient over the duration of the test. We observe a significant decrease of the dry area fraction β_V (plotted in green) over the duration the test, at a rate of -9.6%/min. The wetted fraction β_L increases at the same rate. The decrease of β_V (or equiv. increase of β_L) coincides with a decrease in the likelihood of finding bubbles with large footprint when the surface is increasingly contaminated with CO_2 deposits. Figure 5.9 shows a plot of the contribution of the bubbles with a footprint of size A_f to the dry area fraction α_V, calculated as $N_\mathrm{B}''\mathrm{p}(A_\mathrm{f})A_\mathrm{f}$, where $\mathrm{p}(A_\mathrm{f})$ is the probability distribution function of having a bubble with a footprint area A_f, and N_B'' the average number density of bubbles on the surface at any given time. In brief, $N_\mathrm{B}''\mathrm{p}(A_\mathrm{f})$ is the average number density of bubbles footprint of area A_f found on the boiling surface, and the integral of $N_\mathrm{B}''\mathrm{p}(A_\mathrm{f})A_\mathrm{f}$ in dA_f (i.e., the area under the distributions in Figure 5.9) gives the dry area fraction α_V, i.e., evaluated over Σ_T. As discussed before, the presence of the deposits complicates significantly the segmentation of individual bubbles and the measurement of the bubbles footprint area necessary to evaluate $N_\mathrm{B}''\mathrm{p}(A_\mathrm{f})A_\mathrm{f}$. Thus, for the sake of simplicity, the portion of Σ_S that may be covered by vapor is ignored in its calculation. When comparing the plots of $N_\mathrm{B}''\mathrm{p}(A_\mathrm{f})A_\mathrm{f}$ taken at different times throughout the test (shown in Figure 5.9 at +9.5

s, 39.5 s and + 63.5 s, corresponding to images A, B and C in Figure 5.2, respectively), we observe a noticeable decrease of the large bubbles contribution.

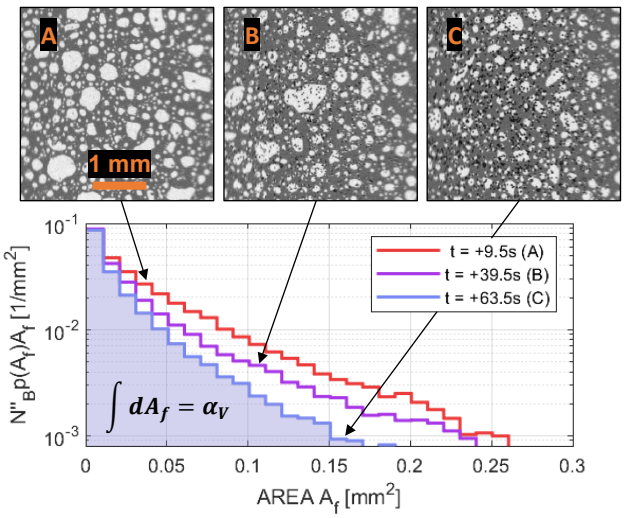

Figure 5.108. Plot of the contribution of bubble footprint of size A_f to the overall dry area fraction α_V, given by $N_B'' p(A_f) A_f$. The different curves show the $N_B'' p(A_f) A_f$ at the beginning (in red), in the middle (in purple) and at the end of test (in blue). Phase-detection images A, B and C are shown in Figure 5.4 for illustration.

Since it did not appear that the number of nucleation site increased throughout the test as the deposits form on already active sites (see Sections 5.1.1 and 5.1.2), the heat transfer enhancement observed at constant heat input must be related to an overall decrease of the nucleation temperature at sites covered with CO_2 fouling. This would be consistent with the decrease in the likelihood of having large bubble.

5.2.2. Case of boiling heat transfer with cycling heat input

In order to further explore the effect of cryogenic contamination on the boiling heat transfer, we performed boiling curves with and without dissolved CO_2 in the liquid nitrogen. Figure 5.12 shows cycling boiling curves with CO_2-saturated nitrogen (shown as blue and green circular markers) and compare them to reference boiling curves performed with clean nitrogen (shown as red and yellow square markers). Unlike the case at constant heat input shown previously, cycling up and down the heat input while boiling contaminated nitrogen allows to dissociate the locations of the normally active nucleation sites (i.e., without CO_2 contamination) and the locations of the deposits (which then depend on the previous boiling steps that the heat surface went through), for a given heat input. The heat input generated by the ITO measured over time is shown in Figure 5.12 for each case, with colored overlays indicating the different portions of the power cycles. Each heat input curve is composed of 20 boiling steps lasting 3 seconds. Temperature

measurement and video recordings are taken during the last second of each step, when the boiling process has reached equilibrium. The 2 cycling boiling curves differ from their maximum heat input. The heat input goes up to 40 W (i.e., near the critical heat flux with uncontaminated nitrogen, measured at 40.9 ± 1.1 W averaged over multiple data points) in the high heat input cycling case (shown in blue), while it limited to 10 W in the low heat input case (shown in green). The difference of maximum heat input translates in different amount of CO_2 deposited on the surface (the mass of evaporated liquid nitrogen being smaller at lower heat input). In both cases, the heat input is increased, decreased, and then increased and decreased again, with each series of boiling steps labeled 1I, 1D, 2I and 2D, respectively. The heated surface is initially free of contamination. The reference boiling curves represented by square markers are performed with uncontaminated nitrogen, either by increasing (in red) or decreasing (in yellow) the heat input. When the heat input is increased (see red squares in Figure 5.12, bottom), an initial heat input step at high heat input is used to pre-activate nucleation sites and prevent a temperature overshoot at low heat input. Initial high heat input step was not necessary in the power cycling cases. The tests are performed close to saturation (~0.4 K below T_{SAT}) at 480.7 ± 4.9 kPa. The blue and green lines (in between the blue and green markers) show the trace of the substrate temperature measured by the RTDs for their respective case.

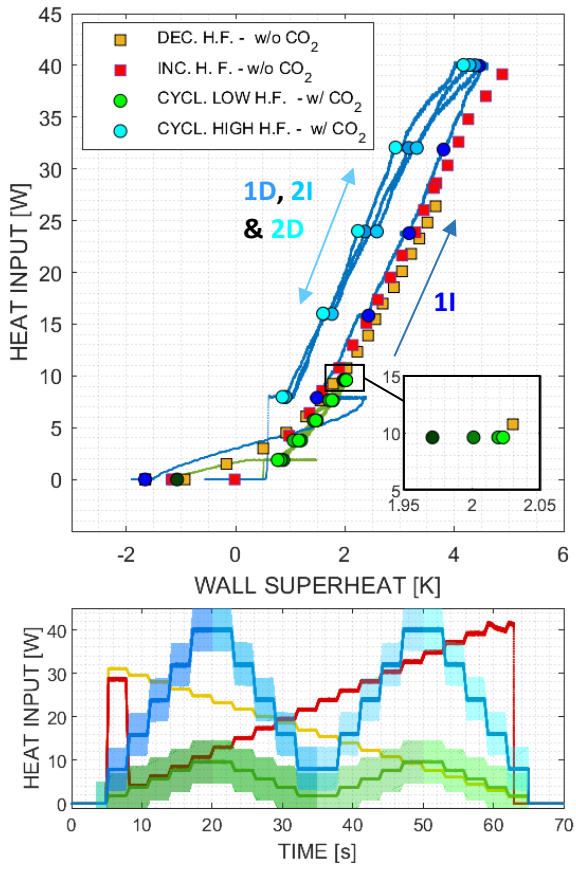

Figure 5.109. Boiling curves for saturated nitrogen pool boiling with CO_2 saturation performed by cycling the heat input (blue and green circular markers). The boiling curves shown with square marker are performed without CO_2 contamination by increasing (in red) and decreasing (in yellow) the heat input.

The boiling curves in yellow, red and green overlap, which indicates negligible or no contamination at all on the heating surface. When contaminated nitrogen is boiled at a sufficiently high heat flux, an increase of the boiling heat transfer coefficient (see curve in blue) is observed. This is highlighted by a shift of the blue boiling curve toward lower wall superheat. Instead, when boiling occurs at low heat input (as illustrated by the test shown in green in Figure 5.12), the boiling curves do not show evidence of heat transfer improvements, i.e., the deposit do not have time to form, suggesting that both the heat flux and time dictates the amount of CO_2 deposition.

The phase-detection images for the reference cases, i.e., without CO_2 contamination (shown with red and yellow square markers in Figure 5.12), are presented in Figure 5.13. Figure 5.14 shows the phase detection images for the boiling case with high heat input cycling (shown by blue circular markers in Figure 5.11). In Figure 5.s 13 and 14, each image is representative a particular boiling step. For each column, the heat input is approximately the same, and therefore the images are sorted chronologically from left to right when the heat input is increased, and from right to left when the heat input is decreased.

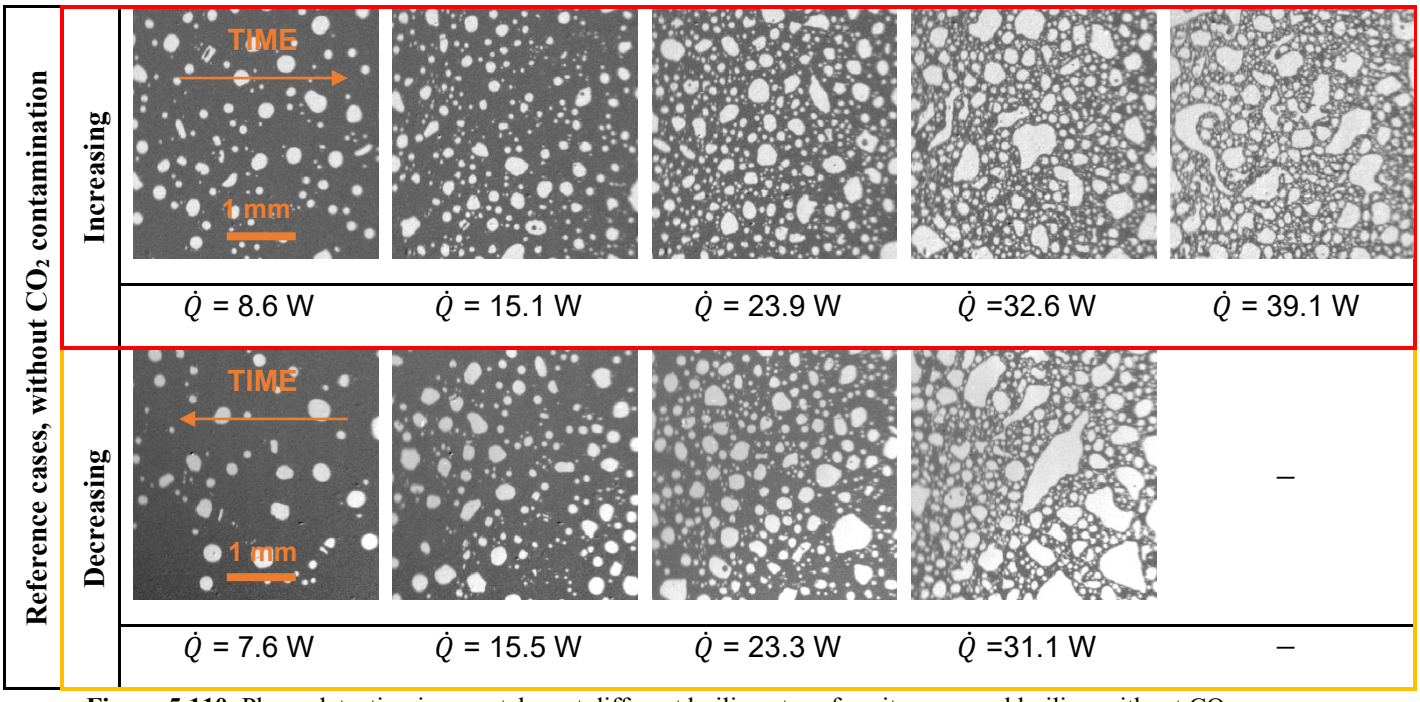

Figure 5.110. Phase-detection images taken at different boiling steps for nitrogen pool boiling without CO_2 contamination corresponding to the reference cases with increasing and decreasing heat input (red and yellow square markers in Figure 5.12, respectively).

The phase-detection images obtained during 1I with contaminated nitrogen (in Figure 5.14) are similar to what is obtained when boiling with uncontaminated liquid nitrogen (shown in Figure 5.13). Little to no deposits is observed on the heated surface throughout 1I. Deposits start being visible when the boiling curve reaches its first heat input peak, shown in image annotated (D) and (E) in Figure 5.14. Light deposition is more easily visible on dry patches, as the higher light reflectivity at the solid-vapor interface contrast sharply with the low reflectivity from the deposits. Image (F) obtained early at the first decrease of the heat input shows more fragmented vapor patches, compared to the phase distribution initially obtained at the same heat input during ramp up (i.e., image C). When the heat input is decreased further, at image (H) and later on (K), the effect of CO_2 deposits becomes even more apparent when compared to the corresponding step obtained for a heated surface free of contamination (i.e., image A). The bubble footprint areas are drastically reduced and the number of bubbles simultaneously present of the heated surface seemingly increased. Only minor changes of the boiling dynamics are observed visually during the following boiling cycles (i.e., during 2I and 2D), despite an increasing contamination of the heated surface (e.g., see image I compared to E). The similarity between the boiling steps during series 1D, 2I and 2D is consistent with the measurement of wall superheat, shown by the boiling curves plotted in Figure 5.12 where the corresponding boiling steps almost overlap. One can see that the final CO_2 deposition observed during the high heat input cycling test (e.g., see image I in Figure 5.14) is significantly more dispersed than observed in the constant heat input test presented in Figure 5.4, even though the total heat deposited in nitrogen (i.e.,$\int \dot{Q} dt$) in those 2 tests only differs by few percent. After establishing that solid deposits form on active nucleation sites (see Section 3.b), the higher dispersion of the deposits is naturally explained by the higher heat input (and wall superheat), and therefore the higher nucleation site density reached during the power cycling test shown in Figure 5.14 (compared to the tests at constant heat flux discussed in Section 3). The low heat input cycling test shown by green circular markers in Figure 5.12 was performed after the high heat input cycling test and after cleaning the surface from contamination by bringing to high temperature in film boiling. The phase-detection of the low heat input cycling test (not shown) looks identical for any heat input to the reference cases shown in Figure 5.13 and performed with clean nitrogen.

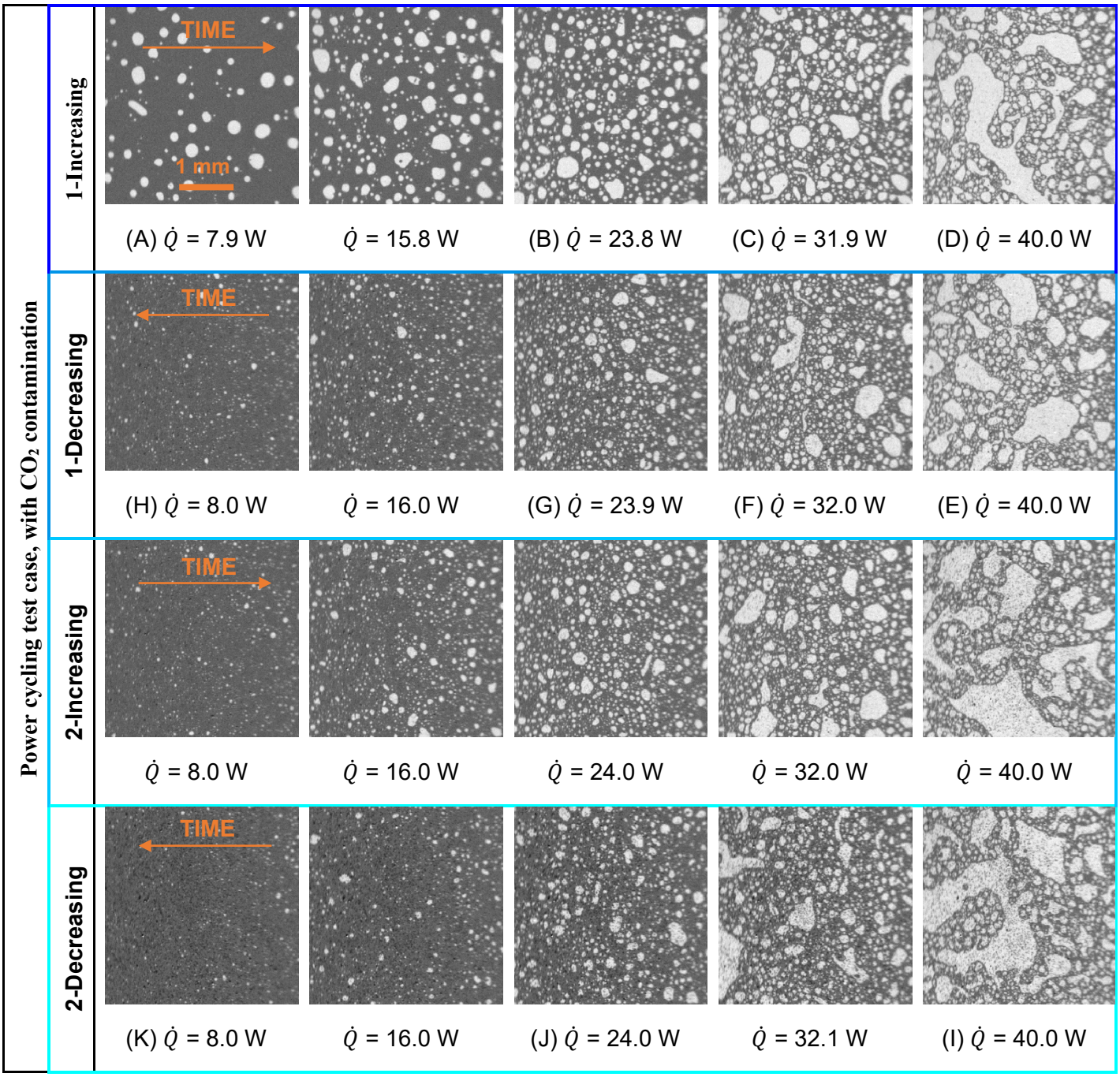

Figure 5.111. Phase-detection images taken for each boiling step of the high heat input cycling test with contaminated nitrogen shown in Figure 5.12 with blue circular markers. For comparison, reference cases performed without CO_2 contamination are shown in Figure 5.13.

5.2.3. Mechanistical effect of the fouling on the boiling heat transfer

Our visual observations of the boiling surface with contaminated nitrogen shows a reduction in bubbles' footprints, and generally a reduction of the dry area fraction α_v for a given heat input. We can reinforce

these observations by providing an evaluation of α_v for the tests whose boiling curves are shown in Figure 5.12. α_v is plotted in Figure 5.13.

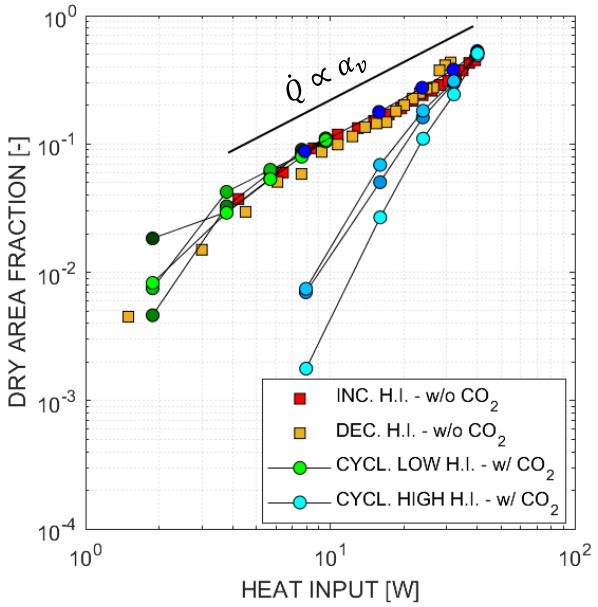

Figure 5.112. Plot of the step-averaged dry area fraction against the heat input (H.I.).

Significantly smaller values of dry area fraction are observed when the surface is contaminated (i.e., for phases 1D, 2I and 2D of the high-input cycling case, while being initially identical to the reference cases during phase 1I (i..e, the dark blue dots). The difference in the dry area fraction between clean and contaminated surface is begligible at the maximum heat input but is significant at lower heat inputs.

Figure 5.14 shows the probability distribution functions of the bubble footprint area for different heat input and level of surface contamination during the high heat input cycling test (shown in Figure 5.10with blue circular markers). The distributions are generated by evaluating the number of bubble footprints having an area inside given bins and during the 2000 frames of each recording (about 142.8 ms). The bubble footprint area distributions are obtained during phases 1I, 1D and 2D (shown with the same color scheme as previously) of the boiling test. A distribution curve measured with uncontaminated nitrogen at 39.1 W, right before reaching DNB measured in this case at 41.3 W, is also plotted in Figure 5.14 (right) as reference.

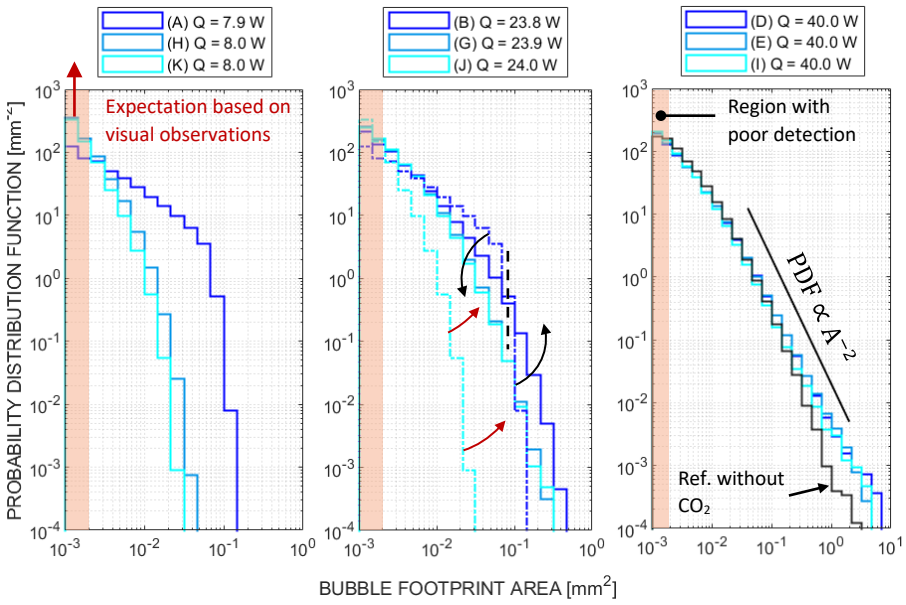

Figure 5.113. Plot of the probability distribution functions of the bubble footprint areas for different heat flux for the cases previous shown with blue circular markers in Figure 5.10 and phase-maps shown in Figure 5.12. The dotted-dashed lines in the center plot corresponds to the distribution functions (A) and (K).

The plots of the distributions quantitatively show what we could observe visually in Figure 5.12. The distributions show a significant drop of the probability of finding bubbles with large footprint area at low heat input (e.g., at ~8 W) when the surface is contaminated. Instead, it is much likely to find bubbles with smaller footprints (i.e., H and K). Small bubble footprints remain challenging to segment using our processing code due to limited spatial resolution, and the deposits obstructing the view. Therefore, the number of bubbles with small footprints (typ. below $2*10^{-3}$ mm^2 or equiv. 25 µm radius) is likely underestimated, which would increase further the gap between the pre-contamination (i.e., A) and post-contamination (i.e., H and K) distributions at low heat input in Figure 5.14 (left). The differences between pre- and post-contamination reduces as the heat input increases, until the difference becomes negligible at the highest heat input (see curves D, E and I at ~40 W). The reference distribution (shown in black) is overall quite similar to D, E and I, showing only slightly lower probability for the largest bubble footprint area, which might be due to the slightly lower heat input. At this power, the process is close to a boiling crisis and the distributions tend to power laws, which corroborates our previous observations and analysis for water and nitrogen on the scale-free nature of the boiling crisis [91]. The similarity between the distributions with (i.e., D, E and F) and without fouling (i.e., the reference case) also suggests that heat input required to reach DNB might not be very sensitive to the level of CO_2 contamination (at least at this level of contamination where the surface is only partially covered by CO_2 deposits). The average instantaneous bubble density, noted N_B'', is plotted against the substrate temperature measured by the RTDs in Figure 5.17. Due to the difficulty of segmenting small bubbles, particularly on a fouled surface, N_B'' was

obtained by counting bubbles manually on randomized samples of phase-detection images. Details of the procedure to evaluate the bubble density are given in Chapter 2. The standard deviations represent the measurement variations between the different samples.

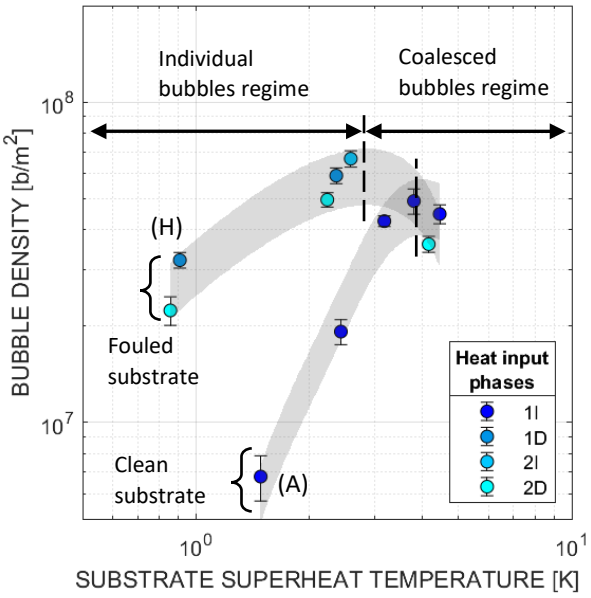

Figure 5.114. Plot of the bubble density N_B'' against the substrate superheat temperature ($T - T_{SAT}$) measured by the RTDs.

Two regimes can be observed in Figure 5.15, highlighting the dependence of N_B'' on the rate of bubbles coalescence. As expected, an increase of the bubble density is seen when substrate temperature increases from low superheat. At the first order, N_B'' is the product of 3 factors, the nucleation frequency, the bubble growth time and the active nucleation site density. The increase of N_B'' is seemingly supported by an increase of the nucleation site density and nucleation frequency. When N_B'' becomes sufficiently large (~ 5-7.10^7 b/m^2), as the temperature increases, N_B'' seems to have a maximum. At higher superheat, a slight decrease of N_B'' with increasing temperature is observed. The decrease of N_B'' may be caused by a rapid increase of coalescence occurring when the characteristic distance between bubbles $1/\sqrt{N_B''}$ becomes smaller than the characteristic size of their footprint. When fouling is introduced on the surface, the same trends of N_B'' with temperature are observed (see phases 1D, 2I and 2D in Figure 5.14 as well). However, significantly larger values of N_B'' are observed at low superheat, which match our observations from Figure 5.12 (e.g., see images A and H). Also, the transition between the peak of N_B'' appears to shift toward lower wall superheat. Note that the dry area fraction α_v, shown in Figure 5.13, can be expressed as $N_B''\langle A \rangle$ with $\langle A \rangle$ being the average bubble footprint of distributions plotted in Figure 5.14.

We saw in Figure 5.5 that deposits form at the location of nucleation sites, and the same occurs in the high-input power cycling test presented in Figure 5.12. It remains to know whether the deposits affect the nucleation site density when the heat input is cycled. A proper quantitative analysis is challenging to the difficulty of segmenting automatically small bubbles, and so is counting active sites. Instead, Figure 5.16 shows qualitatively the increase of the nucleation site density by comparing known locations of active nucleation sites on the heated surface without fouling to the phase-detection images of contaminated nitrogen boiling at the same heat input. Two sources of data are used to infer the locations of active nucleation sites when boiling on the clean surface. One map (shown with blue overlay in Figure 5.16, image 1) is obtained from the step (A), at the very beginning of the high heat input cycling test. The second map (shown with red overlay in image 2) is obtained from the reference test with increasing heat input and uncontaminated nitrogen (highlighted by a red frame in Figure 5.13). Despite not being identical, the 2 maps share common features. Both maps are overlapped on image 4. Locations of active sites common to both maps are colored in green, while the white region does not have any active nucleation sites. The phase detection images with contaminated nitrogen are taken from step (K) (i.e., the last step of the high heat input cycling test, shown in Figure 5.14). Both maps of nucleation sites and the phase-detection images of step (K) are obtained at similar heat input, i.e., about 8 W, and with the same heating surface. The locations of nucleation sites (image 4 in Figure 5.16) and the phase-detection images (image 3) are combined to produce image 5. We can observe on image 5 of Figure 5.16 a significant number of bubbles (visible by white footprints) nucleating from these regions of the surface and others where no nucleation has been observed during tests free of surface contamination. This comparison strongly suggests carbon dioxide deposits can increase the number of active nucleation sites at a given heat input. The key point of this observation lies in the memory effect of boiling surface induced by the carbon dioxide deposits. Unlike the constant heat input case previously shown, the carbon dioxide visible on the phase-detection at step (K) (e.g., on image 3 in Figure 5.16) precipitated on nucleation sites that were activated up to highest heat input (~40 W) during previous boiling steps. Additionally, it appears that the carbon dioxide allows these nucleation sites to stay active when the heat input is reduced, which is consistent with the decrease of the wall temperature with increasing fouling in the constant heat input case. Therefore, at low heat input (e.g., at step K), the boiling heat transfer is enhanced by the much higher active nucleation sites density on the fouled surface than expected if the surface were clean.

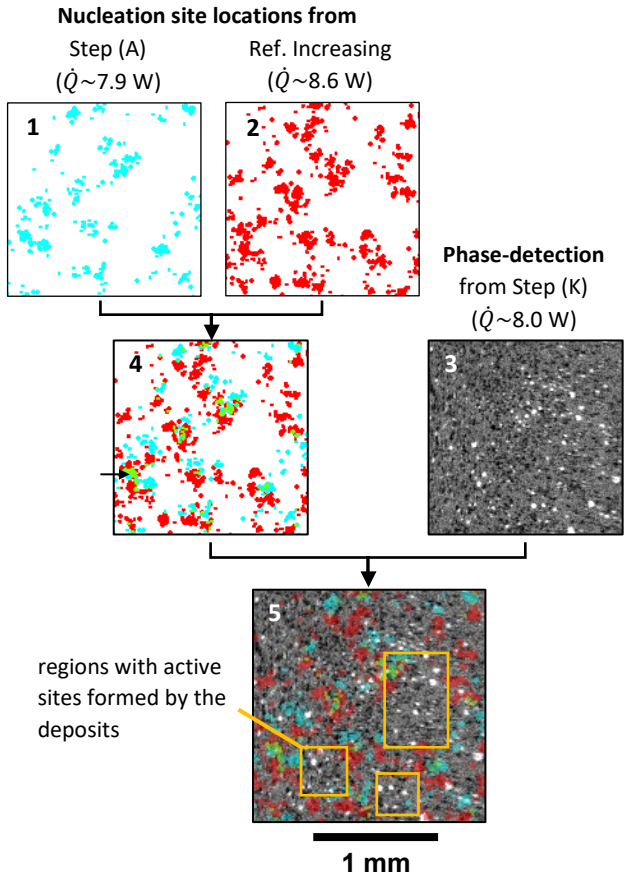

Figure 5.115. Superposition between the phase-detection images of step (K) with the maps of active nucleation sites obtained on surface free of CO_2 contamination (in red and blue). On the phase-detection, the vapor appears white, while the liquid and the solid deposits appear dark grey and black, respectively.

The effect of carbon dioxide fouling on boiling tests with the heat input monotonously increasing or decreasing over time was also investigated. We observe enhancement of boiling heat transfer in both cases (i.e., increasing and decreasing heat input) and changes in boiling dynamics (reduction of the dry area fraction, higher nucleation density) similar to those presented above. The boiling curves and phase-detections images for these tests are presented in Appendix B.

4.1. Discussion of the results

Our data shows consistently that a contamination of liquid nitrogen with CO_2 leads to an enhancement of the boiling heat transfer (see Figures 5.10, 12, and 23, 24 in Appendix A). The contamination acts on the boiling heat transfer only when the CO_2 precipitates and deposits on the boiling surface (see Figures 5.2 and 12). The deposits are very localized on the boiling surface and match the locations of active nucleation

site (see Figure 5.3). The deposits formed at high heat input appear to serve as additional nucleation sites once the heat input is decreased, leading to a higher nucleation site density compared to a reference test without CO_2 contamination (see Figure 5.16) and to an increase of the bubble density in particular at low superheat temperature (see Figure 5.15). We also observed a significant reduction in bubble footprint area (see Figures 5.9 and 14) associated with an overall decrease of the average dry area fraction on the fouled surface with cycling heat input and constant heat input (see Figures 5.8 and 13, respectively).

It remains unclear what causes the reduction of the bubble footprint area. Observations of bubbles using backlit shadowgraphy on contaminated surface seem to show a decrease of bubbles size, and not only of their footprints. A comparison of shadowgraphy images with and without fouling is shown in Figure 5.17, at a similar heat input with and without CO_2 surface contamination. The bubbles footprints, measured from phase-detection, are shown as teal overlay. Both images are taken from tests with decreasing heat input ensuring that all potential nucleation sites can be active. The surface contamination is visualized from the phase-detection recordings and displayed for both cases. The dashed orange frames indicate the location of the displayed surface contamination images. The black spot visible on the image of surface contamination in the clean surface case consists mostly of dusts particles on the optical setup, with few marks on the sapphire from unknown origin. While bubbles footprints (shown in teal) are significantly smaller when nitrogen boils on the fouled surface, it also seems visually that the overall size of the bubbles (shown by their shadow) is reduced.

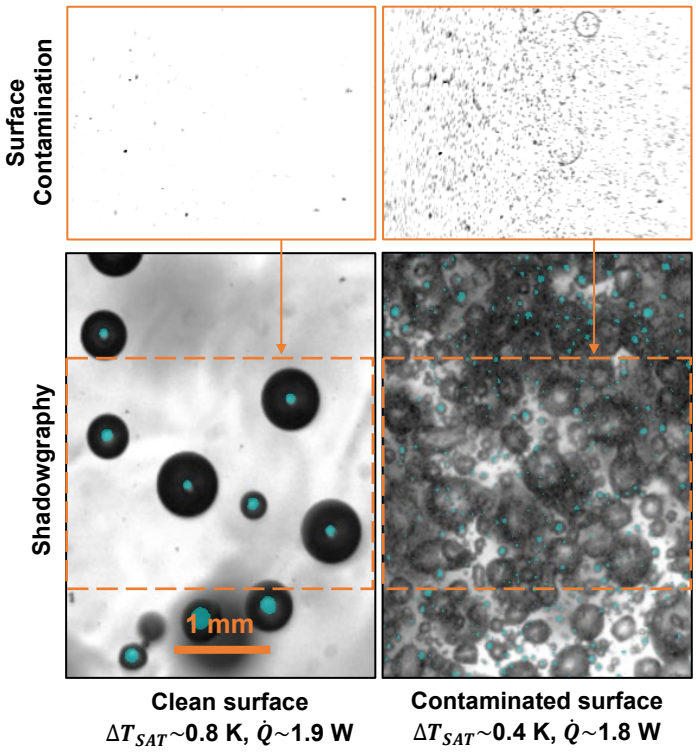

Figure 5.116. Comparison of backlit shadowgraphy images in gray color scale of nitrogen pool boiling without (left) and with carbon dioxide fouling (right). Bubbles footprints are shown as teal overlay. All images are at the same scale. Top images show processed phase-detection images highlighting only the solid deposits on the surface for each case.

Unfortunately, the shadowgraphy videos are not clear enough and so a proper analysis of these images is impossible. The reduction of overall bubble size is also suggested by the fact that bubbles with small footprints which are closely packed, e.g., within few diameters apart, are seen to move independently on phase-detection videos and therefore without coalescing with each other. A lower nucleation temperature permitted by the deposits would translate into a shorter bubble wait time and therefore less heated substrate and thermal boundary layer. As a consequence of the lower amount of heat available to sustain the growth of bubbles, we observe smaller bubbles on the contaminated surface overall.

Then, we are left with an open question on what makes bubble nucleation possible at lower wall superheat on the CO_2 deposits. Several competing arguments are possible, such as local changes of surface wettability (by producing cryophobic nucleation sites) or surface topology (i.e., by producing geometrically favorable cavities) at the locations of the CO_2 deposits. Both hypotheses are consistent with the fact that the enhancement of boiling heat transfer appears to saturate once enough CO_2 has been deposited on the surface (see Figure 5.12). The equilibrium contact angle of nitrogen sessile droplets was measured at saturation and atmospheric pressure on both ITO-coated sapphire substrate and a smooth copper cylinder coated with CO_2

frost to test the wettability hypothesis. The contact angles were estimated by measuring the size of the initial nitrogen droplet, the size of the puddle formed on the surfaces and by solving the axisymmetric Young-Laplace equation. Both tested surfaces show similar results with estimated contact angles well below 10º, with no evidence that CO_2 fouling may be cryophobic. The hypothesis of CO_2 deposits acting as active cavities at low wall superheat is consistent with the well-known improvement of boiling heat transfer observed when roughness is added to a mirror polished heated surface, e.g., shown by Marto et al. [101] with nitrogen. Further investigations, e.g., detailing the morphology of the CO_2 deposits and comparing them to the natural heated surface cavities, are necessary to support this hypothesis.

The enhancement of boiling transfer from surface contamination presented in this study can appear counterintuitive when compared to previously published results, which have mostly shown a degradation of the boiling heat transfer coefficient with contamination (see Refs. [26, 51,57 and 58]), at the exception of Scurlock [58] for its test on polished aluminum surface. Our observations suggest that the spatial distribution of the deposits on the heated surface, the amount (which are closely related the heat flux and the time spent boiling), and the initial surface morphology may play a major role in determining whether we shall expect an enhancement or a degradation of the cryogenic boiling heat transfer. In the cases we presented, the depositions cover a small portion of the heated surface, at most 20 percent in the test shown in Figure 5.2, because of the relatively short duration of boiling (~1 min). Hence, the thermal resistance added by the deposits remains negligible, which may not be the case for frost-like contamination from atmospheric origin as reported by Lyon [54] or crystallization-induced fouling over hours [58]. We observed the deposits to almost always form from pre-existing active nucleation sites. It is not clear what would happen to the boiling heat transfer if ring-shaped deposits (as shown in Figure 5.17 and 22) becomes much more prominent, e.g., by changing the substrate material.

5.3. Summary of the chapter

In this chapter, we conducted cryogenic pool boiling experiments with liquid nitrogen on a transparent nano-smooth surface with micron-size cavities to understand the effect of cryogenic fouling on the boiling dynamics. The apparatus we used allowed us to gather phase-detection images of the boiling surface, enabling detection of liquid, gas, and solids phases. The apparatus was designed to minimize contamination of the liquid nitrogen we boil, in particular from atmospheric origin. Nominally, no cryogenic fouling was observed on the boiling surface with industrial liquid nitrogen (purity above 99.998%(vol)) for boiling test which do not exceed a minute. Then, we saturated our liquid nitrogen with CO_2 and conducted a series a boiling experiment with constant heat input as well as increasing, decreasing and cycling heat input. Our results showed that CO_2 precipitate on the boiling surface upon evaporation of the liquid nitrogen. More

precisely, we matched the locations of cavities generating bubbles on the surface and the location where the CO_2 accumulated, which indicates that the CO_2 precipitates during the nucleation of bubbles. Once the surface contaminated with solid CO_2 deposits, we observed an enhancement of the boiling heat transfer coefficient, in particular, when the heat input was reduced. We showed that the enhancement of the heat transfer is accompanied with changes in bubble dynamics. We observed a drastic reduction of the bubble footprints on the surface and of the overall dry area fraction, as well as an apparent increase of the active nucleation density. Our study highlighted the relationships between boiling parameters (e.g., the nucleation site density) and fouling deposition as well as the effect of the latter on the former. The capability of CO_2 deposits to lower the nucleation temperature of pre-existing cavities remains puzzling, and brings the practical question of the effect of cryogenic fouling on rough surfaces, i.e., surfaces on which boiling is not limited by its cavities whether it is in terms of size or number. More generally, it remains unclear how to reconciliate the observations of heat transfer degradation with the cases of improvement. Although time and heat input conditioned the amount of contaminant precipitating on the surface and surely play a role on the outcome of the heat transfer, the situation might be more complex as a change in boiling dynamics (e.g., by tuning the thermal properties of the substrate or gravity) could result in different fouling characteristics. Finally, the question on how the nature of the foulant (such as CO_2, water, and even nitrogen or oxygen in liquid hydrogen) impacts the boiling characteristics is left opened, e.g., due to difference in solubility, morphology of deposits, etc. Additional understanding in those directions would allow to leverage mechanistic boiling model to predict and potentially minimize the effect of cryogenic fouling, for industrial applications as well as in experimental research.

Appendix 5.A – Evaluation of sublimation time below saturation of CO_2 deposits

The carbon dioxide deposits can be removed from the surface by bringing it to film boiling. We observed the sublimation occurring at much lower temperature than the bulk sublimation temperature of CO_2 (i.e., 220 K at 0.480 kPa). Figure 5.18 shows deposit sublimation in raw phase-detection images alongside temperature measurements. The temperature at the ITO is reconstructed from the measurement of RTD temperature and heat input with the assumption of adiabatic interface at ITO-$N_{2,vap}$ interface. Visually, the appearance of the deposits does not change before reaching ~144 ± 3 K at the ITO (left side of the pink area). Then, we observe a gradual disappearance of the deposit, ending at around ~154 ± 3 K. The large temperature uncertainty considered is due to the calibration used for high temperature (i.e., above 105 K) and the error related to the reconstruction of the ITO temperature from the RTD measurements in transient. The black spots remaining on the surface are mostly dust particles on the optical setup and contaminants other than carbon dioxide on the substrate. The CO_2 deposits shown in Figure 5.18 are slightly smaller (10-40 µm in diameter) than the deposits shown in Figure 5.2 due to a lower deposition time.

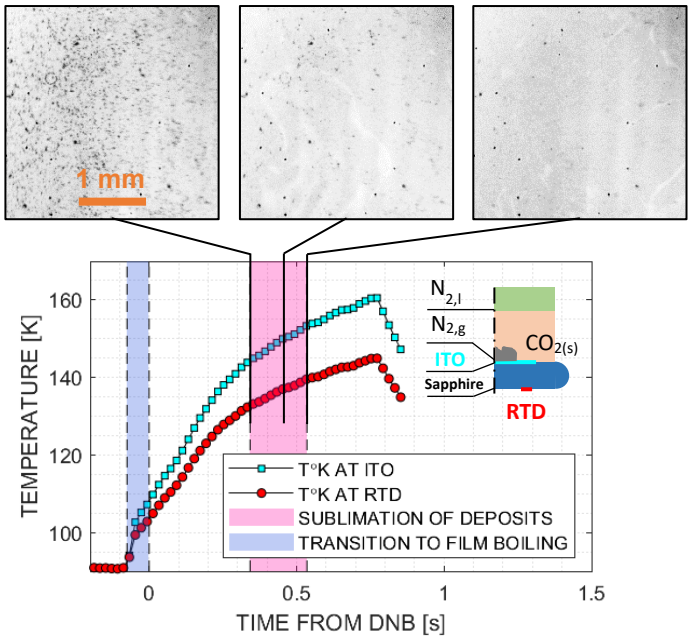

Figure 5.18. Experimental observation of solid carbon dioxide sublimation in nitrogen film boiling

The sublimation below saturation can be explained by molecular diffusion of CO_2 through the nitrogen gas phase. The model proposed is analog to Maxwell's droplet evaporation model. The large relative size of the boundary layer also allows us to assume a spherical diffusion of the CO_2 through the nitrogen. For simplicity, we assumed the diffusion to be purely radial. We can also assume equilibrium at the deposit interface, the Knudsen number being in the order of 10^{-4}. Both CO_2 and N_2 gas are treated as ideal gases,

and the vapor pressure of CO_2 is obtained from the correlation of Giauque and Egan [102]. Therefore, the CO_2 concentrations in the gas mixture at the solid-gas interface ($r = R_0$) and gas-liquid interface ($r \to \infty$) are given by $P_v\big(T(R_0)\big)/RT(R_0)$ and $P_v\left(T_{SAT,N_2}(P)\right)/RT_{SAT,N_2}(P)$, respectively. Chapman and Enskog model [23] is used to evaluate the temperature-dependent molecular diffusion coefficient of $N_{2,Vap}$-$CO_{2,Vap}$. The Spalding mass transfer number B_m (defined by $\frac{\rho_{CO_{2,g}}(R_0)-\rho_{CO_{2,g}}(r\to\infty)}{\rho_{N_{2,g}}(R_0)}$) associated with the problem is below 10^{-2} over the temperature range of the transient, allowing us to neglect Stefan flows [103]. The mass conservation equation on the solid deposit is decoupled from the CO_2 diffusion in the nitrogen gas by assuming a fixed solid-gas boundary, the diffusion boundary layer being much larger than the size of the deposit ($\frac{R_0}{\sqrt{D_{CO2-N2}\Delta t}} \sim 10^{-2}$, with Δt the duration of the transient). The temperature in the gas mixture is assumed uniform and equal to the ITO temperature at any time of the transient. The CO_2 deposit is modeled as a disk of fixed radius R_0 and initial thickness δ_0. The transient diffusion problem is then solved numerically with finite volume method using the time-dependent ITO temperature shown in Figure 5.18. The numerical solutions of the deposit mass vs time for several initial deposit thickness δ_0 are shown in Figure 5.5 and demonstrate that the sublimation of the CO_2 deposit significantly accelerate due to a rapid increase in the vapor pressure of CO_2 with temperature above ~140 K, irrespective of the initial deposit thickness, explaining our observations shown in Figure 5.18.

Appendix 5.B – Effect of fouling of boiling curves with monotonous increase and decrease heat input

The time of occurrence of the surface fouling can be tuned by modifying the heat profile of boiling test. As complement to the data presented in the core of the study, Figure 5.s 19 and 20 show a comparison between a set of boiling curves, with heat input monotonously increasing or decreasing, respectively. The boiling curves are performed at 485.1 ± 2.8 kPa close to saturation (~0.3 K below T_{SAT}). All boiling curve are obtained by varying the heat input piecewise in steps of 3 seconds, and the temperature and heat input measurements are taken after reaching a steady state, during the last second of the step. The heat input is increased gradually for the curves shown in Figure 5.19 and it is decreased in Figure 5.20, after a quasi-instantaneous rise to the maximum heat input. The curves colored in shades of red are performed with uncontaminated liquid nitrogen, while curves in blue shades are measured with contaminated nitrogen. Phase-detection images refer to the curves represented by larger markers, at a high heat input (in Figure 5.10) and low in heat input (in Figure 5.20).

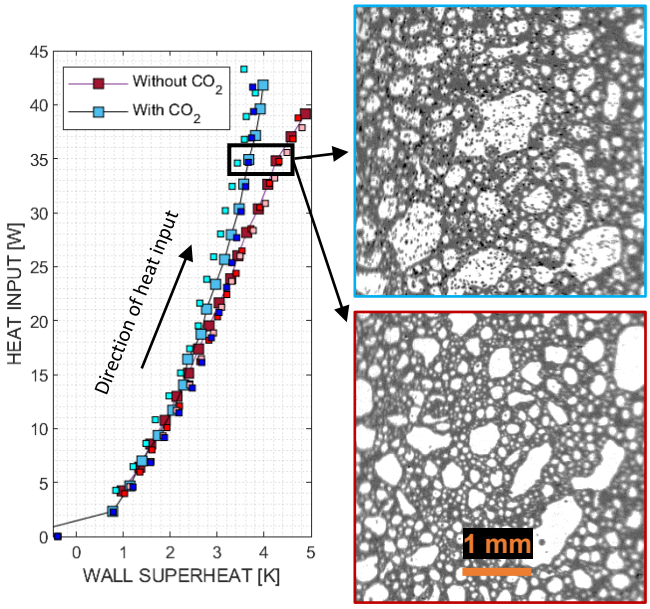

Figure 5.19117. Boiling curves for saturated nitrogen pool boiling with (in blue) and without CO_2 (in red) saturation performed by steady-state heat input increase.

When the heat flux is steadily increased (see Figure 5.19), substantial deposition solid CO_2 is only found when enough nitrogen evaporation has boiled on the heated surface. Consequently, we observe at low heat input an overlapping of the boiling curves with contaminated and clean nitrogen (shown in blue and red, respectively). As the heat input increased, we observe an enhancement of the boiling heat transfer with CO_2 contamination. CO_2 deposits are also visible on the phase-detection images, e.g., as shown in Figure 5.19, but the boiling dynamics and bubble footprints are visually similar. The reason of the heat transfer enhancement is thought to be the same than for the constant heat input case, discussed in Section 5.2.1.

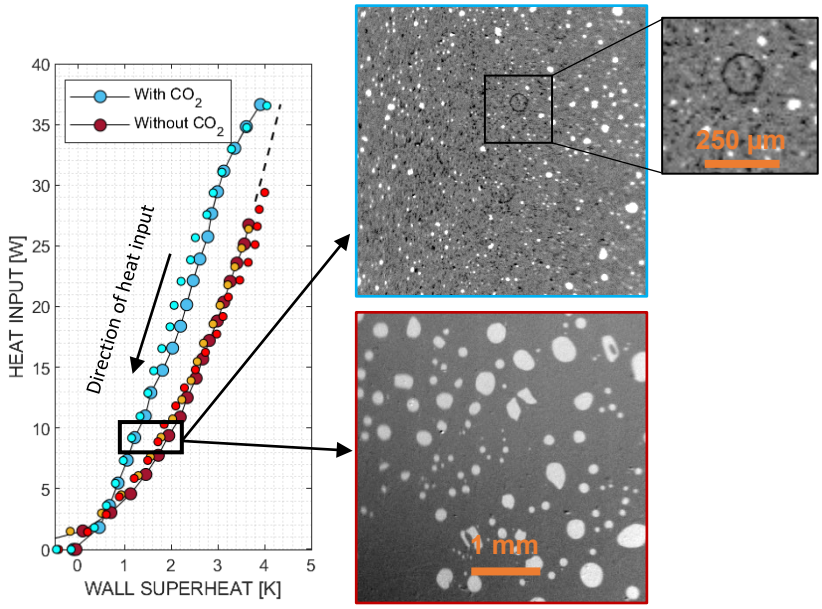

Figure 5.118. Boiling curves for saturated nitrogen pool boiling with (in blue) and without CO_2 (with red-orange) saturation performed by steady-state heat input decrease.

When the heat input is decreased (see Figure 5.20), the initially high heat input leads to CO_2 deposited on the heated surface early on in the boiling test. In this case, we observe an enhancement of the boiling heat transfer with CO_2 contamination. The enhancement is visible irrespective of the heat input, noticeably at low heat flux, where the heat transfer is impacted by the CO_2 deposited at higher heat flux. Boiling with and without CO_2 at low heat flux looks noticeably different, as shown in Figure 5.20. The bubbles footprints (shown in white on phase-detection images) appears significantly smaller in the contaminated case, also suggesting a much lower dry area faction for a fixed heat input.

6. HEAT FLUX PARTITIONING MODEL

6.1. General formulation of the heat flux partitioning model

We propose in this Chapter a closed formulation of heat flux partitioning model adapted to liquid nitrogen boiling. The proposed model is based on the MIT boiling model (see Ref. [2]), which was developed for flow boiling water. Part of the closure models have been reassessed in light of our experimental data for liquid nitrogen. Finally, we provide an evaluation of the model error compared to the boiling curves measured experimentally at different inclination angles.

6.1.1. Evaporative terms

6.1.1.1. Role of the bubble inception

Gilman and Baglietto [35] originally proposed an evaporative heat flux term to account for the heat removed during the inertial-growth of the bubble. The heat is expected to come mostly from the heated wall rather than the superheated thermal boundary layer. Therefore, the latent heat for the bubble inception is not accounted in the sliding conduction term. Instead, the following evaporative heat flux was proposed,

$$q''_{\text{inc}} = \frac{2}{3}\pi R_d^3 \rho_v h_{lv} N''_{s,\alpha} f \tag{6.1}$$

With R_d the bubble optical radius used here to approximate the bubble radius at the end of the inertial growth phase. At that stage of the growth the bubble was assumed hemispherical, resulting in a 2/3 factor in the expression of q''_{inc}. The analytical evaluation of the bubble radius at the end of the inertial growth (if it occurs at all) shows that the radius is about 10^{-7} m, quite far off from R_d assumed originally for boiling water [see Ref. [35]]. This would suggest that q''_{inc} should be negligible. However, the analytical evaluation can be argued upon due to the various assumptions, in particular the lack of solid surface which would be superheated at nucleation, providing a source of heat.

Our measurement doesn't allow us to observe such early stage of bubble growth. Therefore, we can hardly quantify how much heat is transferred, e.g., we cannot measure bubbles radii as we did in Chapter 3 for the triple contact line evaporation. Instead, we can quantify how much energy is removed by bubbles before it appears on our recordings. The threshold of detection for bubble footprint on phase-detection recordings due to the spatial resolution is about 3 pixels in diameter (i.e., about 30 to 40 µm). We can estimate the heat ε required to generate such bubble,

$$\varepsilon = \frac{\pi}{3} {R_{f,min}}^3 \rho_v h_{lv} F\left(\theta_{eff}\right) \tag{6.2}$$

Then we can compare ε to the heat removed at the end of bubble growth (i.e., at lift-off),

$$\frac{\varepsilon}{\varepsilon_{lo}} = \frac{{R_{f,min}}^3}{{R_{f,lo}}^3} \tag{6.3}$$

With ε_{lo} the latent heat required to generate a bubble with a size typical of lift-off. We assumed here that the effective contact angle is constant during bubble growth, which is observed experimentally. Note that the uncertainty on the effective contact angle can be high when the bubble footprint radius is close to $R_{f,min}$.

Using typical values of $R_{f,lo}$ of 100 µm and $R_{f,min}$ of 20 µm, we get that $\varepsilon/\varepsilon_d$ is about $8*10^{-3}$, i.e., that roughly less than 1% of evaporative heat is transferred before we can observe the bubbles. Therefore, assuming that q''_{inc} is physically sounds, this calculation also suggests the term can be safely neglected in the case of nitrogen boiling.

6.1.1.2. Role of microlayer evaporation and triple-contact line evaporation

No microlayer was observed in saturated liquid nitrogen pool boiling for pressure between atmospheric pressure and 480 kPa on sapphire substrate. Instead, our data strongly suggested that liquid evaporation occurs at the triple contact line instead, resulting in bubble footprint larger than expected from the small equilibrium contact angle of nitrogen on sapphire (~5°). We estimated that roughly 20% of the heat transfer is carried by the evaporation from ONB up to DNB. Therefore, the evaporation term has been taken into account in the estimation of the boiling heat flux.

In Chapter 3, we evaluated the linear heat rate of evaporation $\dot{q}'$, corresponding to how much heat is transpired per unit time and per unit length of triple contact line. Then, we defined a triple contact line density l''_3. Therefore, the product $\dot{q}' l''_3$ gives the heat transferred per unit time and per unit area of heated surface due to contact line evaporation. However, from a modeling point of view, it is not necessary to know where the evaporation occurs on the bubbles as long as the product $\dot{q}' l''_3$ is correctly estimated. $\dot{q}'$ was evaluated on selected bubbles by calculating the heat rate (i.e., in W/s) to sustain the bubbles' growth which volume can be deduced from the optical and footprint radius, divided by the length of the bubbles' triple contact line (i.e., their footprint perimeter). So, we have,

$$q''_{cl} = \dot{q}' l''_3 \tag{6.4}$$

A proper evaluation of $\dot{q}'$ is difficult as illustrated by Raj et al.'s model (see Chapter 3, Section 3.2.2.3) which involves solving a system of 4 coupled 1st order differential equations whose solution is particularly unstable. Instead, Eq. 3.68 derived in Chapter 3 offers a partial solution to evaluate $\dot{q}'$,

$$\dot{q}' = \frac{1}{4}\rho_v h_{lv} F(\theta_{\text{eff}}) \frac{{R_{\text{f,lo}}}^2}{t_{\text{g}}} \tag{6.5}$$

With $R_{\text{f,lo}}$ the bubble footprint lift-off radius, t_{g} the bubble growth time (defined as $R_{\text{f,lo}} = R(t_g)$) and θ_{eff} the bubble effective contact angle. F is a function of θ_{eff} given by Eq. 3.48 (in Chapter 3). The triple contact line density l_3'' can be also expressed as a function of more fundamental parameter,

$$l_3'' = N_B'' 2\pi R_{\text{f,lo}} \text{ with } N_B'' \approx N_{s,\alpha}'' \tilde{f} t_g \tag{6.6}$$

Combining Eqs. 6.3 to 6.5, we get a formulation for the triple contact line heat flux,

$$q_{cl}'' = N_{\text{A}}'' \tilde{f} * \left(\frac{\pi}{2} {R_{\text{f,lo}}}^3 \rho_v h_{lv} F(\theta_{\text{eff}}) \right) \tag{6.7}$$

The term in bracket corresponds the total heat removed by liquid evaporation from a single bubble throughout its growth, while $N_{s,\alpha}'' f$ is the average number of bubbles formed per unit time and per unit area of heated surface. Eq. 6.7 has the typical shape of an evaporative term, e.g., shown by Eq. 6.1.

We then require closure formulations for the growth time t_{g}, the bubble footprint radius at lift-off $R_{\text{f,lo}}$ and the effective contact angle θ_{eff}, nucleation site density $N_{\text{s,}\alpha}''$ and nucleation frequency $\tilde{f}$.

6.1.2. Quenching term

The quenching term q_q'' is the heat flux resulting from reestablishing the thermal boundary layer by transient conduction after being disrupted by bubbles movement. The most elementary bubble movement is the case of bubbles lift-off, with bubbles moving normal to heated wall. When one or multiple forces tangential to the heated surface are applied to bubbles, they can start sliding as observed when the heated surface is inclined (hence q_{sc}'' referred as sliding conduction heat flux). In the case of nitrogen boiling, such sliding is very common and even on a horizontal surface, bubbles sliding occurs due the liquid agitation caused by bubbles growth and nucleation as discussed in Chapter 4). The effect of bubbles sliding on the heat removed from the heated surface has been observed experimentally by the experiment of Phillips [110] in flow boiling water using infrared thermometry. A formulation of quenching heat flux was proposed be Gilman and Baglietto (noted originally q_{sc}'' to reflect the sliding conduction mechanism of the quenching),

$$q_q'' = \frac{2\varepsilon_l(T_w - T_b)}{\sqrt{\pi}}\sqrt{t^*} f N_A'' A_{sc} \tag{6.8}$$

With T_w the temperature of the heated wall, T_b the temperature of the liquid bulk, α_l and k_l the thermal diffusivity and conductivity of the liquid, t^* the time required to reestablished the thermal boundary layer after disruption, f the frequency of bubble nucleation events per nucleation site, N_{A}'' the number of nucleation site actively producing bubbles per unit area of heated surface, and A_{sc} the surface area affected by a bubble between departure and lift-off. In the original MIT boiling model, A_{sc} was evaluated strictly as a sliding area, i.e., A_{sc} is proportional to sliding distance (defined as d_s in Chapter 4). More generally, we can consider A_{sc} as an area of influence, i.e., the cumulated area than a single bubble will swiped over between nucleation and lift-off. The term $\frac{2\varepsilon_l(T_w-T_b)}{\sqrt{\pi}}\sqrt{t^*}A_{sc}$ corresponds the amount of energy removed by a single bubble and $f N_A''$ $(= \dot{N}_N'')$ is the number of the bubbles nucleating from the heated surface per unit time and heated surface area. One can see that here the contributions of each bubble to the conduction heat flux are summed. When bubbles areas of influence intersect each other on crowded boiling surface, the assumption of independence of the individual bubble contribution breaks down. One way to see it is to compare the rewetting frequency f_{w} and the average frequency of bubble nucleation $\tilde{f}$. Figure 6.1 shows such comparison using the experimental measurement previously presented for f_{w} and $\tilde{f}$ with boiling nitrogen on a horizontal surface.

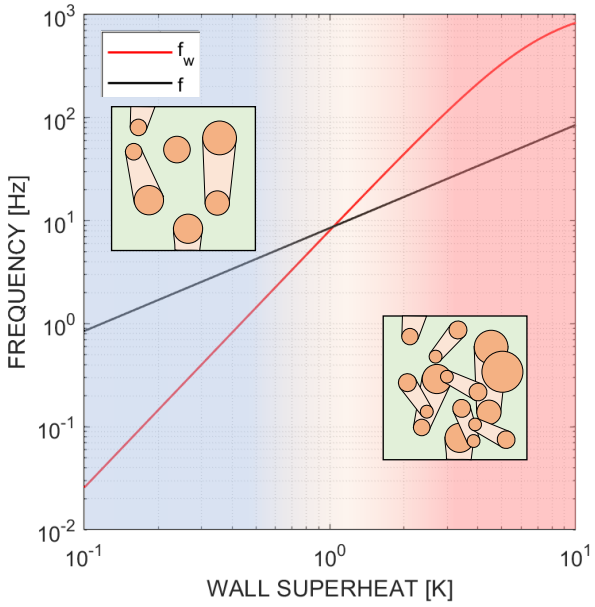

Figure 6.119. Comparison between the rewetting frequency and the average nucleation frequency for nitrogen boiling on a horizontal heating surface.

During boiling (i.e., between 1 and 7 K of wall superheat), one can see that f_{w} is always larger than $\tilde{f}$ (up to ~1 order of magnitude larger near DNB). This corresponds to the area of the plot shown with a red overlay in Figure 6.1. Having f_{w} larger than $\tilde{f}$ means that the time scale associated with the rewetting of the surface is not equal to the wait time associated with active nucleation sites, but depends also on the bubbles density and the overall vapor crowding of the heated surface. On the other hand, the situation is simpler when the bubble density is low enough such that the bubbles areas of influence do not overlap (shown by the blue overlay in Figure 6.1). If one focuses on an arbitrary point on the heated surface that is on the permanently wetted portion of the surface, then the local wetting frequency will be equal to 0. On the other hand, if the point is on the surface area of influence of a bubble, then the local wetting frequency will be equal to the nucleation frequency of the site that generate the bubble. f_{w} would be the surface average of the local rewetting frequency, and is therefore below $\tilde{f}$.

We proposed the following formulation developed in Chapter 4 to account for quenching of the surface (here given by sliding conduction with heat flux imposed boundary condition),

$$q_q'' = \varepsilon_l \sqrt{\pi} (T_w - T_{sat}) f_{\mathrm{w}} \sqrt{t_{\mathrm{w}}} \tag{6.9}$$

With f_w the rewetting frequency and t_w the average wetting duration. One can see by comparing Eqs. 6.8 and 6.9 that the product $\sqrt{t^*} f N_{\mathrm{A}}'' A_{\mathrm{sc}}$ has been replaced by $f_{\mathrm{w}} \sqrt{t_{\mathrm{w}}}$. Note that f_{w} and t_w are much simpler quantities to measure than the wait time, nucleation frequency f, nucleation site density $N_{s,\alpha}''$ and the sliding area A_{sc}, since it is not required to know the locations or the number of active nucleation site on the heated surface.

From Eq. 6.9, we can see that closure formulation are required for f_{w} and t_{w}. For the scope of this work, we leverage experimental measurement to draw fitting formulation for each parameter. However, it is rather clear that proper modeling of f_{w} and t_{w} would be necessary to predict boiling heat flux in conditions other than tested in this work.

6.1.3. Liquid convection heat transfer term

A single-phase term was introduced in the original partitioning model to account the single-phase heat transfer on the regions of the heated surface unaffected by bubbles. An analog formulation is given here,

$$q_c'' = (1 - \alpha_{\mathrm{v}}) h_{\mathrm{c}} (T_{\mathrm{w}} - T_{\mathrm{b}}) \tag{6.10}$$

With α_{v} the average dry area fraction. Our data suggests that h_{c} is very much dependent on the agitation caused by bubbles on the heated surface, as values typical of natural circulation would leave about ½ of the

heat removal from the surface unexplained. In the case of pool boiling irrespective of the surface inclination, we saw in Chapter 4 that the whole heating area gets in contact with vapor at least once over the duration of the phase-detection recording (~140 ms) and for heat flux above 100 kW/m^2 in the horizontal upward facing heat surface and 40 kW/m^2 when the surface is inclined. Since the duration of recording is relatively short, we can assume for practical purpose that this is true for any duration. We can also reasonably expect that if the surface was observed over a longer duration, we could see the surface fully affected by bubbles at lower heat flux (above ONB). Therefore, the single-phase convective term is always supplementing the quenching term, and is applied everywhere liquid is present. It is however clear how the convective term should be accounted. In the Eq. 6.10, we assumed that turbulence contribute to the heat removal throughout the quenching process. If turbulence was present only further away from the heated wall, then the convective heat flux would not be applied on portion of surface on which the thermal boundary layer is yet thin compared to the distance from the wall where turbulent heat transfer is dominant. Note that is not necessarily the case when the active nucleation site density N''_{A} and bubbles sliding area A_{sc} are small enough ($N''_{\mathrm{A}} A_{\mathrm{sc}} \ll 1$). The dry area fraction can be approximated by Eq. 4.2 and 4.5, which results in,

$$\alpha_{\mathrm{v}} = N''_{\mathrm{B}} \pi \langle R_f^2 \rangle \sim N''_{\mathrm{B}} \pi \langle R_f \rangle^2 \tag{6.11}$$

With $\langle R_f \rangle$ the average bubble footprint radius. The averaging brackets $\langle\ \rangle$ are omitted hereafter. Since bubble footprint grow with $\sqrt{t}$, we can approximate R_f by taking relating it to the footprint lift-off radius,

$$R_f = \frac{1}{t_g} \int_0^{t_g} B_f \sqrt{t} dt = \frac{2}{3} R_{f,lo} \tag{6.12}$$

With B_f the growth modulus evaluated from the bubble footprint equivalent radius of bubbles. The bubble density N''_{B} can be evaluated using Eq. 6.6.

6.1.4. Partitioning formulation

We can formulate the following expression for the total boiling heat flux accounting for the heat fluxes of the 3 different mechanisms described above,

$$q''_{\mathrm{w}} = \underbrace{q''_c + q''_q}_{\text{single-phase terms}} + \underbrace{q''_{cL}}_{\text{evaporation term}} \tag{6.13}$$

The quenching terms includes the heat transfer due to the liquid convection from bubbles agitation (q''_c) and the sliding conduction term (q''_{sc}) which accounts for the thermal molecular diffusion occurring shortly after liquid rewet the heated surface. The evaporation term consists of the triple-contact line evaporation

(q''_{cL}). Both microlayer evaporation and bubble inception described in the original MIT boiling model (see Ref. [35]) can be neglected based on our experimental observations.

6.2. Closure formulations

Closure formulations for t_{w}, $N''_{\mathrm{s},\alpha}$, f_{w}, f, $R_{\mathrm{f,lo}}$, h_c, and θ_{eff} are required.

6.2.1. Effective contact angle

The effective contact angle θ_{eff} is described in Chapter 3 and relate the bubble footprint radius to the bubble optical radius in the assumption of the spherical bubble. The angle is required to evaluate the triple contact line evaporation heat flux q''_{cl} given in Eq. 6.7. Modeling the effective contact angle is not trivial as discussed in Chapter 3. Therefore, a simple fitting function obtained from our experimental data is assumed here. The effective contact angle is then given by,

$$\theta_{\mathrm{eff}} = C\Delta T_{\mathrm{sat}}^{n} \tag{6.14}$$

With the pre-factor C equal to 29.3 with dimension [degree/K$^{\mathrm{n}}$] and the exponent n equal to 0.346. θ_{eff} is given in degree.

6.2.2. Bubbles radius at lift-off

The original MIT boiling model and previous partitioning model typically require to know the bubble optical radius R_{o} rather than footprint radius R_{f}, when the bubble lift off in the case of the proposed partitioning model. There are 2 reasons for it. First, the bubbles vapor volume is often better approximated using R_{o} than R_{f} if the actual bubble shape is unknown (in particular the effective contact angle). We can then write that the volume of a bubble as $V \sim \frac{4}{3}\pi {R_{\mathrm{o}}}^3$ which allows to estimate the heat remove by evaporation. Second, most published experimental works provide measurement of R_{o}, rather than R_{f}, as basic measurements of R_{o} at low heat flux are simpler to obtain from shadowgraphy techniques. In our case, the situation is different. Practically, phase-detection techniques allow us to characterize bubbles size through their footprint area (and therefore equivalent radius) from ONB to DNB with simpler segmentation technique. It also allows to directly measure experimentally quantities of interest such as dry area fraction, triple contact line density without approximation (given in Eqs. 6.11 and 6.6, respectively). However, once the effective contact angle θ_{eff} is known (in our case, by measuring simultaneously the optical radius and the footprint radius on some bubbles), one can easily switch between optical radius and footprint radius using $\sin\theta_{\mathrm{eff}} = R_{\mathrm{f}}/R_{\mathrm{o}}$.

An empirical formulation for the bubble lift-off diameter developed for high pressure water flow boiling by Kommajosyula [105] is given by:

$$D_{\mathrm{o,lo}} = 22.7 * 10^{-6} \left(\frac{\rho_l - \rho_v}{\rho_v}\right)^{0.27} {Ja_{\mathrm{sat}}}^{0.75} (1 + Ja_{\mathrm{sub}})^{-0.3} {u_l}^{-0.26} \quad (6.15)$$

With Ja_{sat} the Jakob number evaluated with the wall superheat ($Ja_{sat} = \rho_l c_l (T_{sat} - T_{bulk})/\rho_v h_{fg}$) and u_l the liquid velocity. The same formulation was used for both the departure diameter $D_{o,d}$ with a different pre-factor ($18.9.10^{-6}$ instead of $22.7.10^{-6}$ by assuming $D_{o,lo} = 1.2 D_{o,d}$). In the expression shown in Eq. 6.15, Ja_{sub} goes to 0 in the case of saturated boiling.

As it is, the expression of Eq. 6.15 is not usable for pool boiling. When the mean flow velocity goes to 0, the model indicates that the departure diameter should go to infinity which naturally contradicts the observations. However, local fluctuations in the liquid velocity are expected to cause bubble to depart from their nucleation site even in pool boiling. For any inclination angle of the heated surface from 0° (horizontal upward facing) to 180° (horizontal downward facing), we observed bubbles sliding, with the largest sliding distance for intermediate angles, in particular 90°. While it is rather clear that buoyancy impacts the sliding distance for intermediate inclination angles, at 0° and 180°, the lack of buoyant force tangent to the heated surface and the randomness of the sliding direction strongly suggest that local turbulent induces the bubbles sliding. On the other no strong dependence between the bubble lift-off diameter and the inclination angle of the heated surface has been observed experimentally, suggesting that the bubble lift-off diameter of a bubble does not strongly depend on whether the bubble was sliding. However, care should be taken before drawing conclusion from the average bubble behavior (i.e., the sliding distance) and characteristic (i.e., the lift-off diameter) as potential effect could be depending on the bubble size and therefore masked by the large number of small bubbles when averaging the different quantities (sliding distance and lift-off diameter). For the purpose of the model, we can however remove the dependance on the flow velocity u.

Also, experimental measurement of the average bubble lift-off diameter showed no discernable effect of the wall superheat. We can also exclude Ja_{sat} from Eq. 6.15. Note that the wall superheat does impact the bubble diameter, but the effect is discernable through spectral analysis of bubble (e.g., by drawing the probability distribution function of finding a bubble with certain footprint radius on the heated surface).

Therefore, we propose the following formulation for the bubble footprint diameter at lift-off,

$$D_{\mathrm{f,lo}} = 3.41 * 10^{-5} \left(\frac{\rho_l - \rho_v}{\rho_v}\right)^{0.27} \quad (6.16)$$

With ρ_{L} and ρ_{V} the density of saturated nitrogen liquid and vapor, respectively. The factor in the formulation is in meter. In the case of nitrogen at around 480 kPa, Eq. 6.4 gives $D_{\mathrm{f,lo}}$ around 88.9 µm, matching the average bubble footprint diameter at lift-off found experimentally.

6.2.3. Wetted time t_{w} and rewetting frequency f_{w}

Fittings law based on experimental measurement are used for evaluating t_{w} and f_{w}. f_{w} is well approximated by,

$$f_{\mathrm{w}} = (at_{\mathrm{w}} + b)^{-1} \tag{6.17}$$

With a and b equal to with 1.051 and 0.81 ms, respectively. We can then relate t_{w} to the wall superheat. Experimental measurement suggests that t_{w} follows this simple power function,

$$t_{\mathrm{w}} = C'\Delta T_{sat}^{-5/2} \tag{6.18}$$

With C' a coefficient equal to 0.117 s.K$^{5/2}$. The coefficient c is potentially a function of the heated surface inclination angle, but the relationship is not clear from our experimental data. Therefore, for the scope of this work, c is assumed constant.

6.2.4. Bubble growth time t_{g}

A bubble growth time model was proposed as closure formulation of the original MIT boiling model. The model is given as followed,

$$t_{\mathrm{g}} = \left(\frac{D_{\mathrm{o,d}}}{4K}\right)^2 \tag{6.19}$$

With K the semi-analytical bubble growth modulus given by,

$$K = \frac{\sqrt{\alpha_l}}{0.804\sqrt{Pr_l}} Ja_{sat} + 1.95\chi Ja_{sat}\sqrt{\alpha_l} = Ja_{sat}\sqrt{\alpha_l}\left\{\frac{1}{0.804\sqrt{Pr_l}} + 3.02\right\} \tag{6.20}$$

With χ a fitting parameter equal to 1.55 for saturated boiling. In Ref. [105], the second term is written as $1.95\chi Ja_{sat}\alpha_l$. We suspect it to be an error as the α_l (rather than $\sqrt{\alpha_l}$) makes dimensions in Eq. 6.20 inconsistent. The model given in Eq. 6.19 assumes that most of bubble growth occurs during the heat-transfer controlled growth regime (with $D \propto \sqrt{t}$). This assumption was validated in Chapter 3. However, from our experimental data, the growth time t_{g} cannot be related to the departure diameter, as most of the bubbles' growth occurs after departing from the nucleation site. One way to see it is by comparing the average bubble footprint diameter at departure and lift-off. Using results of Chapter 3 (Figs. 3.30 and 3.32),

one can see that the departure footprint diameter $D_{f,d}$ is about 40 µm while the average lift-off footprint diameter $D_{f,lo}$ is about 90 µm. Since the effective contact angle is mostly constant over the growth of bubbles, we have $D_{f,d}/D_{f,lo} \sim D_{o,d}/D_{o,lo}$. The ratio of bubble volume between departure and lift-off is about $\left(D_{o,d}/D_{o,lo}\right)^3$, which is proportional to the amount of heat removed by vaporization before bubble departure compared to the total amount of heat removed throughout the growth. This ratio is about ~9 % indicating that most of bubble growth occurs after departure.

Figure 6.2 shows a comparison between the growth modulus K evaluated using Eq. 6.19, and the growth modulus B_o associated with the bubbles optical radius measured experimentally (shown in Chapter 3). On the right plot of Figure 6.2, one can see that Eq. 6.19 correctly predicts the order of magnitude of the growth modulus observed experimentally. The values of K are within ± 40% of the measured growth modulus B_o. However, it is rather clear from Figure 6.2 (left) however that some of the variations of B_o between bubbles are not captured by Eq. 15 (i.e., by K) resulting in scattered data points. Figure 6.2 (right) shows a plot of K/B_o against wall superheat. One can see that most of data scattering is due the wrong dependance of K with wall superheat.

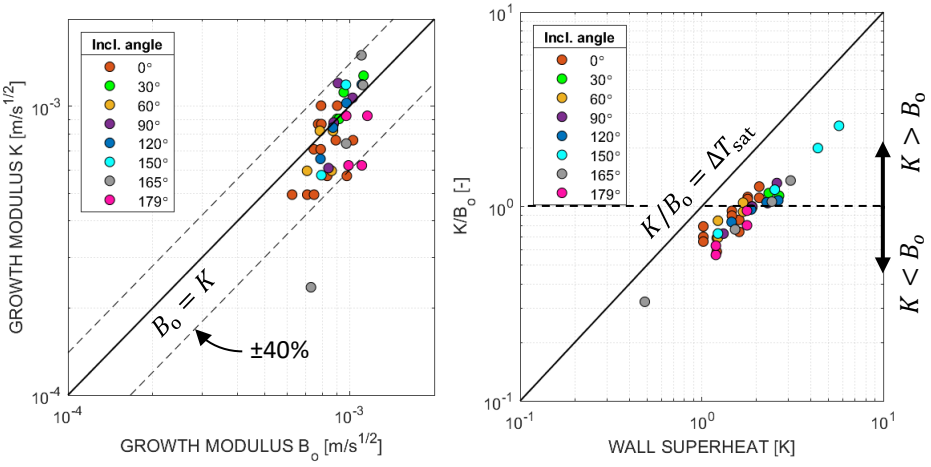

Figure 6.120. Comparison of the growth modulus B_o measured experimentally on the bubble optical radius and the growth modulus K obtained from Eq. 5.13 for the individual nitrogen bubbles analyzed in Chapter 3, on the left plot as K vs. B_o, and on the right plot as K/B_o vs. wall superheat ΔT_{sat}.

We propose a similar expression than given by Eq. 6.19 using the definition of growth time proposed in Chapter 3 ($R_{f,lo} = B_f\sqrt{t_g}$),

$$t_g = \left(\frac{R_{f,lo}}{B_f}\right)^2 \tag{6.21}$$

With B_f the growth modulus associated with the bubble footprint equivalent radius. We observed experimentally the time dependance for the footprint radius and optical radius (both growing as $\propto \sqrt{t}$). Therefore, the growth time could be written equivalently as $t_\mathrm{g} = \left(R_\mathrm{o,lo}/B_\mathrm{o}\right)^2$, with $R_\mathrm{o,lo}$ the optical radius of the bubbles at lift-off. Thus said, dealing with $R_\mathrm{f,lo}$ and B_f is more interesting as both can be measured over the whole range of wall superheat using phase-detection. Since the dependence of K with ΔT_{sat} appears to be disproved by comparing K and B_o, $K \sin\theta_\mathrm{eff}$ cannot predict the trend observed for B_f either. Instead, we provide the following formulation for the growth modulus B_f,

$$B_\mathrm{f} = C''\sqrt{Ja_\mathrm{sat}\alpha_l} \tag{6.22}$$

With C'' a fitting constant. C'' is approximately equal to 2.130 m/s$^{1/2}$. The fitting is shown as a solid black line in Figure 3.34 (see Chapter 3).

6.2.5. Nucleation site density and nucleation frequency

Nucleation site density N''_A and nucleation frequency f are difficult boiling parameters to measure experimentally and to model. One can also see that both parameters appear as a product $N''_\mathrm{A}f$ in 2 of the partitioned heat flux terms q''_{cl} and q''_c. It would typically appear in the quenching heat flux q''_q (as shown in Eq. 6.8). In the present case, this dependance between q''_q and $N''_\mathrm{A}f$ is hidden within $f_\mathrm{w}\sqrt{t_\mathrm{w}}$ (see Eq. 6.9). The product $N''_\mathrm{A}f$, noted $\dot{N}''_\mathrm{N}$, is the nucleation flux (i.e., a number of nucleation events per unit time and heated surface area), and was measured at different wall superheat and inclination angle and plotted in Chapter 4. Since only the product is involved in the estimation of the boiling heat flux, modeling error can be tolerated on N''_A and f as long as the product $\dot{N}''_\mathrm{N}$ is physically accurate. Therefore, in order to minimize the error of the boiling heat flux, it is important that the closure formulations for f and N''_A are used as a pair.

6.2.5.1. Comments on the static interaction correction

Bubbles nucleate from well-located cavities or asperities in the heated surface. Therefore, it is well known that the number of bubbles nucleation events depends on the number of these cavities. However, not all cavities or asperities can produce bubbles and certain conditions needs to be met. Hsu's criterion [92] for nucleation provides a relationship between the size of the cavities, the temperature required to nucleate a bubble and the thermal properties of the fluid. The cavity also requires a vapor embryo to bubbles nucleation at low temperature (i.e., at wall superheat typically observed in boiling curve, 1-10 K in the case of liquid nitrogen above atmospheric pressure). However, in most boiling surfaces used industrially, these 2 criteria

alone are not sufficient to evaluate the density of active nucleation sites on the surface. In order to produce bubbles, a nucleation site has to be covered with liquid. We note N_s'' the density of nucleation sites which satisfy the first 2 criteria (i.e., warm enough and able to keep a vapor embryo), and $N_{s,\alpha}''$ the density of active nucleation sites which satisfy all criteria, and can effectively produce bubbles (i.e., no vapor is present on top of the sites). Note, N_s'' is a much less restrictive quantities as it does not depend on the amount of vapor present on the surface or on the distance between nucleation sites, and therefore should only depends on the heated surface morphology and the wall superheat. There it is easier to obtain a model for N_s'' applicable in a wider range of conditions. Multiple relationships have been proposed to relate N_S'' and N_A'' [35, 105, 106].

$$N_A'' = N_S'' e^{-N_S'' f t_g \frac{\pi}{4} D_{f,lo}{}^2} \text{ from Ref. [35]} \tag{6.23}$$

$$N_A'' = N_S'' e^{-N_A'' f t_g \frac{\pi}{4} D_{f,lo}{}^2} \text{ from Ref. [105]} \tag{6.24}$$

$$N_A'' = N_S'' e^{-N_A'' \frac{\pi}{4} D_{f,lo}{}^2} \text{ from Ref. [106]} \tag{6.25}$$

One can see that these 3 expressions slightly differ from one another, with Eq. 6.23 is explicit in with N_s'', while Eq. 6.24 and 6.25 are implicit. The complete spatial randomness assumption (CSR) was used for deriving the equations. One can see that Eq. 6.25 uses the additional assumption that $f t_g \sim 1$ compared to Eq. 6.24. The multiplicity of these formulation raises a doubt on the validity of at least 2 of them. Another issue is the limits of these expressions when N_s'' gets large.

$$\lim_{N_s'' \to \infty} \text{Eq. } 6.23 = 0 \tag{6.26}$$

$$\lim_{N_s'' \to \infty} \text{Eq. } 6.24 = \infty \tag{6.27}$$

$$\lim_{N_s'' \to \infty} \text{Eq. } 6.25 = \infty \tag{6.28}$$

Note that for small values of N_S'', all expressions lead to N_A'' tending to N_S''. This is consistent with the idea that for a surface where N_S'' is small enough, interaction between sites can be neglected and therefore each site can be active. However, when N_S'' gets large (in particular when the number of bubbles gets large, i.e., $N_{s,\alpha}'' f t_g$), the limits of Eqs. 6.23 to 6.25 appears inconsistent. N_A'' cannot go to 0 (as in Eq. 6.25) which would mean that boiling can be stopped by increasing the number of cavities on the surface. We can however expect that N_A'' tends to infinity when N_S'' grows large. An example would be the idealized case of a heating surface with an infinite number of identical cavities. At a given heat flux, we should then expect the bubble nucleation flux N_N'' (=$N_A'' f$) to be finite (as a finite number of bubbles is necessary to remove

any finite amount of heat from the surface). Since the cavities are all identical, they all have a non-zero probability of generating a bubble. However, as N_A'' grows larger and larger, the probability for a cavity to nucleate a bubble per unit time decreases, which equal to the nucleation frequency f. Therefore, N_A'' can grow infinitely large as long as f becomes infinitely small.

Finally, the formulation given in Eq. 6.28 using the following argument does not appear satisfactory as it uses an additional assumption that a nucleation site cannot be active if it is within a distance $R_{f,lo}$ away from a site already active (or equiv. that $ft_g \sim 1$). With the present data, it is difficult to completely disprove this assumption, because the average value of $R_{f,lo}$ is roughly equal to the minimum distance we required to distinguish active nucleation sites. However, the assumption appears unlikely as we do observe sites producing larger bubbles (with footprint radius at lift-off larger than the average value of $R_{f,lo}$) having active site closer than the footprint radius. For the reasons mentioned above, the formulation given by Eq. 6.27 is used in this work.

We should note the CSR assumption is not valid at any wall superheat. The exact consequence of using the CSR assumption beyond its range of validity to the estimate the boiling heat flux are not clear yet. We present below the analysis used to determine the validity of the CSR assumption (i.e., whether N_A'' follows a homogeneous Poisson distribution) for different values of wall superheat. Also note that unactive nucleation sites cannot be identified during our boiling test as nucleation sites are detected when bubbles nucleate from them, and therefore are active. Figure 6.3 shows an example of the map of active nucleation sites (on the right) for nitrogen pool boiling on an upward facing horizontal surface, obtained from phase-detection images (illustrated on the left).

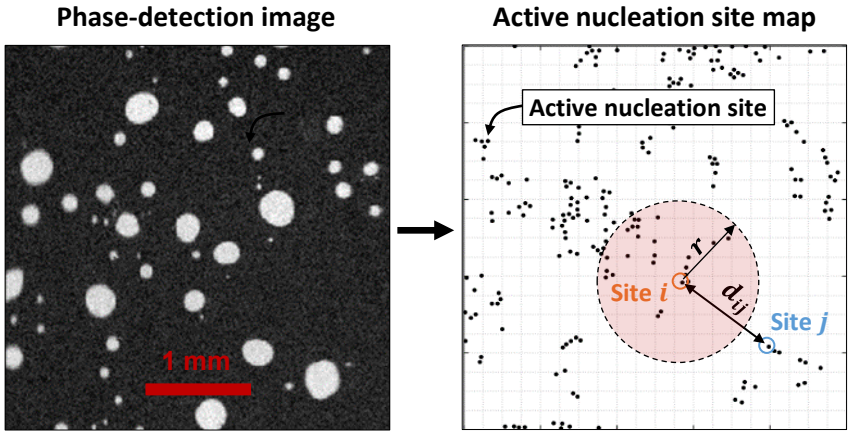

Figure 6.121. Map of active nucleation sites on a horizontal boiling surface superheated at + 2.3 K.

Such active nucleation site maps (illustrated in Figure 6.3 right) can be leveraged to test the CSR assumption. The chosen method to perform this point pattern analysis is Ripley's K statistical test, which

works by comparing the average distance between active nucleation sites maps obtained experimentally to the average distance expected if the sites were distributed with Complete Spatial Randomness. The average distance is evaluating using the Besag's L-function (which is derived from this original Ripley's K function).

$$L(r) = \sqrt{\frac{1}{\pi}\left\{\frac{A}{{N_A}^2}\sum_{i=1}^{N_A}\sum_{j\neq i}^{N_A}\delta(d_{ij})\right\}} \tag{6.29}$$

With i and j the indices representing the nucleation sites, d_{ij} the distance between the site i and j, r the length scale analyzed for potential clustering and δ an indicator function, equal to 1 if $d_{ij} \leq r$ and 0 otherwise. The term within the curly bracket is Ripley's K-function. Figure 6.3 (right) shows the notation used on a nucleation site map obtained experimentally.

Under CSR assumption, $L(r)$ should be equal to r. Figure 6.4 shows an illustrative plot of $L(r) - r$ for the case shown in Figure 6.3 (i.e., horizontal boiling surface at + (4) K. The red line shows the values of $L(r) - r$ using the map of the active nucleation site obtained experimentally, while the blue area shows the simulated values of $L(r) - r$ assuming CSR. The area is bounded by 2 solid black lines corresponding to the 97.5% and 2.5% quantile obtained by drawing 40 random nucleation sites maps with the number of sites equal to the number of sites found experimentally. Positive values of $L(r) - r$ (and in particular above the blue area) translate an anormal number of sites grouped within a disk of a radius r, therefore indicating clustering. Negative values of $L(r) - r$ shows an inhibition of nucleation sites, i.e., nucleation sites tend to have an anormal spacing between them (here anormal means larger than expected assuming CSR). In the case of Figure 6.4, the experimental data highlights a clear clustering of active nucleation sites (the red line is well above the blue area) with a length scale up to 1.2 mm and statistically significant with a p-value of 97.5%.

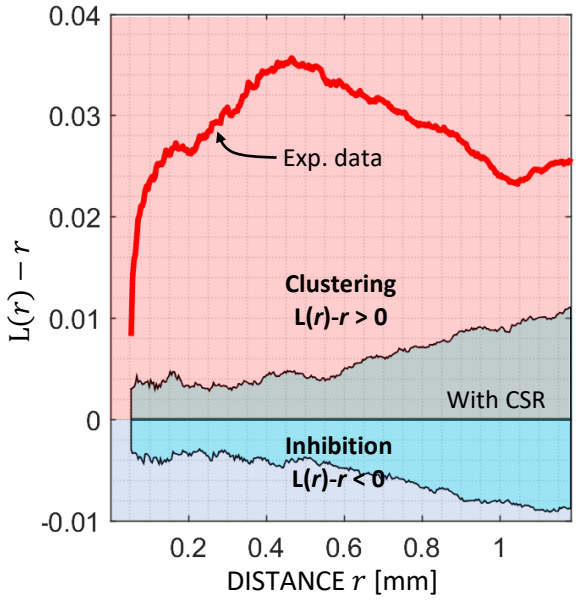

Figure 6.122. Plot of the Besag's L-function obtained with experimental data for horizontal nitrogen pool boiling at + 2.3 K (red line), and under CSR assumption (black line). The blue area indicates the 97.5% and 2.5% quantile of $L(r)$ assuming CSR.

The same analysis than shown in Figures 6.3 and 6.4 can be performed using data obtained at higher wall superheat. Figure 6.5 shows the capture of the phase-detection maps, inferred active nucleation site maps and the Besag's L-function (as $L(r) - r$) for each site maps using experimental data and simulated data assuming CSR. The axis label on the plot of $L(r) - r$ are omitted, but can be seen in Figure 6.4.

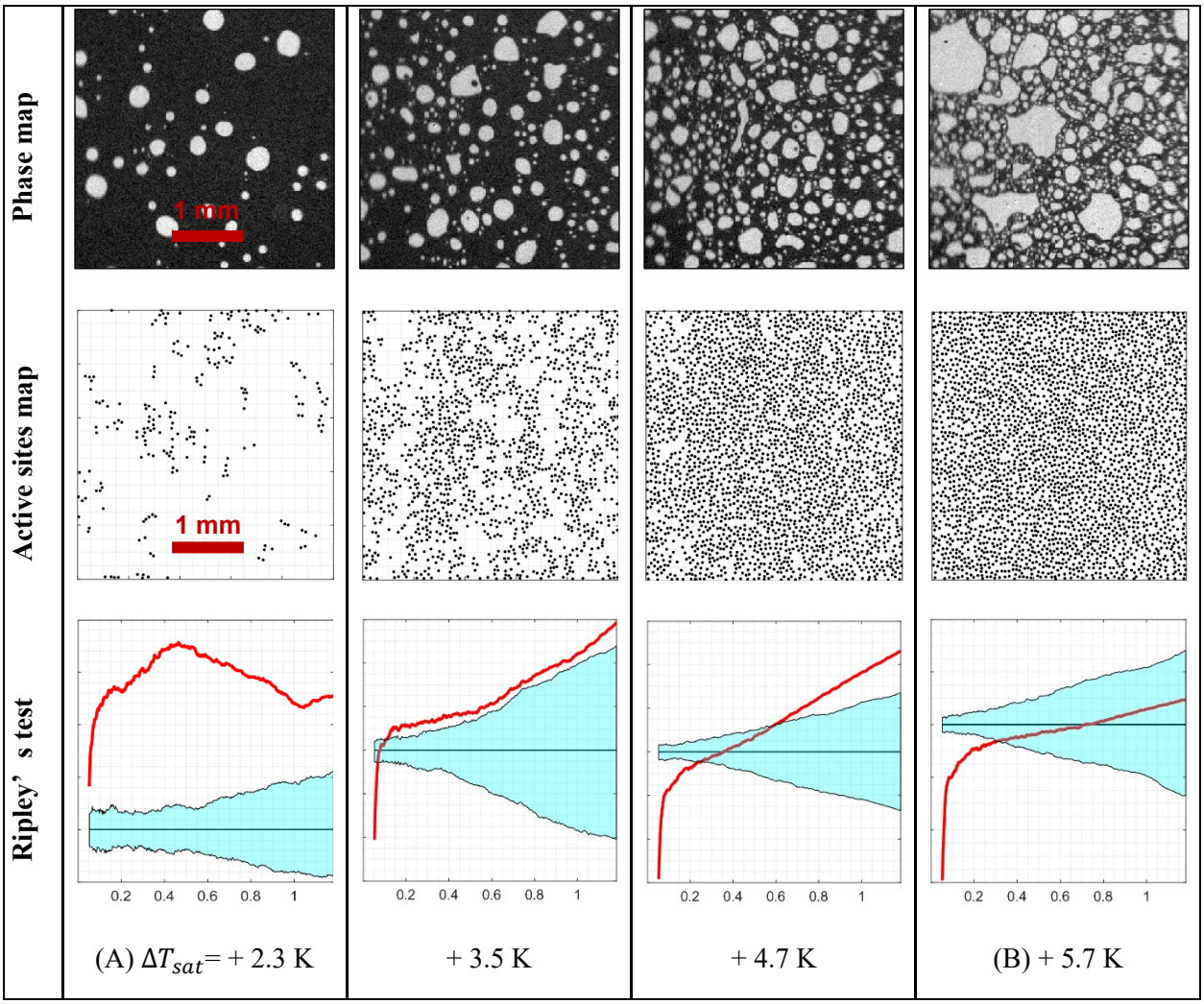

Figure 6.123. Point-pattern analysis of the active nucleation sites maps obtained phase-detection recording for saturated nitrogen pool boiling on a horizontal heated surface. From top to bottom: the phase maps (black indicated vapor while light gray indicated liquid), the corresponding active sites maps with sites represented by a black dot, and the $L(r) - r$ obtained with experimental data (red line), and under CSR assumption (black line). The blue area indicates the 97.5% and 2.5% quantile of the simulated data under CSR.

One can see from Figure 6.5 that the active nucleation site clustering appears at low wall superheat (see column A). However, the tendency for the active nucleation sites to cluster seems to disappear as the wall superheat increases (see column (B)). We suspect that the clustering pattern at low wall superheat is the results of a lack of entrapped vapor embryo in the cavities of the surface. In particular, the presence of large cavities (present in small number) might drive the nucleation on smaller neighboring cavities that cannot trapped vapor for a long enough time by supplying vapor to them. Active nucleation sites inhibition is observed for small distance r. While sites inhibition is a known phenomenon, it would be difficult to draw conclusion here as the method we used to identify nucleation sites prevent us to find 2 sites closer than ~ 60 µm (c.f. Chapter 2 on the nucleation site density measurement technique).

6.2.5.2. Proposed model for nucleation site density

The nucleation site density, noted N_S'', and the active nucleation site density N_A'' are related using Eq. 6.24. N_S'' depends on the morphology of the boiling surface (e.g., cavity size, number and shapes) and on the fluid properties, while N_A'' also depends on the average dry area fraction on the surface. In terms of modelling, it is preferable to model N_S'' since it depends only on data which depends on general boiling conditions (i.e., wall superheat, fluid used, pressure) rather than boiling parameters (i.e., f, t_g, etc.). However, only N_A'' is measured experimentally. We propose the following model to capture the nucleation site density N_S'' (based on Lemmard-Chawla's formulation), such that we can reconstruct the measured values of N_A''

$$N_S'' = N_0'' \Delta T_{sat}{}^{k} \tag{6.30}$$

With N_0'' equal to $1.5*10^7$ s/m^2 and k equal to 2.1. Figure 6.6 shows a plot of N_A'' obtained from experimental measurements for different inclination angles of the heating surface. Note that one can evaluate N_A'' from N_S'' by solving Eq. 6.24, either numerically or by use of the W-Lambert function,

$$N_A'' = \frac{W_0\left(N_S'' f t_g \frac{\pi}{4} D_{f,lo}{}^2\right)}{f t_g \frac{\pi}{4} D_{f,lo}{}^2} \tag{6.31}$$

The fitting line shown in Figure 6.6 is given by Eq. 6.30, 6.31 and the closure formulations for f, t_g and $D_{f,lo}$ given later on in Table 6.1.

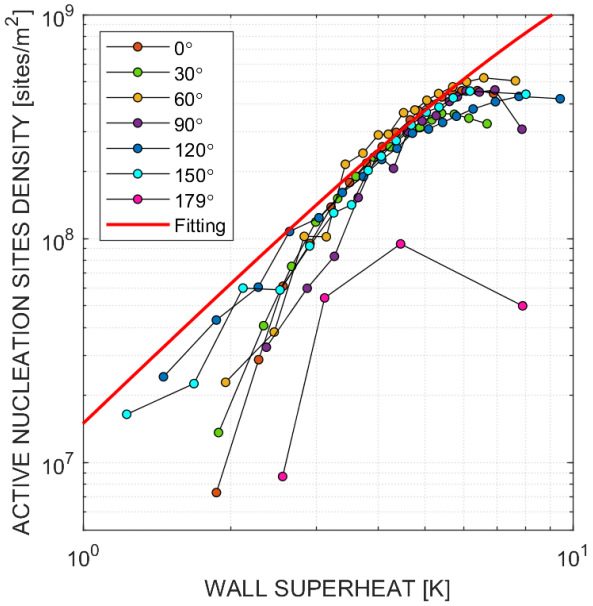

Figure 6.124. Plot of the nucleation site density N_A'' measured experimentally and as modeled by Eq. 6.30-6.31 and the closure formulations of Table 6.1.

All data shows a plateau of the nucleation site density N_A'', which is still appears when N_S'' is back calculated from N_A''. The plateau cannot be captured by any nucleation site density models (e.g., Hibiki-Ishii's model [107]). It might be the consequence of the peculiar morphology of the sapphire substrate we use as heating surface. A lack of very small cavities on the nano-smooth sapphire substrate could explain the lack of new activated sites at high wall superheat. Note that while N_S'' is shown in this model, the proposed formulation (in Eq. 6.30) is expected to quite specific to be heating surface. Therefore, another formulation of N_S'' might be required if the heating surface of interest has a different topology (e.g., a higher roughness) than the sapphire substrate used in this study.

6.2.5.3. Proposed model for nucleation frequency

When bubbles are sliding significantly and interacting, defining a nucleation frequency for a particular nucleation site becomes much more complicated. The typical nucleation frequency model is given by,

$$f = \frac{1}{t_r + t_g} \tag{6.32}$$

With t_r the wait time and t_g the bubble growth time. The issue in this formulation is that the wait time depends on the nucleation sites characteristics (such as their mouth radius if idealized as conical), while the

growth time characterizes bubbles which often do not stay on the nucleation sites they originate from. Therefore, the time needed for a site to reestablish a thermal boundary layer and nucleate a bubble does not depend on the growth time of preceding bubble.

For the present study, we will simply form an expression that allows us to recover the measurement of nucleation flux $\dot{N}_N''$ knowing the values of N_{A}''. The nucleation frequency relating $\dot{N}_N''$ and N_{A}'' is noted $\tilde{f}$, was called systemic frequency. One can easily show that $\tilde{f}$ is also the average nucleation frequency observed among the nucleation sites. In Chapter 4, we showed that $N_{\mathrm{N}}'' \propto {N_{\mathrm{A}}''}^{3/2}$ which leads us to find that $\tilde{f}$ was proportional to ΔT_{sat}. Based on our measurements performed at different values of inclination angle and wall superheat we get that,

$$\tilde{f} = f = 8.5\Delta T_{sat} \tag{6.33}$$

6.2.6. Temperature limit of applicability: onset of nucleate boiling and critical heat flux

The onset of nucleate boiling is difficult to measure experimentally, as it depends on numerous factors, including the boiling surface conditions. Rather than modeling it, the boiling heat flux is extrapolated toward values of wall superheat down to 0. We can easily see from the closure models shown in the previous sections that the active nucleation site density N_{A}'', the nucleation frequency $\tilde{f}$ and the rewetting frequency f_{w} go to 0 when the wall superheat approach 0, leaving only the single-phase convective term q_c''.

The critical heat flux depends on the inclination angle of the heated surface β as shown in Fig. 6. We propose the following correlation,

$$q_{CHF}'' = \begin{cases} q_{CHF,0}'' \text{ for } \beta \leq 90° \\ q_{CHF,0}'' \sqrt{\sin \beta} \text{ for } \beta > 90° \end{cases} \tag{6.34}$$

With $q_{CHF,0}''$ the critical heat flux measured for inclination angle below 90°. $q_{CHF,0}''$ is about 330 kW/m^2 for nitrogen pool boiling at 70 psi-a and is calculated by taking the average of the CHF values observed for a surface inclined between 0° and 90°. A more suitable correlation to evaluate $q_{CHF,0}''$ should be selectable to account for different pressure and fluid.

6.3. Summary of the partitioning model

The partitioning we proposed previously based on our pool boiling data with nitrogen is summarized in Table 6.1.

Table 6.6. Heat flux partitioning model derived from nitrogen pool boiling data.

Partitioning formulation

Partitioning equation	$q''_{\mathrm{w}} = \underbrace{q''_c + q''_q}_{\text{single-phase terms}} + \underbrace{q''_{cL}}_{\text{evaporation term}}$	(P1)
Quenching term q''_q	$q''_q = \varepsilon_l (T_w - T_{sat}) \sqrt{\pi} f_{\mathrm{w}} \sqrt{t_{\mathrm{w}}}$	(P2)
Single-phase convective term q''_c	$q''_c = (1 - \alpha_{\mathrm{v}}) h_{\mathrm{c}} (T_{\mathrm{w}} - T_{\mathrm{b}})$	(P3)
Triple contact line evaporation term q''_{cl}	$q''_{cl} = N''_{\mathrm{A}} \tilde{f} * \left(\frac{\pi}{2} {R_{\mathrm{f,lo}}}^3 \rho_v h_{lv} F(\theta_{\mathrm{eff}}) \right)$	(P4)

Closures formulation

Footprint diameter at lift-off $D_{\mathrm{f,lo}}$	$D_{\mathrm{f,lo}} = 3.41 * 10^{-5} \left(\frac{\rho_l - \rho_v}{\rho_v} \right)^{0.27}$	(P5)
Effective contact angle θ_{eff}	$\theta_{\mathrm{eff}} = C \Delta T_{\mathrm{sat}}^{n}$ With C and n equal to 29.3 and 0.346, respectively, with θ_{eff} in degree.	(P6)
Dry area fraction α_{v}	$\alpha_{\mathrm{v}} = N''_{\mathrm{B}} \frac{\pi}{4} {D_{\mathrm{f}}}^2$ Note that the bubble density N''_{B} is given by $N''_{\mathrm{A}} f t_{\mathrm{g}}$	(P7)
Average footprint diameter	$D_{\mathrm{f}} = 2/3 D_{\mathrm{f,lo}}$	(P8)
Active nucleation site density N''_{A}	$N''_{\mathrm{A}} \approx N''_{\mathrm{S}} * \exp\left(-N''_{\mathrm{A}} f t_{\mathrm{g}} \frac{\pi}{4} {D_{\mathrm{f,lo}}}^2 \right)$	(P9)
Nucleation site density N''_S	$N''_{\mathrm{S}} = N''_0 \Delta {T_{\mathrm{sat}}}^k$ With N''_0 equal to $1.5*10^7$, and k equal to 2.1 with N''_s in site/m^2	(P10)

Growth time t_{g}	$$t_{\mathrm{g}} = \eta \left(\frac{R_{\mathrm{f,lo}}}{B_{\mathrm{f}}}\right)^2$$ With η a correcting factor equal to 0.6.	(P11)
Growth modulus B_{f} ($R_{\mathrm{f}} = B_{\mathrm{f}}\sqrt{t}$)	$$B_{\mathrm{f}} = C''\sqrt{Ja_{\mathrm{sat}}\alpha_l}$$ With C'' equal to 2.130 m/s$^{1/2}$ and $Ja_{\mathrm{sat}} = \frac{\rho_{\mathrm{L}} c_{\mathrm{p,L}} \Delta T_{sat}}{\rho_V h_{LV}}$	(P12)
Nucleation frequency f	$$f = 8.5\Delta T_{\mathrm{sat}}$$	(P13)
Average wetting duration t_{w}	$$t_{\mathrm{w}} = C'\Delta T_{sat}^{-5/2}$$ With C' equal to 0.117 s.K$^{5/2}$	(P14)
Rewetting frequency f_{w}	$$f_{\mathrm{w}} = (at_{\mathrm{w}} + b)^{-1}$$ With a and b equal to 1.051 and 0.81 ms, respectively	(P15)
Critical heat flux q''_{CHF}	$$q''_{CHF} = \begin{cases} q''_{CHF,0} \text{ for } \beta \leq 90° \\ q''_{CHF,0}\sqrt{\sin\beta} \text{ for } \beta > 90° \end{cases}$$ With β the inclination angle of the heated surface measured between its normal and the vertical axis. $q''_{CHF,0}$ is given as 308.8 kW/m^2 (in our operating conditions)	(P16)

6.4. Comparison with experimental data

Figure 6.7 shows plots of the boiling parameters listed in Table 6.1. The experimental measurements of dry area fraction, triple contact line density and bubble density are shown as well for comparison.

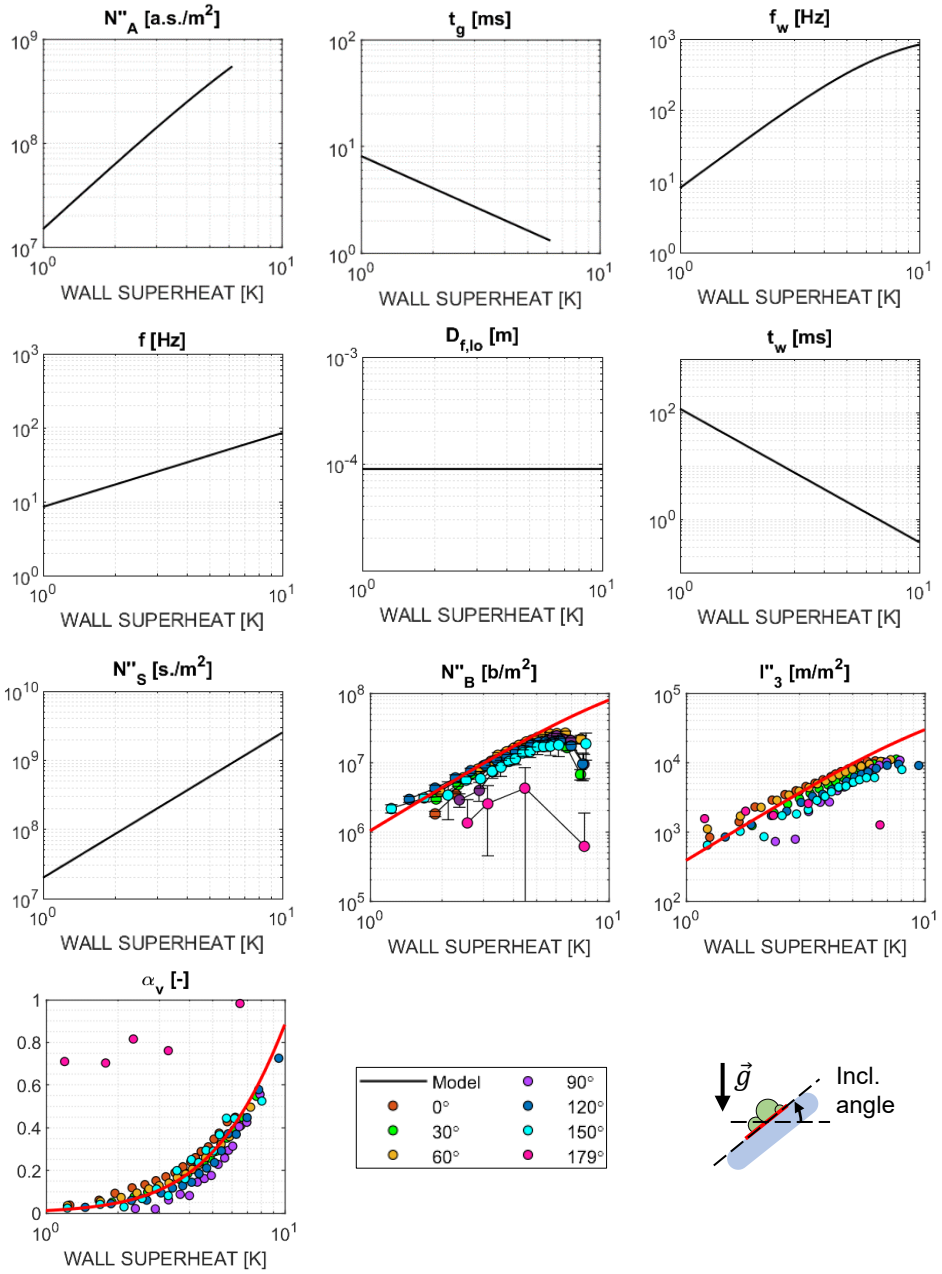

Figure 6.125. Plot of the various boiling parameters obtained from the closure models (shown as solid black line) given in Table 6.1. The colored dots represent the experimental data points on the plot of the dry area fraction α_v and triple contact line density l_3''.

One can see that the order of magnitude for the triple contact line density l_3'', dry area fraction α_v and bubble density N_B'' are well predicted by the closure formulations of the partitioning model. However, it was necessary to add a coefficient η (set to 0.6) in the calculation of the growth time for the model to capture correctly the experimental values of l_3'' , α_v and N_B''. Without it, all three boiling parameters are slightly overestimated. This might be due to the lack of model treating coalescence. N_B'' (and therefore l_3'' and α_v) is evaluated from the nucleation frequency f, growth time t_g and N_A'' alone. None of these parameters accounts for the possibility of bubble coalescence, which will tends to reduce the value of N_B''. Modifying the growth time t_g is a convenient and simple way to reduce N_B''.

A gap between the model and the experimental data is noticeable on the bubble density and dry area fraction for the case of upside-down boiling (with an inclination angle of 179°, shown in pink). This is due to the presence of the large vapor patch early on in the boiling curves. In this case, the process is relatively unstable, as we have shown in Chapter 4, and therefore we should not expect the partitioning model to accurately predict the boiling heat flux.

Figure 6.8 shows the comparison between the heat flux partitioning inferred from the experimental data and the partitioning evaluated using the model given in Table 6.1. The test case is for nitrogen pool boiling on a horizontal heating surface. The cases with other inclination angle are omitted as the boiling curve overlaps for most of the part at the exception of near DNB). The markers are the data points obtained experimentally, showing q_w'', q_{cl}'' and q_q'' in teal, pink and orange. The corresponding heat flux obtained from the model are shown by colored area. The solid black line indicates the boiling curves outputted by the partitioning model. The contributions of each heat transfer mechanism are stack on each other. No single-phase convection is considered here. One can see that the model predicts fairly well the amount of heat removed by each of the mechanisms.

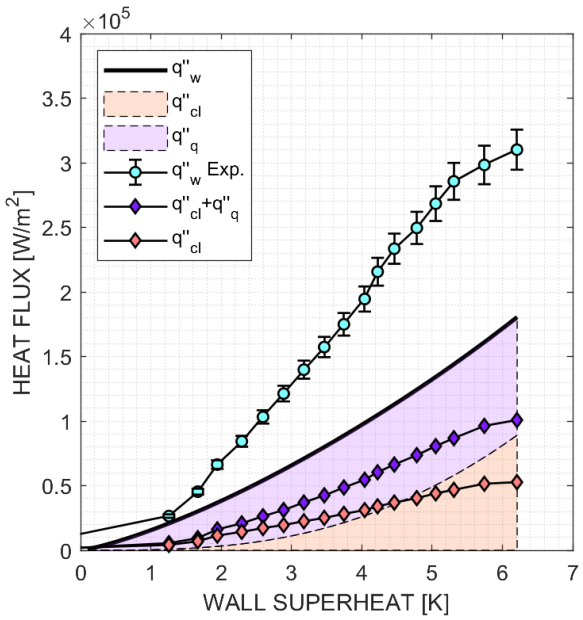

Figure 6.126. Comparison between the boiling curve obtained experimentally (shown with markers) and using the partitioning model (shown by a solid black line) given in Table. 6.1. The colored area indicates the contribution of quenching (purple) and triple contact line evaporation (orange).

6.5. Summary of the chapter

In this chapter, we presented a boiling heat flux partitioning model applicable to cryogens, and in particular liquid nitrogen. The model leverages the observation of the boiling heat transfer discussed in the previous chapters. The partitioning is built around three components: an evaporative heat flux modeling the intense evaporation occurring at the triple contact line, a quenching heat flux due to transient conduction each time the surface is rewetted with cold liquid and a single-phase convection heat flux.

Both the quenching heat flux and the triple contact line evaporation can be well predicted by the partitioning model as long as the required boiling parameters are well predicted themselves by the closure formulation.

In the results presented in this chapter, the heat transfer coefficient associated with the convection heat flux term was to set to 0. The analysis of the experimental data carried out in Chapter 4 shows that about 50% of the boiling heat flux cannot be explained by either the quenching heat flux (assuming transient conduction alone) or the heat flux associated with the triple contact line evaporation. We strongly suspect that turbulence induced by bubbles near the heating surface considerably increases the heat transfer between the surface and the liquid. This also means that the heat transfer coefficient, noted h_c, is likely a complicated function of the triple contact line density and the velocity of the contact line. Formulating a proper model

for h_c is beyond the scope of this work. Nonetheless, the single-phase convective heat flux is implemented in the model for future work.

7. CONCLUSIONS AND FUTURE WORKS

7.1. Conclusions

Predicting accurately boiling heat transfer of cryogens is a critical milestone for the future development of advance technologies with the increasing the range of cryogenic rockets. These technologies include the development cryogenic fuel depot placed in low Earth orbit, and the possibility of reigniting rocket engine in orbit. Boiling takes an important role in these technologies. In the fuel depot, the aims would be to quantify the mass of liquid vaporized over time during boil-off due to environmental heat input, the transient of tank pressure induced by the boil-off gas or during the quenching of fuel transfer line. Boiling heat transfer has been extensively studied over a wide range of working fluid, including cryogens. Yet, models used to predict boiling heat transfer have been incredibly unsuccessful, whether there are empirical models which tends to have only a narrow range of applicability in terms of operating conditions (fluid, pressure, geometric of the heated element, topology of the heated surface, gravitational intensity, etc.), or mechanistic models which simply requires extensive experimental measurements and a thorough understanding of the boiling process to be tuned appropriately. In the latter case, several recent studies have demonstrated the strength of such model, mostly with boiling water [35, 38, 105, 106].

In this work, we aimed at developing the first heat flux partitioning model applicable to cryogens by leveraging new experimental capabilities. Two points of focus were necessary to develop the heat flux partitioning model. First, we needed to gain an understanding on how heat is transferred during boiling of nitrogen. Second, we needed a set of boiling parameters from which we could draw closure models.

A pool boiling setup working with pressurized nitrogen has been designed and built, in which boiling is triggered on the transparent heating element. The transparency of the substrate allowed to us record the boiling process using high-speed shadowgraphy and phase-detection techniques. The space and time resolution of the phase-detection measurement, ~12 μm/px and 14,000 frames per second provide detailed capture of the boiling process, resolving most of the bubbles presented on the boiling surface. Resistance thermometers consisting of chromium oxide thin-film have also been developed as part of this work in order to measure the temperature of the substrate. Along with the measurement of heat input, i.e., the heat generated by the heating thin film (consisting of indium tin oxide), we could reconstruct the space and time average boiling heat flux and the wall surface temperature by solving an inverse conduction problem in the heated substrate. Post-processing tools have been developed to analyze both shadowgraphy and phase-detection images and measure a wide range of boiling parameters, which includes active nucleation site density, bubble growth time, bubble footprint radius and optical radius, etc.

No microlayer has been observed in boiling liquid nitrogen at 480 kPa on our sapphire substrate. Instead, we showed that the large size of the bubble footprint observed experimentally strongly might indicate the presence of an intense evaporation process occurring at the bubbles' triple contact line, starting right after nucleation. Based on this observation, we estimated the evaporation rate at the triple contact line by analyzing 42 bubbles with surface inclination and wall superheat. The linear evaporation rate was measured at around 5 W/m. This result appeared consistent with analytical models describing such evaporation mechanism in other fluids. After evaluating the triple contact line density, we could deduce that the evaporation process accounts for roughly 20% of the boiling heat flux. We also evaluated the amount of heat removed by quenching of the heating surface through transient conduction using phase-detection recordings and assuming a 1-dimension transient conduction heat transfer in the near-wall liquid. The analysis showed that transient conduction during rewetting of the surface accounts for an additional 20% of the boiling heat flux. The remaining 60% of the boiling heat flux could be explained by neither triple contact evaporation nor transient conduction during quenching.

The boiling tests performed with different surface inclination angles from 0° to 179° have shown that the impact of buoyancy is negligible away from DNB. We showed that bubble growth rate does not depend on the surface inclination. More importantly, we showed that the bubbles footprint area probability distribution functions are not impacted by the change of surface inclination at small scale. However, the tail of the footprint area distributions prematurely lift, translating the formation of large vapor patch at lower heat flux for inclination angles above 90°. These observations seemingly coincide with the change in CHF with inclination angle while the boiling heat transfer stay relatively insensitive to it. At DNB, the probability distribution function of bubble footprint area all tend to a scale free distribution with a power law exponent of -2, irrespective of the inclination angle.

In an effort to assess the effect of dissolved contaminant in cryogens, we conducted a series of boiling test comparing high-purity and industrial liquid nitrogen with nitrogen saturated with carbon dioxide. Phase-detection recording and boiling curves measurements showed neither sign of contamination on the heating surface nor differences in the boiling heat transfer when comparing industrial and high-purity nitrogen. The boiling test conducted with carbon dioxide-saturated liquid nitrogen highlighted a build up of carbon dioxide deposits, forming by precipitation during evaporation of the liquid nitrogen. This is consistent with the fact of the amount of fouling on the surface appears to depend on the duration of the deposition as well as the boiling heat flux. We showed that the locations of the deposits match with the location of active nucleation site before the formation of deposits. Surprisingly, the carbon dioxide fouling appeared to enhance the boiling heat transfer. We showed that the presence of the microscopic deposits of carbon dioxide on the heating surface changes the boiling dynamics by lowering the nucleation temperature of the

existing nucleation sites. When the heat flux is decreased to a low value, we showed that the presence of the deposits formed at high heat flux allows to maintain a significant number of nucleation sites that should be active only at high heat flux on clean surface.

Finally, the heat flux partitioning model proposed in this work allows to predict the quenching heat flux, the triple contact line evaporation as well as the observed dry area fraction, contact line density and bubble density during nitrogen boiling. Minimal effect of surface inclination has been observed on the nucleate boiling heat transfer, except at the departure from nucleate boiling. The partitioning model integrates this observation by a simple critical heat flux formulation which depends on surface inclination.

7.2. Future work

- A certain number of fitting coefficients were necessary to write closure models (e.g., for θ_{eff}, $D_{\mathrm{f,lo}}$, f, f_w and t_w). To ensure that the partitioning model does reasonable predictions over a wide range of operating conditions (fluid, pressure, microgravity, etc.), more physically accurate formulations of these models have to be derived.
- This work highlighted the lack of microlayer during bubble growth. Instead, the observations suggested that the evaporative heat transfer occurs at the bubbles' triple contact line. This appears to be the consequence of the liquid evaporation near the contact line occurring faster that the formation of the microlayer from hydrodynamics. In fact, recent nitrogen boiling test performed on a substrate with a lower thermal effusivity have shown some microlayer formation. It would be necessary to evaluate whether the presence of a microlayer evaporation regimes during bubble growth changes the boiling parameters (in particular the lift-off diameter and the growth time). The proposed should be revised for including such behavior.
- The quenching heat flux with transient conduction only, and triple contact line evaporation explains only partially the total heat flux measured. There are several possibilities to solve this discrepancy. Recent investigations using the same setup than used in this study suggest a potential underestimation of the wall temperature by a couple degrees, and therefore an underestimation of the quenching heat flux. Another alternation would be that that the remaining heat flux is transferred by the near-wall turbulence generated by the cohort of nucleating bubbles during boiling. In both cases, more accurate wall temperature measurement with potentially resolving (in space and time) the temperature and heat flux fields in the vicinity of nucleating and growing bubbles would be the

key necessary to probe these hypotheses. This might be done by using phosphor thermometry techniques, or more complex RTDs arrays coated on the substrate.

- Cryogenic fouling was shown to increase the boiling heat transfer by lowering the nucleation temperature of pre-existing nucleation sites. This appears to contradict most previous findings showing the degradation of the heat transfer with increasing foulant. The amount of foulant on the heating surface and the location of the deposits might play a critical role on whether it improves or degrade the heat transfer. It also remains unclear why the nucleation temperature of nucleation sites is lowered in presence of carbon dioxide deposits. Further tests on surfaces with different amount of nucleation sites and with longer duration of deposition might help answering these 2 open questions.

- The heating surface used in this study is expected to show some differences with surfaces more commonly used industrially, with potentially with higher roughness (with a broader range of cavity size and in larger number) and lower thermal conductivity (e.g., the thermal conductivity of stainless steel 316 is about 50 times lower than sapphire). Specific studies of the effect of surface morphology and substrate thermal properties on cryogenic boiling heat transfer would be necessary to assess the applicability of our partitioning model on those surfaces.

8. REFERENCES

[1] Radebaugh, R. (2002). *Macmillan Encyclopedia of Chemistry* (ed. Lagowski, Joseph J.). New York: Macmillan.

[2] Collaudin, B., & Rando, N. (2000). Cryogenics in space: A review of the missions and of the technologies. *Cryogenics*. https://doi.org/10.1016/S0011-2275(01)00035-2

[3] Jenkins, D. R. (2001). Space Shuttle: The History of the National Space Transportation System: The First 100 Missions. Dennis Jenkins.

[4] Tanner, C., Young, J., Thompson, R., & Wilhite, A. (2006). On-orbit propellant resupply options for mars exploration architectures. AIAA 57th International Astronautical Congress, IAC 2006. https://doi.org/10.2514/6.iac-06-d1.1.01

[5] Kutter, B. F., Zegler, F., O'Neil, G., & Pitchford, B. (2008). A practical, affordable cryogenic propellant depot based on ULA's flight experience. Space 2008 Conference. https://doi.org/10.2514/6.2008-7644

[6] Tseng, C. C., & Shyy, W. (2010). Modeling for isothermal and cryogenic cavitation. International Journal of Heat and Mass Transfer. https://doi.org/10.1016/j.ijheatmasstransfer.2009.09.005

[7] Chung, J. N., Darr, S. R., Dong, J., Wang, H., & Hartwig, J. W. (2020). Heat transfer enhancement in cryogenic quenching process. International Journal of Thermal Sciences, 147(August 2018), 106117. https://doi.org/10.1016/j.ijthermalsci.2019.106117

[8] Jin, L., Cho, H., Lee, C., & Jeong, S. (2018). Experimental research and numerical simulation on cryogenic line chill-down process. Cryogenics, 89, 42–52. https://doi.org/10.1016/j.cryogenics.2017.11.003

[9] Hartwig, J., Darr, S., & Asencio, A. (2016). Assessment of existing two phase heat transfer coefficient and critical heat flux correlations for cryogenic flow boiling in pipe quenching experiments. International Journal of Heat and Mass Transfer, 93, 441–463. https://doi.org/10.1016/j.ijheatmasstransfer.2015.09.028

[10] Konishi, C., & Mudawar, I. (2015). Review of flow boiling and critical heat flux in microgravity. International Journal of Heat and Mass Transfer, 80, 469–493. https://doi.org/10.1016/j.ijheatmasstransfer.2014.09.017

[11] Mustafi, S. (2014). High Reynolds number vertical up-flow parameters for cryogenic two-phase helium I, Ph.D. University of Maryland, College Park.

[12] Shah, M. M. (1984). Prediction of heat transfer during boiling of cryogenic fluids flowing in tubes. Cryogenics, 24(5), 231–236. https://doi.org/10.1016/0011-2275(84)90148-6

[13] Stephan, K., & Abdelsalam, M. (1980). Heat-transfer correlations for natural convection boiling. International Journal of Heat and Mass Transfer, 23(1), 73–87. https://doi.org/10.1016/0017-9310(80)90140-4

[14] Klimenko, V. V. (1982). Heat transfer intensity at forced flow boiling of cryogenic liquids in tubes. Cryogenics. https://doi.org/10.1016/0011-2275(82)90003-0

[15] Rohsenow, W.M. (1952). A Method of Correlating Heat Transfer Data for Surface Boiling of Liquids. Trans. ASME (74): 969.

[16] Antar, B. N., & Collins, F. G. (1997). Flow boiling during quench in low gravity environment. Microgravity Science and Technology.

[17] Darr, S., Dong, J., Glikin, N., Hartwig, J., Majumdar, A., Leclair, A., & Chung, J. (2016). The effect of reduced gravity on cryogenic nitrogen boiling and pipe chilldown. Npj Microgravity. https://doi.org/10.1038/npjmgrav.2016.33

[18] Darr, S. R., Hartwig, J. W., Dong, J., Wang, H., Majumdar, A. K., LeClair, A. C., & Chung, J. N. (2019). Two-phase pipe quenching correlations for liquid nitrogen and liquid hydrogen. Journal of Heat Transfer, 141(4). https://doi.org/10.1115/1.4041830

[19] Kawanami, O., Azuma, H., & Ohta, H. (2007). Effect of gravity on cryogenic boiling heat transfer during tube quenching. International Journal of Heat and Mass Transfer, 50(17–18), 3490–3497. https://doi.org/10.1016/j.ijheatmasstransfer.2007.01.025

[20] Chung, J.N., Dong, J., Wang, H., Darr, S.R., and Hartwig, J.W. (2021). An Advance in Transfer Line Chilldown Heat Transfer of Cryogenic Propellants in Microgravity using Microfilm Coatings for Enabling Deep Space Explorations. Nature Microgravity 7, 21.

[21] Hartwig, J.W., Chung, J.N., Dong, J., Han, B., Wang, H., Darr, S.R., Taliaferro, M., Jain, S., and Doherty, M. (2022). Cryogenic Nitrogen Flow Boiling and Chilldown Experiments in Microgravity using Pulse Flow and Low Thermally Conductive Coatings. Nature Microgravity 8, 33.

[22] Lemmon, E.W., Bell, I.H., Huber, M.L., McLinden, M.O. (2010). NIST Standard Reference Database 23: Reference Fluid Thermodynamic and Transport Properties-REFPROP, Version 9.0. National Institute of Standards and Technology, Standard Reference Data Program, Gaithersburg.

[23] Bombardieri, C., & Manfletti, C. (2016). Influence of wall material on nucleate pool boiling of liquid nitrogen. International Journal of Heat and Mass Transfer, 94, 1–8. https://doi.org/10.1016/j.ijheatmasstransfer.2015.10.049
[24] Müller-Steinhagen, H. M. (1988). Fouling phenomena during boiling of cryogenic liquids. Cryogenics. https://doi.org/10.1016/0011-2275(88)90040-9
[25] Müller-Steinhagen, H. (1984). Wärmeübergang und Fouling beim Strömungssieden von Argon und Stickstoff im horizontalen Rohr. Forschung Im Ingenieurwesen. https://doi.org/10.1007/BF02575035
[26] Bewilogua, L., Görner, W., Knöner, R., & Vinzelberg, H. (1974). Heat transfer in liquid hydrogen. Cryogenics. https://doi.org/10.1016/0011-2275(74)90132-5
[27] Bald, W. B. (1973). Cryogenic heat transfer research at Oxford. Part 1 - nucleate pool boiling. Cryogenics, 13(8), 457–469. https://doi.org/10.1016/0011-2275(73)90002-7
[28] Kirichenko, Y. A., Rusanov, K. V., & Tyurina, E. G. (1986). The shapes and sizes of vapor bubbles during boiling on downward-facing flat surfaces. Journal of Engineering Physics. https://doi.org/10.1007/BF00870675
[29] Brennan, P. J. & Skrabek, E. A. (1971). Design and Development of a Prototype Static Cryogenic Heat Transfer System. Technical Report for Goddard Space Flight Center (NASA). Contract NAS5-2U91.
[30] Bowring, R.W. (1962). Physical Model, Based on Bubble Detachment, and Calculation of Steam Voidage in the Subcooled Region of a Heated Channel. Master Thesis. Institutt for atomenergi OECD Halden Reactor Project.
[31] Mikic, B. B., & Rohsenow, W. M. (1969). A new correlation of pool-boiling data including the effect of heating surface characteristics. Journal of Heat Transfer. https://doi.org/10.1115/1.3580136
[32] Judd, R. L., & Hwang, K. S. (1976). A comprehensive model for nucleate pool boiling heat transfer including microlayer evaporation. Journal of Heat Transfer. https://doi.org/10.1115/1.3450610
[33] Kurul, N. & Podowski, M. (1990). Multidimensional effects in forced convection sub- cooled boiling. In: Proceedings of the Ninth International Heat Transfer Conference, vol. 2, pp. 21–26.
[34] Dhir, V. K. (2006). Mechanistic prediction of nucleate boiling heat transfer-achievable or a hopeless task? Journal of Heat Transfer. https://doi.org/10.1115/1.2136366
[35] Gilman, L. and Baglietto, E. (2017). A self-consistent, physics-based boiling heat transfer modeling framework for use in computational fluid dynamics. International Journal of Multiphase Flow, vol. 95, pp. 35–53.
[36] Zuber, N. (1963). Nucleate boiling. The region of isolated bubbles and the similarity with natural convection. International Journal of Heat and Mass Transfer, 6(1), 53–78. https://doi.org/10.1016/0017-9310(63)90029-2
[37] Cole, R. (1960). A photographic study of pool boiling in the region of the critical heat flux. AIChE Journal. https://doi.org/10.1002/aic.690060405
[38] Richenderfer, A., Kossolapov, A., Seong, J. H., Saccone, G., Demarly, E., Kommajosyula, R., Baglietto, E., Buongiorno, J. and Bucci, M. (2018). Investigation of subcooled flow boiling and CHF using high-resolution diagnostics. Experimental Thermal and Fluid Science, 99, 35–58.
[39] Brentari, E. G. (1965). Boiling heat transfer for oxygen, nitrogen, hydrogen, and helium. https://doi.org/10.6028/NBS.TN.317
[40] Kida, M., Kikuchi, Y., Takahashi, O., & Michiyoshi, I. (1981). Pool-boiling heat transfer in liquid nitrogen. Journal of Nuclear Science and Technology. https://doi.org/10.1080/18811248.1981.9733284
[41] Jin, T., Zhang, S. Y., Tang, K., & Huang, Y. Z. (2011). Observation and analysis of the detachment frequency of coalesced bubbles in pool boiling liquid nitrogen. Cryogenics, 51(9), 516–520. https://doi.org/10.1016/j.cryogenics.2011.06.007
[42] Chen, H., Chen, G., Zou, X., Yao, Y., & Gong, M. (2017). Experimental investigations on bubble departure diameter and frequency of methane saturated nucleate pool boiling at four different pressures. International Journal of Heat and Mass Transfer, 112, 662–675. https://doi.org/10.1016/j.ijheatmasstransfer.2017.05.031
[43] Kirichenko, Y. A., Tsybul'skii, V. V., Dolgoi, M. L., Rusanov, K. V., & Konovalov, I. M. (1975). Effect of pressure on internal characteristics of nitrogen and oxygen boiling. Journal of Engineering Physics. https://doi.org/10.1007/BF00878210
[44] Bland, M. E., Bailey, C. A., & Davey, G. (1973). Boiling from metal surfaces immersed in liquid nitrogen and liquid hydrogen. Cryogenics. https://doi.org/10.1016/0011-2275(73)90151-3
[45] Mikic, B. B. (1969). Bubble growth rates in non-uniform temperature field. Progress in Heat and Mass Transfer, 2, 283–293. http://ci.nii.ac.jp/naid/10025228115/en/
[46] Bankoff, S. G. (1958). Entrapment of gas in the spreading of a liquid over a rough surface. AIChE Journal. https://doi.org/10.1002/aic.690040105
[47] Van Carey, P. (2018). Liquid vapor phase change phenomena: An introduction to the thermophysics of vaporization and condensation processes in heat transfer equipment, Second Edition. In Liquid Vapor Phase Change Phenomena:

An Introduction to the Thermophysics of Vaporization and Condensation Processes in Heat Transfer Equipment, Second Edition. https://doi.org/10.1201/9780203748756
[48] Sakurai, A., Shiotsu, M., Hata, K., & Fukuda, K. (2000). Photographic study on transitions from non-boiling and nucleate boiling regime to film boiling due to increasing heat inputs in liquid nitrogen and water. Nuclear Engineering and Design. https://doi.org/10.1016/S0029-5493(99)00325-8
[49] Shiotsu, M., Hata, K., & Sakurai, A. (1990). Heterogeneous spontaneous nucleation temperature on solid surface in liquid nitrogen. In Advances in Cryogenic Engineering. https://doi.org/10.1007/978-1-4613-0639-9_52
[50] Rest, A.J., Scurlock, R.G. and Wu, M.F. (1990). The solubilities of nitrous oxide, carbon dioxide, aliphatic ethers and alcohols, and water in cryogenic liquids. The Chemical Engineering Journal, 43(1), pp.25-31.
[51] Thome, J.R., 1978. Nucleate pool boiling in cryogenic binary mixtures (Doctoral dissertation).
[52] Thome, J.R. and Bald, W.B., 1978. Nucleate pool boiling in cryogenic binary mixtures. In Proceedings of the 7th International Cryogenic Engineering Conference, London, S (pp. 523-530).
[53] Bland, M.E. 1970. Bubble nucleation in cryogenic fluids (Doctoral dissertation).
[54] Lyon, D.N., 1964. Peak nucleate-boiling heat fluxes and nucleate-boiling heat-transfer coefficients for liquid N2, liquid O2 and their mixtures in pool boiling at atmospheric pressure. International Journal of Heat and Mass Transfer, 7(10), pp.1097-1116.
[55] Kosky, P. G., & Lyon, D. N. (1968). Pool boiling heat transfer to cryogenic liquids; I. Nucleate regime data and a test of some nucleate boiling correlations. AIChE Journal. https://doi.org/10.1002/aic.690140307
[56] Ortega, D., Amador, A., Mohiuddin A., Choudhuri, A., and Mahamudur Rahman, M., 2023. Liquid Nitrogen Flow Boiling Critical Heat Flux in Additively Manufactured Cooling Channels. Aerospace. 10 (6), 499.
[57] Müller-Steinhagen, H., Bonn, W. and Steiner, D., 1982. Fouling phenomena during the evaporation of argon. Proceedings of the International Cryogenic Engineering Conference, pp.73-76.
[58] Scurlock, R.G., 1995. Enhanced boiling heat transfer surfaces. Cryogenics, 35 (4), pp.233-237.
[59] Slack, G. A., 1980. Thermal conductivity of ice. Physical Review B, 22 (6), 3065–3071.
[60] Sumarokov, V. V., Stachowiak, P., and Jeżowski, A., 2003. Low-temperature thermal conductivity of solid carbon dioxide. Low Temperature Physics, 29 (5), 449–450.
[61] Jung, S., & Kim, H. (2014). An experimental method to simultaneously measure the dynamics and heat transfer associated with a single bubble during nucleate boiling on a horizontal surface. International Journal of Heat and Mass Transfer. https://doi.org/10.1016/j.ijheatmasstransfer.2014.02.014
[62] Koffman, L. D., & Plesset, M. S. (1983). Experimental observations of the microlayer in vapor bubble growth on a heated solid. Journal of Heat Transfer. https://doi.org/10.1115/1.3245631
[63] Cooper, M. G., & Lloyd, A. J. P. (1969). The microlayer in nucleate pool boiling. International Journal of Heat and Mass Transfer, 12(8), 895–913. https://doi.org/10.1016/0017-9310(69)90154-9
[64] Cooper, M. G., & Lloyd, A. J. P. (1969). The microlayer in nucleate pool boiling. International Journal of Heat and Mass Transfer, 12(8), 895–913. https://doi.org/10.1016/0017-9310(69)90154-9
[65] Guion, A., Afkhami, S., Zaleski, S., & Buongiorno, J. (2018). Simulations of microlayer formation in nucleate boiling. International Journal of Heat and Mass Transfer, 127, 1271–1284. https://doi.org/10.1016/j.ijheatmasstransfer.2018.06.041
[66] Kossolapov, A., Phillips, B., & Bucci, M. (2021). Can LED lights replace lasers for detailed investigations of boiling phenomena? International Journal of Multiphase Flow. https://doi.org/10.1016/j.ijmultiphaseflow.2020.103522
[67] Stephan, P., & Hammer, J. (1994). A new model for nucleate boiling heat transfer. Heat and Mass Transfer, 30(2), 119-125.
[68] Raj, R., Kunkelmann, C., Stephan, P., Plawsky, J., & Kim, J. (2012). Contact line behavior for a highly wetting fluid under superheated conditions. International Journal of Heat and Mass Transfer, 55(9-10), 2664–2675. doi:10.1016/j.ijheatmasstransfer.2011.12.026
[69] Clark, J. A. (1969). Cryogenic Heat Transfer. Advances in Heat Transfer. https://doi.org/10.1016/S0065-2717(08)70132-1
[70] Straub, J. (2001). Boiling heat transfer and bubble dynamics in microgravity. In Advances in Heat Transfer. https://doi.org/10.1016/S0065-2717(01)80020-4
[71] Merte, H., & Clark, J. A. (1964). Boiling heat transfer with cryogenic fluids at standard, fractional, and near-zero gravity. Journal of Heat Transfer, 86(3), 351–358. https://doi.org/10.1115/1.3688689
[72] Nishikawa, K., Fujita, Y., Uchida, S., & Otha, H. (1984). Effect of surface configuration on nucleate boiling heat transfer. International Journal of Heat and Mass Transfer, 27(9), 1559–1571. https://doi.org/10.1016/0017-9310(84)90268-0

[73] Haynes, W.M. (Ed.). (2016). CRC Handbook of Chemistry and Physics (97th ed.). CRC Press. https://doi.org/10.1201/9781315380476
[74] Warkusz, F. (1978). The size effect and the temperature coefficient of resistance in thin films. J. Phys. D: Appl. Phys. 11, 689-694.
[75] Singh, B., & Surplice, N. A. (1972). The electrical resistivity and resistance-temperature characteristics of thin titanium films. Thin Solid Films. 10 (2): 243-253, https://doi.org/10.1016/0040-6090(72)90191-5
[76] Nash, C. R., Fenton, J. C., Constantino, N. G. N., & Warburton, P. A. (2014). Compact chromium oxide thin film resistors for use in nanoscale quantum circuits. Journal of Applied Physics, 116(22). https://doi.org/10.1063/1.4901933
[77] Dobrovinskaya, E.R., Lytvynov, L.A. and Pishchik, V. (2009). Sapphire: Material, Manufacturing, Applications. Springer Science & Business Media, New York.
[78] Ronneberger, O., Fischer, P., Brox, T. (2015). U-Net: Convolutional Networks for Biomedical Image Segmentation. In: Navab, N., Hornegger, J., Wells, W., Frangi, A. (eds) Medical Image Computing and Computer-Assisted Intervention – MICCAI 2015. MICCAI 2015. Lecture Notes in Computer Science, vol 9351. Springer, Cham. https://doi.org/10.1007/978-3-319-24574-4_28
[79] Seong, J. H., Ravichandran, M., Su, G., Phillips, B., & Bucci, M. (2023). Automated bubble analysis of high-speed subcooled flow boiling images using U-net transfer learning and global optical flow. International Journal of Multiphase Flow, 159, 104336.
[80] Bellur, K., Konduru, V., Kulshrestha, M., Tyrewala, D., Medici, E., Allen, J. S., ... & Tamilarasan, A. (2016). Contact angle measurement of liquid hydrogen (LH2) in stainless steel and aluminum cells. Journal of Heat Transfer, 138(2), 020904.
[81] Scriven, L. E. (1995). On the dynamics of phase growth. Chemical engineering science, 50(24), 3907-3917.
[82] Plesset, M. S., & Zwick, S. A. (1954). The growth of vapor bubbles in superheated liquids. Journal of applied physics, 25(4), 493-500.
[83] Brennen, C. (2013). Cavitation and Bubble Dynamics. Cambridge: Cambridge University Press. doi:10.1017/CBO9781107338760
[84] Lorenz, J. J., Mikic, B. B., & Rohsenow, W. M. (1974). The effect of surface conditions on boiling characteristics. In International Heat Transfer Conference Digital Library. Begel House Inc..
[85] Finn, R. (2012). Equilibrium capillary surfaces (Vol. 284). Springer Science & Business Media.
[86] Nikolayev, V. S., & Beysens, D. A. (1999). Boiling crisis and non-equilibrium drying transition. Europhysics Letters, 47(3), 345.
[87] Nikolayev, V. S. (2010). Dynamics of the triple contact line on a nonisothermal heater at partial wetting. Physics of Fluids, 22(8).
[88] Mathieu, B., Lebaigue, O., & Tadrist, L. (2003, May). Dynamic contact line model applied to single bubble growth. In Proceedings of the 41st European Two-Phase Flow Group Meeting.
[89] Moissis, R., & Berenson, P. J. (1963). On the hydrodynamic transitions in nucleate boiling.
[90] Wang, C., Su, G., Akinsulire, O., Zhang, L., Rahman, M. M., & Bucci, M. (2024). Investigation of critical heat flux enhancement on nanoengineered surfaces in pressurized subcooled flow boiling using infrared thermometry. Heat Transfer Engineering, 45(4-5), 417-432.
[91] Zhang, L., Wang, C., Su, G., Kossolapov, A., Matana Aguiar, G., Seong, J. H., ... & Bucci, M. (2023). A unifying criterion of the boiling crisis. Nature Communications, 14(1), 2321.
[92] Hsu, Y. Y. (1962). On the size range of active nucleation cavities on a heating surface.
[93] Zupančič, M., Gregorčič, P., Bucci, M., Wang, C., Aguiar, G. M., & Bucci, M. (2022). The wall heat flux partitioning during the pool boiling of water on thin metallic foils. Applied Thermal Engineering, 200, 117638.
[94] Kakaç, S., Yener, Y., & Naveira-Cotta, C. P. (2018). Heat conduction. CRC press.
[95] Kommajosyula, R. (2020). Development and assessment of a physics-based model for subcooled flow boiling with application to CFD. PhD thesis, Massachusetts Institute of Technology.
[96] Schweizer, N. (2010). Multi-scale investigation of nucleate boiling phenomena in microgravity (Doctoral dissertation, Technische Universität).
[97] Brusstar, M. J., Merte Jr, H., Keller, R. B., & Kirby, B. J. (1997). Effects of heater surface orientation on the critical heat flux—I. An experimental evaluation of models for subcooled pool boiling. International journal of heat and mass transfer, 40(17), 4007-4019.
[98] Tempelmeyer, K. E. and Mills D. W.,1968. Refractive Index of Carbon Dioxide Cryodeposit. Journal of Applied Physics, 39 (6): 2968–2969.
[99] Berce, J., Zupančič, M., Može, M. and Golobič, I., 2021. A Review of Crystallization Fouling in Heat Exchangers. Processes, 9, 1356.

[100] Dash, S., Rapoport, L., and Varanasi, K. K, 2017. Crystallization-Induced Fouling during Boiling: Formation Mechanisms to Mitigation Approaches. Langmuir, 34 (3), 782–788.
[101] Marto, P. J., Moulson, J. A., and Maynard, M. D., 1968. Nucleate Pool Boiling of Nitrogen With Different Surface Conditions. ASME. J. Heat Transfer, 90(4): 437–444.
[102] Giauque, W. F., & Egan, C. J., 1937. Carbon dioxide. The heat capacity and vapor pressure of the solid. The heat of sublimation. Thermodynamic and spectroscopic values of the entropy. The Journal of Chemical Physics, 5(1), 45-54.
[103] Sazhin, S., 2014. Droplets and sprays. London: Springer. 345 pp. ISBN 978-1-4471-6385-5
[104] Phillips B.A., (2014). Experimental investigation of subcooled flow boiling using synchronized high-speed video, infrared thermography, and particle image velocimetry. PhD thesis, Massachusetts Institute of Technology.
[105] Kommajosyula, R. (2020). Development and assessment of a physics-based model for subcooled flow boiling with application to CFD. PhD thesis, Massachusetts Institute of Technology.
[106] Su, G. Y., Wang, C., Zhang, L., Seong, J. H., Kommajosyula, R., Phillips, B., & Bucci, M. (2020). Investigation of flow boiling heat transfer and boiling crisis on a rough surface using infrared thermometry. International Journal of Heat and Mass Transfer, 160, 120134.
[107] Hibiki, T., & Ishii, M. (2003). Active nucleation site density in boiling systems. International Journal of Heat and Mass Transfer, 46(14), 2587-2601.
[108] Lamb, H. (1924). Hydrodynamics. University Press.